

The Ursa Major cluster of galaxies

IV. HI synthesis observations

M. A. W. Verheijen^{1,2} and R. Sancisi^{2,3}

¹ NRAO, PO Box O, Socorro, NM 87801, USA

² Kapteyn Institute, Postbus 800, 9700 AV Groningen, The Netherlands

³ Osservatorio Astronomico di Bologna, Via Ranzani 1, 40127 Bologna, Italy

Received 15 November 2000 / Accepted 1 December 2000

Abstract. In this data paper we present the results of an extensive 21 cm-line synthesis imaging survey of 43 spiral galaxies in the nearby Ursa Major cluster using the Westerbork Synthesis Radio Telescope. Detailed kinematic information in the form of position-velocity diagrams and rotation curves is presented in an atlas together with HI channel maps, 21 cm continuum maps, global HI profiles, radial HI surface density profiles, integrated HI column density maps, and HI velocity fields. The relation between the corrected global HI linewidth and the rotational velocities V_{\max} and V_{flat} as derived from the rotation curves is investigated. Inclination angles obtained from the optical axis ratios are compared to those derived from the inclined HI disks and the HI velocity fields. The galaxies were not selected on the basis of their HI content but solely on the basis of their cluster membership and inclination which should be suitable for a kinematic analysis. The observed galaxies provide a well-defined, volume limited and equidistant sample, useful to investigate in detail the statistical properties of the Tully-Fisher relation and the dark matter halos around them.

Key words. galaxies: fundamental parameters – galaxies: kinematics and dynamics – galaxies: spiral – galaxies: structure

1. Introduction

The statistical properties of the Tully-Fisher relation (TFr), like its scatter and slope, and in more detail the characteristics of dark matter halos around galaxies, like their core densities and radii, are of great interest to those who study galaxy formation scenarios. The relevant observables for the TFr are total luminosities and rotational velocities while actual rotation curves and luminosity profiles are required to obtain constraints on the density profiles of dark matter halos. However, the available data sets from which these observables can be obtained are often suffering from incompleteness, distance uncertainties and inhomogeneous observing and data analysis techniques.

Furthermore, the interpretation of the observables is not always unambiguous. For instance, the rotational velocity of a galaxy is generally inferred from the width of its global HI profile and often this measured width is being related directly to the dark matter potential (e.g. Navarro & Steinmetz 2000). However, the width of the HI profile is a complicated convolution of the 2-dimensional distribution of HI in a galaxy disk and the shape and extent of

its rotation curve as sampled by the HI gas. Needless to say one has to exercise caution when relating the observed scatter and slope in the TFr to the outcome of numerical and semi-analytical simulations of galaxy formation. This is especially the case when the observed TFr was constructed to serve as an empirical distance estimator and the selection criteria and applied corrections to the raw observables were optimized to linearize the relation and minimize its scatter.

To overcome some of the observational issues, we initiated a program to obtain detailed multi-band photometric and kinematic information on individual galaxies in a well-defined, complete sample. The nearby Ursa Major cluster of galaxies provides a particularly suitable sample. In the first place, the galaxies in the cluster are all at roughly the same distance. Therefore, there is little doubt about their relative luminosities, sizes and masses. Furthermore, the Ursa Major cluster contains overwhelmingly gas-rich systems and the morphological mix of its galaxy members is close to that of the lower density field. A detailed discussion on the definition of the Ursa Major cluster is given by Tully et al. (1996) (Paper I). The characteristics of this cluster will be discussed in more detail in Sect. 2.

Send offprint requests to: M. A. W. Verheijen,
e-mail: mverhei@nrao.edu

In this paper we present the results of an extensive 21 cm-line synthesis imaging survey of individual galaxies in the Ursa Major cluster using the Westerbork Synthesis Radio Telescope (WSRT). The HI data are presented in the form of an atlas. Multi-band optical and near-infrared imaging photometry is presented in Paper I together with B -band and K' -band images of all identified cluster members. Forthcoming papers in this series will use these data to investigate the TFr while the HI rotation curves will be supplemented in the inner regions with already obtained high resolution optical rotation curves to derive constraints on the structural properties of the dark matter halos and the mass-to-light ratios of the stellar populations.

This data paper is organized as follows. Section 2 describes the Ursa Major cluster in more detail and contains morphological and photometric information on the galaxies observed with the WSRT. Data acquisition and reduction procedures are explained in Sect. 3. Section 4 explains how the corrected linewidth can be matched to V_{\max} and V_{flat} from the rotation curves through an appropriate correction for turbulent motion. Inclinations are derived from the optical images, HI column density maps and HI velocity fields and Sect. 5 presents a comparison of these inclinations. The layout of the HI atlas is described in Sect. 6 with details about the various elements of the atlas pages. The HI properties of the Ursa Major cluster galaxies as a sample are presented in Sect. 7. Some concluding remarks are given in Sect. 8.

2. The sample

The nearby Ursa Major cluster as defined in Paper I has 79 identified members. It is located in the Supergalactic plane at an angular distance of 38 degrees from the core of the Virgo cluster. It has a recession velocity of 950 km s^{-1} and a velocity dispersion of only $\approx 150 \text{ km s}^{-1}$. In Paper I and in Tully & Verheijen (1997) (Paper II) a distance of 15.5 Mpc was adopted. However, new HST cepheid distances to local TFr calibrators (e.g. Sakai et al. 2000) and a new correction formalism for internal extinction (Tully et al. 1998) now place the Ursa Major cluster galaxies at a mean distance of 18.6 Mpc (Tully & Pierce 2000). At this distance, 1 arcmin corresponds to 5.4 kpc. The morphological mix of the cluster members is made up overwhelmingly by late type systems and only a dozen lenticulars are known members. Morphological and photometric properties in the optical and near-infrared of individual galaxies are described in detail in Paper I. The galaxy distribution shows no concentration toward any core and no X-ray emitting intra-cluster gas has been detected.

It should be noted that individual galaxies in the nearby Virgo (Warmels 1988a, 1988b; Cayatte et al. 1990), A1367 (Dickey & Gavazzi 1991), Hercules (Dickey 1997) and Coma (Bravo-Alfaro et al. 2000) clusters have also been studied in detail and the effect of the dense environment on the properties of the HI disks in these clusters has been clearly demonstrated. The HI disks in the cores

of these rich clusters are in general very small and often offset from the optical galaxy. On the other hand, the volume limited survey of the Hydra cluster (McMahon 1993) does not show such an HI deficiency although some interesting dynamical substructure has been revealed in this system. It should be stressed that the Ursa Major cluster is markedly different from these more massive and denser clusters. In selecting the Ursa Major sample, these environmental effects are carefully avoided as well as fore- and background contamination caused by high velocity dispersions and complex dynamical and spatial substructures.

Since the Ursa Major galaxies are all at the same distance, the effects of incompleteness and uncertain relative distances are minimized. A complete sample of 62 galaxies brighter than $M_B \approx -16.8$, i.e. roughly twice the luminosity of the Small Magellanic Cloud, was constructed and nearly all cluster members were observed with the WSRT. In this paper, however, only those 49 galaxies which are more inclined than 45 degrees, as derived from the optical axis ratio, will be considered for a detailed kinematic study.

Table 1 gives a summary of the positional and morphological properties of these 49 galaxies while photometrics are presented in Table 2, based on a 18.6 Mpc distance. There are 3 additional galaxies in the tables which do not meet the luminosity (f) and inclination (i) criteria but happened to be in the same WSRT fields as galaxies from the complete sample. Of all those 52 galaxies, the HI synthesis data of 30 were fully analyzed. Thirteen systems were observed and detected but the HI data of these galaxies are presented in an abbreviated form comprising only the channel maps, global profiles and position-velocity diagrams. Two of the smaller galaxies were detected in HI but they are confused with the HI emission from their more massive companions. Finally, there are 7 galaxies in the complete sample which have not been observed or detected because of their low HI content known from single dish observations. These are in general S0 or Sa systems.

Table 1 presents the following positional and morphological information:

Column (1) gives the NGC or UGC numbers.

Columns (2) and (3) provide the equatorial coordinates (B1950) derived from the optical images.

Columns (4) and (5) give the Galactic coordinates.

Column (6) provides the morphological type.

Column (7) gives the observed major axis diameter of the 25th mag arcsec^{-2} blue isophote.

Column (8) contains the position angle of the receding side of the galaxy. For galaxies which are not observed or not detected in HI, this is the smallest position angle of the major axis measured eastward from the north.

Column (9) contains the observed ellipticity of the optical galaxy image.

Column (10) gives the inclination i_{opt} as derived from the observed axis ratio (b/a). See Sect. 5.1 for further details.

Column (11) gives the adopted inclination angle as derived from several methods described in Sect. 5.

Column (12) indicates whether a galaxy has a low (LSB)

or high surface brightness (HSB) according to Paper II. *Columns* (13) and (14) provide the galactic extinction in the *B*-band according to Burstein & Heiles (1984) (BH) and Schlegel et al. (1998) (SFD) as reported by the NASA Extragalactic Database.

Table 2 presents the following photometric information:

Column (1) gives the NGC or UGC numbers.

Columns (2)–(5) give the observed total magnitudes in the *B*, *R*, *I* and *K'* passbands from Paper I.

Column (6) contains the corrected HI line widths at the 20% level, used to calculate the internal extinction as explained below.

Columns (7)–(10) present the calculated internal extinction corrections in the *B*, *R*, *I* and *K'* passbands toward face-on $A_{\lambda}^{i \rightarrow 0}$, calculated according to Tully et al. (1998):

$$A_{\lambda}^{i \rightarrow 0} = \gamma_{\lambda} \log(a/b)$$

where a/b is the observed axis ratio of the galaxy as an indication of inclination while γ_{λ} depends on the luminosity and is calculated according to

$$\gamma_B = 1.57 + 2.75(\log W_{R,I}^i - 2.5)$$

$$\gamma_R = 1.15 + 1.88(\log W_{R,I}^i - 2.5)$$

$$\gamma_I = 0.92 + 1.63(\log W_{R,I}^i - 2.5)$$

$$\gamma_{K'} = 0.22 + 0.40(\log W_{R,I}^i - 2.5)$$

where $W_{R,I}^i$ is the distance independent HI line width corrected for instrumental resolution as described in Sect. 3.2, corrected for turbulent motion according to Tully & Fouqué (1985) (TFq hereafter) with $W_{t,20} = 22 \text{ km s}^{-1}$ as motivated in Sect. 4 and corrected for inclination using i_{adopt} from Table 1. For dwarf galaxies with $W_{R,I}^i < 85 \text{ km s}^{-1}$ and for lenticulars with no dust features, the value of γ_{λ} is set to zero at all passbands.

Columns (11)–(14) give the total absolute *B*, *R*, *I* and *K'* magnitudes corrected for Galactic and internal extinction and a distance modulus of 31.35 corresponding to a distance to the Ursa Major cluster of 18.6 Mpc:

$$M_{\lambda}^{b,i} = m_{\lambda}^{\text{tot}} - A_{\lambda}^b - A_{\lambda}^{i \rightarrow 0} - 31.35$$

where the Galactic extinction A_B^b is taken from SFD as listed in Table 1. Extinction corrections in the other passbands are made according to the Galactic reddening law given by Cardelli et al. (1989) as summarized by SFD under the Landolt filters in their Table 6. It's given by $A_R^b/A_B^b = 0.62$, $A_I^b/A_B^b = 0.45$ and $A_{K'}^b/A_B^b = 0.08$.

Column (15) gives the diameter of the 25th mag arcsec $^{-2}$ blue isophote corrected for both galactic and internal extinction and projection according to TFq:

$$\text{Log}(D_{25}^{b,i}) = \text{Log}(D_{25}) - 0.22 \text{ Log}(D_{25}/d_{25}) + 0.09 A_B^b$$

where d_{25} is the minor axis diameter at the 25th mag arcsec $^{-2}$ blue isophote and A_B^b is taken from SFD.

3. Data acquisition and reduction

The HI data presented in this paper were obtained with the Westerbork Synthesis Radio Telescope (WSRT) between 1991 and 1996. The integration times varied between $1 \times 12^{\text{h}}$ and $5 \times 12^{\text{h}}$ depending on the required signal-to-noise. The angular resolution at the center of the cluster is $12'' \times 16''$ or 1.08×1.44 kpc at the adopted distance of 18.6 Mpc. The *FWHM* of the primary beam is 37.4 arcminutes or 202 kpc. As a result, often more than one galaxy was mapped in a single field of view. The observed bandwidth was either 2.5 or 5 MHz, depending on the width of the global profiles. The observations of the NGC 3992-group and the NGC 4111-group required a broad frequency band of 5 MHz and at the same time also sufficient velocity resolution for the dwarf systems. To comply with the correlator restrictions, those two fields were observed only in one polarization (XX) which allowed for a velocity resolution of 10 km s^{-1} but resulted in less sensitivity. During the earlier measurements an on-line Hanning taper was applied but this tapering was abandoned later to obtain the highest possible velocity resolution. The various obtained velocity resolutions (dependent on the correlator restrictions) were 5, 8, 10, 20 or 33 km s^{-1} , corresponding to typical rms-noise levels of respectively 3.1, 1.9, 2.9, 1.6 and $1.0 \text{ mJy beam}^{-1}$ for a single 12h observation at the highest angular resolution. The data of NGC 4013 were kindly made available by R. Bottema who studied this system in great detail (Bottema 1996 and references therein).

More details on the observational parameters for each field are tabulated in the atlas along with the data. What follows is a brief description of the reduction procedures.

The raw UV-data were calibrated, interactively flagged and Fast Fourier Transformed (FFT) using the NEWSTAR software developed at the NFRA in Dwingeloo. The UV points were weighted according to the local density of points in the UV plane and a Gaussian baseline taper was applied with a *FWHM* of 2293 (m) which attenuates the longest baseline by 50%. To deal with the frequency dependent antenna pattern, five antenna patterns were calculated for each data cube at a regular frequency separation throughout the bandpass. Pixel sizes of 5 arcsec in RA and $\frac{5}{\sin(\delta)}$ arcsec in declination ensure an adequate sampling of the synthesized beam, $12'' \times 12''/\sin(\delta)$.

After the FFT, the datacubes and antenna patterns were further processed using the Groningen Image Processing SYstem (GIPSY). Several channels at the low and high velocity end of the bandpass were discarded because of their higher noise. As a result, there are 110 or 53 usable channels for a bandpass of 2.5 or 5 MHz respectively, except for the N3992 and N4111 fields which had 110 channels across a 5 MHz bandpass. All datacubes were smoothed to lower angular resolutions of $30'' \times 30''$ and $60'' \times 60''$. This facilitates the detection of extended low level HI emission and the identification of the “continuum” channels which are free from line emission.

Table 1. All galaxies in the Ursa Major cluster brighter than $M^{b,i}(B) = -16.8$ and more inclined than 45 degrees

Name	RA (1950)	Dec (3)	Galactic Long. (4)	Lat. (5)	Type (6)	$D_{25}(B)$ (')	PA (8)	$1-b/a$ (°) (9)	i_{opt} (°) (10)	i_{adopt} (°) (11)	S.B. (12)	[BH] mag (13)	A_B^b [SFD] (14)
<i>Galaxies with fully analyzed HI data:</i>													
U6399	11 20 35.9	51 10 09	152.08	60.96	Sm	2.40	140	0.72	79	75 ± 2	LSB	0.00	0.07
U6446	11 23 52.9	54 01 21	147.56	59.14	Sd	2.27	200	0.38	54	51 ± 3	LSB	0.00	0.07
N3726	11 30 38.7	47 18 20	155.38	64.88	SBc	5.83	194	0.38	54	53 ± 2	HSB	0.01	0.07
N3769	11 35 02.8	48 10 10	152.72	64.75	SBb	2.97	150	0.69	76	70 ± 2	HSB	0.01	0.10
U6667	11 39 45.3	51 52 32	146.27	62.29	Scd	3.43	88	0.88	90	89 ± 1	LSB	0.00	0.07
N3877	11 43 29.3	47 46 21	150.72	65.96	Sc	5.40	36	0.78	84	76 ± 1	HSB	0.01	0.10
N3893	11 46 00.2	48 59 20	148.15	65.23	Sc	3.93	352	0.33	49	49 ± 2	HSB	0.02	0.09
N3917	11 48 07.7	52 06 09	143.65	62.79	Scd	4.67	257	0.76	82	79 ± 2	LSB	0.01	0.09
N3949	11 51 05.5	48 08 14	147.63	66.40	Sbc	2.90	297	0.38	54	55 ± 2	HSB	0.03	0.09
N3953	11 51 12.4	52 36 18	142.21	62.59	SBbc	6.10	13	0.50	62	62 ± 1	HSB	0.01	0.13
N3972	11 53 09.0	55 35 56	138.85	60.06	Sbc	3.43	298	0.72	79	77 ± 1	HSB	0.00	0.06
U6917	11 53 53.1	50 42 27	143.46	64.45	SBd	3.17	123	0.46	59	56 ± 2	LSB	0.03	0.12
U6923	11 54 14.4	53 26 19	140.51	62.06	Sdm	1.97	354	0.58	68	65 ± 2	LSB	0.00	0.12
U6930 ⁱ	11 54 42.3	49 33 41	144.54	65.51	SBd	3.00	39	0.14	32	31 ± 3	LSB	0.05	0.13
N3992	11 55 00.9	53 39 11	140.09	61.92	SBbc	6.93	248	0.44	58	56 ± 2	HSB	0.01	0.13
U6940 ^f	11 55 12.4	53 30 46	140.17	62.06	Scd	0.83	135	0.72	79	75 ± 3	LSB	0.00	0.12
U6962 ⁱ	11 55 59.5	43 00 44	154.08	71.05	SBcd	2.33	179	0.20	38	37 ± 3	HSB	0.00	0.09
N4010	11 56 02.0	47 32 16	146.68	67.36	SBd	4.63	65	0.88	90	89 ± 1	LSB	0.00	0.11
U6969	11 56 12.9	53 42 11	139.70	61.96	Sm	1.50	330	0.69	76	76 ± 2	LSB	0.01	0.13
U6973	11 56 17.8	43 00 03	153.97	71.10	Sab	2.67	40	0.61	70	71 ± 3	HSB	0.00	0.09
U6983	11 56 34.9	52 59 08	140.27	62.62	SBcd	3.20	270	0.34	50	49 ± 1	LSB	0.01	0.12
N4051	12 00 36.4	44 48 36	148.88	70.08	SBbc	5.90	311	0.34	50	49 ± 3	HSB	0.00	0.06
N4085	12 02 50.4	50 37 54	140.59	65.17	Sc	2.80	255	0.76	82	82 ± 2	HSB	0.01	0.08
N4088	12 03 02.0	50 49 03	140.33	65.01	Sbc	5.37	231	0.63	71	69 ± 2	HSB	0.01	0.09
N4100	12 03 36.4	49 51 41	141.11	65.92	Sbc	5.23	344	0.71	77	73 ± 2	HSB	0.03	0.10
N4102	12 03 51.3	52 59 22	138.08	63.07	SBab	3.00	38	0.44	58	56 ± 2	HSB	0.01	0.09
N4157	12 08 34.2	50 45 47	138.47	65.41	Sb	6.73	63	0.83	90	82 ± 3	HSB	0.02	0.09
N4183	12 10 46.5	43 58 33	145.39	71.73	Scd	4.77	346	0.86	90	82 ± 2	LSB	0.00	0.06
N4217	12 13 21.6	47 22 11	139.90	68.85	Sb	5.67	230	0.74	80	86 ± 2	HSB	0.00	0.08
N4389	12 23 08.8	45 57 41	136.73	70.74	SBbc	2.50	276	0.34	50	50 ± 4	HSB	0.00	0.06
<i>Galaxies with partially analyzed HI data:</i>													
N3718	11 29 49.9	53 20 39	147.01	60.22	Sa	7.53	195	0.58	68	69 ± 3	HSB	0.00	0.06
N3729	11 31 04.9	53 24 08	146.64	60.28	SBab	2.80	164	0.32	48	49 ± 3	HSB	0.00	0.05
U6773	11 45 22.1	50 05 12	146.89	64.27	Sm	1.53	341	0.47	60	58 ± 3	LSB	0.00	0.07
U6818	11 48 10.1	46 05 09	151.76	67.78	Sd	2.20	77	0.72	79	75 ± 3	LSB	0.00	0.09
U6894	11 52 47.3	54 56 08	139.52	60.63	Scd	1.67	269	0.84	90	83 ± 3	LSB	0.00	0.06
N3985	11 54 06.4	48 36 48	145.94	66.27	Sm	1.40	70	0.37	53	51 ± 3	HSB	0.05	0.11
N4013	11 55 56.8	44 13 31	151.86	70.09	Sb	4.87	245	0.76	88	90 ± 1	HSB	0.00	0.07
U7089	12 03 25.4	43 25 18	149.90	71.52	Sdm	3.50	215	0.81	90	80 ± 3	LSB	0.00	0.07
U7094	12 03 38.5	43 14 05	150.14	71.70	Sdm	1.60	39	0.64	72	70 ± 3	LSB	0.00	0.06
N4117	12 05 14.2	43 24 17	149.07	71.72	S0	1.53	21	0.56	67	68 ± 3	LSB	0.00	0.06
N4138	12 06 58.6	43 57 49	147.29	71.40	Sa	2.43	151	0.37	53	53 ± 3	HSB	0.00	0.06
N4218	12 13 17.4	48 24 36	138.88	67.88	Sm	1.17	316	0.40	55	53 ± 3	HSB	0.00	0.07
N4220	12 13 42.8	48 09 41	138.94	68.13	Sa	3.63	140	0.69	76	78 ± 3	HSB	0.00	0.08
<i>Galaxies with confused HI data:</i>													
1135+48	11 35 09.2	48 09 31	152.71	64.77	Sm	1.23	114	0.69	76	73 ± 3	LSB	0.01	0.10
N3896	11 46 18.6	48 57 10	148.10	65.29	Sm	1.60	308	0.33	49	48 ± 3	LSB	0.02	0.09
<i>Not observed or too little HI content:</i>													
N3870	11 43 17.5	50 28 40	147.02	63.75	S0a	1.13	17	0.31	47	48 ± 3	HSB	0.00	0.07
N3990	11 55 00.3	55 44 13	138.25	60.04	S0	1.47	40	0.50	62	63 ± 3	HSB	0.00	0.07
N4026	11 56 50.7	51 14 24	141.94	64.20	S0	4.37	177	0.74	80	84 ± 3	HSB	0.04	0.10
N4111	12 04 31.0	43 20 40	149.53	71.69	S0	4.47	150	0.78	84	90 ± 3	HSB	0.00	0.06
U7129	12 06 23.6	42 01 08	151.00	72.99	Sa	1.27	72	0.31	47	48 ± 3	HSB	0.00	0.06
N4143	12 07 04.6	42 48 44	149.18	72.40	S0	2.60	143	0.46	59	60 ± 3	HSB	0.00	0.06
N4346	12 21 01.2	47 16 15	136.57	69.39	S0	3.47	98	0.67	75	77 ± 3	HSB	0.00	0.06

Table 2. Photometrics of all galaxies in the UMa cluster brighter than $M^{b,i}(B) = -16.8$ and more inclined than 45 degrees

Name	m_B^{tot}	m_R^{tot}	m_I^{tot}	$m_{K'}^{\text{tot}}$	$W_{R,I}^i$	A_B^i	A_R^i	A_I^i	$A_{K'}^i$	$M_B^{b,i}$	$M_R^{b,i}$	$M_I^{b,i}$	$M_{K'}^{b,i}$	$D_{25}^{b,i}$	
	mag	mag	mag	mag	km s ⁻¹	mag	mag	mag	mag	mag	mag	mag	mag	(")	
(1)	(2)	(3)	(4)	(5)	(6)	(7)	(8)	(9)	(10)	(11)	(12)	(13)	(14)	(15)	
<i>Galaxies with fully analyzed HI data:</i>															
U6399	14.33	13.31	12.88	11.09		172	0.47	0.36	0.27	0.06	-17.56	-18.44	-18.77	-20.33	1.84
U6446	13.52	12.81	12.58	11.50		174	0.18	0.14	0.10	0.02	-18.08	-18.72	-18.90	-19.88	2.07
N3726	11.00	9.97	9.51	7.96		331	0.34	0.25	0.20	0.05	-20.76	-21.67	-22.07	-23.45	5.32
N3769	12.80	11.56	10.99	9.10		256	0.67	0.50	0.39	0.09	-19.32	-20.35	-20.80	-22.35	2.34
U6667	14.33	13.11	12.63	10.81		167	0.74	0.58	0.43	0.10	-17.83	-18.87	-19.18	-20.65	2.18
N3877	11.91	10.46	9.72	7.75		335	1.06	0.78	0.62	0.15	-20.60	-21.73	-22.29	-23.76	3.95
N3893	11.20	10.19	9.71	7.84		382	0.31	0.23	0.18	0.04	-20.55	-21.45	-21.86	-23.56	3.67
N3917	12.66	11.42	10.85	9.08		276	0.87	0.64	0.51	0.12	-19.65	-20.63	-21.05	-22.40	3.48
N3949	11.55	10.69	10.28	8.43		321	0.33	0.24	0.20	0.05	-20.22	-20.96	-21.31	-22.98	2.66
N3953	11.03	9.66	9.02	7.03		446	0.60	0.43	0.35	0.08	-21.05	-22.20	-22.74	-24.41	5.38
N3972	13.09	11.90	11.34	9.39		264	0.76	0.56	0.44	0.11	-19.08	-20.05	-20.48	-22.08	2.62
U6917	13.15	12.16	11.74	10.30		224	0.31	0.23	0.18	0.04	-18.63	-19.49	-19.84	-21.10	2.84
U6923	13.91	12.97	12.36	11.04		160	0.28	0.22	0.16	0.04	-17.84	-18.67	-19.20	-20.36	1.67
U6930 ⁱ	12.70	11.71	11.39	10.33		231	0.08	0.06	0.05	0.01	-18.86	-19.78	-20.07	-21.04	2.98
N3992	10.86	9.55	8.94	7.23		547	0.56	0.40	0.33	0.08	-21.18	-22.28	-22.80	-24.21	6.27
U6940 ^f	16.45	15.65	15.44	13.99		50	0.00	0.00	0.00	0.00	-15.02	-15.77	-15.96	-17.37	0.64
U6962 ⁱ	12.88	11.88	11.42	10.11		327	0.16	0.11	0.09	0.02	-18.72	-19.64	-20.06	-21.27	2.26
N4010	13.36	12.14	11.55	9.22		254	1.20	0.89	0.70	0.17	-19.30	-20.17	-20.55	-22.31	2.97
U6969	15.12	14.32	14.04	12.58		117	0.20	0.17	0.11	0.02	-16.56	-17.28	-17.48	-18.80	1.19
U6973	12.94	11.26	10.53	8.23		364	0.71	0.52	0.42	0.10	-19.21	-20.67	-21.28	-23.23	2.21
U6983	13.10	12.27	11.91	10.52		221	0.21	0.16	0.12	0.03	-18.58	-19.31	-19.61	-20.87	2.99
N4051	10.98	9.88	9.37	7.86		308	0.28	0.21	0.17	0.04	-20.71	-21.72	-22.18	-23.54	5.45
N4085	13.09	11.87	11.28	9.20		247	0.78	0.58	0.46	0.11	-19.12	-20.11	-20.57	-22.27	2.08
N4088	11.23	10.00	9.37	7.46		362	0.74	0.54	0.43	0.10	-20.95	-21.94	-22.45	-24.00	4.40
N4100	11.91	10.62	10.00	8.02		386	0.97	0.70	0.57	0.14	-20.51	-21.49	-21.97	-23.48	4.07
N4102	12.04	10.54	9.93	7.86		393	0.46	0.34	0.27	0.07	-19.86	-21.20	-21.73	-23.57	2.69
N4157	12.12	10.60	9.88	7.52		399	1.40	1.02	0.82	0.20	-20.72	-21.83	-22.33	-24.04	4.64
N4183	12.96	11.99	11.51	9.76		228	1.01	0.76	0.59	0.14	-19.46	-20.16	-20.46	-21.74	3.13
N4217	12.15	10.62	9.84	7.61		381	1.05	0.76	0.62	0.15	-20.33	-21.54	-22.16	-23.90	4.29
N4389	12.56	11.33	10.87	9.12		212	0.20	0.15	0.12	0.03	-19.05	-20.21	-20.63	-22.27	2.31
<i>Galaxies with partially analyzed HI data:</i>															
N3718	11.28	9.95	9.29	7.47		476	0.77	0.55	0.45	0.11	-20.90	-21.99	-22.54	-24.00	6.30
N3729	12.31	10.94	10.30	8.60		296	0.25	0.18	0.15	0.03	-19.34	-20.62	-21.22	-22.78	2.60
U6773	14.42	13.61	13.15	11.23		112	0.09	0.08	0.05	0.01	-17.09	-17.87	-18.28	-20.14	1.35
U6818	14.43	13.62	13.15	11.70		151	0.39	0.31	0.22	0.05	-17.40	-18.10	-18.46	-19.71	1.69
U6894	15.27	14.31	14.00	12.40		124	0.37	0.31	0.21	0.05	-16.51	-17.39	-17.59	-19.01	1.13
N3985	13.25	12.26	11.81	10.19		180	0.18	0.14	0.10	0.02	-18.39	-19.30	-19.69	-21.19	1.29
N4013	12.44	10.79	9.95	7.68		377	1.10	0.80	0.64	0.15	-20.08	-21.40	-22.07	-23.83	3.61
U7089	13.73	12.77	12.36	11.11		138	0.42	0.34	0.24	0.05	-18.11	-18.96	-19.26	-20.30	2.46
U7094	14.74	13.70	13.22	11.58		76	0.00	0.00	0.00	0.00	-16.67	-17.69	-18.16	-19.78	1.29
N4117	14.05	12.47	11.81	9.98		285	0.00	0.00	0.00	0.00	-17.36	-18.92	-19.57	-21.38	1.29
N4138	12.27	10.72	10.09	8.19		374	0.36	0.26	0.21	0.05	-19.50	-20.93	-21.50	-23.22	2.22
N4218	13.69	12.83	12.41	10.83		150	0.15	0.12	0.09	0.02	-17.88	-18.68	-19.06	-20.55	1.06
N4220	12.34	10.79	10.03	8.36		399	0.94	0.68	0.55	0.13	-20.03	-21.29	-21.91	-23.13	2.85
<i>Galaxies with confused HI data:</i>															
1135+48	14.95	14.05	13.61	11.98		111	0.17	0.15	0.09	0.02	-16.67	-17.51	-17.88	-19.40	0.97
N3896	13.75	12.96	12.47	11.35		83	0.00	0.00	0.00	0.00	-17.69	-18.45	-18.92	-20.01	1.49
<i>Not observed or too little HI content:</i>															
N3870	13.67	12.71	12.16	10.73		127	0.08	0.06	0.04	0.01	-17.83	-18.74	-19.26	-20.64	1.06
N3990	13.53	12.08	11.36	9.54		...	0.00	0.00	0.00	0.00	-17.89	-19.31	-20.02	-21.82	1.28
N4026	11.71	10.25	9.57	7.65		...	0.00	0.00	0.00	0.00	-19.74	-21.16	-21.82	-23.71	3.32
N4111	11.40	9.95	9.25	7.60		...	0.00	0.00	0.00	0.00	-20.01	-21.44	-22.13	-23.76	3.24
U7129	14.13	12.80	12.19	0.08	0.06	0.04	0.01	-17.36	-18.65	-19.23	...	1.19
N4143	12.06	10.55	9.84	7.86		...	0.00	0.00	0.00	0.00	-19.35	-20.83	-21.54	-23.50	2.30
N4346	12.14	10.69	9.96	8.21		...	0.00	0.00	0.00	0.00	-19.27	-20.70	-21.42	-23.15	2.75

Table 3. A comparison of the widths and integrated fluxes from the present WSRT survey and from the literature

Name (1)	This study						Literature						Ref. (12)
	W_{20}	\pm	Res.	$\int Sdv$	\pm		W_{20}	\pm	Res.	$\int Sdv$	\pm		
	km s ⁻¹	km s ⁻¹		Jy km s ⁻¹	Jy km s ⁻¹		km s ⁻¹	km s ⁻¹		Jy km s ⁻¹	Jy km s ⁻¹		
U6399	188.1	1.4	8.3	10.5	0.3	178	20	22	10.1	1.9	1		
U6446	154.1	1.0	5.0	40.6	0.5	162	10	22	45.9	4.1	1		
N3718 ^(c)	492.8	1.0	33.2	140.9	0.9	480	10	5.5	84.9	26.4	1		
				508 ^m	..	33	120	8 ^{WSRT}		
N3726	286.5	1.6	5.0	89.8	0.8	290	10	5.5	83.9	10.8	1		
N3729 ^{noSD}	270.8	1.5	33.2	5.5	0.3	8 ^{WSRT}	
				279 ^m	..	33	25 [?]		
N3769 ⁱ	265.3	6.7	8.3	62.3	0.6	276	20	7.4	44.1	4.2	2		
U6667	187.5	1.4	5.0	11.0	0.4	210	20	22	11.6	2.2	1		
N3877	373.4	5.0	33.2	19.5	0.6	352	10	22	24.8	5.6	1		
U6773	110.4	2.3	8.3	5.6	0.4	118	8	22	5.6	0.7	6		
N3893 ^(c)	310.9	1.0	5.0	69.9	0.5	313	8	22	85.3	5.1	1		
N3917	294.5	1.9	8.3	24.9	0.6	284	10	22	21.9	4.7	1		
U6818	166.9	2.3	8.3	13.9	0.2	168	15	22	14.8	2.1	1		
N3949	286.5	1.4	8.3	44.8	0.4	289	10	22	42.7	5.4	1		
N3953 ^l	441.9	2.4	33.1	39.3	0.8	423	10	22	41.0	3.9	1		
U6894	141.8	1.1	8.3	5.8	0.2	159	20	7.4	5.1	1.7	2		
N3972	281.2	1.4	8.3	16.6	0.4	270	15	22	14.0	2.6	1		
U6917	208.9	3.2	8.3	26.2	0.3	211	10	22	31.5	4.1	1		
N3985	160.2	3.7	8.3	15.7	0.6	168	..	22	14.1	0.9	5		
U6923	166.8	2.4	10.0	10.7	0.6	175	15	22	8.2	2.9	1		
				189 ^m	15	41.4	15.6	12 ^{VLA}		
U6930	136.5	0.5	8.3	42.7	0.3	145	8	22	38.2	3.5	1		
N3992 ^l	478.5	1.4	10.0	74.6	1.5	480	10	22	81.2	5.3	1		
				507 ^m	15	41.4	79.9	12 ^{VLA}		
U6940	59.3	3.8	10.0	2.1	0.3	226	..	22	7.0	1.0	3		
				121 ^m	15	41.4	2.7	12 ^{VLA}		
N4013	425.0	0.9	33.0	41.5	0.2	403	10	22	33.8	3.7	1		
U6962 ^(c)	220.3	6.6	8.3	10.0	0.3	22	21.6	4.4	1		
				235	..	33	9.2	1.0	...	4 ^{WSRT}			
N4010	277.7	1.0	8.3	38.2	0.3	281	10	22	38.1	3.4	1		
U6969 ^c	132.1	6.4	10.0	6.1	0.5	146	..	13.2	6.0	1.4	3		
				159 ^m	15	41.4	6.9	12 ^{VLA}		
U6973 ^{noSD}	367.8	1.8	8.3	22.9	0.2	4 ^{WSRT}	
				408	..	33	18.3	1.2		
U6983	188.4	1.3	5.0	38.5	0.6	205	10	22	36.2	4.4	1		
N4051 ^l	255.4	1.8	5.0	35.6	0.8	274	15	22	43.4	3.3	1		
N4085 ^c	277.4	6.6	19.8	14.6	0.9	299	20	7.4	23.3	2.5	2		
				311 ^m	..	33	24 ^l	13 ^{WSRT}			
N4088 ^(c)	371.4	1.7	19.8	102.9	1.1	381	8	22	109.2	6.4	1		
				378 ^m	..	33	128 ^l	13 ^{WSRT}			
U7089 ^(c)	156.7	1.7	10.0	17.0	0.6	162	10	22	17.8	2.2	1		
				176	..	33.4	18.9	11 ^{WSRT}			
N4100	401.8	2.0	19.9	41.6	0.7	420	20	22	54.0	7.3	1		
U7094 ^c	83.7	1.7	10.0	2.9	0.2	112	8	22	6.0	0.6	6		
				153 [?]	..	33.4	2.5	11 ^{WSRT}		
N4102	349.8	2.0	8.3	8.0	0.2	327	20	7.4	10.3	2.1	2		
N4117 ^{noSD}	289.4	7.5	10.0	6.9	1.1	11 ^{WSRT}	
				314	..	33.4	5.3		
N4138	331.6	4.5	19.9	19.2	0.7	354 ^m	30	6.8	16	...	14		
				340	5	5.2	20.6	0.3	...	7 ^{VLA}			
N4157 ^{(c),l}	427.6	2.2	19.9	107.4	1.6	436	10	22	123.9	9.5	1		
N4183	249.6	1.2	8.3	48.9	0.7	258	10	22	49.6	5.3	1		
N4218	138.0	5.0	8.3	7.8	0.2	160	20	13	5.7	0.9	9		
N4217	428.1	5.1	33.2	33.8	0.7	426	20	22	51.8	7.2	1		
N4220	438.1	1.3	33.1	4.4	0.3	382 ^m	..	11	3.3	...	10		
N4389	184.0	1.5	8.3	7.6	0.2	174	20	7.4	7.6	0.8	2		

Table 3. continued. Notes

^(c) :	the authors suggest possible confusion with a dwarf companion.														
^c :	flagged by the authors as confused with near companion.														
^l :	large correction factor (>1.20) applied for primary beam flux attenuation.														
ⁱ :	flagged by the authors as possibly interacting.														
^{noSD} :	no useful single dish profile available due to obvious confusion.														
^m :	line width directly measured from the published HI profile.														
[!] :	the integrated flux as quoted by the author is a factor 2 larger than is quoted by any other source. Therefore, half the integrated flux was adopted from this source.														
WSRT:	synthesis observation with the WSRT.														
VLA:	synthesis observation with the VLA.														
References:	<table style="width: 100%; border-collapse: collapse;"> <tbody> <tr> <td style="width: 50%;">1: Fisher & Tully (1981)</td><td style="width: 50%;">8: Schwarz (1985)</td></tr> <tr> <td>2: Appleton & Davies (1982)</td><td>9: Thuan & Martin (1981)</td></tr> <tr> <td>3: Richter & Huchtmeier (1991)</td><td>10: Magri (1994)</td></tr> <tr> <td>4: Oosterloo & Shostak (1993)</td><td>11: Van der Burg (1987)</td></tr> <tr> <td>5: Huchtmeier & Richter (1986)</td><td>12: Gottesman et al. (1984)</td></tr> <tr> <td>6: Schneider et al. (1992)</td><td>13: Van Moorsel (1983)</td></tr> <tr> <td>7: Jore et al. (1996)</td><td>14: Grewing & Mebold (1975)</td></tr> </tbody> </table>	1: Fisher & Tully (1981)	8: Schwarz (1985)	2: Appleton & Davies (1982)	9: Thuan & Martin (1981)	3: Richter & Huchtmeier (1991)	10: Magri (1994)	4: Oosterloo & Shostak (1993)	11: Van der Burg (1987)	5: Huchtmeier & Richter (1986)	12: Gottesman et al. (1984)	6: Schneider et al. (1992)	13: Van Moorsel (1983)	7: Jore et al. (1996)	14: Grewing & Mebold (1975)
1: Fisher & Tully (1981)	8: Schwarz (1985)														
2: Appleton & Davies (1982)	9: Thuan & Martin (1981)														
3: Richter & Huchtmeier (1991)	10: Magri (1994)														
4: Oosterloo & Shostak (1993)	11: Van der Burg (1987)														
5: Huchtmeier & Richter (1986)	12: Gottesman et al. (1984)														
6: Schneider et al. (1992)	13: Van Moorsel (1983)														
7: Jore et al. (1996)	14: Grewing & Mebold (1975)														

3.1. The radio continuum emission

The channels free from HI emission were averaged and the resulting continuum map was subtracted from all channels in the data cube. The residuals of the frequency dependent grating rings were only a minor fraction of the noise in the channels containing the line emission. The dirty continuum maps were cleaned (Högbom 1974) down to 0.3σ . The clean-components were restored with a Gaussian beam of similar $FWHM$ as the synthesized beam. When radio continuum emission from a galaxy was detected, its continuum flux was determined from the cleaned continuum map. In cases of no detection, an upper limit for extended emission was derived by calculating the rms scatter in the flux values obtained by integrating the noise in each of fifteen elliptical areas enclosed by the 25th mag blue isophote and positioned at various emission-free regions in the map.

3.2. The HI channel maps and the global HI profiles

At all three spatial resolutions, the regions of HI emission were defined by the areas enclosed by the 2σ contours in the “dirty” 60'' resolution maps. Grating rings and noise peaks above this level were removed manually. The selected regions were enlarged by moving their boundaries 1 armin outwards to account for possible emission in the sidelobes. The resulting masks vary from channel to channel in shape, size and position due to the rotation of the HI disk. These masks defined the regions that were cleaned down to 0.3σ at all three spatial resolutions.

The clean-components were restored with a Gaussian beam of similar $FWHM$ as the synthesized beam. The global HI profiles were derived by determining the primary beam corrected flux in each cleaned region. Since the size and shape of the clean masks vary as a function of velocity, the uncertainty in the flux densities at each velocity in the

global HI profile varies as well. The noise on the global HI profile was determined by projecting each clean mask at nine different line-free positions in a channel map and integrating over each of them.

For further analysis, each profile was divided up in three equal velocity bins in which the peak fluxes $F_{\text{low}}^{\text{peak}}$, $F_{\text{mid}}^{\text{peak}}$ and $F_{\text{high}}^{\text{peak}}$ were determined for the low, middle and high velocity bin respectively. These three peak fluxes were then used to classify a global profile shape according to:

Double peaked: $F_{\text{low}}^{\text{peak}} > F_{\text{mid}}^{\text{peak}} < F_{\text{high}}^{\text{peak}}$

Gaussian: $F_{\text{low}}^{\text{peak}} < F_{\text{mid}}^{\text{peak}} > F_{\text{high}}^{\text{peak}}$

Distorted: $F_{\text{low}}^{\text{peak}} < F_{\text{mid}}^{\text{peak}} < F_{\text{high}}^{\text{peak}}$

or $F_{\text{low}}^{\text{peak}} > F_{\text{mid}}^{\text{peak}} > F_{\text{high}}^{\text{peak}}$

Boxy: $F_{\text{low}}^{\text{peak}} \approx F_{\text{mid}}^{\text{peak}} \approx F_{\text{high}}^{\text{peak}}$.

In case of a double peaked profile, the peak fluxes on both sides were considered separately when calculating the 20% and 50% levels. In all other cases, the overall peak flux was used. The four velocities $V_{\text{low}}^{20\%}$, $V_{\text{low}}^{50\%}$, $V_{\text{high}}^{50\%}$ and $V_{\text{high}}^{20\%}$ corresponding to these 20% and 50% levels were determined by linear interpolation between the data points, going from the center outward. In the few cases of non-monotonically decreasing edges, this procedure tends to slightly underestimate the widths. The widths are calculated according to

$$W_{20} = V_{\text{high}}^{20\%} - V_{\text{low}}^{20\%} \text{ and } W_{50} = V_{\text{high}}^{50\%} - V_{\text{low}}^{50\%}.$$

The systemic velocity is calculated according to

$$V_{\text{sys}} = 0.25(V_{\text{low}}^{20\%} + V_{\text{low}}^{50\%} + V_{\text{high}}^{50\%} + V_{\text{high}}^{20\%}).$$

Because in interferometric measurements some flux may be lost due to the missing short baselines, it is useful to compare the widths and flux densities from the WSRT profiles with those from published single dish observations. However, a meaningful comparison requires that the

profile widths are all corrected in the same way for instrumental broadening. In general, the widths that are published by various authors were corrected for instrumental broadening using nearly as many different methods. Therefore, the published line widths had to be de-corrected first to ensure a uniformly applied correction. The de-corrected widths and integrated HI fluxes from the literature are compiled in Cols. (7)–(11) of Table 3 along with the results from this study in Cols. (2)–(6).

Column (1) gives the NGC or UGC numbers.

Columns (2, 3) and (7, 8) give the widths of the global profiles at the 20% levels and the formal uncertainties.

Columns (4) and (9) give the velocity resolutions of the observations.

Columns (5, 6) and (10, 11) contain the integrated HI fluxes derived from the global profiles.

Column (12) provides the references to the literature sources.

In case the authors suggest that the single dish profile of a particular galaxy may be confused and synthesis data on that galaxy do exist, these synthesis data are included as well and used in the following comparison. However, first it will be explained how the observed linewidths are corrected for the different instrumental resolutions.

3.2.1. Correcting W_{20} for instrumental broadening

The most widely used method to correct for broadening of the global HI profiles due to a finite instrumental velocity resolution was provided by Bottinelli et al. (1990). For the widths at the 20% and 50% levels of the peak flux they advocate the following linear relations:

$$W_{20,R} = W_{20} - \delta W_{20} = W_{20} - 0.55R$$

$$W_{50,R} = W_{50} - \delta W_{50} = W_{50} - 0.13R$$

where W_{20} is the observed linewidth and $W_{20,R}$ is the linewidth corrected for the instrumental velocity resolution R in km s^{-1} . This empirical prescription is based on comparing linewidths obtained at different resolutions.

However, the correction method applied here deviates from Bottinelli et al.'s method and is based on more analytic considerations. It is easy to imagine that both edges of an intrinsic global profile, when chopped off at their peaks and glued together, approximate a Gaussian with dispersion σ_0 . The width at the 20% level of this "true" Gaussian is then given by

$$W_{20,R} = \sigma_0 \sqrt{8\ln(5)}.$$

A spectral Hanning smoothing was applied to most of the WSRT observations presented in this paper. This smoothing function can also be approximated by a Gaussian with a $FWHM$ equal to the instrumental velocity resolution R and has a dispersion σ_R

$$\sigma_R = \frac{R}{\sqrt{8\ln(2)}}.$$

The dispersion σ_c of the convolved observed Gaussian is then given by

$$\sigma_c = \sqrt{\sigma_0^2 + \sigma_R^2}$$

and the 20% line width of this convolved or observed Gaussian is given by

$$\begin{aligned} W_{20} &= \sigma_c \sqrt{8\ln(5)} \\ &= \sqrt{8\ln(5)} \cdot \sqrt{\sigma_0^2 + \sigma_R^2} \\ &= \sqrt{8\ln(5)} \cdot \sqrt{\sigma_0^2 + \frac{R^2}{8\ln(2)}}. \end{aligned}$$

So, at the 20% level, the intrinsic width $W_{20,R}$ is broadened to W_{20} by δW given by

$$\begin{aligned} \delta W_{20} &= W_{20} - W_{20,R} \\ &= \sqrt{8\ln(5)} \cdot \sqrt{\sigma_0^2 + \frac{R^2}{8\ln(2)}} - \sigma_0 \sqrt{8\ln(5)} \\ &= \sigma_0 \sqrt{8\ln(5)} \cdot \left[\sqrt{1 + \frac{(R/\sigma_0)^2}{8\ln(2)}} - 1 \right]. \end{aligned}$$

The broadening δW_{20} does not only depend on the instrumental resolution R but also on the steepness of the slopes of the edges of the profile, expressed by σ_0 . Fitting Gaussians to the edges of a profile yields σ_c from which σ_0 can be calculated given the known value of σ_R . The equation above can be rewritten using σ_c instead which results in

$$\delta W_{20} = \sigma_c \sqrt{8\ln(2)} \left(\frac{\ln(5)}{\ln(2)} \right)^2 \left[1 - \sqrt{1 - \frac{(R/\sigma_c)^2}{8\ln(2)}} \right].$$

However, no Gaussians were fitted to the edges of the new WSRT profiles. Instead it is assumed that the slopes of the edges of the profiles are more or less determined by the turbulent motion of the gas with a canonical velocity dispersion of $\sigma_0 = 10 \text{ km s}^{-1}$. This results in

$$\delta W_{20} = 35.8 \cdot \left[\sqrt{1 + \left(\frac{R}{23.5} \right)^2} - 1 \right]$$

and similarly for the 50% level

$$\delta W_{50} = 23.5 \cdot \left[\sqrt{1 + \left(\frac{R}{23.5} \right)^2} - 1 \right].$$

The differences between Bottinelli et al.'s linear prescription and our corrections ($\Delta\delta W = \delta W^{Bot} - \delta W^{our}$) are only minor and tabulated below for typical instrumental resolutions of the WSRT.

level	$\Delta\delta W$				
	$R (\text{km s}^{-1})$				
	5.0	8.3	16.5	19.9	33.1
20%	2.0	2.4	1.2	0.2	-7.8
50%	0.2	-0.3	-3.1	-4.7	-12.8

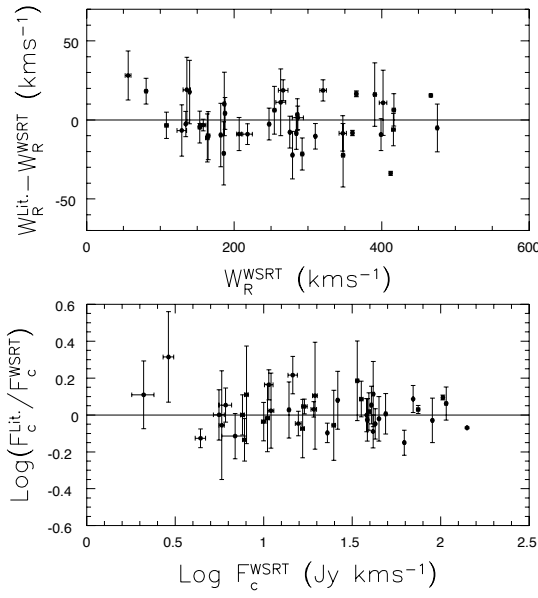


Fig. 1. A comparison of the present WSRT results with pre-existing single dish and synthesis data from the literature

The larger differences occur for the poorest resolutions at which only the broadest profiles were observed. Consequently, the differences are a negligible fraction of the line widths.

Figure 1 shows the comparison of the widths and integrated fluxes derived from the new WSRT global profiles and those from the literature. There are no significant systematic differences. The unweighted average difference in widths is $-0.9 \pm 2.1 \text{ km s}^{-1}$ with a rms scatter of 14 km s^{-1} . The unweighted average difference in integrated flux is 4.7 ± 3.5 percent with a rms scatter of 25 percent. It can therefore be concluded that on average the WSRT results are in excellent agreement with the results from single dish observations.

3.3. The total HI maps

As a next step, the total integrated HI maps were constructed from the *cleaned* datacubes. The *clean*-masks were used to define the regions with HI emission. Outside these regions, the pixels were set to zero and all the channels containing a non-zero area were added to build up the integrated column density map. This was then corrected for attenuation by the primary beam. Although the advantage of this procedure is a higher signal-to-noise ratio at a certain pixel in the HI map, the disadvantage is that the noise is no longer uniform across the map. As a result, the 3σ -contour level in an integrated HI map is not defined. Signal-to-noise maps have been made, however, using the prescription outlined in Appendix A and the average pixel value of all pixels with $2.75 < (\frac{S}{N}) < 3.25$ was determined. This average value was adopted as the “ 3σ ” level for the column density.

3.4. The radial HI surface density profiles

The integrated column density maps were used to derive the radial HI surface density profiles by azimuthally averaging in concentric ellipses. The orientations and widths of the ellipses were the same as those of the projected tilted rings fitted to the HI velocity field (see Sect. 3.6.1). In the case of a warp with overlapping ellipses, the flux in the overlapping regions was proportionally assigned to each ellipse. The azimuthal averaging was done separately for the receding and approaching halves of each tilted ring to reveal possible asymmetries. Pixels in the HI map without any measured signal were set to zero. Finally, the entire radial profile was scaled by the total HI mass as derived from the global HI profile. No attempt was made to correct the profiles for the effect of beam smearing.

This method for extracting the surface density profiles from integrated HI maps breaks down for nearly edge-on systems; the highly inclined annuli with large major axis diameters could still pick up some flux along the minor axis due to beam smearing. In such cases, Lucy's (1974) iterative deprojection scheme as adapted and developed by Warmels (1988b) might be preferable.

Due to the complex noise structure of the integrated HI map, no attempt was made to estimate the errors on the radial HI surface density profiles.

3.5. The HI velocity fields

The HI data cubes were smoothed to velocity resolution of $\approx 19 \text{ km s}^{-1}$ in order to obtain a good spectral signal-to-noise ratio. HI velocity fields were then constructed by fitting single Gaussians to the velocity profiles at each pixel. Initial estimates for the fits were given by the various moments of the profiles determined over the velocity range covered by the masks. Only those fits were accepted for which 1) the central velocity of the fitted Gaussian lies inside the masked volume, 2) the amplitude is larger than five times the rms noise in the profile and 3) the uncertainty in the central velocity is smaller than $\frac{1}{3}$ the velocity resolution.

Due to projection effects and beam smearing, the velocity profiles in highly inclined systems and in the central regions of galaxies may deviate strongly from a Gaussian shape. The exact shape depends on the spatial and kinematic distribution of the gas within a synthesized beam. Fitting single Gaussians to these usually skewed profiles results in an underestimate of the rotational velocity at that position. As a consequence, the gradients in the velocity field become shallower. There are several methods to correct for the effects of beam smearing. In the present cases, however, the signal-to-noise was in general too low to allow a useful application of these methods, and, since only a small number of systems were recognized as seriously affected, the HI velocity fields were not corrected for the effects of beam smearing.

3.6. Rotation curves

The rotation curves were derived in two ways; 1) by fitting tilted-rings to the velocity fields (Begeman 1987) and 2) by estimating the rotational velocities by eye from the position-velocity diagrams.

3.6.1. Using the velocity fields

The determination of the rotation curves from the velocity fields was done in three steps by fitting tilted rings to the velocity field (see Begeman 1987, 1989). The widths of the rings were set at $\frac{2}{3}$ of the width of the synthesized beam (i.e. 10'', 20'' or 40'').

First, the systemic velocity and the dynamical center were determined. In this first step the inclination and position angles were the same for each ring and kept fixed at the values derived from the optical images. The systemic velocity, center and rotational velocity were fitted for each ring. All the points along the tilted ring were considered and weighted uniformly. In general, no significant trend as a function of radius could be detected for the systemic velocity and center. The adopted values were calculated as the average of all rings.

Second, the systemic velocity and center of rotation were kept fixed for each ring while the position angle, inclination and rotational velocity were fitted. All the points along the tilted ring were considered but weighted with $\cos(\theta)$ where θ is the angle in the plane of the galaxy measured from the receding side. Hence, points along the minor axis have zero weight. While the position angle can be determined accurately, the inclination and rotational velocity are rather strongly correlated for inclinations below 60 degrees and above 80 degrees (Begeman 1989). As a result, the fitted inclinations can vary by a large amount from one ring to another. However, a possible trend in the inclination with radius due to a central bar or a warp can be detected. A change in inclination angle often goes together with a change in the more accurately determined position angle.

Third, the rotational velocity was fitted again for each ring while keeping the systemic velocity, center of rotation, inclination and position angle fixed. Again, all the points along the tilted ring were considered but weighted with $\cos(\theta)$. The fixed values for the inclination and position angles were determined in the second step by averaging the solutions over all the rings or fixing a clear trend. For nearly edge-on galaxies, the inclinations determined in the second step were often overruled by higher values based on the clear presence of a dust lane (e.g. N4010, N4157, N4217) or the very thin distribution of gas in the column density maps (e.g. U6667). However, uncertainty in the inclinations of nearly edge-on systems does not significantly influence the amplitude of the rotational velocity.

The results of this 3-step procedure were used to construct a model velocity field. This model was subtracted from the actual observed velocity field to yield a map of the residual velocities. In some cases (e.g. N3769, N4051,

N4088) this residual map shows significant systematic residuals, indicative of non-circular motion or a bad model fit due to a noisy observed velocity field. As a further check, the derived rotation curve is projected onto the position-velocity maps along the major and minor axis.

The errors on the inclination and position angles and the rotational velocity are formal errors. They do not include possible systematic uncertainties due to, for instance, the beam smearing.

3.6.2. Using the position-velocity diagrams

It has already been remarked (see Sect. 3.5) that beam smearing affects the determination of the velocity fields, especially in the central regions of galaxies and in highly inclined disks. As a consequence, the rotation curves derived from such velocity fields are underestimated as one can see from their projection on the XV-maps. In order to overcome this problem, the rotation curves were derived directly from the major axis XV-maps in a manner similar to that used for edge-on systems (cf. Sancisi & Allen 1979). This was done by two independent human neural networks trained to estimate the maximum rotational velocity from the asymmetric velocity profiles, taking into account the instrumental band- and beam-widths and the random gas motions. This was done for both the receding and approaching side of a galaxy. The rotation curves were then deprojected (also accounting for possible warps) by using the same position and inclination angles as fixed in the third step described in the previous section. In general, the average rotation curves derived from the XV-diagrams are in reasonable agreement with those obtained by the tilted ring fits. As expected, significant differences can only be noted for galaxies which are highly inclined or have a steeply rising rotation curve.

From the XV-diagrams it is clear that many galaxies have kinematic asymmetries in the sense that the rotation curve often rises more steeply on one side of a galaxy than on the other side (e.g. N3877, N3949). The rotation curves as derived from the velocity fields and XV-diagrams are tabulated in Table 4 for the approaching and receding parts separately. The adopted changes in inclination and position angles of N3718 and N4138 are motivated in the notes on the atlas pages of these galaxies. The uncertainties quoted in Table 4 are not 1-sigma Gaussian errors but rather reflect fiducial velocity ranges, based on the position-velocity diagrams.

4. Matching HI linewidths to V_{\max} and V_{flat}

In this section, it will be investigated how the linewidth correction for turbulent motion can be used to match the finally corrected global HI linewidths to the actual rotational velocities measured from the rotation curves.

Table 4. Rotation curves derived from velocity fields and XV-diagrams

	Rad.	$V_{\text{rot}}^{\text{app}}$	\pm	$V_{\text{rot}}^{\text{rec}}$	\pm	$V_{\text{rot}}^{\text{ave}}$	i	PA
	(")	- - - km s ⁻¹	- - - - km s ⁻¹	- - - km s ⁻¹	- - - km s ⁻¹	- - - km s ⁻¹	(°)	(°)
<i>U6399</i>								
10	25	12	7	25	10	7	25	75 141
20	44	10	7	49	7	7	46	75 141
30	61	12	7	61	7	5	61	75 141
40	70	7	5	69	5	5	70	75 141
50	77	7	5	78	3	5	78	75 141
60	82	10	5	84	5	5	83	75 141
70	84	5	5	-	-	-	84	75 141
80	86	5	5	-	-	-	86	75 141
90	88	5	5	-	-	-	88	75 141
<i>U6446</i>								
10	39	8	8	23	10	10	31	51 188
20	49	8	8	61	8	10	55	51 188
30	57	5	5	65	5	8	61	51 188
40	63	5	5	65	5	8	64	51 188
50	69	8	5	65	5	5	67	51 188
60	71	5	5	70	5	5	70	51 188
70	75	5	5	72	5	5	74	51 188
80	79	8	5	77	5	5	78	51 188
90	81	8	5	81	5	5	81	51 188
100	81	5	5	80	5	5	81	51 188
110	81	5	5	82	5	5	81	51 189
120	82	8	5	83	5	8	82	51 191
131	82	8	5	84	5	8	83	51 193
142	83	8	8	86	8	8	85	51 195
153	83	8	8	86	8	8	84	51 197
164	82	11	11	85	8	11	83	51 199
176	80	11	11	-	-	-	80	51 201
<i>N3726</i>								
40	112	10	7	92	12	10	102	53 195
60	131	7	7	119	10	10	125	53 195
80	144	5	5	146	7	10	145	53 195
100	156	5	5	172	5	7	164	53 195
120	154	7	7	171	5	7	162	53 195
140	155	7	5	166	7	7	160	53 195
160	152	7	7	159	5	7	156	53 195
183	145	10	7	148	5	5	147	57 188
256	157	8	8	159	6	6	158	72 180
316	169	9	12	-	-	-	169	75 179
344	169	9	12	-	-	-	169	75 179
373	167	15	15	-	-	-	167	75 179
<i>N3769</i>								
20	89	13	10	86	20	10	88	70 149
40	103	10	8	109	13	10	106	70 149
60	112	8	8	119	8	8	116	70 149
80	120	8	8	130	8	10	125	70 149
100	123	5	8	129	5	8	126	70 149
120	124	5	8	122	5	8	123	70 150
141	120	5	5	115	8	8	118	70 152
166	120	8	10	110	8	10	115	70 155
196	122	14	17	-	-	-	122	70 158
364	121	10	10	-	-	-	121	70 167
396	118	10	10	-	-	-	118	70 167
426	113	11	11	-	-	-	113	70 168
<i>U6667</i>								
10	27	5	5	27	7	7	27	89 89
20	43	2	2	47	5	5	45	89 89
30	55	5	5	59	7	5	57	89 89
40	64	2	5	74	5	5	69	89 89

Table 4. continued

	Rad.	$V_{\text{rot}}^{\text{app}}$	\pm	$V_{\text{rot}}^{\text{rec}}$	\pm	$V_{\text{rot}}^{\text{ave}}$	i	PA
	(")	- - - km s ⁻¹	- - - - km s ⁻¹	- - - km s ⁻¹	- - - km s ⁻¹	- - - km s ⁻¹	(°)	(°)
<i>U6667 (cont.)</i>								
50	73	5	5	82	5	5	77	89 89
60	78	5	5	84	5	7	81	89 89
70	82	2	5	87	5	5	84	89 89
80	83	2	5	87	5	5	85	89 89
90	83	5	5	89	5	5	86	89 89
<i>N3877</i>								
10	35	10	10	40	15	15	38	76 37
20	81	10	10	80	15	15	80	76 37
30	129	10	10	113	15	12	121	76 37
40	150	8	8	134	12	12	142	76 37
50	157	8	8	149	10	10	153	76 37
60	161	8	8	159	8	8	160	76 37
70	163	8	8	163	8	8	162	76 37
80	164	8	8	171	5	5	167	76 37
90	163	8	8	174	8	8	169	76 37
100	164	8	8	177	8	5	171	76 37
110	165	8	8	176	8	5	171	76 37
120	165	8	8	174	10	8	170	76 37
130	166	10	10	171	10	10	169	76 37
<i>N3893</i>								
20	140	10	10	150	10	10	145	49 345
40	175	10	10	173	10	10	174	49 345
60	191	10	10	197	10	7	194	49 345
80	192	7	7	189	10	7	191	49 346
101	192	10	8	181	8	8	186	47 351
125	194	8	11	182	8	11	188	45 362
151	190	10	13	184	10	16	187	43 371
176	179	11	15	-	-	-	179	41 377
<i>N3917</i>								
10	21	5	5	28	7	5	24	80 257
20	45	5	5	54	7	5	50	80 257
30	69	7	7	78	7	7	74	80 257
40	99	7	5	103	5	7	101	80 257
50	102	5	5	113	5	5	107	80 257
60	108	5	5	122	5	5	115	80 257
70	118	5	5	128	5	7	123	80 257
80	127	5	5	134	5	7	130	80 257
90	133	5	5	134	5	5	134	79 257
100	137	7	5	136	5	5	136	78 257
110	137	7	5	136	5	5	137	77 257
120	137	5	5	136	5	5	136	77 257
130	137	5	5	137	5	5	137	76 257
140	137	5	5	138	5	5	137	75 257
150	137	5	5	-	-	-	137	75 257
160	138	5	5	-	-	-	138	74 257
170	137	8	8	-	-	-	137	73 257
<i>N3949</i>								
10	58	10	10	79	14	14	68	55 298
20	106	10	7	141	7	7	123	55 298
30	138	7	10	152	7	7	145	55 298
40	150	5	7	155	10	12	152	55 298
50	156	7	7	159	7	14	157	55 297
60	161	5	5	161	10	24	161	55 295
70	165	7	7	165	7	34	165	55 294
81	-	-	-	169	7	44	169	55 293

Table 4. continued

Rad. (")	$V_{\text{rot}}^{\text{app}}$ km s ⁻¹	\pm	$V_{\text{rot}}^{\text{rec}}$ km s ⁻¹	\pm	$V_{\text{rot}}^{\text{ave}}$ km s ⁻¹	i (°)	PA (°)
<i>N3953</i>							
40	178	7	10	184 15	10	181 62	13
60	200	10	10	207 10	7	203 62	13
80	214	7	10	219 7	7	217 62	13
100	218	7	10	227 10	7	223 62	13
120	219	7	7	229 10	7	224 62	13
140	222	7	7	224 10	10	223 62	13
160	229	10	7	218 7	10	224 62	13
175	234	10	7	- -	-	234 62	13
180	- -	-	215	10	10	215 62	13
<i>N3972</i>							
10	24	5	5	55 10	7	40 77	297
20	68	7	7	78 7	7	73 77	297
30	86	12	10	93 7	7	89 77	297
40	101	10	7	103 5	7	102 77	297
50	111	7	5	110 5	7	110 77	297
60	117	7	5	116 5	7	116 77	297
70	122	5	5	124 7	7	123 77	297
80	129	5	5	131 5	7	130 77	297
86	131	7	7	- -	-	131 77	297
90	- -	-	134	5	7	134 77	297
100	- -	-	134	5	5	134 77	297
<i>U6917</i>							
20	60	5	5	59 5	5	59 56	123
30	71	5	8	72 5	5	71 56	123
40	86	8	5	83 8	5	85 56	123
50	96	8	8	91 5	5	94 56	123
60	98	5	5	97 5	5	98 56	123
70	100	5	5	100 5	5	100 56	123
80	101	8	5	101 5	5	101 56	123
90	105	5	5	102 5	5	103 56	123
100	110	5	5	101 5	8	105 56	123
110	116	7	7	104 5	7	110 57	123
120	- -	-	111	5	7	111 60	124
<i>U6923</i>							
11	41	6	9	- -	-	41 65	341
23	54	6	6	- -	-	54 65	341
34	70	6	6	76 9	6	73 65	341
44	80	6	6	77 6	6	78 65	344
53	- -	-	79	5	5	79 65	347
61	- -	-	81	5	5	81 65	350
<i>U6930</i>							
20	58	12	10	52 12	12	55 32	39
40	88	10	7	83 12	10	85 32	39
60	94	7	7	94 10	10	94 32	39
80	98	7	7	100 7	7	99 32	39
100	102	7	7	105 7	7	103 32	39
120	105	7	7	109 7	7	107 32	39
140	107	7	7	110 7	7	109 32	39
150	- -	-	110	7	7	110 32	39
160	108	7	7	- -	-	108 32	39
180	108	7	7	- -	-	108 32	39
190	108	7	7	- -	-	108 32	39
<i>N3992</i>							
80	253	7	10	244 10	12	249 56	248
120	264	7	10	265 7	12	264 56	248
160	273	7	10	272 7	7	272 56	248
200	274	7	7	268 7	10	271 56	248
240	273	7	7	256 7	7	264 56	248
280	- -	-	242	7	7	242 56	248

Table 4. continued

Rad. (")	$V_{\text{rot}}^{\text{app}}$ km s ⁻¹	\pm	$V_{\text{rot}}^{\text{rec}}$ km s ⁻¹	\pm	$V_{\text{rot}}^{\text{ave}}$ km s ⁻¹	i (°)	PA (°)
<i>N3992 (cont.)</i>							
320	247	7	7	242 7	7	244 56	248
360	241	7	7	242 10	10	241 56	248
400	237	7	10	- -	-	237 56	248
<i>U6940</i>							
10	19	5	5	18 5	5	18 79	315
20	41	5	5	34 5	8	37 79	315
<i>U6962</i>							
10	50	20	15	75 12	10	62 37	359
20	107	10	7	106 10	7	106 37	359
30	129	7	7	126 7	7	128 37	359
40	142	7	7	145 10	7	144 37	359
50	155	7	7	163 10	10	159 37	359
60	171	7	7	- -	-	171 37	359
<i>N4010</i>							
0	34	15	15	-34 15	15	0 90	66
10	59	12	10	20 7	7	39 90	66
20	66	7	10	43 7	7	55 90	66
30	69	5	10	62 12	10	66 90	66
40	80	5	5	88 10	7	84 90	66
50	84	5	5	104 12	10	94 90	66
60	96	5	5	113 10	10	104 90	66
70	108	7	5	122 7	7	115 90	66
80	125	7	5	129 7	7	127 90	66
90	128	7	5	131 7	7	129 90	66
100	123	7	5	131 7	7	127 90	66
110	119	7	5	129 7	7	124 90	66
120	119	5	5	125 5	7	122 90	66
<i>U6969</i>							
10	- -	-	-	26 5	7	26 76	330
20	34	5	7	44 7	7	39 76	330
31	46	5	5	58 5	7	52 76	330
41	60	5	5	69 5	7	65 76	330
51	- -	-	-	79 5	5	79 76	330
<i>U6973</i>							
20	162	5	10	179 5	7	170 71	41
30	174	5	7	174 5	7	174 71	41
40	170	5	7	170 5	7	170 71	42
50	170	5	7	170 5	7	170 71	44
61	171	5	7	172 7	7	171 71	45
72	174	5	8	174 8	8	174 71	46
78	- -	-	-	177 10	10	177 71	47
84	178	5	8	- -	-	178 71	47
90	180	5	10	- -	-	180 71	48
<i>U6983</i>							
20	58	10	10	56 10	7	57 49	270
30	93	7	5	82 7	7	87 49	270
40	87	7	7	97 10	7	92 49	270
50	84	7	7	103 7	7	94 49	270
60	93	5	5	103 7	7	98 49	270
70	94	5	5	105 7	7	100 49	270
80	95	5	5	108 5	5	102 49	270
90	100	7	7	113 5	5	107 49	270
100	105	7	7	112 5	5	108 49	270
110	111	7	7	110 5	5	111 49	270
120	113	7	7	112 5	5	113 49	270
130	111	7	7	110 7	7	111 49	270
140	107	7	7	109 7	10	108 49	270
145	102	10	10	- -	-	102 49	270
150	- -	-	-	109 7	10	109 49	270

Table 4. continued

Rad.	$V_{\text{rot}}^{\text{app}}$	\pm	$V_{\text{rot}}^{\text{rec}}$	\pm	$V_{\text{rot}}^{\text{ave}}$	i	PA
(")	km s $^{-1}$		km s $^{-1}$		km s $^{-1}$	(°)	(°)
<i>U6983 (cont.)</i>							
160	-	-	-	108 10	10	108 49	270
170	-	-	-	108 10	10	108 49	270
180	-	-	-	109 12	12	109 49	270
<i>N4051</i>							
20	-	-	-	121 15	15	121 49	310
25	123	15	15	-	-	123 49	310
40	119	12	10	114 12	10	116 49	310
60	146	10	10	133 10	10	140 49	310
80	163	7	10	156 10	10	160 49	310
100	158	7	7	165 7	7	162 49	310
115	-	-	-	170 7	7	170 49	310
120	154	7	7	-	-	154 49	310
140	153	10	10	-	-	153 49	310
<i>N4085</i>							
10	35	10	5	50 15	10	42 82	256
20	71	7	5	89 10	10	80 82	256
31	110	12	7	113 7	7	112 82	256
41	126	7	5	127 7	7	127 82	256
51	131	7	7	130 7	5	130 82	256
61	134	7	7	133 5	5	133 82	256
71	136	7	7	-	-	136 82	256
<i>N4088</i>							
20	92	15	15	78 20	15	85 69	230
40	138	10	15	135 20	10	136 69	230
60	156	7	12	168 15	10	162 69	230
80	167	7	10	191 10	10	179 69	230
100	177	7	10	187 10	7	182 69	230
120	185	7	12	174 10	10	179 69	230
140	187	7	12	162 7	7	174 69	230
160	185	12	12	158 7	7	171 69	230
180	175	10	10	161 7	7	168 69	230
200	171	7	7	160 10	7	165 69	230
210	-	-	-	156 10	7	156 69	229
221	171	10	7	-	-	171 69	227
246	174	8	8	-	-	174 69	224
<i>N4100</i>							
20	67	15	15	-	-	67 73	345
30	102	15	20	139 15	7	121 73	345
40	138	12	12	159 10	7	148 73	345
50	164	7	10	173 10	7	168 73	345
60	177	10	7	188 10	7	182 73	345
70	188	7	7	193 7	7	191 73	345
80	193	7	7	195 10	7	194 73	345
90	195	10	7	195 10	7	195 73	345
100	193	5	7	194 7	7	193 73	345
110	192	5	5	192 7	5	192 73	345
120	193	5	5	191 5	5	192 73	345
130	192	5	5	190 7	7	191 73	345
140	188	7	7	189 7	5	189 73	345
150	183	7	10	187 7	5	185 73	345
160	180	7	7	185 5	5	182 73	345
170	175	10	10	183 10	7	179 72	346
180	172	7	10	181 10	7	177 71	346
190	168	10	10	179 10	8	174 71	346
200	-	-	-	178 10	8	178 70	346
210	-	-	-	177 8	5	177 70	347
220	160	5	8	178 10	10	169 69	347
230	158	5	8	-	-	158 69	347
241	158	8	8	-	-	158 68	348

Table 4. continued

Rad.	$V_{\text{rot}}^{\text{app}}$	\pm	$V_{\text{rot}}^{\text{rec}}$	\pm	$V_{\text{rot}}^{\text{ave}}$	i	PA
(")	km s $^{-1}$		km s $^{-1}$		km s $^{-1}$	(°)	(°)
<i>N4100 (cont.)</i>							
251	158	8	-	-	-	-	158 68 348
261	159	10	8	-	-	-	159 67 348
<i>N4102</i>							
20	179	12	12	184 12	12	181 56	39
30	177	12	10	181 10	12	179 56	39
40	174	12	10	178 10	10	176 56	39
50	-	-	-	178 15	10	178 56	39
<i>N4157</i>							
20	66	18	14	127 23	14	96 82	63
40	142	18	14	173 14	14	157 82	63
60	192	9	14	191 11	14	192 82	63
80	202	7	9	201 11	11	201 82	63
100	198	11	11	204 9	9	201 82	63
120	192	9	9	197 9	9	195 82	63
140	191	9	9	188 9	7	190 82	63
160	191	9	9	181 9	9	186 82	63
180	192	9	9	176 9	9	184 82	63
200	191	9	9	173 11	11	182 82	63
220	190	7	7	173 14	9	181 82	63
240	189	9	7	177 11	9	183 82	63
260	189	11	7	181 9	9	185 82	63
280	186	11	7	-	-	-	186 82 63
300	186	11	11	-	-	-	186 82 63
320	185	14	14	-	-	-	185 82 63
340	185	14	14	-	-	-	185 82 63
<i>N4183</i>							
10	56	12	10	38 15	10	47 82	346
20	71	7	7	61 12	10	66 82	346
30	78	7	7	74 10	7	76 82	346
40	88	7	7	84 10	7	86 82	346
50	97	7	7	97 7	7	97 82	346
60	100	7	7	99 7	7	99 82	346
70	103	7	7	103 7	7	103 82	346
80	106	7	7	107 7	7	107 82	346
90	110	7	7	113 7	7	111 82	346
100	112	7	7	117 10	10	114 82	346
110	112	7	7	118 10	10	115 82	346
120	108	7	7	114 10	7	111 82	346
130	108	7	7	113 10	7	110 82	347
141	111	7	7	112 7	7	111 82	347
151	108	7	5	110 7	7	109 82	347
161	106	5	5	109 7	7	108 82	347
172	109	7	7	109 7	7	109 82	347
183	112	7	7	110 7	7	111 82	348
194	108	5	8	111 8	8	110 82	348
205	106	5	8	111 8	8	109 82	348
217	107	7	8	112 8	8	110 82	348
229	-	-	-	112 10	10	112 82	348
241	-	-	-	113 13	10	113 82	349
<i>N4217</i>							
10	38	10	10	57 14	12	48 86	230
20	82	10	12	116 14	10	99 86	230
30	145	10	10	148 14	10	146 86	230
40	162	7	10	165 10	10	164 86	230
50	176	7	10	172 7	10	174 86	230
60	176	7	10	175 10	7	175 86	230
70	189	7	10	179 10	10	184 86	230
80	188	7	10	182 10	10	185 86	230
90	187	5	10	188 12	10	188 86	230

Table 4. continued

Rad. (")	$V_{\text{rot}}^{\text{app}}$ - - - km s $^{-1}$	\pm	$V_{\text{rot}}^{\text{rec}}$ - - - km s $^{-1}$	\pm	$V_{\text{rot}}^{\text{ave}}$ - - - km s $^{-1}$	i ($^{\circ}$)	PA ($^{\circ}$)
<i>N4217 (cont.)</i>							
100	188	7	10	192	12	12	190 86 230
110	191	7	10	191	10	10	191 86 230
120	192	7	7	189	10	7	191 86 230
130	191	10	7	187	10	7	189 86 230
140	187	10	7	185	12	10	186 86 230
150	183	10	7	183	10	10	183 86 230
160	180	12	7	178	10	10	179 86 230
170	177	10	10	177	10	12	177 86 230
181	178	12	12	177	10	14	177 86 230
191	178	12	12	-	-	178	86 230
<i>N4389</i>							
10	30	8	8	25	10	8	27 50 277
20	56	10	8	50	13	8	53 50 277
31	70	13	8	69	10	8	69 50 277
41	79	13	8	88	8	8	84 50 277
51	92	10	10	99	8	8	96 50 277
61	-	-	-	110	8	8	110 50 277
<i>Rotation curves derived from XV-diagrams only.</i>							
<i>N3718</i>							
40	228	10	10	228	10	10	228 76 114
80	228	10	10	228	10	10	228 80 130
120	228	10	10	228	10	10	228 84 143
160	228	10	10	228	10	10	228 90 162
200	228	10	10	228	10	10	228 85 175
240	220	10	10	235	10	10	228 80 186
280	225	10	10	239	10	10	232 75 195
320	240	10	10	245	10	10	242 70 196
360	245	10	10	242	10	10	244 65 196
400	235	10	10	240	10	10	237 65 194
420	227	10	10	-	-	-	65 194
<i>N3729</i>							
20	118	34	24	138	12	10	128 48 164
40	157	17	12	141	12	12	149 48 164
50	-	-	-	144	10	10	144 48 164
60	151	12	10	-	-	-	151 48 164
<i>U6773</i>							
10	28	10	7	34	10	7	31 60 341
20	38	7	7	48	7	5	43 60 341
30	46	5	5	44	7	7	45 60 341
40	47	5	5	44	10	7	45 60 341
<i>U6818</i>							
10	27	7	7	20	10	7	23 79 77
20	28	10	7	28	7	5	28 79 77
30	31	7	5	43	7	5	37 79 77
40	43	7	5	53	7	5	48 79 77
50	66	7	7	61	7	5	63 79 77
60	77	7	10	66	7	5	71 79 77
70	68	7	5	-	-	-	68 79 77
80	74	7	5	-	-	-	74 79 77
<i>N3985</i>							
0	8	15	10	-8	15	10	0 53 70
10	41	10	7	37	12	7	39 53 70
20	60	7	10	89	15	7	75 53 70
25	68	10	10	-	-	-	68 53 70
30	-	-	-	93	7	7	93 53 70
<i>U6894</i>							
10	28	7	7	28	12	10	28 89 269
20	45	7	7	45	7	7	45 89 269

Table 4. continued

Rad. (")	$V_{\text{rot}}^{\text{app}}$ - - - km s $^{-1}$	\pm	$V_{\text{rot}}^{\text{rec}}$ - - - km s $^{-1}$	\pm	$V_{\text{rot}}^{\text{ave}}$ - - - km s $^{-1}$	i ($^{\circ}$)	PA ($^{\circ}$)
<i>U6894 (cont.)</i>							
30	56	7	5	56	5	5	56 89 269
40	62	5	5	63	7	7	63 89 269
<i>N4013</i>							
65	-	-	-	198	10	10	198 90 245
73	-	-	-	195	5	5	195 90 245
82	193	5	5	195	3	3	194 90 245
91	195	4	4	195	3	3	195 90 245
99	195	3	3	195	3	3	195 90 245
108	195	3	3	193	4	4	195 90 245
117	196	3	3	185	5	5	192 90 245
125	195	3	3	178	5	5	188 90 245
134	190	4	4	178	8	8	186 90 245
143	190	4	4	-	-	-	186 90 245
151	188	5	5	-	-	-	186 90 245
160	187	6	6	-	-	-	185 90 245
168	179	10	10	-	-	-	180 90 243
177	163	8	8	-	-	-	163 90 240
186	161	6	6	-	-	-	162 90 238
194	162	5	5	-	-	-	164 90 236
203	164	5	5	170	5	5	166 90 235
212	164	6	6	168	5	5	166 90 233
220	165	8	8	166	5	5	166 90 232
229	165	7	7	166	5	5	166 90 230
238	169	5	5	168	5	5	168 90 229
246	173	5	5	-	-	-	172 90 228
255	173	5	5	-	-	-	173 90 226
264	172	5	5	-	-	-	171 90 225
272	169	6	6	170	5	5	170 90 224
281	162	10	10	172	5	5	172 90 224
289	-	-	-	174	5	5	173 90 223
298	-	-	-	176	5	5	176 90 222
307	-	-	-	178	5	5	178 90 221
315	-	-	-	180	6	6	180 90 221
324	-	-	-	180	8	8	180 90 220
333	-	-	-	180	5	5	180 90 219
341	-	-	-	180	5	5	180 90 219
350	-	-	-	178	5	5	178 90 218
359	-	-	-	174	5	5	174 90 218
367	-	-	-	170	10	10	170 90 218
<i>U7089</i>							
10	25	7	7	17	7	5	21 89 215
20	38	5	5	35	7	7	36 89 215
30	45	5	5	42	7	7	43 89 215
40	51	7	7	51	5	5	51 89 215
50	57	7	5	62	5	5	60 89 215
60	63	10	5	66	5	5	65 89 215
70	66	7	5	69	5	5	68 89 215
75	-	-	-	73	7	7	73 89 215
80	70	7	5	-	-	-	70 89 215
<i>U7089 (cont.)</i>							
90	74	7	5	-	-	-	74 89 215
100	78	7	5	-	-	-	78 89 215
105	79	7	7	-	-	-	79 89 215
<i>U7094</i>							
20	32	5	5	32	5	5	32 72 39
40	36	7	5	36	7	5	36 72 39
60	-	-	-	35	7	5	35 72 39

Table 4. continued

Rad. (")	$V_{\text{rot}}^{\text{app}}$ km s ⁻¹	\pm	$V_{\text{rot}}^{\text{rec}}$ km s ⁻¹	\pm	$V_{\text{rot}}^{\text{ave}}$ km s ⁻¹	i (°)	PA (°)
<i>N4138</i>							
30	178	19	34	181	12	12	179 53 151
60	191	10	10	200	10	10	195 53 151
90	181	10	10	181	15	20	181 53 147
122	-	-	-	162	26	15	162 51 143
154	145	14	14	145	14	14	145 48 140
184	-	-	-	147	18	18	147 43 138
213	-	-	-	150	21	21	150 35 138
<i>N4218</i>							
10	51	10	7	70	12	10	60 55 316
20	83	10	5	62	12	10	73 55 316

After the correction for instrumental resolution, the profile widths are generally corrected for broadening due to turbulent motions of the HI gas by applying TFq's formula

$$W_{R,l}^2 = W_l^2 + W_{t,l}^2 \left[1 - 2e^{-\left(\frac{W_l}{W_{c,l}}\right)^2} \right] - 2W_l W_{t,l} \left[1 - e^{-\left(\frac{W_l}{W_{c,l}}\right)^2} \right]$$

where the subscript l refers to the widths at the $l = 20\%$ or the $l = 50\%$ level of peak flux. This formula yields a linear subtraction of $W_{t,l}$ if $W_l > W_{c,l}$ and a quadratic subtraction if $W_l < W_{c,l}$. Values of $W_{t,l}$ and $W_{c,l}$ are different for line width corrections at the 20% and 50% levels. The values of $W_{c,l}$ indicate the profile widths where the transition from a boxy to a Gaussian shape occurs. The amount by which a global profile is broadened due to random motions is given by $W_{t,l} = 2k_l\sigma$ where, for a Gaussian velocity dispersion σ , $k_{20} = 1.80$ and $k_{50} = 1.18$.

The generally adopted values for $W_{c,l}$ are $W_{c,20} = 120 \text{ km s}^{-1}$ and $W_{c,50} = 100 \text{ km s}^{-1}$. The more important values of $W_{t,l}$, however, have been subject of some debate among various authors. With our new HI synthesis data we can give a meaningful contribution to this debate.

Bottinelli et al. (1983) came up with an empirical approach, based on a minimization of the scatter in the TF-relation. They assumed an anisotropic velocity dispersion of the HI gas of $\sigma_x = \sigma_y = 1.5\sigma_z$ and a velocity dispersion perpendicular to the plane of $\sigma_z = 10 \text{ km s}^{-1}$. They determined the values of k_l by minimizing the scatter in the TF-relation and found $k_{20} = 1.89$ and $k_{50} = 0.71$, indicating deviations from a Gaussian distribution (broader wings). Due to the assumed velocity anisotropy, $W_{t,l}$ has become a function of inclination angle and varies in the range $45 < W_{t,20} < 57$ and $17 < W_{t,50} < 21$ for inclinations ranging between $45^\circ < i < 90^\circ$.

The same value of $k_{20} = 1.89$ was adopted by TFq but they assumed an isotropic velocity dispersion of

$\sigma_x = \sigma_y = \sigma_z = 10 \text{ km s}^{-1}$ and consequently advocate $W_{t,20} = 2 \cdot 1.89 \cdot 10 = 38 \text{ km s}^{-1}$, independent of inclination. They did not address the situation at the 50% level.

Fouqué et al. (1990) also assumed isotropy but adopted $\sigma = 12 \text{ km s}^{-1}$. They determined k_l in a more direct way by comparing the corrected line width to the observed maximum rotational velocity V_{max} as derived from HI velocity fields. They found $k_{20} = 1.96$ and $k_{50} = 1.13$, indicating a near-Gaussian distribution, contrary to the findings of Bottinelli et al. Consequently, Fouqué et al. advocate the much larger values of $W_{t,20} = 47 \text{ km s}^{-1}$ and $W_{t,50} = 27 \text{ km s}^{-1}$ respectively.

A similar procedure was followed by Broeils (1992) using a sample of 21 galaxies with well defined HI velocity fields. Broeils made no a priori assumptions about the intrinsic velocity dispersion and did not decouple k_l and σ . He did, however, recognize that V_{max} may exceed V_{flat} and he determined for each galaxy the values of $W_{t,l}^{\text{max}}$ and $W_{t,l}^{\text{flat}}$ for which the differences

$$\Delta W_{R,l}^{\text{max}} = W_{R,l} - 2V_{\text{max}} \sin(i)$$

and

$$\Delta W_{R,l}^{\text{flat}} = W_{R,l} - 2V_{\text{flat}} \sin(i)$$

become zero for each galaxy. He found mean values of

$$W_{t,20}^{\text{max}} = 21 \pm 2, \quad W_{t,50}^{\text{max}} = 7 \pm 1$$

$$W_{t,20}^{\text{flat}} = 37 \pm 5, \quad W_{t,50}^{\text{flat}} = 25 \pm 4.$$

(Note that he quoted the much larger scatters instead of the errors in the mean quoted above.) He rejected his results, probably discouraged by the large *scatters*, and adopted the values $W_{t,20} = 38$ and $W_{t,50} = 14 \text{ km s}^{-1}$ which he erroneously identifies with Bottinelli et al.'s results.

Finally, Rhee (1996a) performed the same investigation using 28 galaxies, most of them in common with Broeils' (1992) sample. Not surprisingly, he found

$$W_{t,20}^{\text{max}} = 20 \pm 2, \quad W_{t,50}^{\text{max}} = 8 \pm 2$$

$$W_{t,20}^{\text{flat}} = 30 \pm 3, \quad W_{t,50}^{\text{flat}} = 18 \pm 3$$

similar to Broeils' result.

Here, with our new and independent dataset, we follow the same strategy as Broeils and Rhee by investigating which values of $W_{t,l}$ allow an accurate retrieval of V_{max} and V_{flat} from the broadened global profile. For this purpose we will only consider those 22 galaxies in our Ursa Major sample that show a flat part in their rotation curves (with a significant amount of HI gas) and that are free from a major change in inclination angle. Of these 22, there are 6 galaxies with $V_{\text{max}} > V_{\text{flat}}$. Note that both Broeils and Rhee used Bottinelli et al.'s prescription to correct for instrumental broadening which we are forced to adopt here to ensure a valid comparison between their

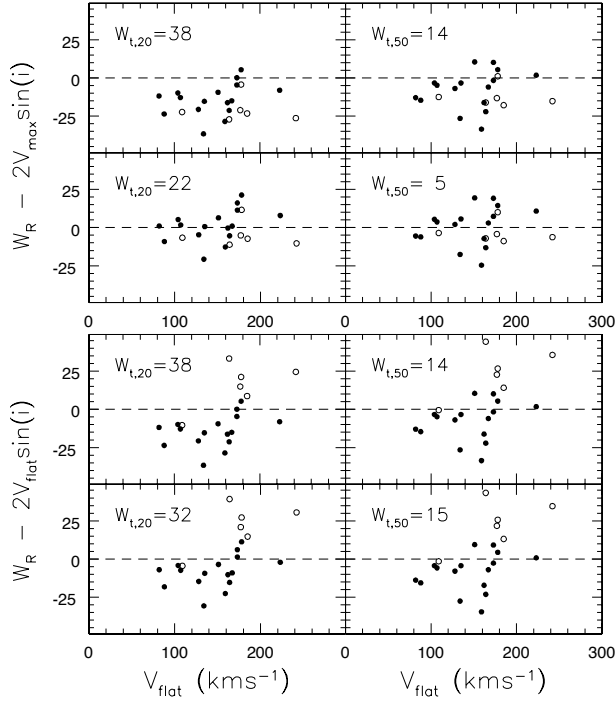


Fig. 2. Comparison of the global profile widths $W_{R,l}$, corrected for instrumental broadening and random motions, with $2V_{\max} \sin(i)$ (upper panels) and with $2V_{\text{flat}} \sin(i)$ (lower panels). The left panels consider $W_{R,20}$ and the right panels $W_{R,50}$. Different values of the random motion parameters $W_{t,l}$ are used. Open symbol indicate galaxies with declining rotation curves ($V_{\max} > V_{\text{flat}}$) and filled symbols indicated galaxies without a declining part ($V_{\max} = V_{\text{flat}}$). See Sect. 4 for further details

and our results. We calculated the values of $W_{t,l}^{\max}$ and $W_{t,l}^{\text{flat}}$ for which the average values

$$\begin{aligned}\Delta W_{R,l}^{\max} &= \frac{1}{N} \sum (W_{R,l} - 2V_{\max} \sin(i)) \\ \Delta W_{R,l}^{\text{flat}} &= \frac{1}{N} \sum (W_{R,l} - 2V_{\text{flat}} \sin(i))\end{aligned}$$

become zero. This is done for both the entire sample of $N = 22$ galaxies and for the subsample of $N = 16$ galaxies with $V_{\max} = V_{\text{flat}}$. For the entire sample we find

$$\begin{aligned}W_{t,20}^{\max} &= 22, \quad W_{t,50}^{\max} = 5 \\ W_{t,20}^{\text{flat}} &= 32, \quad W_{t,50}^{\text{flat}} = 15.\end{aligned}$$

These values are in good agreement with the (rejected) results of Broeils and in excellent agreement with the results of Rhee. The values of $W_{t,l}^{\text{flat}}$ are larger than the values of $W_{t,l}^{\max}$ because the galaxies with $V_{\max} > V_{\text{flat}}$ in our sample have considerable amounts of HI gas at their peak velocity in the rotation curve. This gas, rotating at V_{\max} broadens the global profile somewhat further. If we consider only the 16 galaxies for which $V_{\max} = V_{\text{flat}}$ we find

$$W_{t,20}^{\max} = W_{t,20}^{\text{flat}} = 23, \quad W_{t,50}^{\max} = W_{t,50}^{\text{flat}} = 6$$

in agreement with the values of $W_{t,l}^{\max}$ we found when using all 22 galaxies.

Our results are illustrated in Fig. 2 where we show, for each of the 22 galaxies, the deviations $\Delta W_{R,l}^{\max}$ (upper panels) and $\Delta W_{R,l}^{\text{flat}}$ (lower panels) as a function of V_{flat} . Galaxies with $V_{\max} = V_{\text{flat}}$ are indicated by filled symbols, galaxies with $V_{\max} > V_{\text{flat}}$ are indicated by open symbols. The upper two panels in each block show the results one obtains when using Broeil's adopted values of $W_{t,20} = 38$ and $W_{t,50} = 14 \text{ km s}^{-1}$.

From the upper panels in the upper block it is clear that the maximum rotational velocity as derived from the corrected global profiles is severely underestimated when using the values of $W_{t,l}$ derived by TFq and adopted by Broeils. This systematic underestimation disappears when $W_{t,20}$ is decreased from 38 to 22 km s^{-1} and $W_{t,50}$ is decreased from 14 to 5 km s^{-1} . The upper two panels in the lower block show that if one is interested in the amplitude of the flat part, which is smaller than the maximum rotational velocity for galaxies with a declining rotation curve (open symbols), the average offset becomes less significant simply because the open symbols scatter upward. In this case, to obtain an average zero offset, we find similar values for $W_{t,l}$ as those adopted by Broeils. However, we find the curious situation that the corrected width of the global profile systematically overestimates V_{flat} for galaxies with a declining rotation curve (open symbols) and systematically underestimates V_{flat} for galaxies with a purely flat rotation curve (filled symbols).

From this we can conclude that, in a statistical sense, the maximum rotational velocity of a galaxy can be reasonably well retrieved from the width of the global profile when using $W_{t,20} = 22$ or $W_{t,50} = 5 \text{ km s}^{-1}$. The amplitude of the flat part can not be retrieved consistently for a mixed sample containing galaxies with declining rotation curves. Note that we have explored only a restricted range of rotational velocities: 8–200 km s^{-1} .

Our results also indicate a non-Gaussian distribution of random velocities in the sense that $W_{t,20}/W_{t,50} \neq 1.80/1.18$. Interpreting $W_{t,20}$ and $W_{t,50}$ in terms of velocity dispersions it follows that

$$\begin{aligned}\sigma_{20} &= W_{t,20}/2k_{20} = 6.1 \text{ km s}^{-1} \\ \sigma_{50} &= W_{t,50}/2k_{50} = 2.1 \text{ km s}\end{aligned}$$

where $k_{20} = 1.80$ and $k_{50} = 1.18$ for a Gaussian distribution. Recall, however, that we advocate a different correction for instrumental broadening than Bottinelli et al.'s scheme used by Broeils and Rhee. With our correction method for instrumental broadening we find the somewhat smaller values of:

$$W_{t,20} = 22, \quad W_{t,50} = 2.$$

These smaller values of $W_{t,l}$ allow to retrieve V_{flat} from the global profiles of galaxies with purely flat rotation curves and V_{\max} for galaxies with declining rotation curves. Applying our correction method for instrumental resolution and the above-mentioned value of $W_{t,20} = 22 \text{ km s}^{-1}$ we find an rms scatter in $\Delta W_{20} = 0.5W_R^i - V_{\max}$ of 6.8 km s^{-1} .

5. A comparison of inclinations

Present day instrumentation allows accurate measurements of the luminosities and global HI profiles of galaxies. In general, the observed scatter in the TF-relation is larger than can be explained by the observational uncertainties in these measured parameters alone. However, the uncertainty in corrections sensitive to inclination contribute significantly to the observed scatter. For a sample of randomly oriented galaxies more inclined than 45 degrees, an uncertainty of 1, 3 or 5 degrees in the inclination angle contributes respectively 0.04, 0.12 or 0.19 magnitudes to the scatter due to the uncertainty in line widths alone, assuming a slope in the TF-relation of -10 . Therefore, it is important to determine the inclination angle of a galaxy as accurate as possible and this issue deserves some special attention.

From the photometric and HI synthesis data available, three independent measurements of the inclination angle of a galaxy can in principle be obtained; i_{opt} from the optical axis ratio, i_{HI} from the apparent ellipticity of the HI disk, and i_{VF} from fitting tilted rings to the HI velocity field. Each of these methods has its own systematic limitations which are important to recognize when estimating the actual inclination of a galaxy. In the following discussion we will briefly address those limitations and make an intercomparison of i_{opt} , i_{HI} , and i_{VF} .

5.1. i_{opt} from optical axis ratios

The most widely used formula to infer the inclination angle from the observed optical axis ratio ($b/a \equiv q$) was provided by Hubble (1926):

$$\cos^2(i_{\text{opt}}) = \frac{q^2 - q_0^2}{1 - q_0^2}$$

where q_0 is the intrinsic thickness of an oblate stellar disk. Holmberg (1946) determined an average value of $q_0 = 0.20$ which is still commonly used although it is obvious from images of edge-on systems that large variations in q_0 exist. For instance, Fouqué et al. (1990) found q_0 to vary from 0.30 to 0.16 for spirals of morphological types Sa to Sd respectively and $q_0 = 0.42$ for galaxies of type Sdm-Im. Apart from the debate on the intrinsic thickness, the observed axis ratio q itself has limited meaning since it is often defined at a certain isophote around which q may still vary as a function of radius. From images of edge-on disks in the Ursa major cluster (see Paper I) it can often be observed that the axis ratio keeps increasing outward until the faintest isophotes. An extreme example is NGC 4389, dominated by a narrow bar and surrounded by an extended faint halo. The axis ratios presented in Table 1 were not determined at a fixed isophote but were chosen to represent the stellar disk instead of a bulge, lopsided structures or a faint halo.

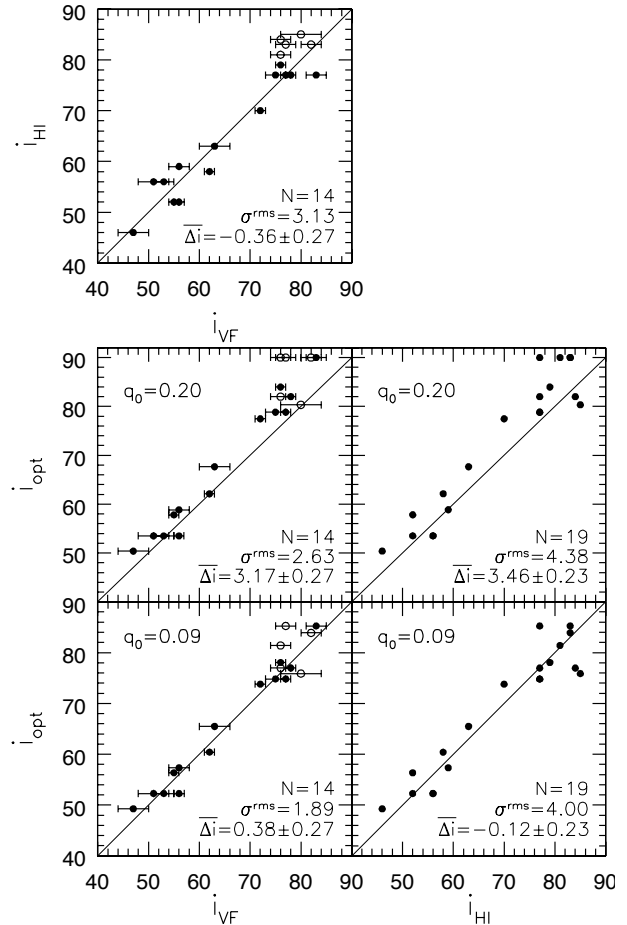


Fig. 3. Intercomparison of the three independently determined inclination angles i_{opt} , i_{HI} and i_{VF} . Only the filled symbols ($i_{\text{HI}} < 80^\circ$ when i_{VF} is involved) are considered for the unweighted quantitative assessment

5.2. i_{HI} from the inclined HI disk

Apart from the oblate stellar disk, the HI disk can also be used to determine the inclination. In general, the HI disk is much thinner than the stellar disk and its intrinsic thickness is of no concern. However, its patchiness, lopsidedness and the existence of warps and tidal tails may complicate the interpretation of the results from fitting ellipses to a certain HI isophote. Here, no correction for the intrinsic thickness of the HI layer was applied. However, the relatively large synthesized beams of imaging arrays at 21 cm may smear the observed HI disks to a rounder appearance. Therefore, a simple correction for beam smearing was applied to our measurements and the inclination of the HI disk was determined according to

$$\cos^2(i_{\text{HI}}) = \frac{d_{\text{HI}}^2 - \Theta_d^2}{D_{\text{HI}}^2 - \Theta_D^2}$$

where D_{HI} and d_{HI} are the observed major and minor axis diameters of the inclined HI disk obtained by fitting an ellipse to the outer column density levels. Θ_D and Θ_d are the sizes of the synthesized beam in the direction of the major and minor axis of the HI disk.

5.3. i_{VF} from HI velocity fields

The inclination angle of an HI disk can also be measured by fitting tilted-rings to its velocity field (Begeman 1989). However, the inclination angle and the rotational velocity are strongly coupled and reasonable results can only be obtained for inclination angles between roughly 50 and 75 degrees. This procedure requires accurate velocity fields with high signal-to-noise ratios as well as many independent points along a ring. The advantage that velocity fields offer is the possibility to identify warps and to check the kinematic regularity of the HI disk. For instance, the optical appearance of a galaxy may look very regular while the outer regions of the HI disk may be strongly warped toward edge-on (e.g. N3726). Such a warp would broaden the global profile and an inclination correction based on the optical axis ratio would lead to an overestimate of the rotational velocity when dividing the “warp-broadened” line width by $\sin(i_{opt})$.

Note that the inclination measurement of a tilted ring may be affected by non-circular motions due to spiral arms, bars and lopsidedness.

5.4. The comparison

For the comparison between the three differently inferred inclination angles we considered only those 27 galaxies with fully reduced HI data for which the velocity fields and integrated HI maps are available. We excluded the interacting galaxies (N3769, N3893, U6973) because their outer isophotes (optical and HI) are affected by tidal tails. We also excluded galaxies with perturbed or inadequately sampled velocity fields (N4088, U6969, N4389), galaxies with excessively patchy HI maps (N4102) and obviously lopsided galaxies (N4051). These eliminations leave us with 19 galaxies that have smooth outer isophotes, well filled HI disks and regular HI velocity fields.

Figure 3 presents the comparison between the three differently inferred inclination angles using two different values for q_0 . When calculating mean differences and scatters using i_{VF} , only galaxies with $i_{HI} < 80^\circ$ are considered because kinematic inclinations of highly inclined galaxies are systematically underestimated. The error bars on i_{VF} are based on the variations in i_{VF} between the various fitted rings but are not considered any further here.

The upper most panel compares i_{VF} with i_{HI} . No significant offset is found for the 14 galaxies that meet the above-mentioned criteria. Assuming that i_{VF} and i_{HI} contribute equally to the scatter of 3.1 degrees implies that the inclination angle can be determined with an accuracy of 2.2 degrees from either the velocity fields or from the inclined HI disk. Note that the correlation turns up for $i_{HI} > 80^\circ$ due to the systematic underestimation of i_{VF} for highly inclined disks.

Comparing i_{opt} with i_{VF} and i_{HI} does show a significant offset of roughly 3 degrees when assuming $q_0 = 0.20$ (middle panels). This offset is biggest toward edge-on as would be expected in case of an overestimate of the intrin-

sic thickness. Note that there are several galaxies with an observed optical axis ratio less than 0.20 which have been assigned an inclination angle of 90° .

This 3° offset disappears when $q_0 = 0.09$ is used (lower panels) and the rms scatter is reduced to only 1.9 degrees for i_{opt} versus i_{VF} but is still 4.0 degrees in case of i_{opt} versus i_{HI} . In the latter case, the scatter is caused by a few nearly edge-on systems for which the higher uncertainties have no influence on the deprojection of the rotational velocities.

The adopted inclinations and their errors, listed in Col. 11 of Table 1 are best estimates based on all the information available for a particular galaxy, including the morphology of dust lanes if present. For galaxies which lack fully reduced HI synthesis data, the inclination angles were inferred from the optical axis ratios using $q_0 = 0.09$ for galaxies of type Sc and later and $q_0 = 0.24$ for galaxies of type Sbc and earlier. The latter value of q_0 seemed justified by the observed axis ratios of the (nearly) edge-on systems N4013, N4026 and N4111 of types Sb, S0 and S0 respectively. Unfortunately, there are not enough suitable galaxies available to determine q_0 as a function of morphology.

6. The atlas

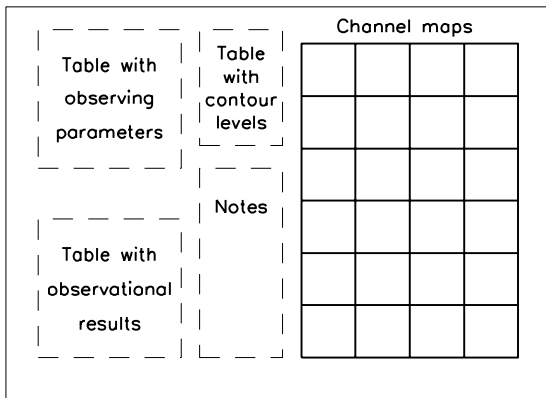
The atlas is presented in Appendix B and consists of two parts. The first part presents the data for the 30 galaxies which have been fully reduced and analyzed. The second part gives a less elaborate presentation of the remaining 13 galaxies which have been only partially reduced.

The reduction procedures described in Sect. 3 were applied to the data at all three angular resolutions. However, to facilitate the intercomparison of various results for a galaxy, it was decided to present the data of a particular galaxy at the same angular resolution as much as possible. The rotation curves are in some cases a combination of the rotation curves at various resolutions, the inner parts at the highest spatial resolution and the outer parts from data of lower resolution but higher signal-to-noise ratio. The channel maps are sometimes presented at a lower angular resolution than the other data.

Figure 4 shows the graphical layout for each of the 30 galaxies in the first part of the atlas. The data for each of the 13 galaxies in the second part of the atlas are presented on a single page which contains the tables and notes as well as the mosaic of channel maps, the global profile and the XV-diagram along the major axis. The contents of the various tables and panels are described below.

Tables and Notes – There are three tables presented for each galaxy. The upper left table contains information on the observations like date, integration time and correlator settings. The lower left table presents some of the quantities derived from the HI data like global profile widths, integrated HI flux, systemic velocity etc. The upper right table provides the noise and contour levels for the maps in the various panels. The contours in the

First page



Second page

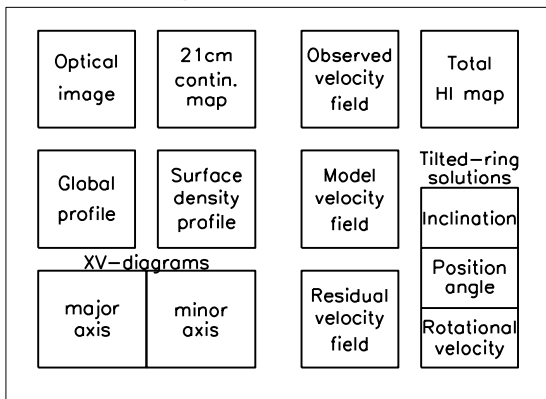


Fig. 4. Layout of the HI atlas pages for the 30 galaxies with fully reduced data. All the data for these galaxies are presented on two facing pages. Results for the 13 galaxies with partially reduced data are presented on a single page per galaxy and include only the channel maps, the global profile and the XV-diagram. The linear scale is 5.4 kpc per arcminute

channel maps, 21 cm continuum maps and XV-diagrams are always drawn at levels which are related to the rms noise.

The notes contain information about specific aspects of a particular galaxy like optical and HI appearance.

Channel maps – The channel maps show how the HI emission behaves as a function of velocity. From these maps it is possible to recognize the presence of warps, non-circular motions and HI-bridges between interacting galaxies like N3769/1135+48 and N3893/N3896. The contours are drawn at levels of $-3, -1.5$ (dashed), $1.5, 3, 4.5, 6, 9, 12, 15, \dots\sigma$. The value of the rms noise level σ is given in the upper right table. In each panel, the cross indicates the adopted dynamical center of the galaxy. The ellipse in the upper left panel is centered on this position and the position angle is set at the kinematic major axis of the inner regions. The ellipticity represents the inclination as derived from the optical axis ratio and the major axis diameter is equal to $D_{25}^{b,i}$. The synthesized beam at half power is shown in the lower left corners of the left

panels. The panel at the lower right shows the subtracted, “dirty” continuum map.

Optical image – The optical image of a galaxy was scanned from the blue POSS plates. In the upper left corner, the morphological type according to the RC3 is given. CCD images of far superior quality can be found in Paper I. An example is given for N3726 in which case the CCD image is pasted into the POSS image.

Radio continuum map – The cleaned 21 cm radio continuum map is plotted at the same scale as the optical image. The contours are drawn at levels of $-4, -2$ (dashed), $2, 4, 8, 16, 32, 64, \dots\sigma$. The value of the rms noise σ is given in the upper right table. The ellipse represents the optical image as in the upper left panel in the channels maps. The synthesized beam is plotted in the lower left corner and the small cross indicates the adopted position of the center of rotation.

Global profile – Each point in the global HI profile gives the primary-beam corrected, total HI flux density integrated over a single channel map. The errors are derived as explained in Sect. 3.2. The vertical arrow indicates the systemic velocity (lower left table on the first page) as derived from the HI velocity field and does not necessarily indicate the center of the global HI profile. A significant offset from the center could indicate non-circular motions or a strong lopsidedness. These anomalies can often be traced in the individual channel maps.

Surface density profile – The open and filled symbols indicate the azimuthally averaged radial surface densities for the approaching and receding sides. The solid line follows the average value. At the adopted distance of 18.6 Mpc, 1 arcmin corresponds to 5.4 kpc. The vertical arrow indicates $R_{25}^{b,i}$. The profile becomes unreliable for highly inclined systems since no correction for beam smearing was applied.

XV-diagrams – The position-velocity diagrams are shown for two orthogonal cuts through the adopted center of rotation along the kinematic major (left) and minor (right) axes. The position angles of these two axes are printed in the upper right corner of each panel. Note that the quoted position angles refer to the positive offset axes. Consequently, the position angle of the major axis refers to the receding side which also can be inferred from the channel maps. The vertical dashed line indicates the position of the center of rotation. The horizontal dashed line indicates the systemic velocity as derived from either the velocity field for galaxies with fully reduced data, or from the XV-diagram for galaxies in the second part of the atlas. The two vertical arrows show where the ellipse with major axis diameter $D_{25}^{b,i}$ intersects the XV-slice. The horizontal arrows in the left panel show the systemic velocity V_{sys}^{GP} derived from the global profile and $V_{sys}^{GP} \pm \frac{1}{2}W_{R,I}$ where $W_{R,I}$ is the width of the global profile at the 20% level of peak flux, corrected for instrumental broadening (see Sect. 3.2) and turbulent motions according to TFq.

Contours are at levels of $-3, -1.5$ (dashed), $1.5, 3, 4.5, 6, 9, 12, 15, \dots\sigma$. The value of the rms noise σ is given in the upper right table. The cross in the lower left corners

indicates the angular and velocity resolutions. An offset of 1 arcmin corresponds to a projected distance of 5.4 kpc from the center.

The crosses give the projected rotational velocities as derived from the tilted rings fit. In some cases, at large radii, a cross can be found without any underlying signal in the XV-diagram. In such cases, the rotational velocity at that radius is defined by points in the velocity field away from the major axis. The open and filled circles indicate the projected rotational velocity estimated directly from these XV-diagrams. These points must be deprojected using the appropriate inclination and position angles to obtain the actual rotation curve for both halves of the galaxy.

Total HI map – All pixels in the total HI map with a positive signal have a greyscale value assigned. Because the signal-to-noise ratio along a contour is not constant, the “ 3σ -contour” is not defined. Section 3.3 and the appendix explain why and how the noise varies across an integrated HI map.

The second contour in the total HI maps corresponds to the *average* value of all pixels with a signal-to-noise ratio between 2.75 and 3.25 and this contour can thus be considered as a pseudo 3σ -contour. Wherever a contour goes through an area with $(\frac{S}{N}) < 3$, the contour is plotted much thinner. Consequently, the lowest contour, plotted at the “ 1.5σ ” level, is plotted thin over most of its stretch. The various contour levels in atoms cm⁻² are given in the upper right table. The size of the synthesized beam is plotted in the lower left corner. The beamwidths are the same as in the channel maps unless specified otherwise in the note. The small cross indicates the adopted position of the center of rotation (1 arcmin corresponds to 5.4 kpc).

Velocity fields – The greyscales indicate the pixels where a radial velocity was measured. Darker greyscales and white isovelocity contours indicate the receding side. The thick first black contour adjacent to the white ones indicates the adopted systemic velocity. In the ideal case of circular motion and no noise, this thick contour should be a straight line through the center and coinciding with the kinematic minor axis of the galaxy. The isovelocity contours are plotted with constant velocity intervals as given by the upper right table. The synthesized beam is plotted in the lower left corner.

The observed velocity field was modeled by fitting tilted rings to it. The orientation and rotational velocity of each ring were then used to construct the model velocity field. The model velocity field is plotted with the same orientation and on the same scale as the observed velocity field. The isovelocity contours are plotted at the same velocities in the observed as in the model velocity fields. For nearly edge-on systems, the model velocity field is only one or two pixels wide in which case no contours could be drawn.

The residual velocity field was made by subtracting the model from the observed velocity field. White contours indicate positive residuals, black contours indicate negative

residuals. The contour levels are ..., $-15, -10, -5, 5, 10, 15, \dots$ km s⁻¹.

Tilted-ring fits – The three combined panels show the results from the tilted-ring fits to the observed velocity field. The upper panel shows the inclination angle, the middle panel the position angle and the lower panel the rotational velocity.

The crosses with errorbars in the panels for inclination and position angle are the results from the second step of the fitting procedure as explained in Sect. 3.6.1. The dashed lines, mostly coinciding with the solid lines, in these upper two panels indicate the final values of the inclination and position angles kept fixed when the rotational velocity was fitted. The resulting rotation curve is shown by crosses with errorbars in the lower panel. The errorbars indicate the formal errors, as given by the least squares minimization algorithm.

The horizontal arrows in the upper two panels indicate the inclination and position angles as derived from the optical isophotes in the outer regions. The diamonds indicate the inclination and position angles as determined from the total HI maps. When the total HI maps are very patchy, these diamonds are very uncertain. The horizontal arrow in the lower panel indicates the rotational velocity as derived from the width of the global HI profile corrected for instrumental broadening, turbulent motion and inclination. The adopted inclination is representative for the outer parts. The vertical arrow in the lower panel indicates $R_{25}^{b,i}$.

The solid lines in the upper and middle panels show the inclination and position angles that were adopted to deproject the radial velocities determined from the XV-diagrams. This deprojection results in the rotation curves plotted as open and filled circles in the lower panel (same symbols as in the XV-diagrams). Note that although the rotational velocities at a certain radius may be different for the approaching and receding sides, both sides were assumed to have the same inclination and position angles at that radius. The solid line in the lower panel shows the mean rotation curve derived from the XV-diagram. 1 arcmin on the horizontal axis corresponds to 5.4 kpc.

Tabulated data – The various parameters derived from the HI data presented here are summarized in Table 5. *Column* (1) gives the NGC or UGC numbers.

Columns (2)–(5) give the uncorrected widths with formal errors of the global profiles at 20% and 50% of the peak flux.

Column (6) gives the instrumental velocity resolution at which the global profiles were observed.

Columns (7) and (8) contain the heliocentric systemic velocities and their uncertainties as derived from the global profiles.

Table 5. Results from the HI synthesis observations

Name	$W_{20} \pm$	$W_{50} \pm$	Res.	$V_{\text{hel}} \pm$	$\int Sdv \pm$	$F_{\nu} \pm$	R_{HI}	R^{imp}	$V_{\text{rot}}^{\text{imp}} \pm$	shape	$V_{\text{max}} \pm$	$V_{\text{flat}} \pm$									
	(1)	(2)	(3)	(4)	(5)	(6)	(7)	(8)	(9)	(10)	(11)	(12)	(13)	(14)	(15)	(16)	(17)	(18)	(19)	(20)	(21)
<i>Galaxies with fully reduced HI data:</i>																					
U6399	188.1	1.4	172.5	2.9	8.3	791.5	0.6	10.5	0.3	<2.5	1.68	1.50	88	5	R/F	88	5	88	5		
U6446	154.1	1.0	131.9	1.2	5.0	644.3	0.8	40.6	0.5	<7.2	2.96	2.93	80	11	F L	82	4	82	4		
N3726	286.5	1.6	260.6	1.8	5.0	865.6	0.9	89.8	0.8	49.7	5.0	4.24	6.22	167	15	F/(D)	162	9	162	9	
N3769	265.3	6.7	230.5	3.6	8.3	737.3	1.8	62.3	0.6	12.1	2.9	4.31	7.10	113	11	F/(D)	122	8	122	8	
U6667	187.5	1.4	178.1	1.9	5.0	973.2	1.2	11.0	0.4	<2.7	1.64	1.50	86	3	R L	86	3	86	3		
N3877	373.4	5.0	344.5	6.2	33.2	895.4	3.8	19.5	0.6	35.6	2.4	2.17	2.17	169	7	F L	167	11	167	11	
N3893	310.9	1.0	277.9	4.1	5.0	967.2	1.0	69.9	0.5	137.4	2.9	3.98	3.88	148	19	F/(D)	188	11	188	11	
N3917	294.5	1.9	279.1	2.1	8.3	964.6	1.4	24.9	0.6	<7.2	2.69	2.83	137	8	F	135	3	135	3		
N3949	286.5	1.4	258.3	1.7	8.3	800.2	1.2	44.8	0.4	134.1	3.6	2.62	1.35	169	8	F L	164	7	164	7	
N3953	441.9	2.4	413.9	3.2	33.1	1052.3	2.0	39.3	0.8	50.9	2.5	3.32	3.00	215	10	F	223	5	223	5	
N3972	281.2	1.4	260.7	5.5	8.3	852.2	1.4	16.6	0.4	<5.8	1.92	1.67	134	5	R L	134	5		
U6917	208.9	3.2	189.6	1.6	8.3	910.7	1.4	26.2	0.3	<4.4	2.42	2.00	111	7	R/F	104	4	104	4		
U6923	166.8	2.4	147.1	4.5	10.0	1061.6	2.2	10.7	0.6	<2.6	1.29	1.02	81	5	R L	81	5		
U6930	136.5	0.5	122.1	0.7	8.3	777.2	0.4	42.7	0.3	<5.8	3.20	3.17	108	7	R/F	107	4	107	4		
N3992	478.5	1.4	461.4	2.4	10.0	1048.2	1.2	74.6	1.5	30.2	7.6	4.75	6.67	237	9	F/D	272	6	242	5	
U6940	59.3	3.8	40.6	7.8	10.0	1118.0	1.7	2.1	0.3	<1.3	0.61	0.33	37	4	R	37	4		
U6962	220.3	6.6	182.4	3.7	8.3	807.4	3.2	10.0	0.3	13.4	1.7	1.38	1.00	171	7	R L	171	7	
N4010	277.7	1.0	264.1	1.2	8.3	901.9	0.8	38.2	0.3	16.9	1.6	3.36	2.00	122	2	(R)/F L	128	9	128	9	
U6969	132.1	6.4	123.5	2.9	10.0	1118.5	2.4	6.1	0.5	<3.8	0.95	0.85	79	5	R	79	5		
U6973	367.8	1.8	350.4	1.2	8.3	700.5	1.0	22.9	0.2	127.5	2.1	2.21	1.50	180	8	F/(D)	173	10	173	10	
U6983	188.4	1.3	173.0	1.1	5.0	1081.9	0.8	38.5	0.6	<5.4	3.07	3.00	109	12	F	107	7	107	7		
N4051	255.4	1.8	224.6	1.5	5.0	700.3	1.2	35.6	0.8	26.5	2.6	2.89	2.33	153	10	R/F L	159	13	159	13	
N4085	277.4	6.6	255.4	7.8	19.8	745.7	5.0	14.6	0.9	44.1	1.3	1.94	1.18	136	7	R/F L	134	6	134	6	
N4088	371.4	1.7	342.1	1.9	19.8	756.7	1.2	102.9	1.1	222.3	1.9	4.25	4.10	174	8	F/(D) L	173	14	173	14	
N4100	401.8	2.0	380.5	1.8	19.9	1074.4	1.3	41.6	0.7	54.3	1.7	3.45	4.35	159	9	F/D	195	7	164	13	
N4102	349.8	2.0	322.4	8.5	8.3	846.3	2.0	8.0	0.2	276.0	1.5	1.16	0.83	178	12	F	178	11	178	11	
N4157	427.6	2.2	400.7	3.1	19.9	774.4	1.8	107.4	1.6	179.6	2.3	4.60	5.67	185	14	F/D	201	7	185	10	
N4183	249.6	1.2	232.5	1.5	8.3	930.1	1.0	48.9	0.7	<5.8	3.07	4.02	113	11	F/D L	115	6	109	4		
N4217	428.1	5.1	395.6	3.8	33.2	1027.0	3.0	33.8	0.7	115.6	2.2	3.19	3.17	178	12	F/D	191	6	178	5	
N4389	184.0	1.5	164.9	1.6	8.3	718.4	1.2	7.6	0.2	23.3	1.2	1.30	1.02	110	8	R	110	8	
<i>Galaxies with partially reduced HI data:</i>																					
N3718	492.8	1.0	465.7	1.0	33.2	993.0	0.8	140.9	0.9	11.4	0.4		6.67	223	12	F	232	11	232	11	
N3729	270.8	1.5	253.2	3.9	33.2	1059.8	1.4	5.5	0.3	18.0	0.9		1.00	151	11	F	151	11	151	11	
U6773	110.4	2.3	91.1	2.2	8.3	923.6	1.6	5.6	0.4	<2.6			0.67	45	5	R L	45	5	
U6818	166.9	2.3	141.9	5.7	8.3	808.1	2.1	13.9	0.2	2.4	1.0		1.33	74	7	R/(F) L	73	5	73	5	
U6894	141.8	1.1	132.2	1.5	8.3	848.6	1.8	5.8	0.2	<2.7			0.67	63	5	R	63	5	
N3985	160.2	3.7	88.0	2.4	8.3	948.2	2.0	15.7	0.6	9.7	1.4		0.50	93	7	R	93	7	
N4013	425.0	0.9	395.0	0.8	33.0	831.3	0.6	41.5	0.2	36.3	0.8		6.12	170	10	F/D	195	3	177	6	
U7089	156.7	1.7	97.7	3.0	10.0	770.0	1.5	17.0	0.6	<3.4			1.75	79	7	R L	79	7	
U7094	83.7	1.7	71.9	5.5	10.0	779.6	1.6	2.9	0.2	<2.6			1.00	35	6	R L	35	6	
N4117	289.4	7.5	260.3	5.2	10.0	934.0	1.5	6.9	1.1	3.7	1.2					?					
N4138	331.6	4.5	266.0	7.8	19.9	893.8	3.9	19.2	0.7	16.7	4.6		3.55	150	21	F/D	195	7	147	12	
N4218	138.0	5.0	79.9	1.9	8.3	729.9	1.7	7.8	0.2	6.3	0.8		0.33	73	7	R	73	7	
N4220	438.1	1.3	423.3	3.3	33.1	914.2	1.2	4.4	0.3	<4.9						?					

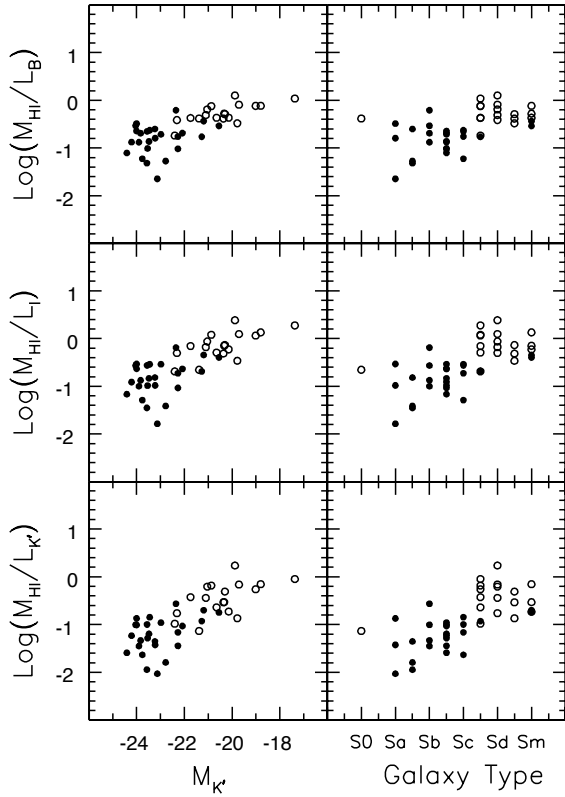


Fig. 5. Correlations between HI mass-to-light ratios and absolute K' -band magnitudes (left column) and morphological type (right column). Solid symbols indicate HSB galaxies and open symbols denote galaxies of the LSB type

Columns (9) and (10) provide the integrated HI flux and the uncertainty in Jy km s^{-1} .

Columns (11) and (12) contain the 21 cm continuum flux density and its uncertainty in mJy. In case no continuum flux was detected, a 3σ upper limit for extended emission is given.

Column (13) gives the radius of the HI disk, R_{HI} in arcmin, at the azimuthally averaged surface density of $1 M_{\odot} \text{ pc}^{-2}$, measured from the radial surface density profiles.

Column (14) gives the radius R^{lmp} of the last measured point of the rotation curve in arcmin. The differences between R^{lmp} and R_{HI} depend on the sensitivity of the measurement and the distribution of the HI gas along the kinematic major axis.

Columns (15) and (16) give the rotational velocity of the last measured point V^{lmp} and its uncertainty.

Column (17) contains information on the overall shape of the rotation curve; R: rising rotation curve, F: the rotation curve shows a flat part, D: the rotation curve shows a declining part, L: lopsided.

Columns (18) and (19) give the maximum observed rotational velocity V_{max} and its uncertainty. For galaxies with a rising rotation curve (R) $V_{\text{max}} = V^{\text{lmp}}$.

Columns (20) and (21) give the average rotational velocity of the flat part of the rotation curve V_{flat} and its uncertainty. For galaxies with a flat rotation curve (F)

$V_{\text{flat}} = V_{\text{max}}$ may deviate from V^{lmp} because V_{flat} was averaged over the flat part of the rotation curve while V^{lmp} was measured at a single point.

7. HI properties of spirals

The HI survey of the Ursa Major cluster presented here provides not only the kinematical information necessary for the study of the Tully-Fisher relation and of the dark and luminous matter for a well defined sample of galaxies. It also serves to investigate the general HI properties of disks and to make a comparison with galaxies in the field and with galaxies in denser environments. The HI studies of the Virgo cluster galaxies by Warmels (1988a, 1988b) and especially by Cayatte et al. (1990) have shown that the spiral galaxies in the central parts of the cluster have smaller HI disks of lower surface density. In the Hydra Cluster McMahon (1993) did not find any such significant HI deficiency. She did find, however, a surprisingly large number of isolated HI-rich dwarf galaxies near the center of the cluster. Dickey (1997) surveyed the more distant Hercules SuperCluster and found a similar HI deficiency of spirals near the X-ray gas as in the case of Virgo.

The Ursa Major cluster differs from those just mentioned. It has no central concentration, no X-ray emitting gas and contains mainly spirals of late morphological types. In many respects its conditions are very similar to those of a field environment. For this reason it is useful to compare the properties of the Ursa Major spirals not only with those of galaxies in dense cluster environments but also with those of field galaxies as found in various recent studies (see e.g. Broeils 1992; Puche & Carignan 1991; Rhee 1996a; Swaters 1999).

Here we give only a brief description of the global parameters and of the main properties of the HI disks of the Ursa Major galaxies. A more detailed discussion and a comparison with results from previous work is beyond the scope of this data paper.

7.1. Global parameters

Integral properties and global parameters of spiral galaxies have been derived for a large number of objects from single-dish observations (cf. Roberts & Haynes 1994). In recent years also synthesis observations (Broeils 1992; Rhee 1996a) have been used to obtain similar information for smaller samples of galaxies.

The M_{HI}/L ratios obtained for the galaxies of the Ursa Major sample listed in Table 5 are shown here in Fig. 5 as a function of absolute magnitude and of morphological type. It is well known (see refs. above) that the M_{HI}/L ratio of galaxies depends on luminosity and morphological type. The present sample of galaxies shows a clear increase of the HI mass fraction with decreasing luminosity and from early to late morphological types. The correlation is clearly stronger for the K' -band magnitudes which is a better tracer of the stellar mass.

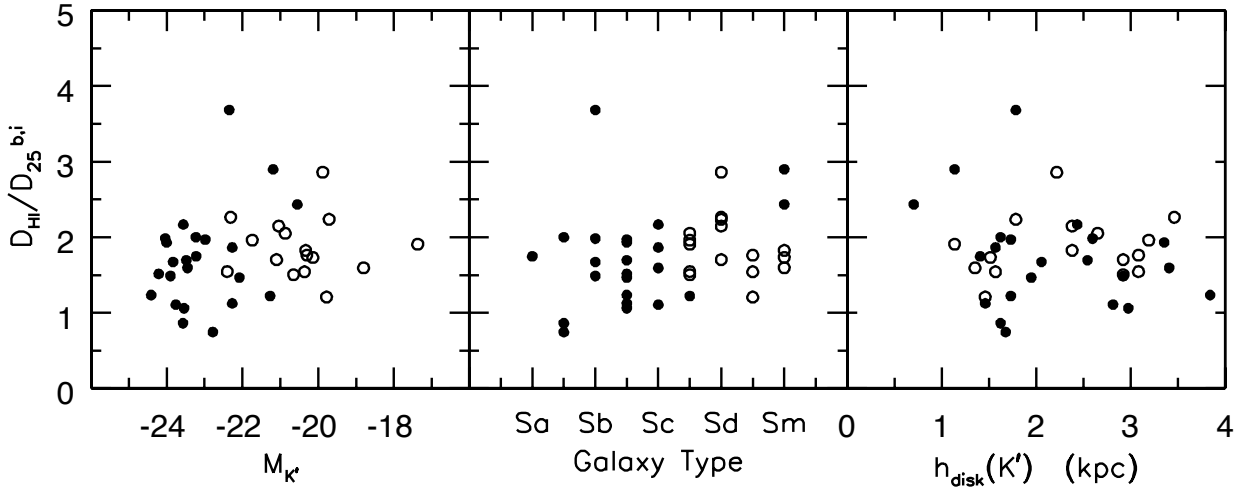


Fig. 6. Ratio of HI-to-optical diameter as a function of K' magnitudes, morphological type and disk scale length. The HI diameters were measured at the $1 M_{\odot} \text{ pc}^{-2}$ isodensity contour. Solid symbols indicate HSB galaxies and open symbols denote galaxies of the LSB type

7.2. Sizes of HI disks and radial surface density profiles

Detailed information on the sizes and radial distributions of HI disks has been obtained recently from synthesis observations of limited samples of field and cluster galaxies (Broeils & Van Woerden 1994; Cayatte et al. 1994; Rhee 1996a and 1996b). Here we present only some of the main results on the comparison of HI and optical diameters, on the relation between HI mass and diameter and on the radial density profiles for the Ursa Major sample.

Figure 6 shows the ratio of the HI diameter D_{HI} (defined at an HI surface density of $1 M_{\odot} \text{ pc}^{-2}$) to the optical diameter $D_{25}^{b,i}$ as a function of luminosity, morphological type and disk scale-length. The diagrams do not indicate any clear trend or dependence of the diameter ratio on any of those quantities. The spread is large. There may be a hint of a slight increase of the ratio from early to later types and from more luminous to less luminous systems. For almost all galaxies D_{HI} is larger than $D_{25}^{b,i}$.

As shown in previous investigations (see refs. above), there is a tight correlation between HI mass and HI diameter as illustrated in Fig. 7. This implies a nearly constant mean HI surface density regardless of size. The HI mass correlates also with the optical diameter, but, as in previous work, with a much larger scatter.

7.3. Warps, asymmetries and interactions

The radial distributions of the HI surface densities are shown in Fig. 8. Only galaxies with fully reduced data, more inclined than 80 degrees and with $R_{\text{HI}} < 1$ arcmin are considered in order to avoid the most severe cases of beam smearing. There is clearly a considerable diversity of shapes and intensities. The upper row shows the profiles grouped for galaxies of similar morphological types. The dotted lines represent low surface brightness galaxies. No obvious trend with morphological type

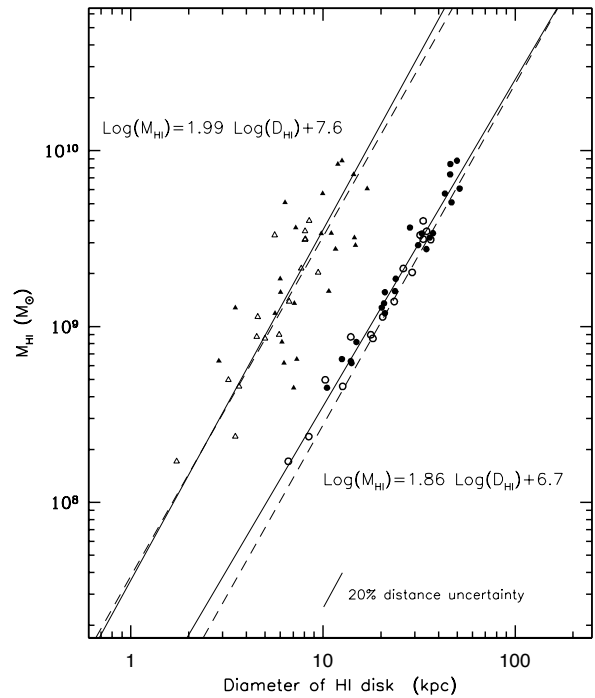


Fig. 7. Correlations between HI mass and the isophotal diameters of the stellar (triangles) and HI disks (circles). Solid lines indicate fits to the plotted data points while the dashed lines represent the fits found by Broeils (1992). Filled symbols indicate HSB galaxies and open symbols denote galaxies of the LSB type. Triangles are offset to the left

or surface brightness can be discerned. However, in the lower row, the profiles are grouped according to the galaxy properties as listed in Table 6. In this case, a clear trend is visible in the sense that galaxies with high HI surface densities in their inner regions are either involved in interactions, are lopsided or display a warped HI disk. Especially in the case of interacting and strongly lopsided systems, no

Table 6. Warps, asymmetries and interactions

Name	Type	Warped	Lopsided	Inter-
		HI distr.	HI kin.	acting
U6399	Sm		×	
U6446	Sd			×
N3718	Sa	×		
N3726	SBc	×		
N3729	SBab			
N3769	SBb	×		×
U6667	Scd			×
N3877	Sc			×
U6773	Sm			×
N3893	Sc			×
N3917	Scd		×	
U6818	Sd			×
N3949	Sbc		×	×
N3953	SBbc			
U6894	Scd			
N3972	Sbc			×
U6917	SBd	×		
N3985	Sm	×		
U6923	Sdm	×		×
U6930	SBd		×	
N3992	SBbc			
U6940	Scd			
N4013	Sb	×		
U6962	SBcd			×
N4010	SBd	×		×
U6969	Sm			
U6973	Sab	×		×
U6983	SBcd			
N4051	SBbc			×
N4085	Sc			×
N4088	Sbc	×	×	×
U7089	Sdm		×	
N4100	Sbc	×		
U7094	Sdm		×	
N4102	SBab			
N4117	S0			
N4138	Sa	×		×
N4157	Sb	×		
N4183	Scd	×		
N4218	Sm			
N4217	Sb			
N4220	Sa			
N4389	SBbc			

longlived stable gas orbits can be expected and evidently, the cold gas becomes concentrated toward the inner regions of the disk. Note that some galaxies appear in more than one panel.

Warps are thought to be a quite common feature of the outer HI layers of spiral galaxies. But, in spite of attempts made in recent years (Bosma 1991), a good statistics on their occurrence does not exist yet. The information on HI warps provided by the present survey of the Ursa Major sample is somewhat limited mainly because of the already noted small radial extent of the HI layers with respect

to the optical. There are pronounced HI warps like the well-known ones found in NGC 3718 (Schwarz 1985) and NGC 4013 (Bottema 1995) and those seen in other galaxies (N3726, N3985 N4010, N4157, N4183). In most cases the warps are visible in the outer parts beyond the optical bright disk and are present in normal, regular, not interacting disks. But there are also systems, like NGC 4088, which are strongly distorted in their optical appearance and also in their kinematics. Similar distortions are found in clearly interacting systems like NGC 3769. In the sample of 43 galaxies (Table 6) there are at least 13 objects with clear indications of warping.

Also asymmetries are thought to occur frequently in field spirals (Richter & Sancisi 1994). In the present sample we see a large number of objects (at least half, see Table 6) with a lopsided HI distribution and/or kinematics. The majority shows kinematical asymmetries: on one side of the disk the rotation curve rises more slowly and reaches its flat part at a larger radius than on the other side (see for example NGC 3877, 3949, 4051). Note that this occurs in the inner parts of non-interacting, regular, normal systems.

Finally, there are four galaxies in this sample of 43 which have close companions and show clear HI signs of tidal interactions. A few more objects (examples NGC 3718, 4088) show distortions or peculiar structures in their density and velocity maps.

8. Concluding remarks

This data paper has presented the results of an extensive HI synthesis imaging survey with the WSRT of a well-defined complete equidistant sample of spiral galaxies in the nearby Ursa Major cluster. Figures B.1 and B.2 show a compilation of all the available HI maps. Individual galaxies are at their proper position on the sky but they are individually four times enlarged. Some galaxies had to be shifted to avoid overlapping maps. Rotation curves have been derived for most galaxies as well as detailed information on the kinematical state of the galaxy disks as indicated by the presence of global perturbations, warps, interactions and lopsidedness. Since the galaxies were not selected on the basis of their HI size or content, the quality of the kinematical data varies widely from galaxy to galaxy. Nevertheless, these data will be useful for an analysis of the statistical properties of the Tully-Fisher relation and the rotation curves may be decomposed into contributions from the main dynamical constituents like the stellar and gaseous disks, the bulge and the dark matter halo. These issues will be addressed in forthcoming papers.

Those who would like to use the rotation curves for their own purposes are advised not to take the rotation curves at face value but to check their validity against the actual data and to take notice of the comments provided on the atlas pages. It should be realized that the rotation curves presented here are derived from the kinematics of the HI gas which is assumed to be a tracer of a galaxy's potential. There are some caveats to be aware of like the

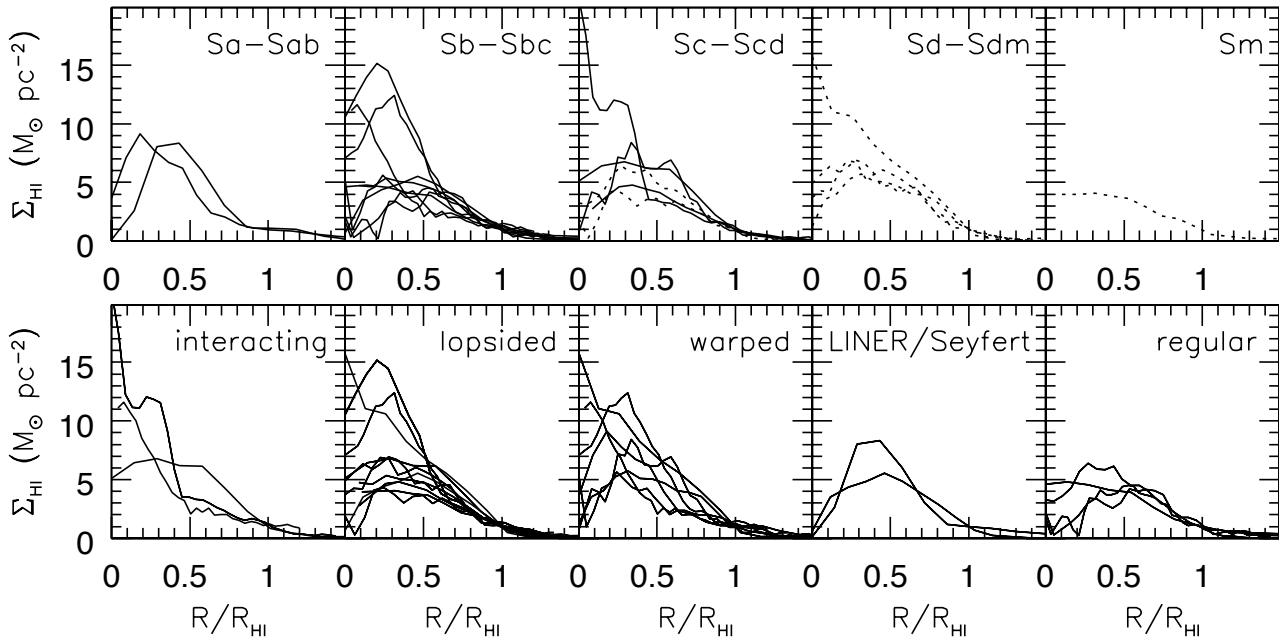


Fig. 8. Azimuthally averaged deprojected radial HI surface density profiles of galaxies with fully reduced data, less inclined than 80 degrees and with $R_{\text{HI}} > 1$ arcmin. The profiles were scaled in radius by the radius of the HI disk measured at the $1 M_{\odot} \text{ pc}^{-2}$ isodensity contour. Upper row: Σ_{HI} as a function of morphological type. The dashed lines indicate low surface brightness galaxies. Lower row: Σ_{HI} as a function of the kinematic state, according to Table 6, and nuclear activity

projection effects of streaming motions and partially filled HI disks of edge-on systems.

Finally, optical long-slit spectroscopy is already available for nearly all galaxies in the sample. These high resolution optical rotation curves will be used to supplement the HI rotation curves in the inner regions, allowing for better decompositions and maximum-disk constraints.

Acknowledgements. The Westerbork Synthesis Radio Telescope is operated by the Netherlands Foundation for Research in Astronomy (NFRA/ASTRON), with financial support by The Netherlands Organization for Scientific Research (NWO). This research has made use of the NASA/IPAC Extragalactic Database (NED) which is operated by the Jet Propulsion Laboratory, Caltech, under agreement with the National Aeronautics and Space Association. The results presented in this paper were obtained during MV's thesis research at the Kapteyn Institute of the University of Groningen, The Netherlands. This paper was finalized at the National Radio Astronomy Observatory which is a facility of the National Science Foundation operated under cooperative agreement by Associated Universities, Inc. This research has been supported by NATO Collaborative Research Grant 940271.

References

- Appleton, P. N., & Davies, R. D. 1982, MNRAS, 201, 1073
- Begeman, K. G. 1987, Thesis, University of Groningen
- Begeman, K. G. 1989, A&A, 223, 47
- Bosma, A. 1991, Warped and flaring HI disks, in Warped disks and inclined rings around galaxies, ed. S. Casertano, P. Sackett, & F. Briggs (Cambridge University Press), 181
- Bottema, R., 1995 A&A, 295, 605
- Bottema, R. 1996, A&A, 306, 345
- Bottinelli, L., Gouguenheim, L., Paturel, G., & De Vaucouleurs, G. 1983, A&A, 118, 4
- Bottinelli, L., Gouguenheim, L., Fouqué, P., & Paturel, G. 1990, A&AS, 82, 391
- Bravo-Alfaro, H., Cayatte, V., Van Gorkom, J. H., & Balkowski, C. 2000, AJ, 119, 580
- Broeils, A. H. 1992, Thesis, University of Groningen
- Broeils, A. H., & van Woerden, H. 1994, A&AS, 107, 129
- Burstein, D., & Heiles, C. 1984, ApJS, 54, 33
- Cardelli, J. A., Clayton, G. C., & Mathis, J. S. 1989, ApJ, 345, 245
- Cayatte, V., van Gorkom, J. H., Balkowski, C., & Kotanyi, C. G. 1990, AJ, 100, 604
- Cayatte, V., Kotanyi, C. G., Balkowski, C., & van Gorkom, J. H. 1994, AJ, 107, 1003
- Dickey, J. M., & Gavazzi, G. 1991, ApJ, 373 347
- Dickey, J. M. 1997, AJ, 113, 1939
- Fisher, J. R., & Tully, R. B. 1981, ApJS, 47, 139
- Fouqué, P., Bottinelli, L., Gouguenheim, L., & Paturel, G. 1990, ApJ, 349, 1
- Gottesman, S. T., Ball, R., & Hunter Jr, J. H. 1984, ApJ, 286, 471
- Grewing, M., & Mebold, U. 1975, A&A, 42, 119
- Höggbom, J. A. 1974, A&AS, 15, 417
- Holmberg, E. 1946, Medd. Lunds Astr. Obs., Ser. II, No. 117
- Hubble, E. 1926, ApJ, 64, 321
- Huchtmeier, W. K., & Richter, O.-G. 1986, A&AS, 63, 323
- Jore, K. P., Broeils, A. H., & Haynes, M. P. 1996, AJ, 112, 438
- Lucy, L. B. 1974, AJ, 79, 745
- Magri, C. 1994, AJ, 108, 896
- McMahon, P. M. 1993, Thesis, University of Columbia
- Navarro, J. F., & Steinmetz, M. 2000, ApJ, 538, 477
- Oosterloo, T., & Shostak, S. 1993, A&AS, 99, 379
- Puche, D., & Garignan, C. 1991, AJ, 378, 487
- Rhee, M.-H. 1996a, Thesis, University of Groningen

- Rhee, M.-H. 1996b, A&AS, 115, 407
 Richter, O.-G., & Huchtmeier, W. K. 1991, A&AS, 87, 425
 Richter, O.-G., & Sancisi, R. 1994, A&A, 295, 605
 Roberts, M. S., & Haynes, M. P. 1994, ARA&A, 32, 115
 Sakai, S., Mould, J. R., Hughes, S. M. G., et al. 2000, ApJ, 529, 698
 Sancisi, R., & Allen, R. J. 1979, A&A, 74, 73
 Schlegel, D. J., Finkbeiner, D. P., & Davis, M. 1998, ApJ, 500, 525
 Schneider, S. E., Thuan, T. X., Mangum, J. G., & Miller, J. 1992, ApJS, 81, 5
 Schwarz, U. J. 1985, A&A, 142, 273
 Swater, R. A. 1999, Dark Matter in late type dwarf galaxies, Ph.D. Thesis, University of Groningen
 Thuan, T. X., & Martin, G. E. 1981, ApJ, 247, 823
 Tully, R. B., & Fouqu , P. 1985, ApJS, 58, 67 (TFq)
 Tully, R. B., Verheijen, M. A. W., Pierce, M. J., Huang, J.-S., & Wainscoat, R. J. 1996, AJ, 112, 2471 (Paper I)
 Tully, R. B., & Verheijen, M. A. W. 1997, ApJ, 484, 145 (Paper II)
 Tully, R. B., Pierce, M. J., Huang, J.-S., et al. AJ, 115, 2264
 Tully, R. B., & Pierce, M. J. 2000, ApJ, 533, 744
 Van der Burg, G. 1987, Ph.D. Thesis, University of Groningen
 Van Moorsel, G. A. 1983, A&AS, 54, 1
 Warmels, R. H. 1988a, A&AS, 72, 19
 Warmels, R. H. 1988b, A&AS, 72, 57

Appendix A: The noise in an integrated HI map

This Appendix explains how the noise in a total HI map can be calculated. A total HI map is usually constructed from a 3 dimensional datacube containing a number of so called channelmaps. Each channelmap shows an HI image of the galaxy at a certain velocity. A total HI map is made by adding those channelmaps which contain the HI signal. Before adding the channel maps the signal in each channelmap should be isolated. When the signal is not isolated one merely adds noise to the total HI map because the location of the signal in a channel map varies with velocity due to the galactic rotation. The signals can be isolated interactively by blotting away the surrounding noise or in a more objective way by taking a certain contour level in the smoothed maps as a mask. As a consequence of adding channel maps with isolated regions, the noise in the total HI map is not constant but varies from pixel to pixel. The noise at a certain pixel in the total HI map depends on the number N of non-blank pixels at the same position in the individual channel maps that were added.

In case the data cube was obtained with an uniform taper during the observation, the noise σ^u in two channelmaps will be independent. The noise equivalent bandwidth B^u in a uniform tapered spectrum is equal to the channel separation b . When adding N uniform tapered channelmaps at a certain pixel the noise σ_N^u at the same pixel position in the total HI map will be increased by a factor \sqrt{N} :

$$\sigma_N^u = \sqrt{N} \sigma^u.$$

Usually, the observations are made using a hanning taper in which case the noise in two adjacent channelmaps is no

longer independent. A hanning taper effectively smooths the data in velocity by convolving the velocity profile at each pixel. If U_i is the pixel value in the i th uniform tapered channel map, the value H_i in the i th hanning tapered channelmap is given by

$$H_i = \frac{1}{4}U_{i-1} + \frac{1}{2}U_i + \frac{1}{4}U_{i+1}.$$

Since the σ_i^u 's are independent and all equal to σ^u , the noise σ_i^h in the i th hanning tapered channelmap can be calculated according to

$$\begin{aligned} \sigma_i^h &= [(\frac{1}{4}\sigma_{i-1}^u)^2 + (\frac{1}{2}\sigma_i^u)^2 + (\frac{1}{4}\sigma_{i+1}^u)^2]^{\frac{1}{2}} \\ &= [\frac{1}{16} + \frac{1}{4} + \frac{1}{16}]^{\frac{1}{2}} \sigma^u \\ &= \frac{\sqrt{6}}{4} \sigma^u = 0.61 \sigma^u. \end{aligned}$$

In this case the noise equivalent bandwidth B^h for a hanning tapered spectrum is given by

$$B^h = \frac{16}{6} B^u = 2.67 B^u.$$

As a consequence, the noise in two hanning tapered channelmaps may be correlated depending on their separation. Two channelmaps separated by one channelmap are correlated because both contain a quarter of the flux from the channel map between them. Only channel maps separated by more than one channel are independent. This will be shown in the following three cases in which two hanning tapered channel maps at different separations will be added.

- Adding two adjacent hanning tapered channelmaps i and $(i+1)$ gives a signal $H_{(i)+(i+1)}$ of

$$\begin{aligned} H_{(i)+(i+1)} &= H_i + H_{i+1} \\ &= (\frac{1}{4}U_{i-1} + \frac{1}{2}U_i + \frac{1}{4}U_{i+1}) \\ &\quad + (\frac{1}{4}U_i + \frac{1}{2}U_{i+1} + \frac{1}{4}U_{i+2}) \\ &= \frac{1}{4}U_{i-1} + \frac{3}{4}U_i + \frac{3}{4}U_{i+1} + \frac{1}{4}U_{i+2} \end{aligned}$$

and the noise $\sigma_{(i)+(i+1)}^h$ in that map will be

$$\begin{aligned} \sigma_{(i)+(i+1)}^h &= [(\frac{1}{4}\sigma_{i-1}^u)^2 + (\frac{3}{4}\sigma_i^u)^2 \\ &\quad + (\frac{3}{4}\sigma_{i+1}^u)^2 + (\frac{1}{4}\sigma_{i+2}^u)^2]^{\frac{1}{2}} \\ &= \frac{\sqrt{20}}{4} \sigma^u = \frac{\sqrt{20}}{4} \frac{4}{\sqrt{6}} \sigma^h \\ &= \sqrt{3\frac{1}{3}} \sigma^h = 1.83 \sigma^h. \end{aligned}$$

- Adding the hanning tapered channels i and $(i+2)$ gives

$$\begin{aligned} H_{(i)+(i+2)} &= H_i + H_{i+2} \\ &= (\frac{1}{4}U_{i-1} + \frac{1}{2}U_i + \frac{1}{4}U_{i+1}) \\ &\quad + (\frac{1}{4}U_{i+1} + \frac{1}{2}U_{i+2} + \frac{1}{4}U_{i+3}) \\ &= \frac{1}{4}U_{i-1} + \frac{1}{2}U_i + \frac{1}{2}U_{i+1} \\ &\quad + \frac{1}{2}U_{i+2} + \frac{1}{4}U_{i+3} \end{aligned}$$

and the noise becomes

$$\begin{aligned}\sigma_{(i)+(i+2)}^h &= [(\frac{1}{4}\sigma_{i-1}^u)^2 + (\frac{1}{2}\sigma_i^u)^2 + (\frac{1}{2}\sigma_{i+1}^u)^2 \\ &\quad + (\frac{1}{2}\sigma_{i+2}^u)^2 + (\frac{1}{4}\sigma_{i+3}^u)^2]^{\frac{1}{2}} \\ &= \frac{\sqrt{14}}{4}\sigma^u = \frac{\sqrt{14}}{4}\frac{4}{\sqrt{6}}\sigma^h \\ &= \sqrt{2\frac{1}{3}}\sigma^h = 1.53\sigma^h.\end{aligned}$$

3. Adding the hanning tapered channels i and $(i+3)$ gives

$$\begin{aligned}H_{(i)+(i+3)} &= H_i + H_{i+3} \\ &= (\frac{1}{4}U_{i-1} + \frac{1}{2}U_i + \frac{1}{4}U_{i+1}) \\ &\quad + (\frac{1}{4}U_{i+2} + \frac{1}{2}U_{i+3} + \frac{1}{4}U_{i+4})\end{aligned}$$

with a resulting noise of

$$\begin{aligned}\sigma_{(i)+(i+3)}^h &= [(\frac{1}{4}\sigma_{i-1}^u)^2 + (\frac{1}{2}\sigma_i^u)^2 + (\frac{1}{4}\sigma_{i+1}^u)^2 \\ &\quad + (\frac{1}{4}\sigma_{i+2}^u)^2 + (\frac{1}{2}\sigma_{i+3}^u)^2 + (\frac{1}{4}\sigma_{i+4}^u)^2]^{\frac{1}{2}} \\ &= \frac{\sqrt{12}}{4}\sigma^u = \frac{\sqrt{12}}{4}\frac{4}{\sqrt{6}}\sigma^h \\ &= \sqrt{2}\sigma^h = 1.41\sigma^h.\end{aligned}$$

So, channelmaps i and $(i+3)$ are independent.

Because the noise is correlated, adding N adjacent hanning tapered channelmaps does not give an increase of the noise with a factor \sqrt{N} but with a factor $\sqrt{N - \frac{3}{4}} \cdot \frac{4}{\sqrt{6}}$ as is shown below. First the total signal H_N is calculated.

Channel	U_{i-1}	U_i	U_{i+1}	\dots	U_{i+N-2}	U_{i+N-1}	U_{i+N}
i	$\frac{1}{4}$	$\frac{1}{2}$	$\frac{1}{4}$				
$i+1$		$\frac{1}{4}$	$\frac{1}{2}$	\dots			
$i+2$			$\frac{1}{4}$	\dots			
\dots				\dots			
$i+N-3$				$\frac{1}{4}$			
$i+N-2$				\dots	$\frac{1}{2}$	$\frac{1}{4}$	
$i+N-1$					$\frac{1}{4}$	$\frac{1}{2}$	$\frac{1}{4}$
	$\frac{1}{4}U_{i-1}$	$\frac{3}{4}U_i$	U_{i+1}	\dots	U_{i+N-2}	$\frac{3}{4}U_{i+N-1}$	$\frac{1}{4}U_{i+N}$

and thus

$$\begin{aligned}H_N &= \frac{1}{4}U_{i-1} + \frac{3}{4}U_i + U_{i+1} + \dots \\ &\quad + U_{i+N-2} + \frac{3}{4}U_{i+N-1} + \frac{1}{4}U_{i+N}.\end{aligned}$$

From this it follows that the noise σ_N^h is given by

$$\begin{aligned}\sigma_N^h &= [(\frac{1}{4})^2 + (\frac{3}{4})^2 + (N-2) \cdot 1^2 + (\frac{3}{4})^2 + (\frac{1}{4})^2]^{\frac{1}{2}}\sigma^u \\ &= [N - \frac{3}{4}]^{\frac{1}{2}}\sigma^u = [N - \frac{3}{4}]^{\frac{1}{2}}\frac{4}{\sqrt{6}}\sigma^h \\ &= \sqrt{(N - \frac{3}{4})B^h}\sigma^h.\end{aligned}$$

However, before the hanning tapered channelmaps are added to form a total HI map, the continuum must be subtracted. This operation introduces extra noise in the channelmaps which doesn't behave like a hanning tapered correlation. Here, it will be assumed that the average continuum map is formed by averaging N_1 line free channels

at the low velocity end of the datacube and N_2 channels at the high velocity end which gives

$$C_{\text{low}} = \frac{1}{N_1} \sum_{j=1}^{N_1} H_j \quad \text{and} \quad C_{\text{high}} = \frac{1}{N_2} \sum_{j=1}^{N_2} H_j.$$

Since all channels are hanning tapered the noise in these maps can be calculated according to

$$\sigma_{C_{\text{low}}} = \frac{1}{N_1} \sqrt{(N_1 - \frac{3}{4})}\sigma^u$$

and

$$\sigma_{C_{\text{high}}} = \frac{1}{N_2} \sqrt{(N_2 - \frac{3}{4})}\sigma^u.$$

The average continuum map to be subtracted is then formed by

$$\langle C \rangle = \frac{1}{2}(C_{\text{low}} + C_{\text{high}}).$$

Since $\sigma_{C_{\text{low}}}$ and $\sigma_{C_{\text{high}}}$ are independent it follows that the noise $\sigma_{\langle C \rangle}$ in the finally averaged continuum map is given by

$$\begin{aligned}\sigma_{\langle C \rangle} &= \frac{1}{2} \sqrt{\sigma_{C_{\text{low}}}^2 + \sigma_{C_{\text{high}}}^2} \\ &= \sigma^u \sqrt{\left(\frac{N_1 - \frac{3}{4}}{4N_1^2} + \frac{N_2 - \frac{3}{4}}{4N_2^2}\right)} \\ &\equiv \sigma^u \mathcal{N}.\end{aligned}$$

After subtraction of the continuum the channelmaps only contain signal from the HI emission line. The signal in the channelmaps containing the line emission is now given by

$$\begin{aligned}L_i &= H_i - \langle C \rangle \\ &= \frac{1}{4}U_{i-1} + \frac{1}{2}U_i + \frac{1}{4}U_{i+1} - \langle C \rangle.\end{aligned}$$

Because $\sigma_{\langle C \rangle}$ is independent from σ_i^u in the velocity range which is not used to form the averaged continuum map, it can be written

$$\begin{aligned}\sigma_i^l &= [(\frac{1}{4}\sigma_{i-1}^u)^2 + (\frac{1}{2}\sigma_i^u)^2 + (\frac{1}{4}\sigma_{i+1}^u)^2 + \sigma_{\langle C \rangle}^2]^{\frac{1}{2}} \\ &= [\frac{1}{16} + \frac{4}{16} + \frac{1}{16} + \mathcal{N}^2]^{\frac{1}{2}}\sigma^u \\ &= \sqrt{(\frac{3}{8} + \mathcal{N}^2)}\sigma^u.\end{aligned}$$

When adding N adjacent hanning tapered and continuum subtracted channelmaps containing the line emission, the signal L_N will be

$$\begin{aligned}L_N &= \frac{1}{4}U_{i-1} + \frac{3}{4}U_i + U_{i+1} + \dots \\ &\quad + U_{i+N-2} + \frac{3}{4}U_{i+N-1} + \frac{1}{4}U_{i+N} \\ &\quad - N \cdot \langle C \rangle.\end{aligned}$$

The noise σ_N^l at each pixel in the final map can be derived analogous to the calculation of σ_N^h and is given by

$$\begin{aligned}\sigma_N^l &= [(N - \frac{3}{4}) + N^2\mathcal{N}^2]^{\frac{1}{2}}\sigma^u \\ &= B^h \sqrt{\left(\frac{(N - \frac{3}{4}) + N^2\mathcal{N}^2}{B^h}\right)}\sigma^h.\end{aligned}$$

Appendix B: The HI atlas

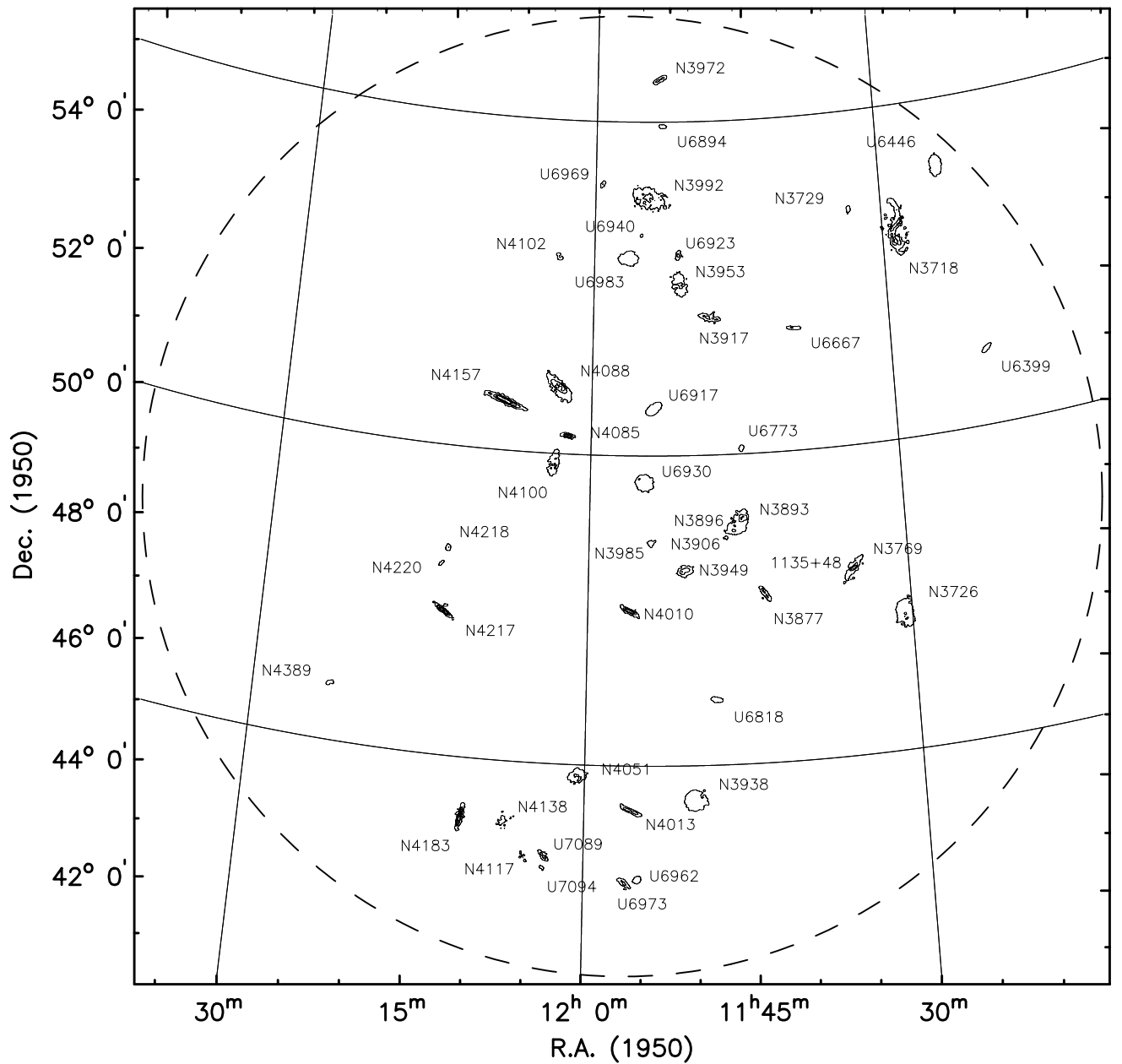


Fig. B.1. Integrated HI maps of all galaxies in the cluster more inclined than 45 degrees and brighter than $M(B) = -16.5$. The angular resolution is 30×30 arcsec. Contour levels are at column densities of 0.5, 2.0, 3.5 and 5.0×10^{21} atoms cm^{-2} . Individual galaxies are four times enlarged. To avoid overlap, some galaxies are slightly displaced from their actual position. N3906, N3938, U6962 and U6930 are more face-on than 45 degrees. U6940 is fainter than the complete sample limit. The dashed circle indicates the adopted boundary of the cluster

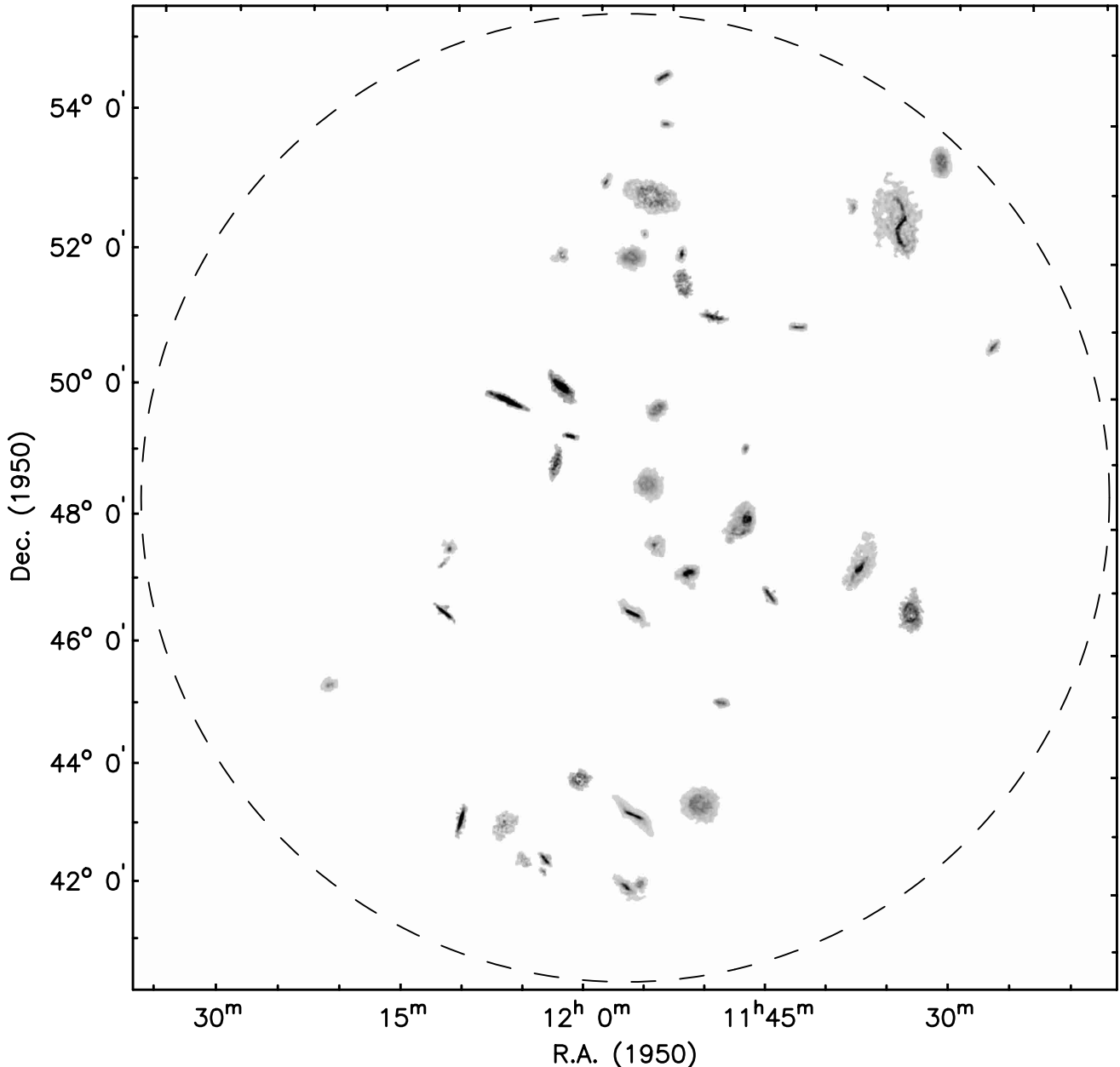


Fig. B.2. Same as Fig. B.1, displayed here in grayscale. Note the interacting pairs N3769/1135+48, N3893/N3896 and U6962/U6973. The galaxies N3718, N3726, N4010, N4013, N4088 and N4138 are strongly warped. It is clear that the integrated column density strongly depends on inclination. Many of the more face-on galaxies show a depletion of the HI gas in their inner regions

Observing parameters for UGC 6399

Length of observation	(hours)	1×12
Dates of observation		6Aug90
Field center, α (1950)		11:20:30
δ (1950)		51:10:00
Central frequency	(MHz)	1416.56
V_{hel} of central channel	(km s^{-1})	810
Primary beam FWHM	(arcmin)	37.4
Nr. of interferometers		40
Baselines (min-max-incr)	(m)	36-2700-72
Synthesized beam ($\alpha \times \delta$)(arcsec)		12.9×16.6
Bandwidth	(MHz)	2.5
Number of channels		127
Channel separation	(km s^{-1})	4.15
Velocity resolution	(km s^{-1})	8.29
rms noise in one channel	(K)	5.54
K-mJy conversion, equiv. of 1mJy/beam	(K)	2.84

Contour levels for U6399

Channel maps:	$\sigma = 3.55$ (K)
Raw continuum map:	$\sigma = 1.35$ (K)
Cleaned continuum map:	$\sigma = 1.19$ (K)
Position-Velocity diagrams:	$\sigma = 3.12$ (K)
Velocity fields:	$794.5 \pm n \times 15$ (km s^{-1})
Residual velocity field:	$\pm n \times 5$ (km s^{-1})
Integrated HI map:	0.52, 1.04, $1.56 (\times 10^{21} \text{ atoms cm}^{-2})$

Results from WSRT data

From continuum map:

21-cm flux density:	
central point source (mJy)	<1.3 (3σ)
extended source (mJy)	<2.5 (3σ)

From global profile:

Integrated HI-flux	(Jy km s^{-1})	10.5 ± 0.3
Hel. systemic velocity	(km s^{-1})	791.5 ± 0.6
HI profile width, 20%	(km s^{-1})	188.1 ± 1.4
50%	(km s^{-1})	172.5 ± 2.9

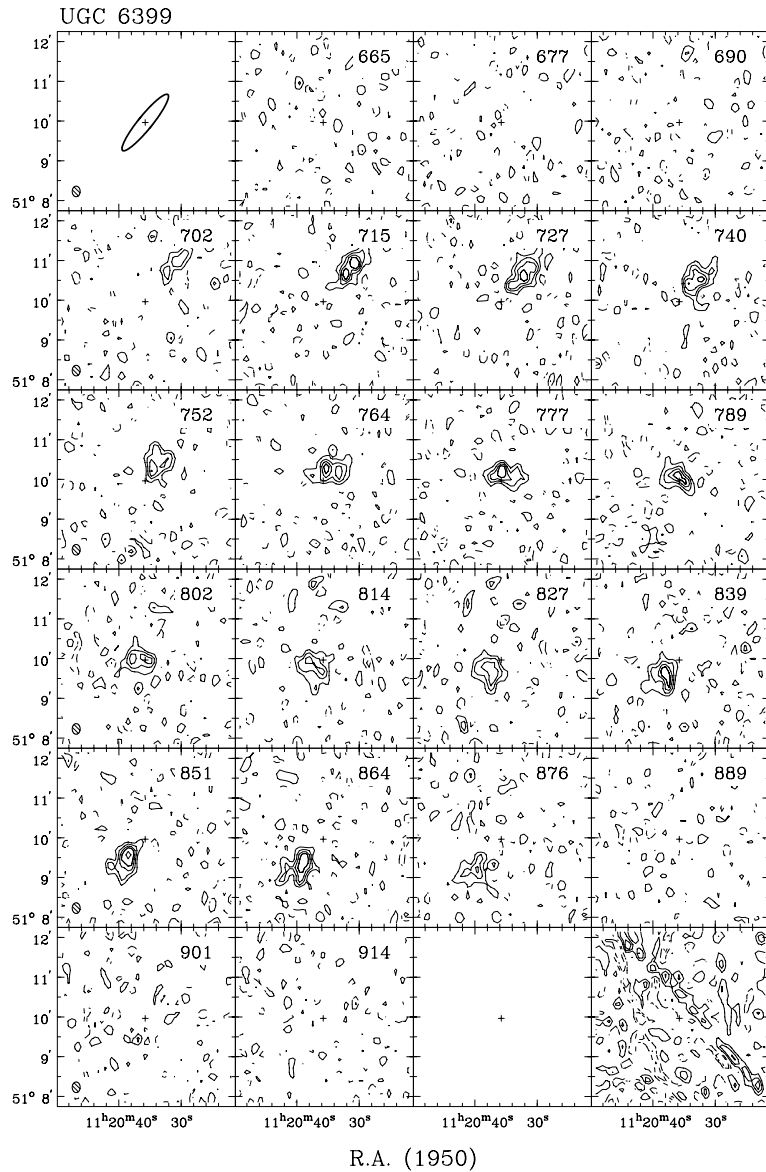
From velocity field:

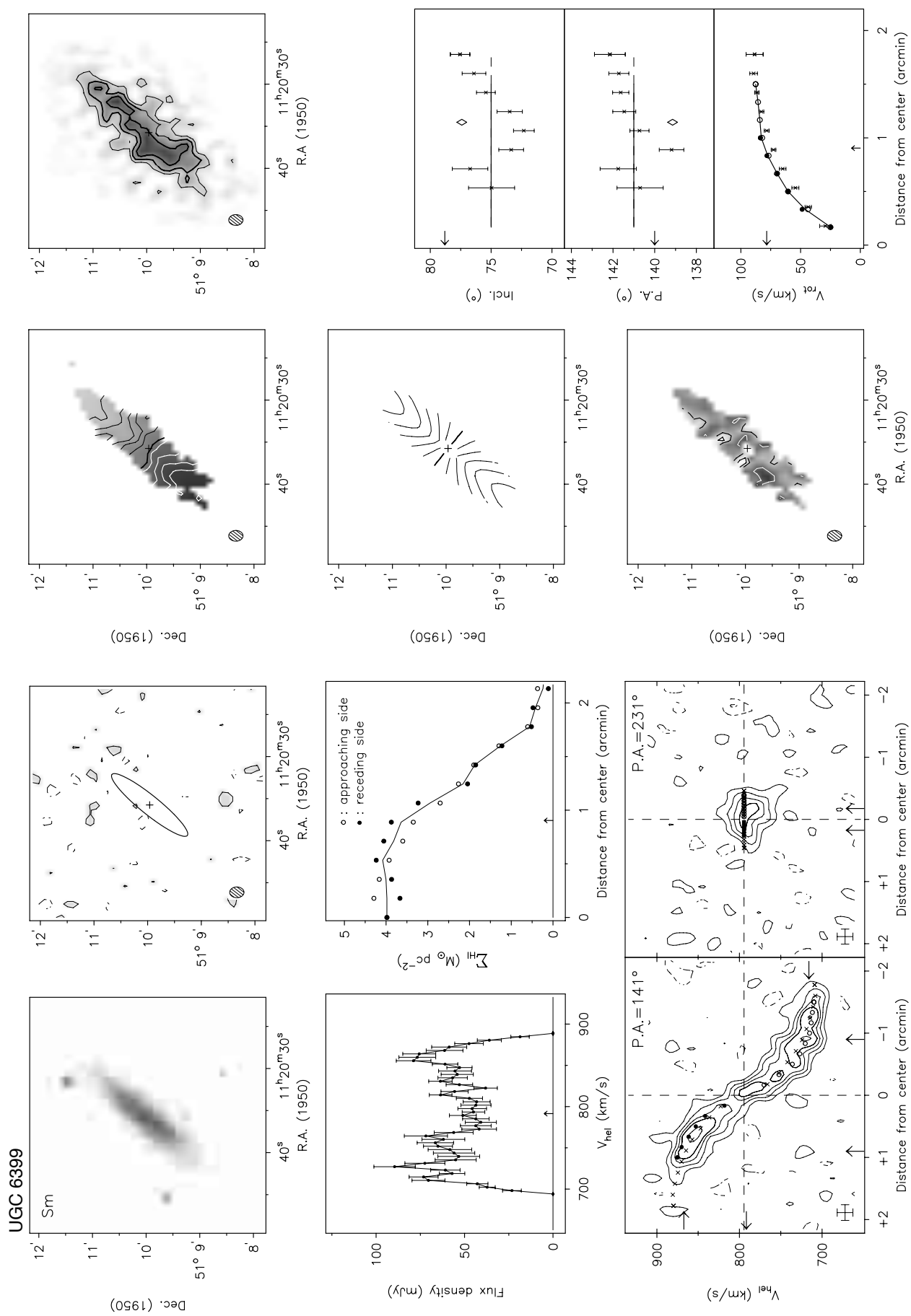
Hel. systemic velocity	(km s^{-1})	794.5 ± 1.3
Dynamical center, α (1950)		11:20:35.8

 δ (1950) 51:09:58From total HI map:

Geometric center, α (1950)		11:20:35.7
δ (1950)		51:10:01
Position angle	(deg)	139
Inclination angle	(deg)	77
Diameter of HI disk	(arcmin)	3.4

Note: This is the most isolated system in the cluster. The rotation curve does not show a flat part on the receding side and maybe just barely on the approaching side.

Channel maps at a resolution of $12'' \times 16'' \times 19 \text{ km s}^{-1}$.Contour levels at $-3, -1.5$ (dashed), $1.5, 3, 4.5, \dots \times \sigma$.

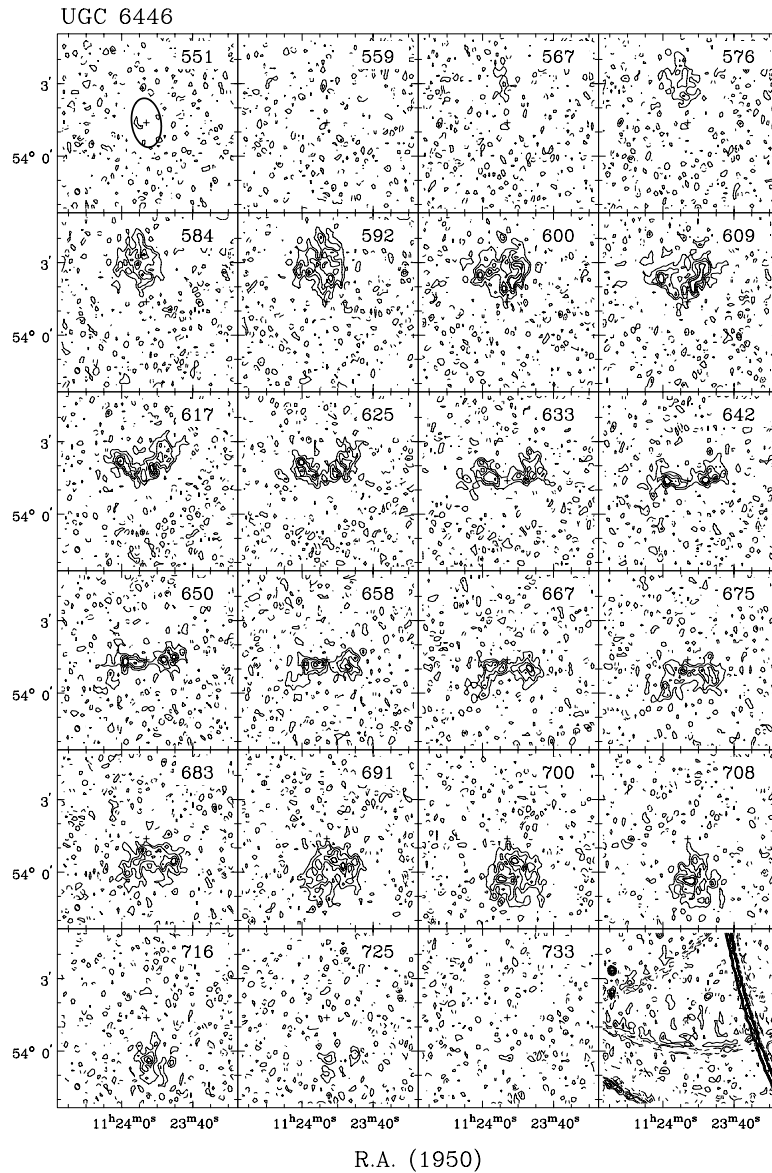


Observing parameters for UGC 6446

Length of observation	(hours)	1×12
Date of observation		07Jan94
Field center, α (1950)		11:23:53
δ (1950)		54:01:28
Central frequency	(MHz)	1417.40
V_{hel} of central channel	(km s $^{-1}$)	650
Primary beam FWHM	(arcmin)	37.4
Nr. of interferometers		40
Baselines (min-max-incr)	(m)	36-2700-72
Synthesized beam ($\alpha \times \delta$)	(arcsec)	12.1×15.0
Bandwidth	(MHz)	2.5
Number of channels		127
Channel separation	(km s $^{-1}$)	4.14
Velocity resolution	(km s $^{-1}$)	4.97
rms noise in one channel	(K)	10.1
K-mJy conversion, equiv. of 1mJy/beam	(K)	3.32

Contour levels for U6446

Channel maps:	$\sigma=3.98$ (K)
Raw continuum map:	$\sigma=1.44$ (K)
Cleaned continuum map:	$\sigma=1.28$ (K)
Position-Velocity diagrams:	$\sigma=3.49$ (K)
Velocity fields:	$645.4 \pm n \times 15$ (km s $^{-1}$)
Residual velocity field:	$\pm n \times 5$ (km s $^{-1}$)
Integrated HI map:	0.59, 1.19, $1.78 (\times 10^{21} \text{ atoms cm}^{-2})$



Channel maps at a resolution of $12'' \times 15'' \times 19 \text{ km s}^{-1}$.

Contour levels at $-3, -1.5$ (dashed), $1.5, 3, 4.5, \dots \times \sigma$.

Results from WSRT data

From continuum map:

21-cm flux density:	
central point source (mJy)	<1.2 (3 σ)
extended source (mJy)	<7.2 (3 σ)

From global profile:

Integrated HI-flux (Jy km s $^{-1}$)	40.6 ± 0.5
Hel. systemic velocity (km s $^{-1}$)	644.3 ± 0.8
HI profile width, 20% (km s $^{-1}$)	154.1 ± 1.0
50% (km s $^{-1}$)	131.9 ± 1.2

From velocity field:

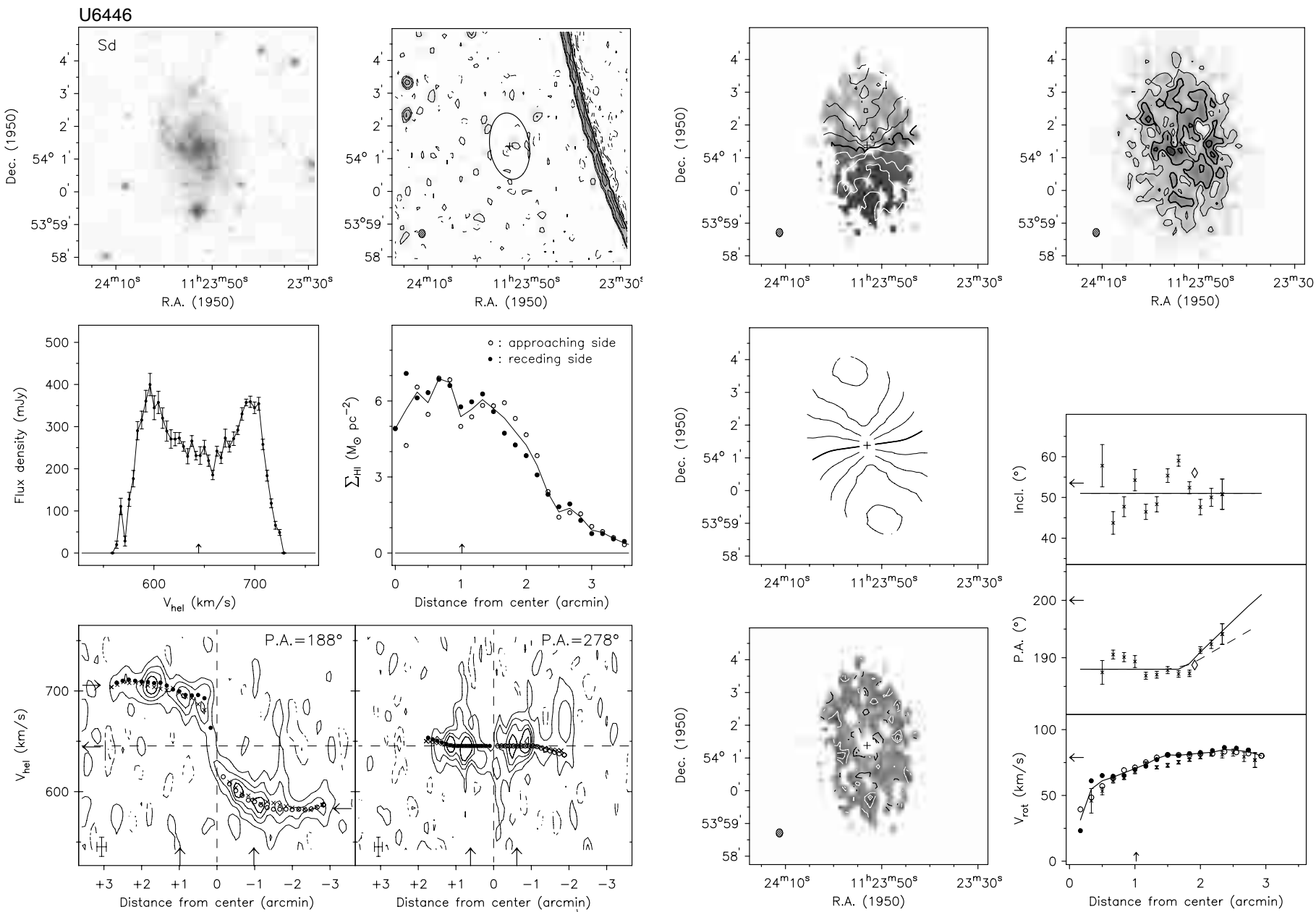
Hel. systemic velocity (km s $^{-1}$)	645.4 ± 0.4
Dynamical center, α (1950)	11:23:53.0

δ (1950) 54:01:23

From total HI map:

Geometric center, α (1950)	11:23:52.9
δ (1950)	54:01:29
Position angle (deg)	188
Inclination angle (deg)	55
Diameter of HI disk (arcmin)	5.9

Note: This is a low surface brightness galaxy with possibly asymmetric rotation in the inner part; the rotation curve on the receding southern side seems to rise steeper than on the approaching northern side. The continuum map shows a grating ring from a source outside the mapped field of view.



Observing parameters for NGC 3726

Length of observation	(hours)	1×12
Date of observation		27 Dec 93
Field center, α (1950)		11:30:38
δ (1950)		47:18:13
Central frequency	(MHz)	1416.39
V_{hel} of central channel	(km s $^{-1}$)	870
Primary beam FWHM	(arcmin)	37.4
Nr. of interferometers		40
Baselines (min-max-incr)	(m)	36-2700-72
Synthesized beam ($\alpha \times \delta$)	(arcsec)	12.2 \times 16.5
Bandwidth	(MHz)	2.5
Number of channels		127
Channel separation	(km s $^{-1}$)	4.13
Velocity resolution	(km s $^{-1}$)	4.95
rms noise in one channel	(K)	9.12
K-mJy conversion, equiv. of 1 mJy/beam	(K)	2.99

Contour levels for N3726

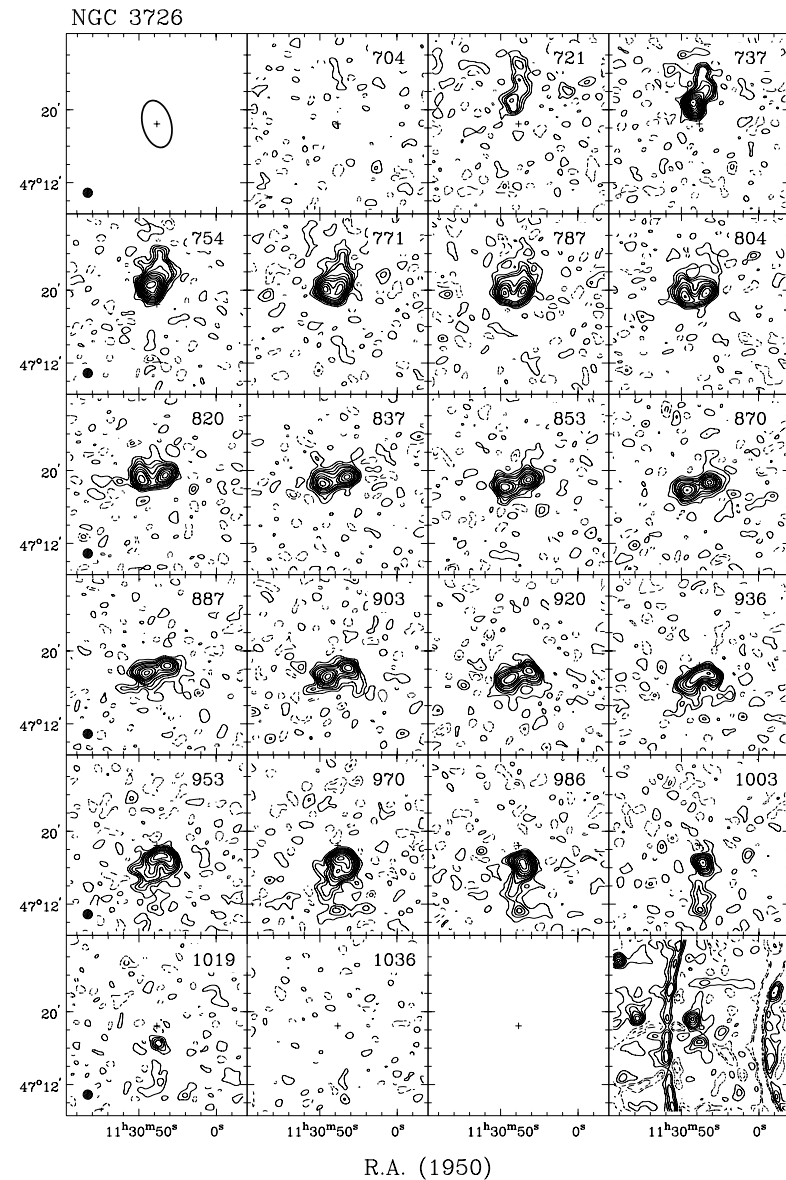
Channel maps:	$\sigma = 0.36$ (K)
Raw continuum map:	$\sigma = 0.37$ (K)
Cleaned continuum map:	$\sigma = 0.37$ (K)
Position-Velocity diagrams:	$\sigma = 0.99$ (K)
Velocity fields:	$862.6 \pm n \times 20$ (km s $^{-1}$)
Residual velocity field:	$\pm n \times 5$ (km s $^{-1}$)
Integrated HI map:	0.41, 0.82, $1.23 (\times 10^{21} \text{ atoms cm}^{-2})$

Results from WSRT data

<i>From continuum map:</i>	
21-cm flux density	(mJy) 49.7 ± 5.0
<i>From global profile:</i>	
Integrated HI-flux	(Jy km s $^{-1}$) 89.8 ± 0.8
Hel. systemic velocity	(km s $^{-1}$) 865.6 ± 0.9
HI profile width, 20%	(km s $^{-1}$) 286.5 ± 1.6
50%	(km s $^{-1}$) 260.6 ± 1.8
<i>From velocity field:</i>	
Hel. systemic velocity	(km s $^{-1}$) 862.6 ± 1.2
Dynamical center, α (1950)	11:30:38.3
δ (1950)	47:18:28
<i>From total HI map:</i>	
Geometric center, α (1950)	11:30:39.3
δ (1950)	47:18:34
Position angle	(deg) 189
Inclination angle	(deg) 56
Diameter of HI disk	(arcmin) 8.5

Note: This bright spiral is optically lopsided; the northern part has a higher surface brightness than the southern part. However, the faintest isophotes are elliptical and centered on the bright nucleus.

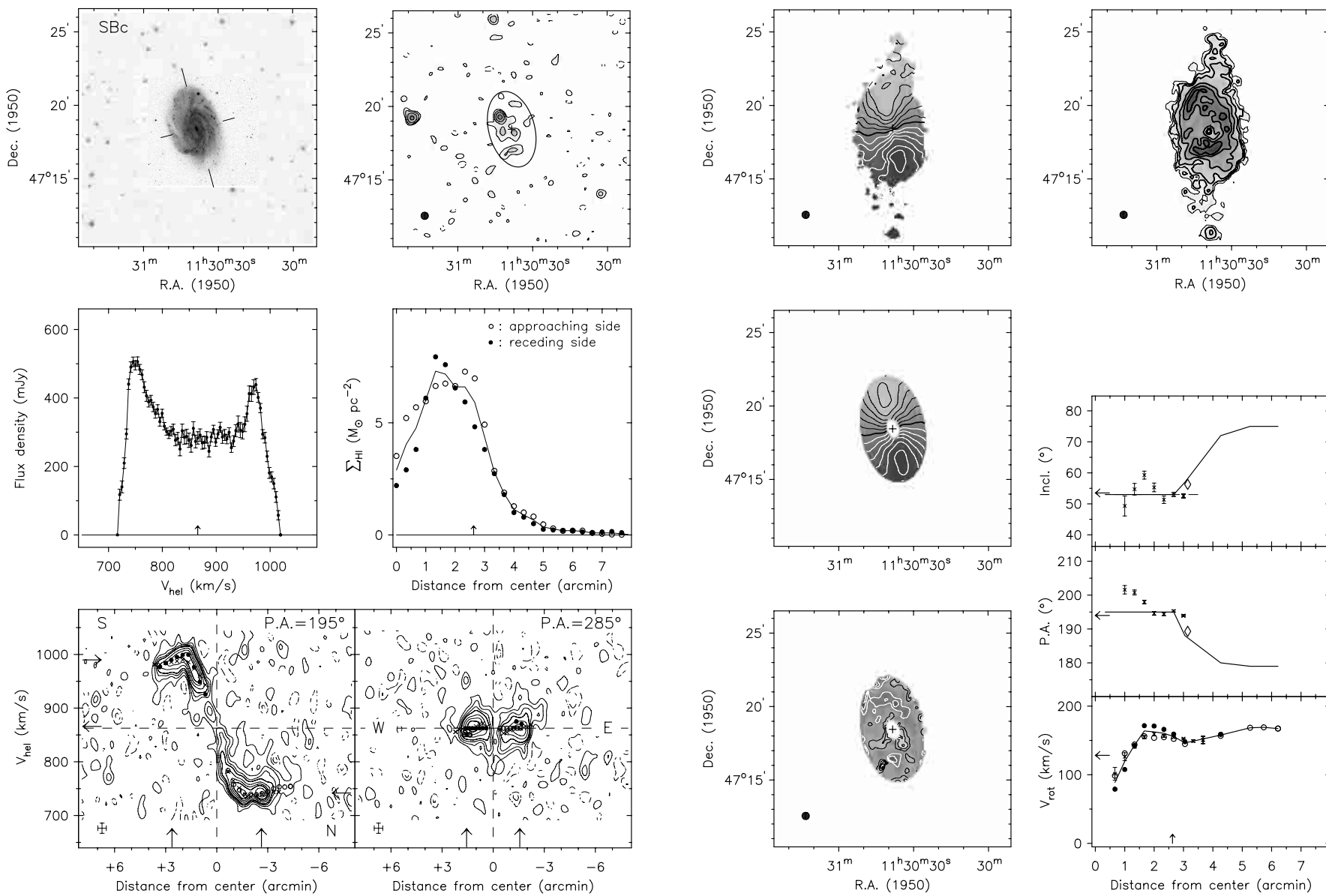
The channel maps are shown at a resolution of $60'' \times 60''$ arcsec while the other data are presented at a spatial resolution of $30'' \times 30''$ arcsec. The channel maps suggest that the HI disk is strongly warped toward edge-on beyond a radius of 3 arcmin. From the channel maps, the position angle of the outer disk is estimated at 179 degrees and the inclination angle at a minimum value of 75 degrees based upon the extent along the minor axis near the systemic velocity. The rotation curve in the inner region is asymmetric. The signature of the small bar can also be discerned in the slightly twisted velocity field.



Channel maps at a resolution of $60'' \times 60'' \times 19 \text{ km s}^{-1}$.

Contour levels at $-3, -1.5, 1.5, 3, 4.5, \dots \times \sigma$.

N3726



Observing parameters for NGC 3769

Length of observation	(hours)	1×12
Date of observation		2 Aug 90
Field center, α (1950)		11:35:00
δ (1950)		48:11:00
Central frequency	(MHz)	1416.87
V_{hel} of central channel	(km s $^{-1}$)	740
Primary beam FWHM	(arcmin)	37.4
Nr. of interferometers		40
Baselines (min-max-incr)	(m)	36-2700-72
Synthesized beam ($\alpha \times \delta$)	(arcsec)	11.9 \times 15.9
Bandwidth	(MHz)	2.5
Number of channels		127
Channel separation	(km s $^{-1}$)	4.14
Velocity resolution	(km s $^{-1}$)	8.29
rms noise in one channel	(K)	6.53
K-mJy conversion, equiv. of 1 mJy/beam	(K)	3.18

Contour levels for N3769

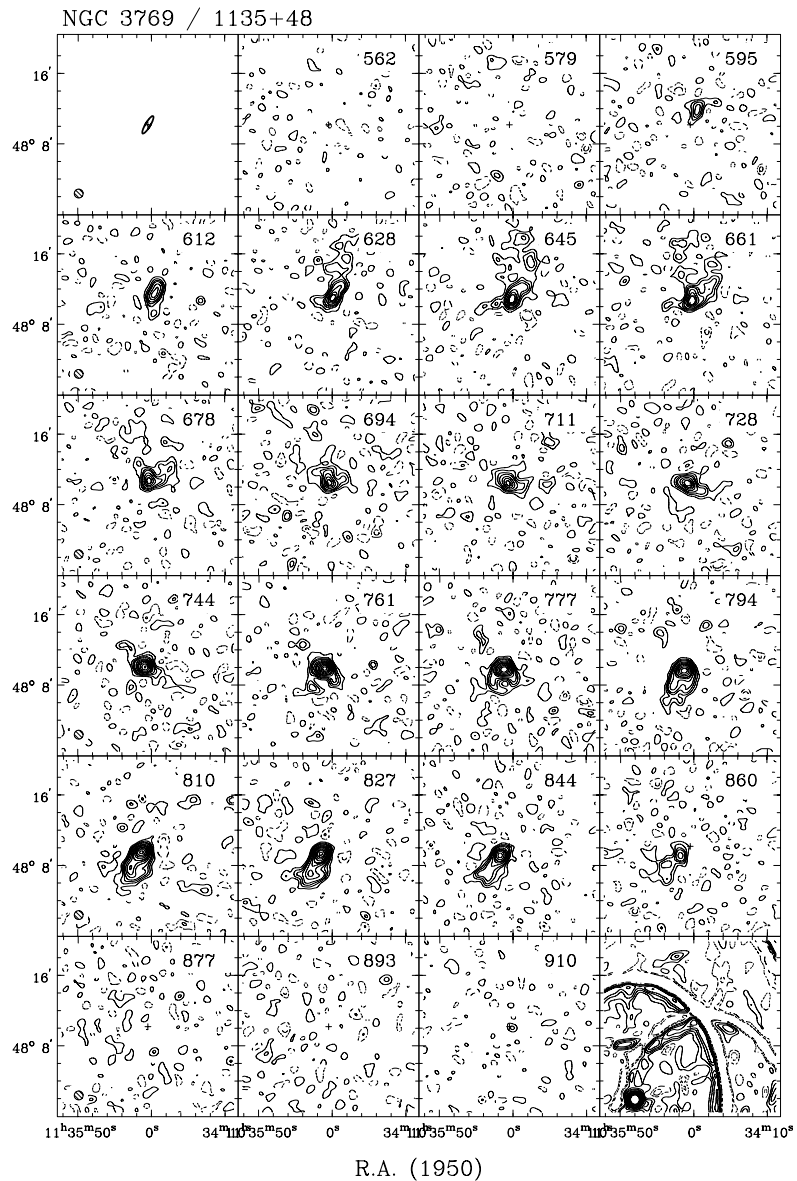
Channel maps:	$\sigma = 0.42$ (K)
Raw continuum map:	$\sigma = 0.72$ (K)
Cleaned continuum map:	$\sigma = 0.52$ (K)
Position-Velocity diagrams:	$\sigma = 1.14$ (K)
Velocity fields:	$722.9 \pm n \times 20$ (km s $^{-1}$)
Residual velocity field:	$\pm n \times 5$ (km s $^{-1}$)
Integrated HI map:	0.18, 0.36, 0.53, 0.71, 0.89 1.07, 1.24 ($\times 10^{21}$ atoms cm $^{-2}$)

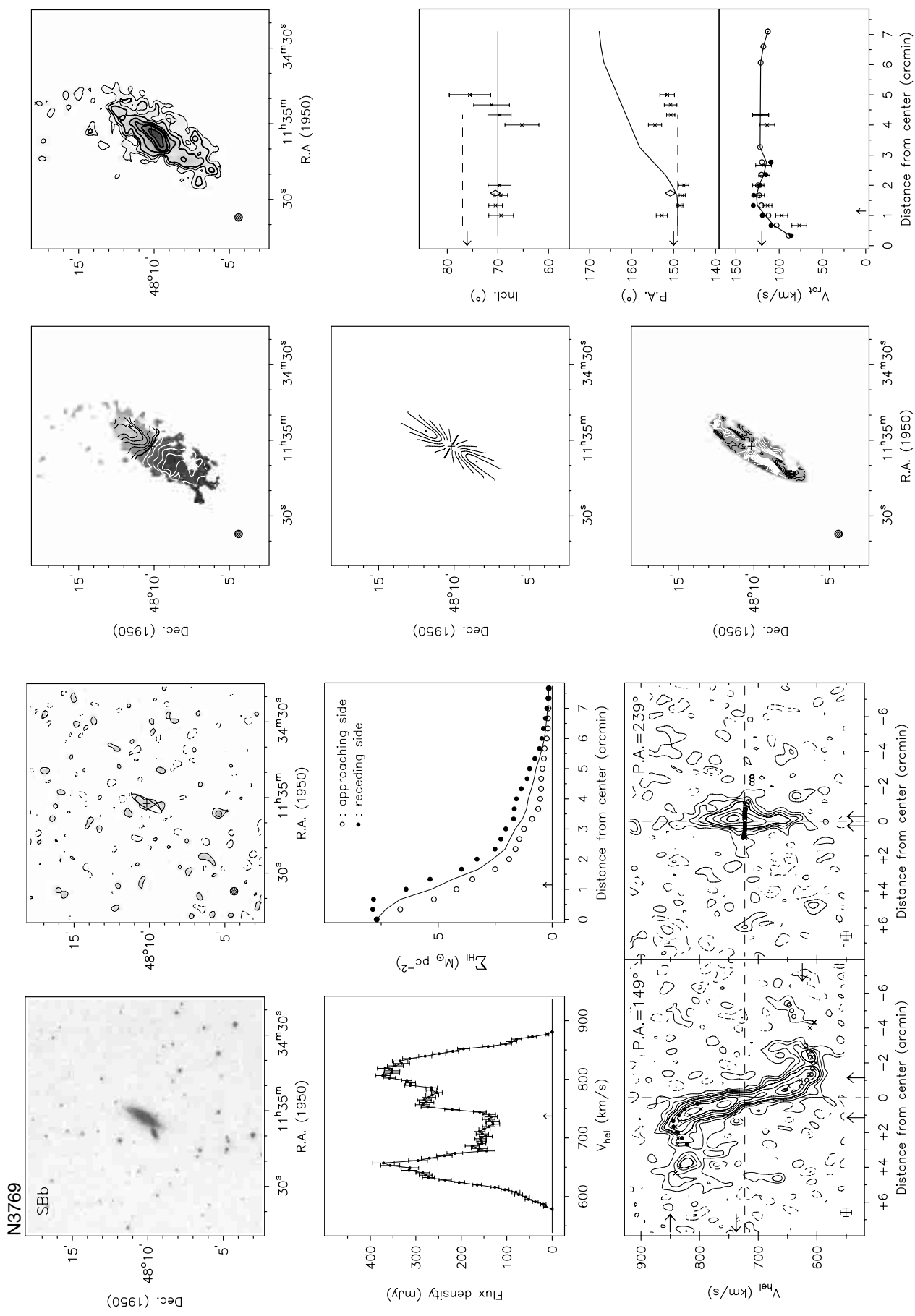
Results from WSRT data

<i>From continuum map:</i>	
21-cm flux density	(mJy)
(mJy)	12.1 ± 2.9
<i>From global profile:</i>	
Integrated HI-flux	(Jy km s $^{-1}$)
62.3 ± 0.6	
Hel. systemic velocity	(km s $^{-1}$)
737.3 ± 1.8	
HI profile width, 20%	(km s $^{-1}$)
265.3 ± 6.7	
50%	(km s $^{-1}$)
230.5 ± 3.6	
<i>From velocity field:</i>	
Hel. systemic velocity	(km s $^{-1}$)
722.9 ± 1.9	
Dynamical center, α (1950)	
$11:35:02.4$	
δ (1950)	
$48:10:12$	
<i>From total HI map:</i>	
Geometric center, α (1950)	
$11:35:03.9$	
δ (1950)	
$48:10:09$	
Position angle	(deg)
151	
Inclination angle	(deg)
71	
Diameter of HI disk	(arcmin)
8.6	

Note: N3769 is strongly interacting with its dwarf companion 1135+48. This pair is also known as Arp 280. The HI disk is clearly warped and extends far beyond D₂₅. Confusion with its companion and with the tidal debris makes the velocity field in the southern part quite complex. The change in position angle is estimated from the channel maps around 645 km s $^{-1}$ at 60 arcsec resolution. The rotational velocity is very uncertain beyond 2 arcmin where the warp sets in. Large scale non-circular motions are likely to occur in this system.

The channel maps are shown at a resolution of 60'' \times 60'' \times 19 km s $^{-1}$. The other data are presented with a resolution of 30'' \times 30'' arcsec.

Channel maps at a resolution of 60'' \times 60'' \times 19 km s $^{-1}$.Contour levels at $-3, -1.5, 1.5, 3, 4.5, \dots \times \sigma$.



Observing parameters for UGC 6667

Length of observation	(hours)	1×12
Date of observation		16Dec94
Field center, α (1950)		11:39:42
δ (1950)		51:50:00
Central frequency	(MHz)	1415.78
V_{hel} of central channel	(km s^{-1})	1000
Primary beam FWHM	(arcmin)	37.4
Nr. of interferometers		40
Baselines (min-max-incr)	(m)	36-2700-72
Synthesized beam ($\alpha \times \delta$)	(arcsec)	12.0 \times 15.4
Bandwidth	(MHz)	2.5
Number of channels		127
Channel separation	(km s^{-1})	4.15
Velocity resolution	(km s^{-1})	4.98
rms noise in one channel	(K)	10.4
K-mJy conversion, equiv. of 1mJy/beam	(K)	3.26

Contour levels for U6667

Channel maps:	$\sigma = 4.23$ (K)
Raw continuum map:	$\sigma = 1.55$ (K)
Cleaned continuum map:	$\sigma = 1.43$ (K)
Position-Velocity diagrams:	$\sigma = 3.58$ (K)
Velocity fields:	$970.5 \pm n \times 15$ (km s^{-1})
Residual velocity field:	$\pm n \times 5$ (km s^{-1})
Integrated HI map:	0.71, 1.42, $2.13 (\times 10^{21} \text{ atoms cm}^{-2})$

Results from WSRT data

From continuum map:

21-cm flux density:	
central point source (mJy)	<1.3 (3 σ)
extended source (mJy)	<2.7 (3 σ)

From global profile:

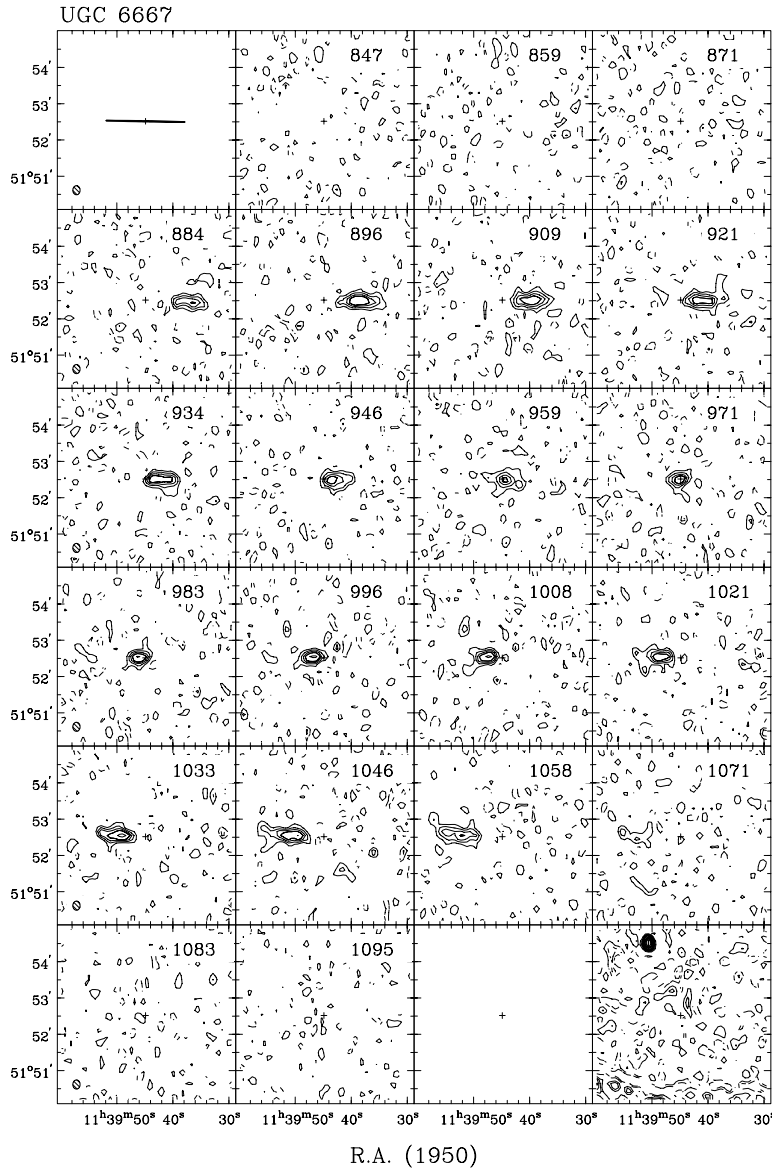
Integrated HI-flux	(Jy km s^{-1})	11.0 ± 0.4
Hel. systemic velocity	(km s^{-1})	973.2 ± 1.2
HI profile width, 20%	(km s^{-1})	187.5 ± 1.4
50%	(km s^{-1})	178.1 ± 1.9

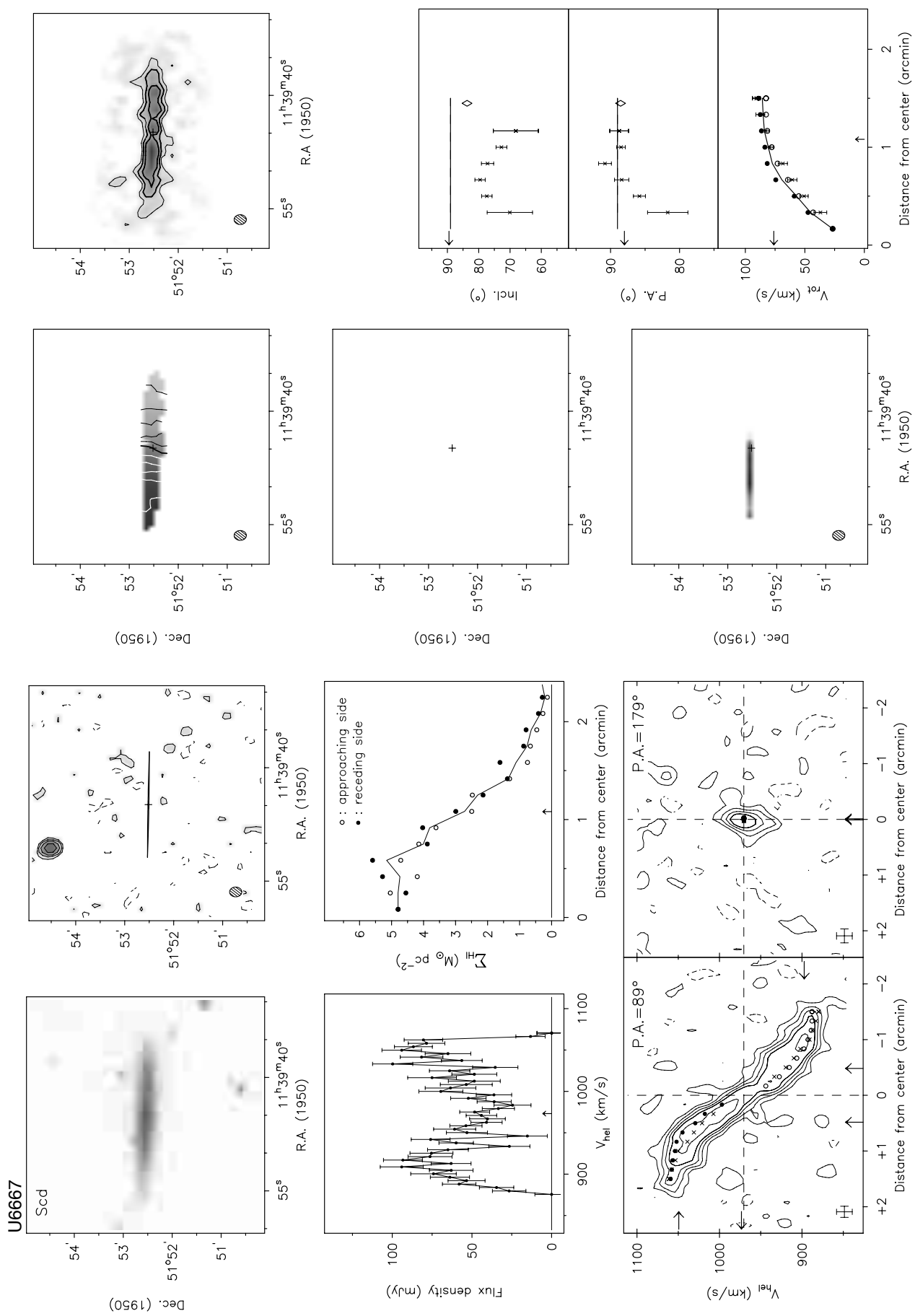
From velocity field:

Hel. systemic velocity	(km s^{-1})	970.5 ± 4.5
Dynamical center, α (1950)		11:39:44.9

 δ (1950) 51:52:31From total HI map:

Geometric center, α (1950)		11:39:45.0
δ (1950)		51:52:31
Position angle	(deg)	88
Inclination angle	(deg)	48
Diameter of HI disk	(arcmin)	3.3

Channel maps at a resolution of $12'' \times 15'' \times 19 \text{ km s}^{-1}$.Contour levels at $-3, -1.5$ (dashed), $1.5, 3, 4.5, \dots \times \sigma$.



Observing parameters for NGC 3877

Length of observation	(hours)	2×12
Dates of observation		3,9,14 Aug 90
Field center, α (1950)		11:43:30
δ (1950)		47:45:00
Central frequency	(MHz)	1416.12
V_{hel} of central channel	(km s $^{-1}$)	900
Primary beam FWHM	(arcmin)	37.4
Nr. of interferometers		40
Baselines (min-max-incr)	(m)	36-2700-72
Synthesized beam ($\alpha \times \delta$)	(arcsec)	12.2×17.6
Bandwidth	(MHz)	5.0
Number of channels		63
Channel separation	(km s $^{-1}$)	16.59
Velocity resolution	(km s $^{-1}$)	33.18
rms noise in one channel	(K)	1.96
K-mJy conversion, equiv. of 1mJy/beam	(K)	2.81

Contour levels for N3877

Channel maps:	$\sigma = 1.96$ (K)
Raw continuum map:	$\sigma = 0.71$ (K)
Cleaned continuum map:	$\sigma = 0.67$ (K)
Position-Velocity diagrams:	$\sigma = 1.68$ (K)
Velocity fields:	$893.2 \pm n \times 25$ (km s $^{-1}$)
Residual velocity field:	$\pm n \times 5$ (km s $^{-1}$)
Integrated HI map:	0.80, 1.61, $2.41 (\times 10^{21} \text{ atoms cm}^{-2})$

Results from WSRT data

From continuum map:

21-cm flux density	(mJy)	35.6 ± 2.4
Central point source position		
α (1950)		11:43:29.2
δ (1950)		47:46:21

From global profile:

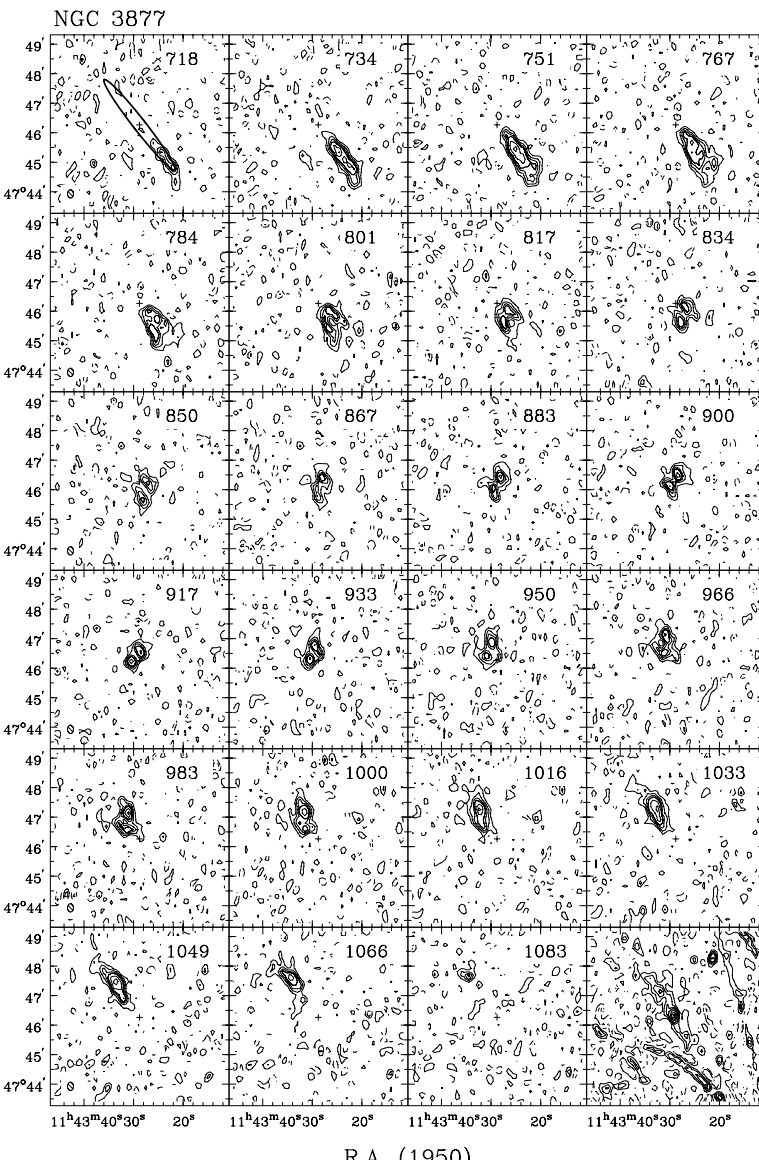
Integrated HI-flux	(Jy km s $^{-1}$)	19.5 ± 0.6
Hel. systemic velocity	(km s $^{-1}$)	895.4 ± 3.8
HI profile width, 20%	(km s $^{-1}$)	373.4 ± 5.0
50%	(km s $^{-1}$)	344.5 ± 6.2

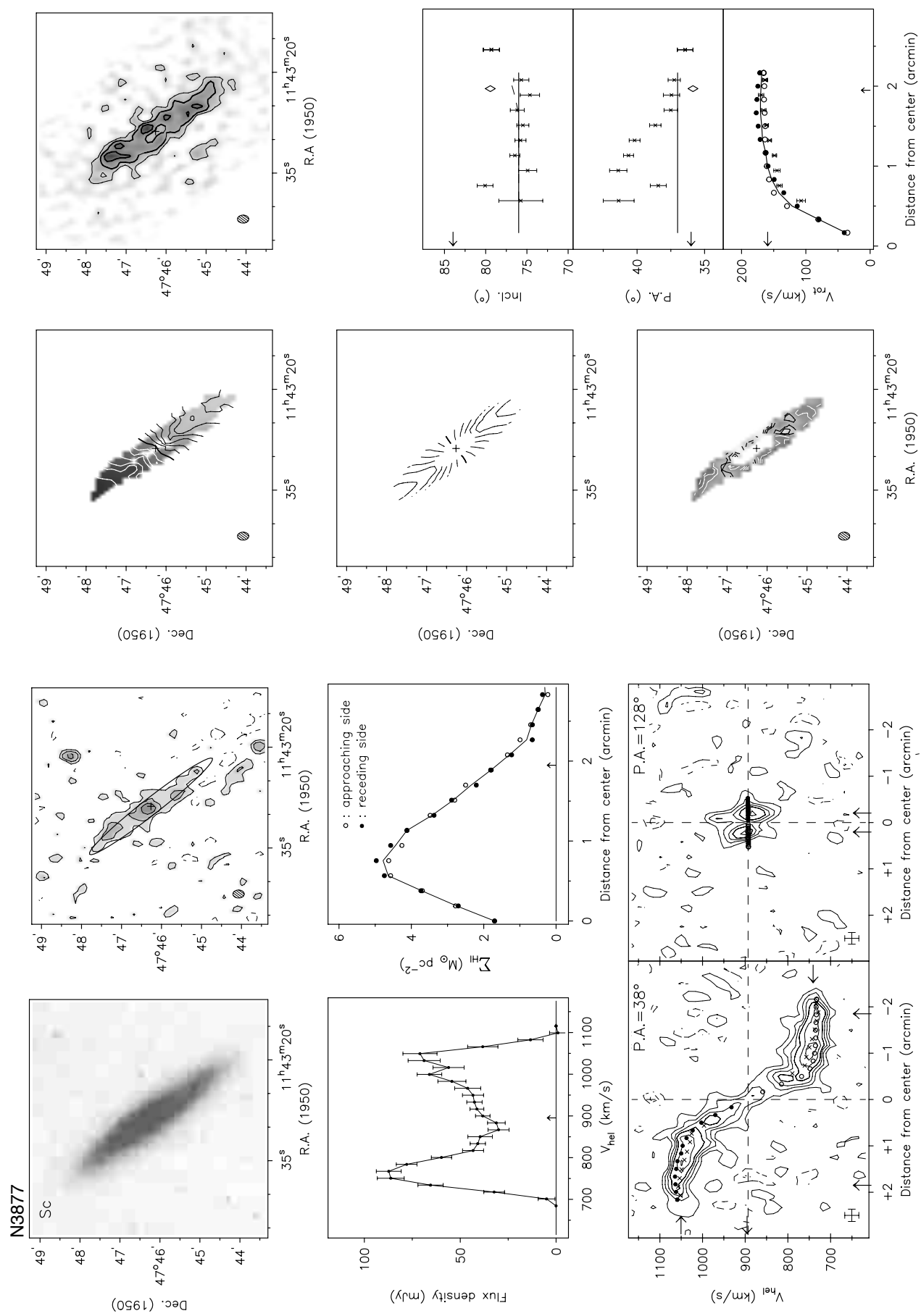
From velocity field:

Hel. systemic velocity	(km s $^{-1}$)	893.2 ± 4.4
Dynamical center, α (1950)		11:43:28.9
δ (1950)		47:46:16

From total HI map:

Geometric center, α (1950)		11:43:28.6
δ (1950)		47:46:15
Position angle	(deg)	36
Inclination angle	(deg)	80
Diameter of HI disk	(arcmin)	4.4

Channel maps at a resolution of $12'' \times 17'' \times 33 \text{ km s}^{-1}$.Contour levels at $-3, -1.5, 1.5, 3, 4.5, \dots \times \sigma$.



Observing parameters for NGC 3893/3896

Length of observation	(hours)	1×12
Date of observation		31Dec93
Field center, α (1950)		11:46:01
δ (1950)		48:59:20
Central frequency	(MHz)	1415.86
V_{hel} of central channel	(km s $^{-1}$)	980
Primary beam FWHM	(arcmin)	37.4
Nr. of interferometers		40
Baselines (min-max-incr)	(m)	36-2700-72
Synthesized beam ($\alpha \times \delta$)	(arcsec)	12.1 \times 16.1
Bandwidth	(MHz)	2.5
Number of channels		127
Channel separation	(km s $^{-1}$)	4.15
Velocity resolution	(km s $^{-1}$)	4.98
rms noise in one channel	(K)	9.11
K-mJy conversion, equiv. of 1mJy/beam	(K)	3.09

Contour levels for N3893

Channel maps:	$\sigma = 1.04$ (K)
Raw continuum map:	$\sigma = 0.56$ (K)
Cleaned continuum map:	$\sigma = 0.50$ (K)
Position-Velocity diagrams:	$\sigma = 0.95$ (K)
Velocity fields:	$966.0 \pm n \times 25$ (km s $^{-1}$)
Residual velocity field:	$\pm n \times 5$ (km s $^{-1}$)
Integrated HI map:	0.20, 0.40, 0.60, 0.80 $1.00, 1.20 (\times 10^{21} \text{ atoms cm}^{-2})$

Results from WSRT data

From continuum map:

21-cm flux density	(mJy)	137.4 ± 2.9
Central point source position		
α (1950)		11:45:59.6
δ (1950)		48:59:23

From global profile:

Integrated HI-flux	(Jy km s $^{-1}$)	69.9 ± 0.5
Hel. systemic velocity	(km s $^{-1}$)	967.2 ± 1.0
HI profile width, 20%	(km s $^{-1}$)	310.9 ± 1.0
50%	(km s $^{-1}$)	277.9 ± 4.1

From velocity field:

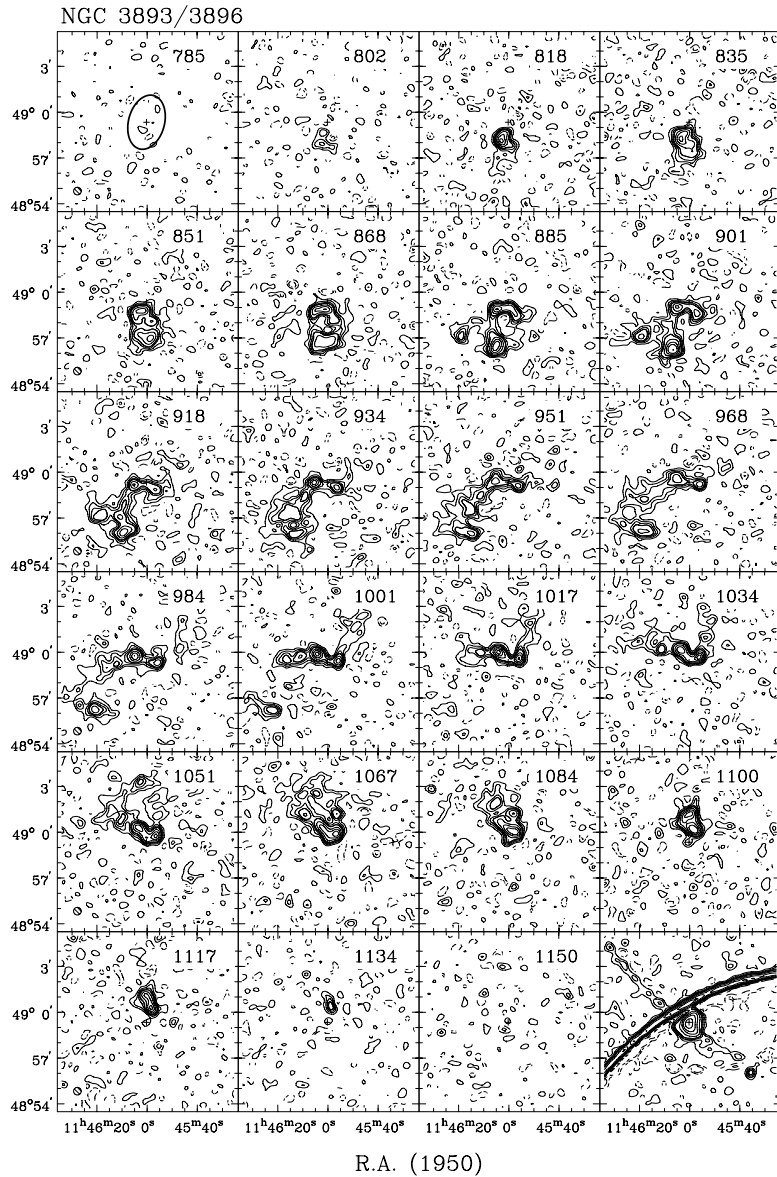
Hel. systemic velocity	(km s $^{-1}$)	966.0 ± 0.8
Dynamical center, α (1950)		11:46:00.2
δ (1950)		48:59:21

From total HI map:

Geometric center, α (1950)		11:46:01.3
δ (1950)		48:59:23
Position angle	(deg)	51
Inclination angle	(deg)	49
Diameter of HI disk	(arcmin)	8.0

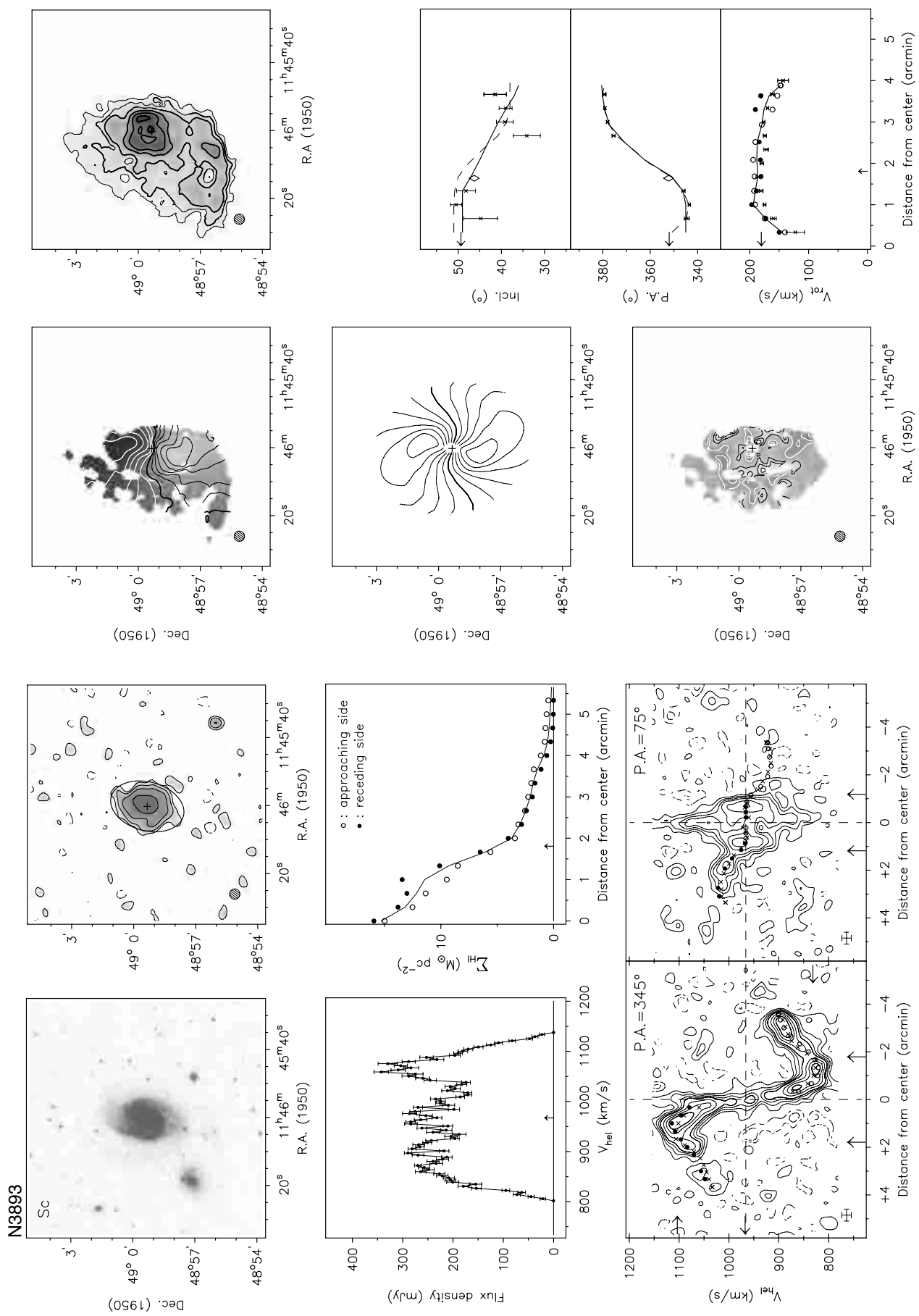
Note: The rotation curve beyond 2 arcmin is quite uncertain because of the tidal interaction with its companion N3896.

Compare this interacting pair with N3769/1135+48 which shows a similar optical configuration but a very different kinematical structure.



Channel maps at a resolution of $30'' \times 30'' \times 19 \text{ km s}^{-1}$.

Contour levels at $-3, -1.5$ (dashed), $1.5, 3, 4.5, \dots \times \sigma$.



Observing parameters for NGC 3917

Length of observation	(hours)	1×12
Date of observation		29Jul93
Field center, α (1950)		11:48:08
δ (1950)		52:06:14
Central frequency	(MHz)	1415.78
V_{hel} of central channel	(km s $^{-1}$)	970
Primary beam FWHM	(arcmin)	37.4
Nr. of interferometers		40
Baselines (min-max-incr)	(m)	36-2700-72
Synthesized beam ($\alpha \times \delta$)	(arcsec)	11.7×15.0
Bandwidth	(MHz)	2.5
Number of channels		127
Channel separation	(km s $^{-1}$)	4.15
Velocity resolution	(km s $^{-1}$)	8.30
rms noise in one channel	(K)	6.35
K-mJy conversion, equiv. of 1mJy/beam	(K)	3.43

Contour levels for N3917

Channel maps:	$\sigma=4.29$ (K)
Raw continuum map:	$\sigma=1.89$ (K)
Cleaned continuum map:	$\sigma=1.87$ (K)
Position-Velocity diagrams:	$\sigma=3.60$ (K)
Velocity fields:	$966.7 \pm n \times 20$ (km s $^{-1}$)
Residual velocity field:	$\pm n \times 5$ (km s $^{-1}$)
Integrated HI map:	1.39, 2.78, $4.17 (\times 10^{21} \text{ atoms cm}^{-2})$

Results from WSRT data

From continuum map:

21-cm flux density	
central point source (mJy)	<1.6 (3 σ)
extended source (mJy)	<7.2 (3 σ)

From global profile:

Integrated HI-flux (Jy km s $^{-1}$)	24.9 ± 0.6
Hel. systemic velocity (km s $^{-1}$)	964.6 ± 1.4
HI profile width, 20% (km s $^{-1}$)	294.5 ± 1.9
50% (km s $^{-1}$)	279.1 ± 2.1

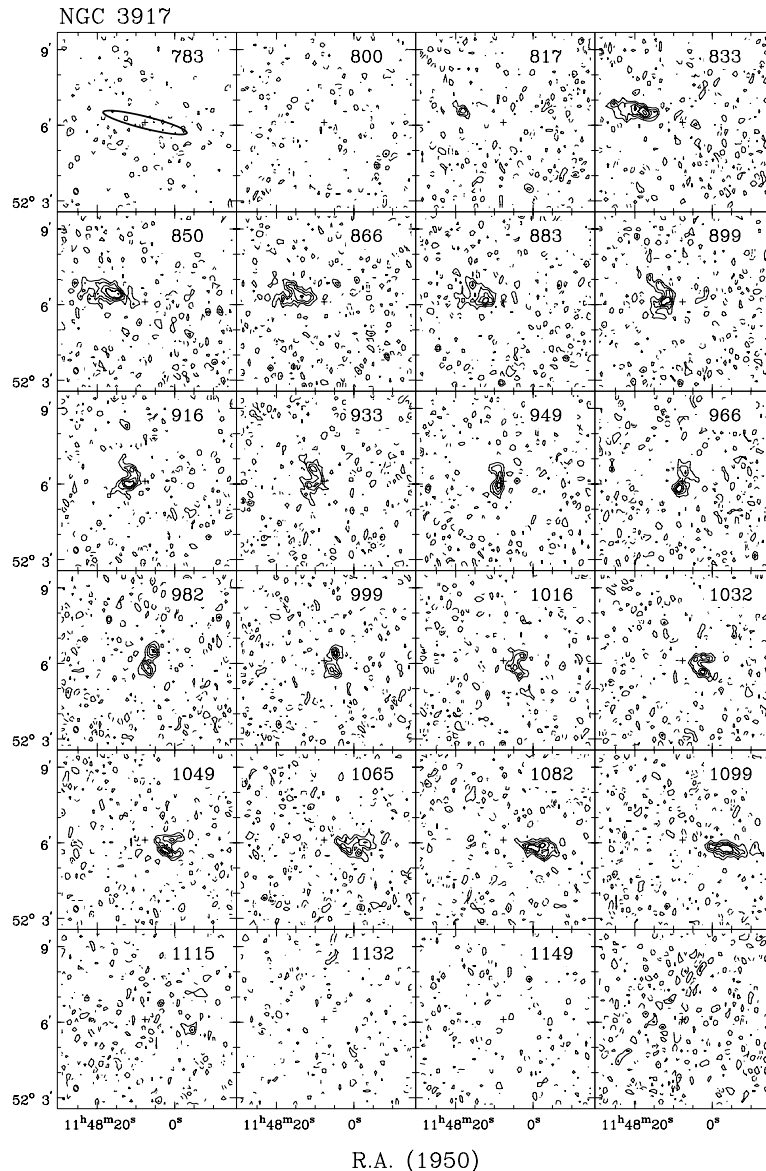
From velocity field:

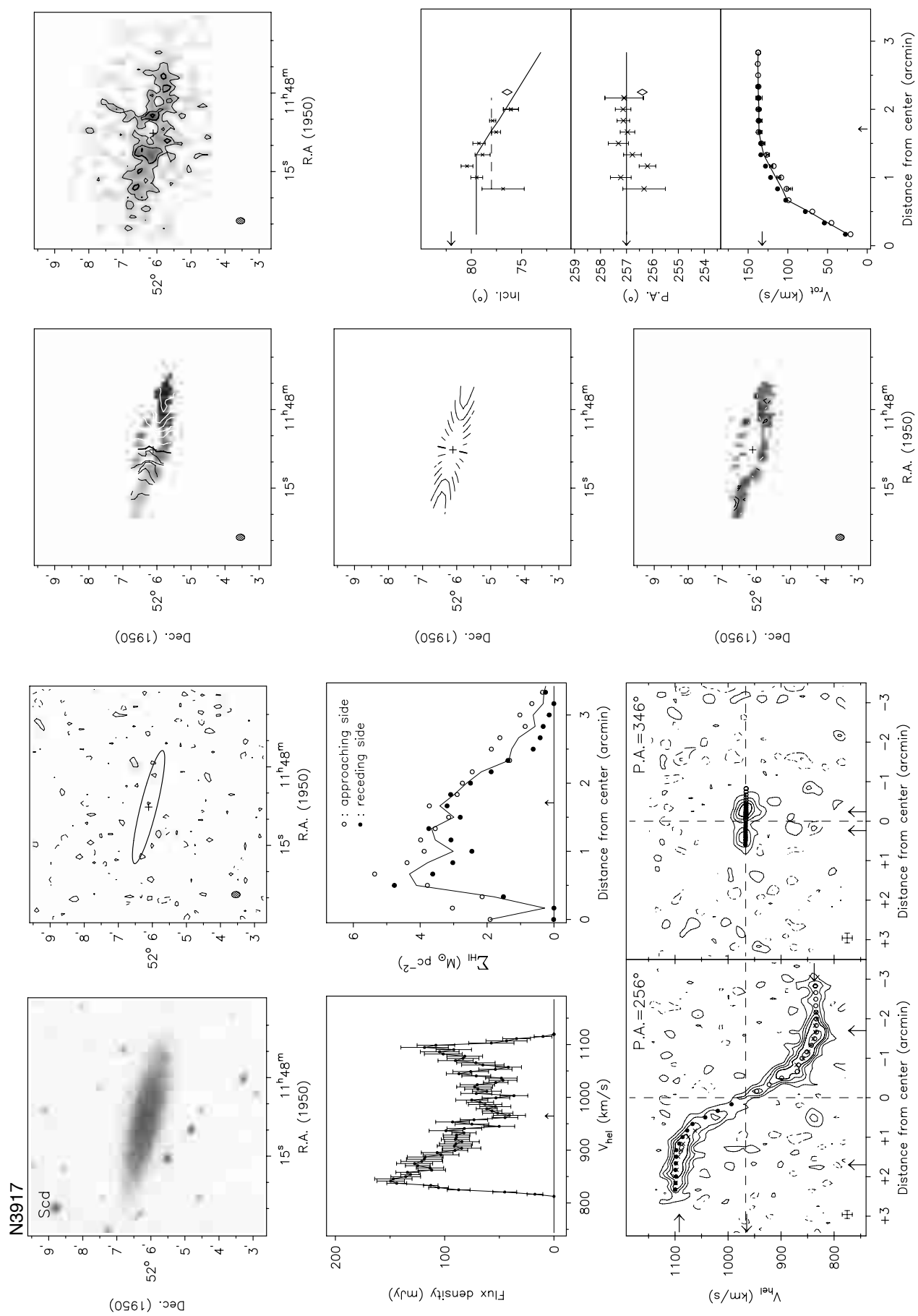
Hel. systemic velocity (km s $^{-1}$)	966.7 ± 1.8
Dynamical center, α (1950)	11:48:07.7
δ (1950)	52:06:07

From total HI map:

Geometric center, α (1950)	11:48:08.9
δ (1950)	52:06:10
Position angle (deg)	256
Inclination angle (deg)	76
Diameter of HI disk (arcmin)	5.4

Note: This galaxy has a well defined symmetric rotation curve. The HI disk is a bit more extended at the approaching side. It has a dwarf companion (N3931) at 11 arcmin to the NNE.

Channel maps at a resolution of $11'' \times 15'' \times 19$ km s $^{-1}$.Contour levels at $-3, -1.5, 1.5, 3, 4.5, \dots \times \sigma$.

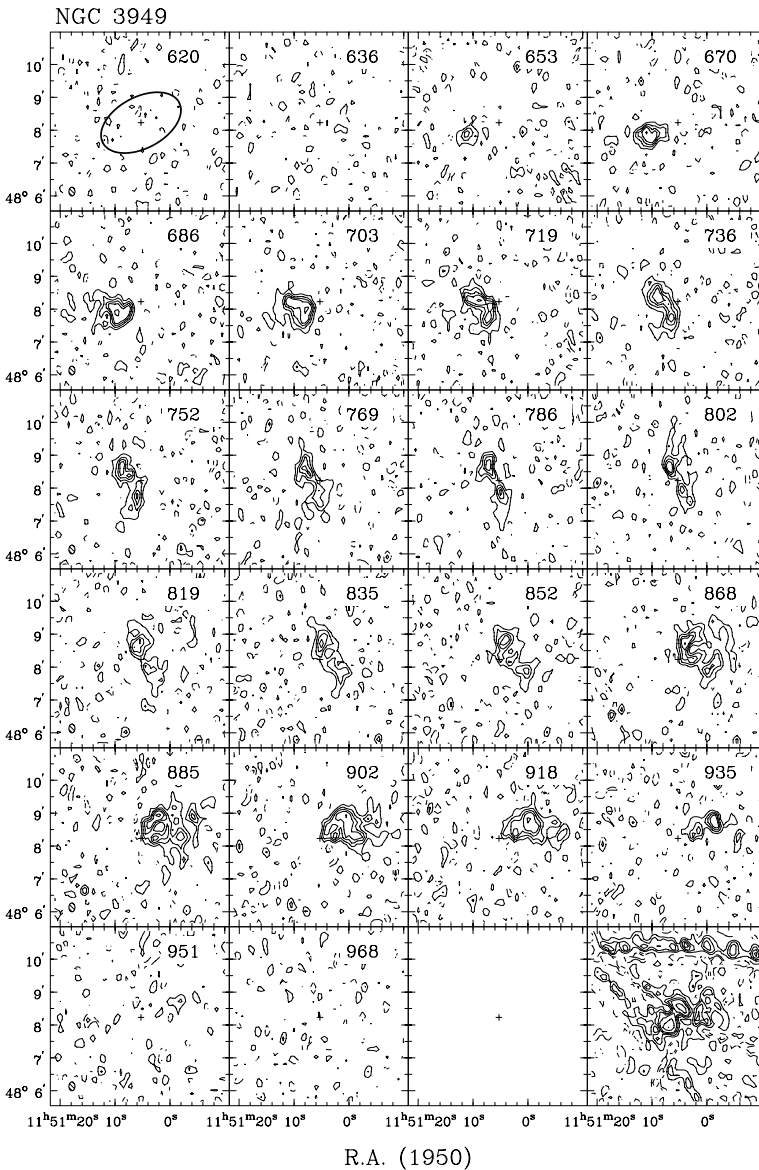


Observing parameters for NGC 3949

Length of observation	(hours)	1×12
Date of observation		10 Aug 93
Field center, α (1950)		11:51:05
δ (1950)		48:08:16
Central frequency	(MHz)	1416.61
V_{hel} of central channel	(km s $^{-1}$)	798
Primary beam FWHM	(arcmin)	37.4
Nr. of interferometers		40
Baselines (min-max-incr)	(m)	36-2700-72
Synthesized beam ($\alpha \times \delta$)	(arcsec)	11.9 \times 16.0
Bandwidth	(MHz)	2.5
Number of channels		127
Channel separation	(km s $^{-1}$)	4.14
Velocity resolution	(km s $^{-1}$)	8.29
rms noise in one channel	(K)	5.85
K-mJy conversion, equiv. of 1 mJy/beam	(K)	3.16

Contour levels for N3949

Channel maps:	$\sigma = 3.80$ (K)
Raw continuum map:	$\sigma = 1.69$ (K)
Cleaned continuum map:	$\sigma = 1.63$ (K)
Position-Velocity diagrams:	$\sigma = 3.48$ (K)
Velocity fields:	$799.0 \pm n \times 20$ (km s $^{-1}$)
Residual velocity field:	$\pm n \times 5$ (km s $^{-1}$)
Integrated HI map:	0.85, 1.71, $2.56 (\times 10^{21} \text{ atoms cm}^{-2})$



Channel maps at a resolution of $11'' \times 16'' \times 19$ km s $^{-1}$.
Contour levels at $-3, -1.5$ (dashed), $1.5, 3, 4.5, \dots \times \sigma$.

Results from WSRT data

From continuum map:

21-cm flux density (mJy) 134.1 ± 3.6

From global profile:

Integrated HI-flux (Jy km s $^{-1}$) 44.8 ± 0.4

Hel. systemic velocity (km s $^{-1}$) 800.2 ± 1.2

HI profile width, 20% (km s $^{-1}$) 286.5 ± 1.4

50% (km s $^{-1}$) 258.3 ± 1.7

From velocity field:

Hel. systemic velocity (km s $^{-1}$) 799.0 ± 1.0

Dynamical center, α (1950) 11:51:05.3

δ (1950) 48:08:14

From total HI map:

Geometric center, α (1950) 11:51:04.5

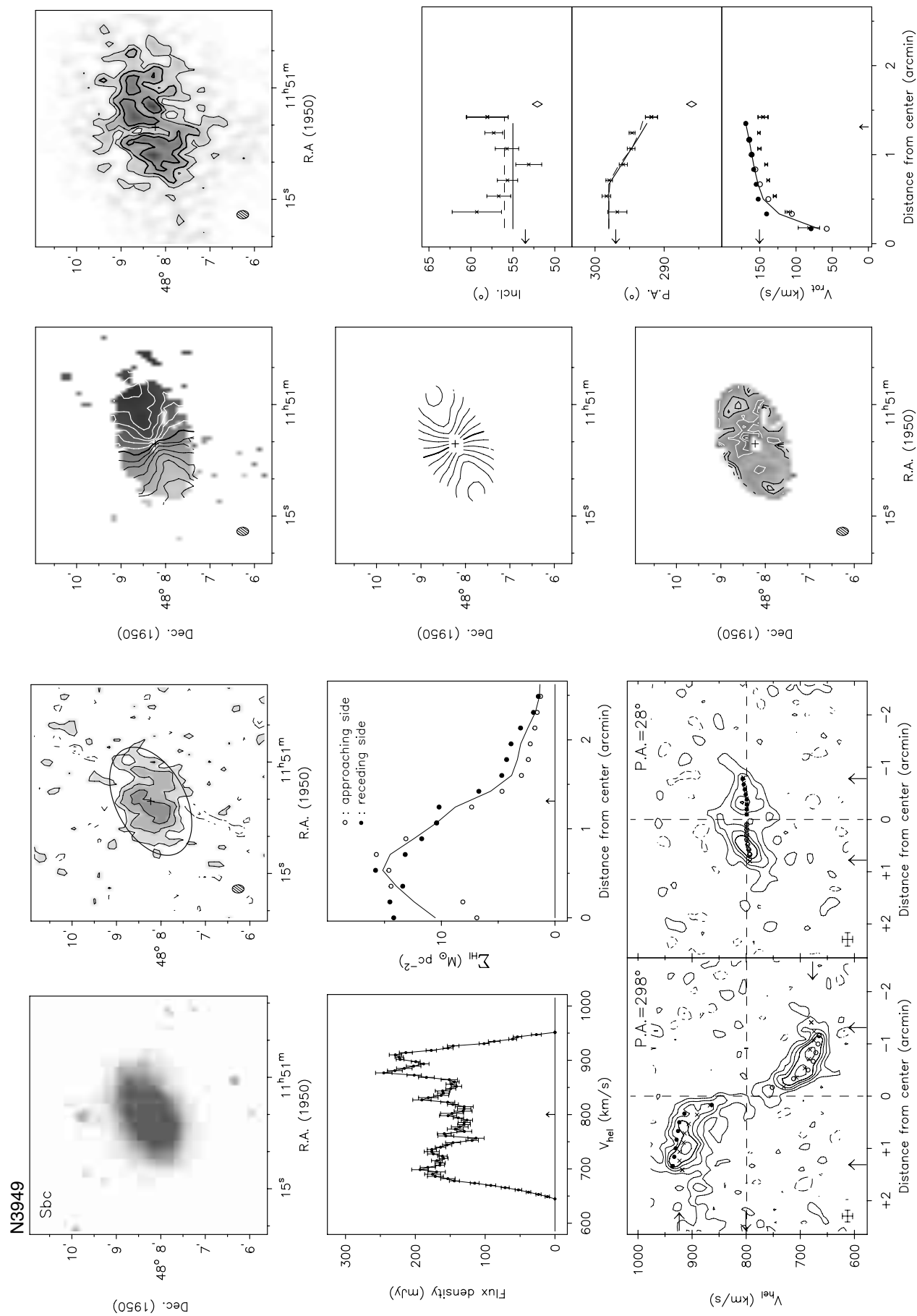
δ (1950) 48:08:21

Position angle (deg) 286

Inclination angle (deg) 52

Diameter of HI disk (arcmin) 5.4

Note: The rotation curve rises more steeply on the receding side than on the approaching side. There is a possible companion about 1.5 arcmin to the north which may be interacting with N3949 and be responsible for the faint trace of HI gas on the west side of N3949 in the velocity range 868-918 km/s.



Observing parameters for NGC 3953

Length of observation	(hours)	1x12
Date of observation		13Jul90
		29Jun92
Field center, α (1950)		11:51:10
δ (1950)		52:40:00
Central frequency	(MHz)	1415.38
V_{hel} of central channel	(km s $^{-1}$)	1060
Primary beam FWHM	(arcmin)	37.4
Nr. of interferometers		40
Baselines (min-max-incr)	(m)	36-2700-72
Synthesized beam ($\alpha \times \delta$)	(arcsec)	13.8 \times 16.4
Bandwidth	(MHz)	5.0
Number of channels		63
Channel separation	(km s $^{-1}$)	16.55
Velocity resolution	(km s $^{-1}$)	33.1
rms noise in one channel	(K)	2.79
K-mJy conversion, equiv. of 1mJy/beam	(K)	2.66

Results from WSRT data

From continuum map:21-cm flux density (mJy) 50.9 ± 2.5 From global profile:Integrated HI-flux (Jy km s $^{-1}$) 39.3 ± 0.8 Hel. systemic velocity (km s $^{-1}$) 1052.3 ± 2.0 HI profile width, 20% (km s $^{-1}$) 441.9 ± 2.4 50% (km s $^{-1}$) 413.9 ± 3.2 From velocity field:Hel. systemic velocity (km s $^{-1}$) 1051.4 ± 0.8 Dynamical center, α (1950) 11:51:12.4 δ (1950) 52:36:16From total HI map:Geometric center, α (1950) 11:51:12.5 δ (1950) 52:36:14

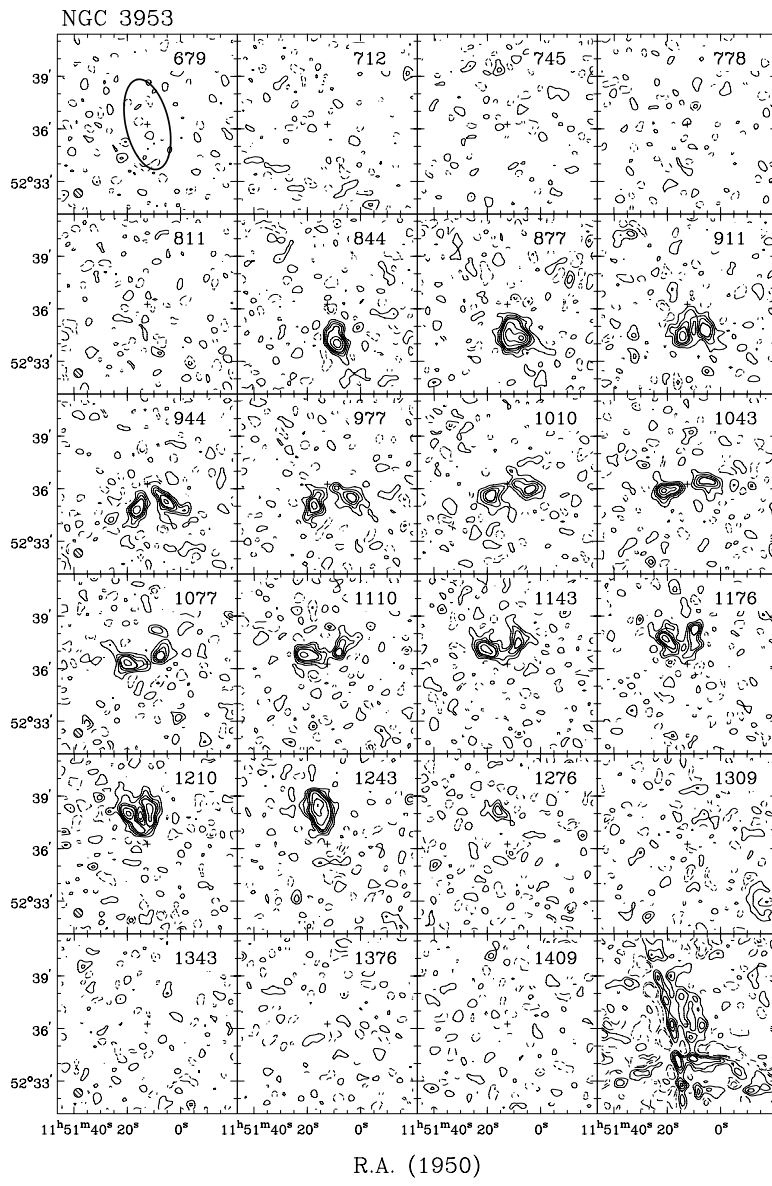
Position angle (deg) 11

Inclination angle (deg) 58

Diameter of HI disk (arcmin) 6.6

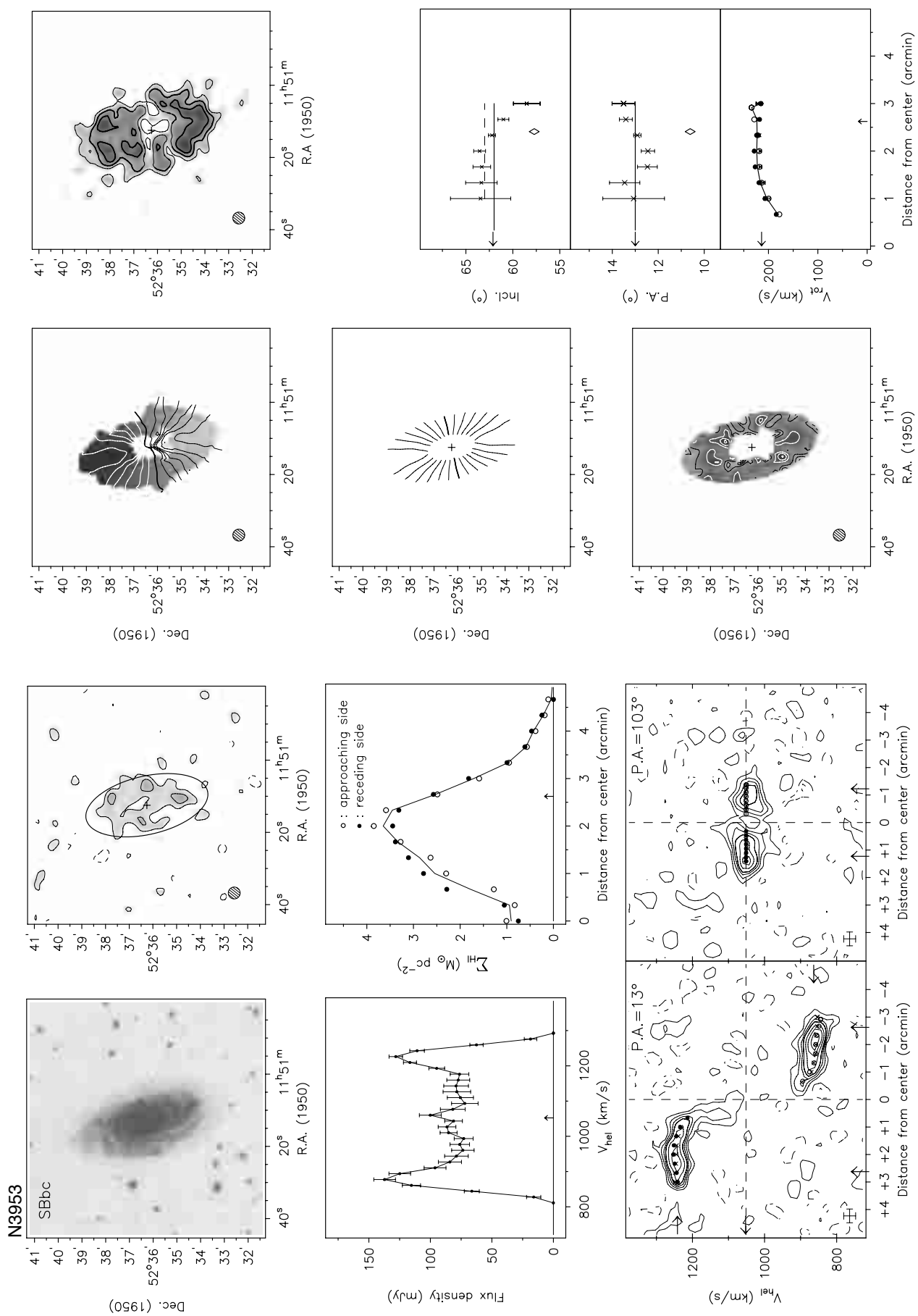
Contour levels for N3953

Channel maps:	$\sigma = 0.80$ (K)
Raw continuum map:	$\sigma = 0.33$ (K)
Cleaned continuum map:	$\sigma = 0.30$ (K)
Position-Velocity diagrams:	$\sigma = 0.81$ (K)
Velocity fields:	$1051.4 \pm n \times 30$ (km s $^{-1}$)
Residual velocity field:	$\pm n \times 5$ (km s $^{-1}$)
Integrated HI map:	0.33, 0.66, $0.99 (\times 10^{21} \text{ atoms cm}^{-2})$



Note: NGC 3953 is one of the most massive spirals in the cluster. It is rather poor in HI and the HI surface density drops strongly near D₂₅.

Channel maps at a resolution of $30'' \times 30'' \times 33 \text{ km s}^{-1}$.Contour levels at $-3, -1.5$ (dashed), $1.5, 3, 4.5, \dots \times \sigma$.



Observing parameters for NGC 3972

Length of observation	(hours)	1×12
Date of observation		10 Aug 90
Field center, α (1950)		11:53:05
δ (1950)		55:33:00
Central frequency	(MHz)	1416.37
V_{hel} of central channel	(km s $^{-1}$)	850
Primary beam FWHM	(arcmin)	37.4
Nr. of interferometers		40
Baselines (min-max-incr)	(m)	36-2700-72
Synthesized beam ($\alpha \times \delta$)	(arcsec)	11.7 \times 15.2
Bandwidth	(MHz)	2.5
Number of channels		127
Channel separation	(km s $^{-1}$)	4.15
Velocity resolution	(km s $^{-1}$)	8.29
rms noise in one channel	(K)	6.60
K-mJy conversion, equiv. of 1 mJy/beam	(K)	3.39

Contour levels for N3972

Channel maps:	$\sigma = 4.24$ (K)
Raw continuum map:	$\sigma = 2.37$ (K)
Cleaned continuum map:	$\sigma = 1.78$ (K)
Position-Velocity diagrams:	$\sigma = 3.64$ (K)
Velocity fields:	$848.8 \pm n \times 20$ (km s $^{-1}$)
Residual velocity field:	$\pm n \times 5$ (km s $^{-1}$)
Integrated HI map:	1.00, 1.99, $2.99 (\times 10^{21} \text{ atoms cm}^{-2})$

Results from WSRT data

From continuum map:

21-cm flux density	
central point source (mJy)	<1.6 (3 σ)
extended source (mJy)	<5.8 (3 σ)

From global profile:

Integrated HI-flux (Jy km s $^{-1}$)	16.6 ± 0.4
Hel. systemic velocity (km s $^{-1}$)	852.2 ± 1.4
HI profile width, 20% (km s $^{-1}$)	281.2 ± 1.4
50% (km s $^{-1}$)	260.7 ± 5.5

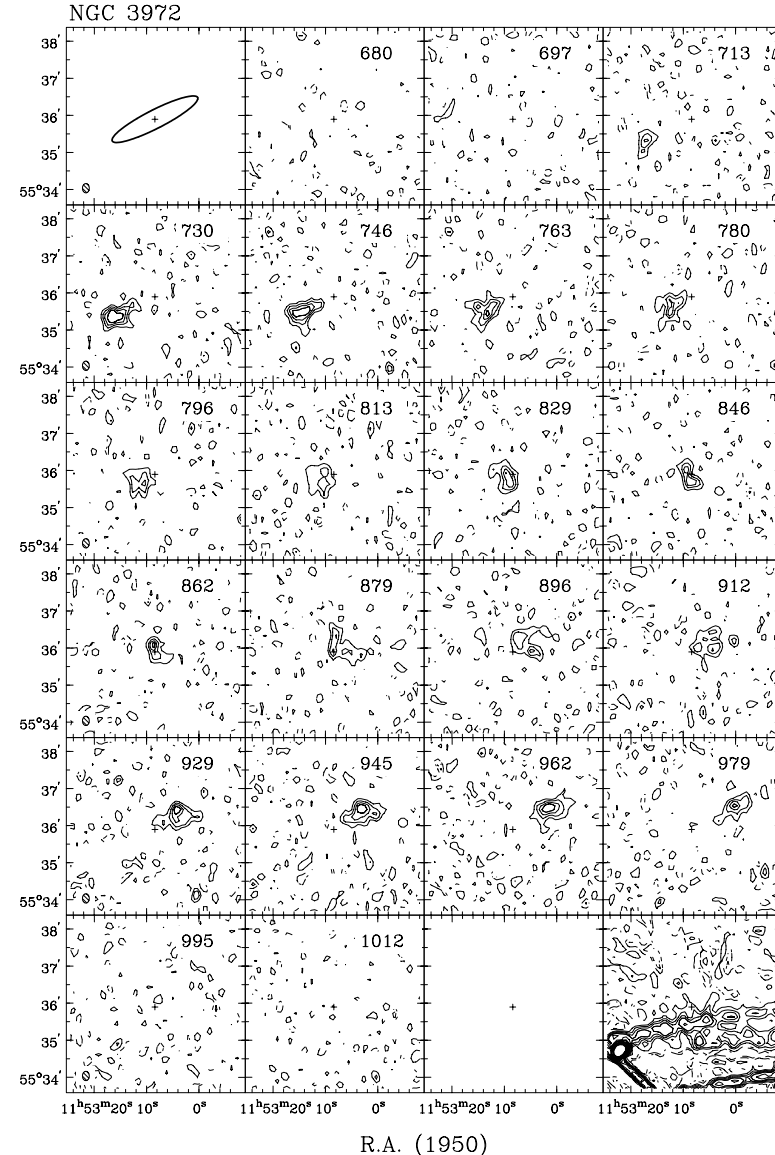
From velocity field:

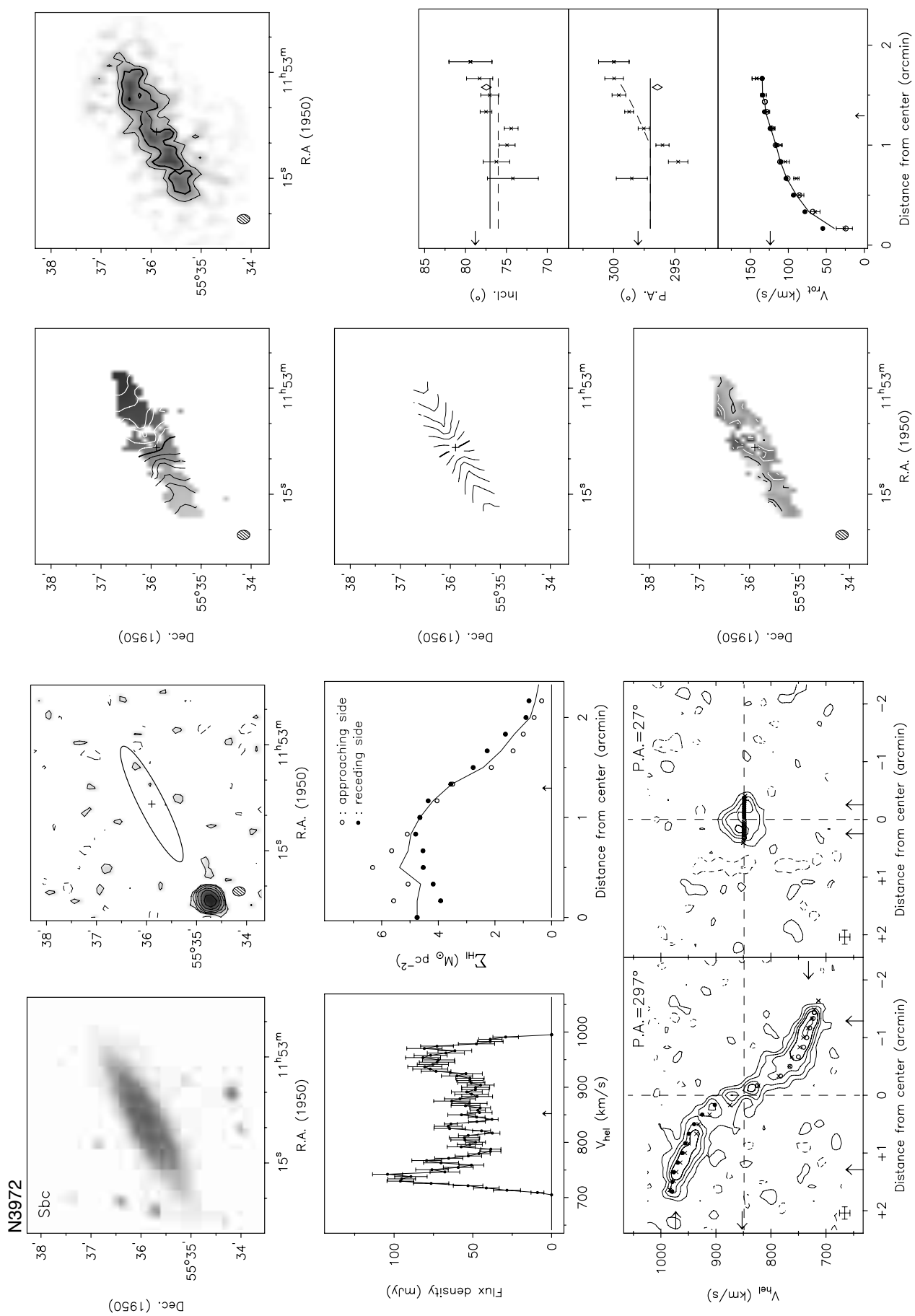
Hel. systemic velocity (km s $^{-1}$)	848.8 ± 2.8
Dynamical center, α (1950)	11:53:08.5

 δ (1950) 55:35:54From total HI map:

Geometric center, α (1950)	11:53:08.1
δ (1950)	55:35:54
Position angle (deg)	297
Inclination angle (deg)	77
Diameter of HI disk (arcmin)	3.8

Note: The HI disk does not extend much beyond D₂₅ and the rotation curve is still somewhat rising at the last measured points.

Channel maps at a resolution of $11'' \times 15'' \times 19$ km s $^{-1}$.Contour levels at $-3, -1.5$ (dashed), $1.5, 3, 4.5, \dots \times \sigma$.



Observing parameters for UGC 6917

Length of observation	(hours)	1×12
Date of observation		19Apr91
Field center, α (1950)		11:53:55
δ (1950)		50:40:00
Central frequency	(MHz)	1415.96
V_{hel} of central channel	(km s $^{-1}$)	925
Primary beam FWHM	(arcmin)	37.4
Nr. of interferometers		40
Baselines (min-max-incr)	(m)	36-2700-72
Synthesized beam ($\alpha \times \delta$)	(arcsec)	11.6×17.2
Bandwidth	(MHz)	2.5
Number of channels		127
Channel separation	(km s $^{-1}$)	4.15
Velocity resolution	(km s $^{-1}$)	8.30
rms noise in one channel	(K)	5.28
K-mJy conversion, equiv. of 1mJy/beam	(K)	3.02

Contour levels for U6917

Channel maps:	$\sigma = 0.90$ (K)
Raw continuum map:	$\sigma = 1.19$ (K)
Cleaned continuum map:	$\sigma = 1.18$ (K)
Position-Velocity diagrams:	$\sigma = 2.94$ (K)
Velocity fields:	$909.6 \pm n \times 20$ (km s $^{-1}$)
Residual velocity field:	$\pm n \times 5$ (km s $^{-1}$)
Integrated HI map:	0.49, 0.98, $1.47 (\times 10^{21} \text{ atoms cm}^{-2})$

Results from WSRT data

From continuum map:

21-cm flux density	
central point source (mJy)	$< 1.2 (3\sigma)$
extended source (mJy)	$< 4.4 (3\sigma)$

From global profile:

Integrated HI-flux	(Jy km s $^{-1}$)	26.2 ± 0.3
Hel. systemic velocity	(km s $^{-1}$)	910.7 ± 1.4
HI profile width, 20%	(km s $^{-1}$)	208.9 ± 3.2
50%	(km s $^{-1}$)	189.6 ± 1.6

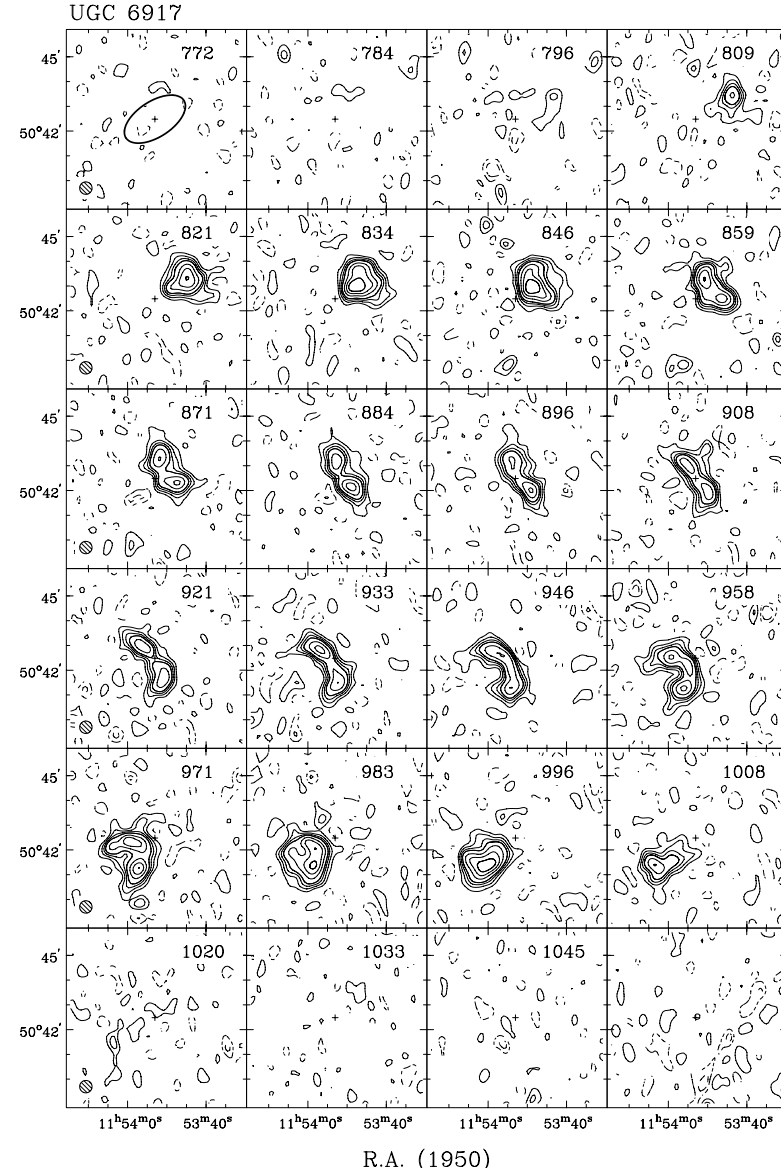
From velocity field:

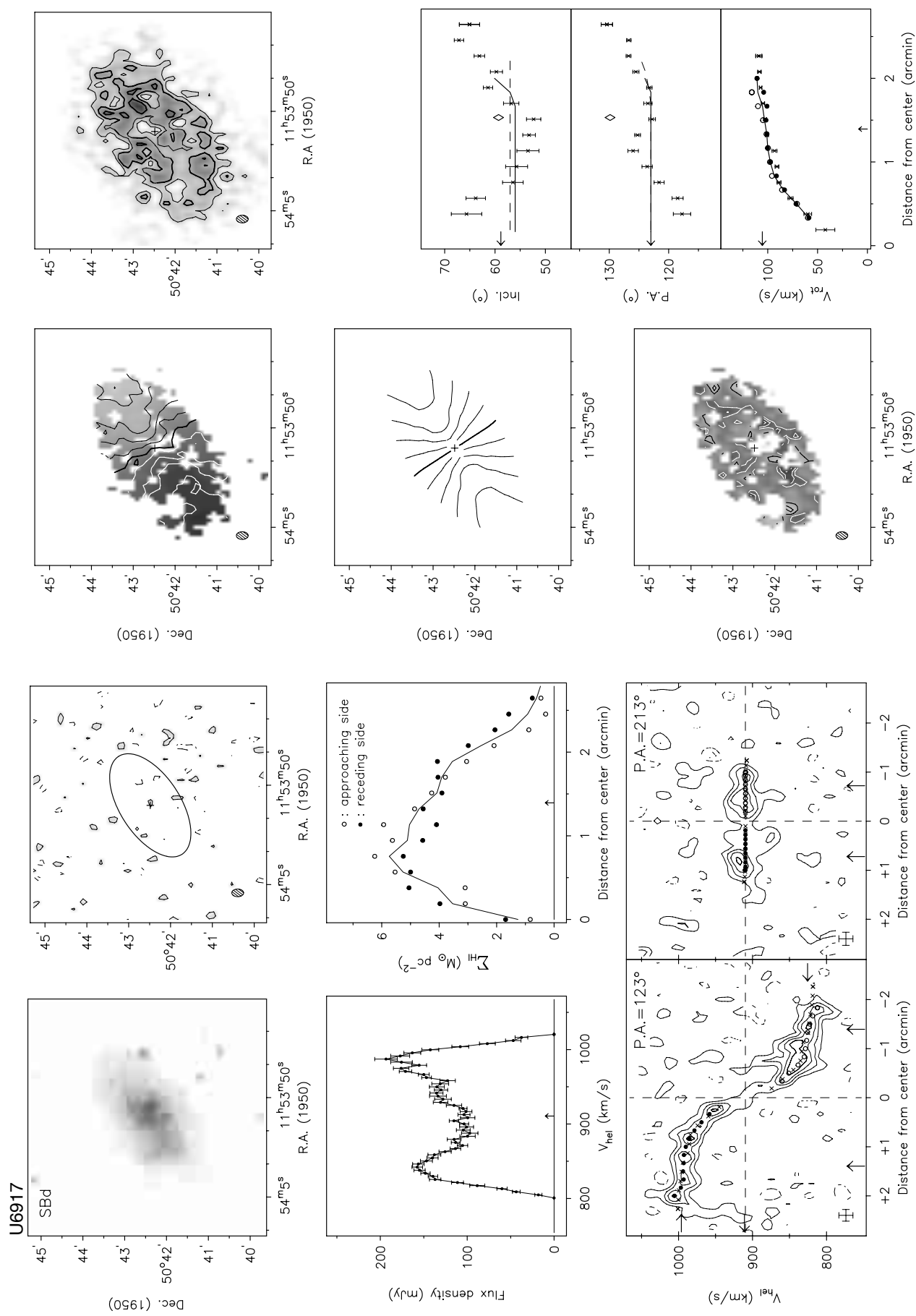
Hel. systemic velocity	(km s $^{-1}$)	909.6 ± 0.9
Dynamical center, α (1950)		11:53:53.1

 δ (1950) 50:42:29From total HI map:

Geometric center, α (1950)		11:53:53.3
δ (1950)		50:42:25
Position angle	(deg)	130
Inclination angle	(deg)	59
Diameter of HI disk	(arcmin)	4.8

Note: The apparent upturn of the rotation curve at the last measured points is not necessarily real. The disk seems to be warped toward more edge-on in the outer regions but the amplitude of this warp is difficult to measure. A flat rotation curve in the outer regions would mean that the inclination angle increases by about 6 degrees which is well within the uncertainties. The channel maps are presented at a resolution of $30'' \times 30''$ arcsec while the other data are shown for the highest resolution of $11'' \times 15''$ arcsec.

Channel maps at a resolution of $30'' \times 30'' \times 19 \text{ km s}^{-1}$.Contour levels at $-3, -1.5, 1.5, 3, 4.5, \dots \times \sigma$.



Observing parameters for UGC 6923

Length of observation	(hours)	1×12
Date of observation		23Dec94
Field center, α (1950)		11:55:07
δ (1950)		53:31:54
Central frequency	(MHz)	1415.53
V_{hel} of central channel	(km s $^{-1}$)	1054
Primary beam FWHM	(arcmin)	37.4
Nr. of interferometers		40
Baselines (min-max-incr)	(m)	36-2700-72
Synthesized beam ($\alpha \times \delta$)	(arcsec)	12.1 \times 15.1
Bandwidth	(MHz)	5.0
Number of channels		127
Channel separation	(km s $^{-1}$)	8.31
Velocity resolution	(km s $^{-1}$)	9.97
rms noise in one channel	(K)	9.71
K-mJy conversion, equiv. of 1mJy/beam	(K)	3.29

Note: To achieve a sufficient velocity resolution over a 5 MHz bandwidth, only the XX dipoles could be correlated due to limitations of the backend.

Results from WSRT data

From continuum map:

21-cm flux density	
central point source (mJy)	<1.3 (3 σ)
extended source (mJy)	<2.6 (3 σ)

From global profile:

Integrated HI-flux	(Jy km s $^{-1}$)	10.7 ± 0.6
Hel. systemic velocity	(km s $^{-1}$)	1061.6 ± 2.2
HI profile width, 20% (km s $^{-1}$)		166.8 ± 2.4
50% (km s $^{-1}$)		147.1 ± 4.5

From velocity field:

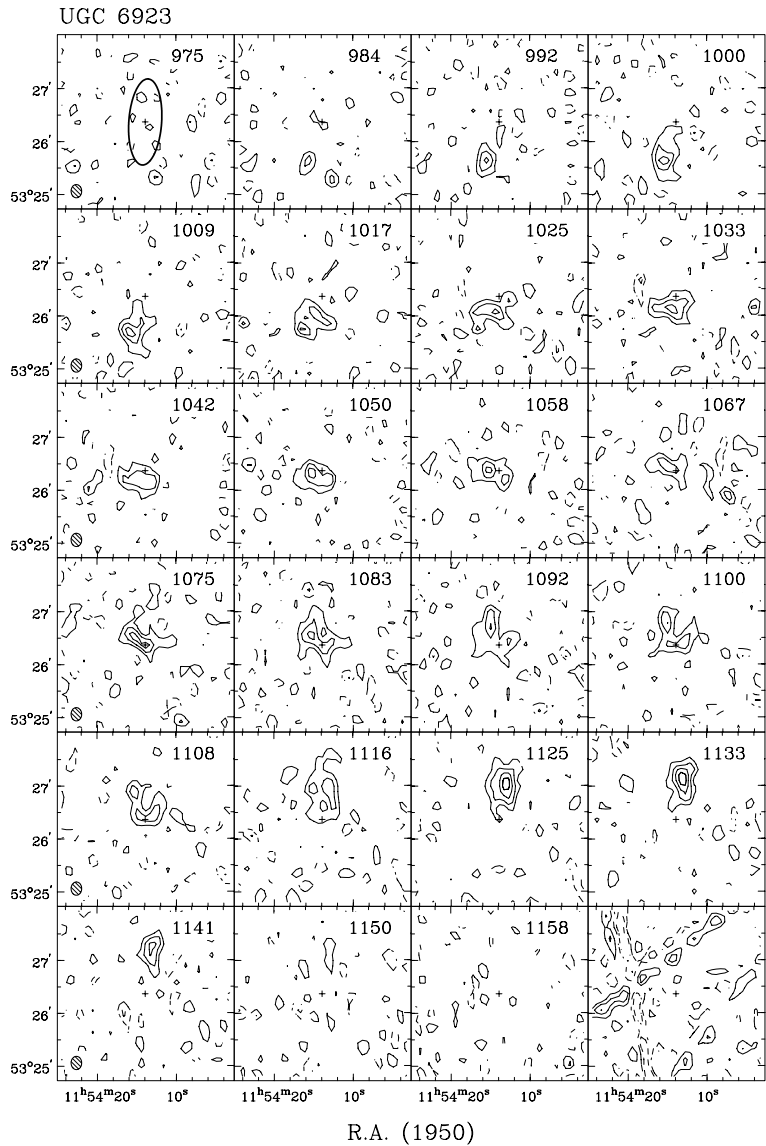
Hel. systemic velocity	(km s $^{-1}$)	1066.0 ± 1.7
Dynamical center, α (1950)		11:54:13.9
δ (1950)		53:26:22

From total HI map:

Geometric center, α (1950)		11:54:14.4
δ (1950)		53:26:24
Position angle	(deg)	346
Inclination angle	(deg)	64
Diameter of HI disk	(arcmin)	2.6

Contour levels for U6923

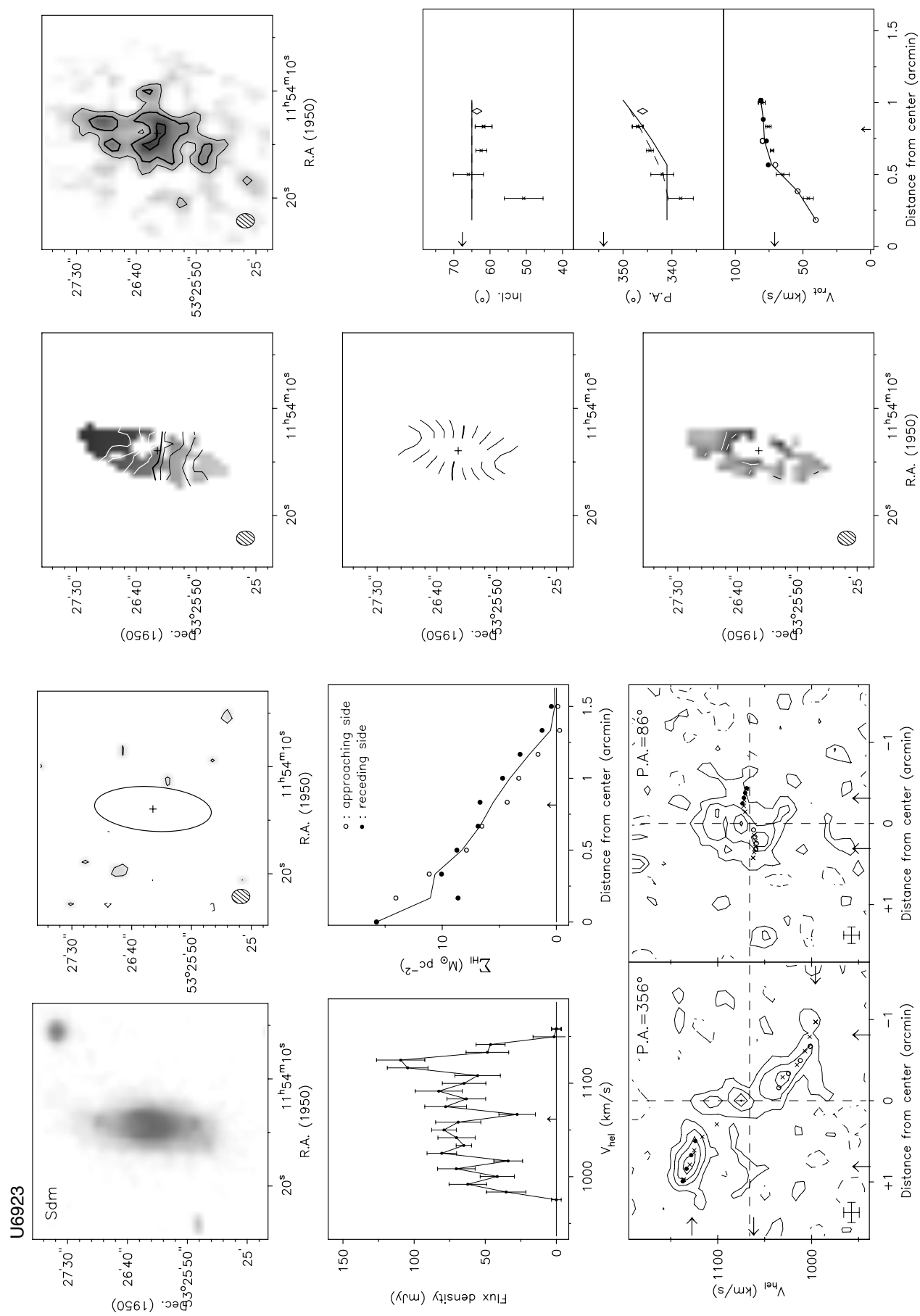
Channel maps:	$\sigma=5.93$ (K)
Raw continuum map:	$\sigma=1.45$ (K)
Cleaned continuum map:	$\sigma=1.42$ (K)
Position-Velocity diagrams:	$\sigma=5.10$ (K)
Velocity fields:	$1066.0 \pm n \times 15$ (km s $^{-1}$)
Residual velocity field:	$\pm n \times 5$ (km s $^{-1}$)
Integrated HI map:	1.19, 2.39, $3.58 (\times 10^{21} \text{ atoms cm}^{-2})$



Channel maps at a resolution of $12'' \times 15'' \times 17 \text{ km s}^{-1}$.

Contour levels at $-3, -1.5, 1.5, 3, 4.5, \dots \times \sigma$.

Note: This dwarf galaxy is a companion of NGC 3992. Optically, the disk seems to be warped which is also suggested by the HI velocity field. The HI surface density in this system is quite high and centrally concentrated.



Observing parameters for UGC 6930

Length of observation	(hours)	1×12
Date of observation		20 Aug 93
Field center, α (1950)		11:54:42
δ (1950)		49:33:50
Central frequency	(MHz)	1416.72
V_{hel} of central channel	(km s $^{-1}$)	778
Primary beam FWHM	(arcmin)	37.4
Nr. of interferometers		40
Baselines (min-max-incr)	(m)	36-2700-72
Synthesized beam ($\alpha \times \delta$)	(arcsec)	12.3 \times 16.8
Bandwidth	(MHz)	2.5
Number of channels		127
Channel separation	(km s $^{-1}$)	4.14
Velocity resolution	(km s $^{-1}$)	8.29
rms noise in one channel	(K)	5.54
K-mJy conversion, equiv. of 1 mJy/beam	(K)	2.92

Contour levels for U6930

Channel maps:	$\sigma = 1.00$ (K)
Raw continuum map:	$\sigma = 0.37$ (K)
Cleaned continuum map:	$\sigma = 0.33$ (K)
Position-Velocity diagrams:	$\sigma = 0.97$ (K)
Velocity fields:	$777.7 \pm n \times 15$ (km s $^{-1}$)
Residual velocity field:	$\pm n \times 5$ (km s $^{-1}$)
Integrated HI map:	0.08, 0.15, 0.23, 0.30 $0.38, 0.45 (\times 10^{21} \text{ atoms cm}^{-2})$

Results from WSRT data

From continuum map:

21-cm flux density	
central point source (mJy)	<1.2 (3 σ)
extended source (mJy)	<5.8 (3 σ)

From global profile:

Integrated HI-flux	(Jy km s $^{-1}$)	42.7 ± 0.3
Hel. systemic velocity	(km s $^{-1}$)	777.2 ± 0.4
HI profile width, 20%	(km s $^{-1}$)	136.5 ± 0.5
50%	(km s $^{-1}$)	122.1 ± 0.7

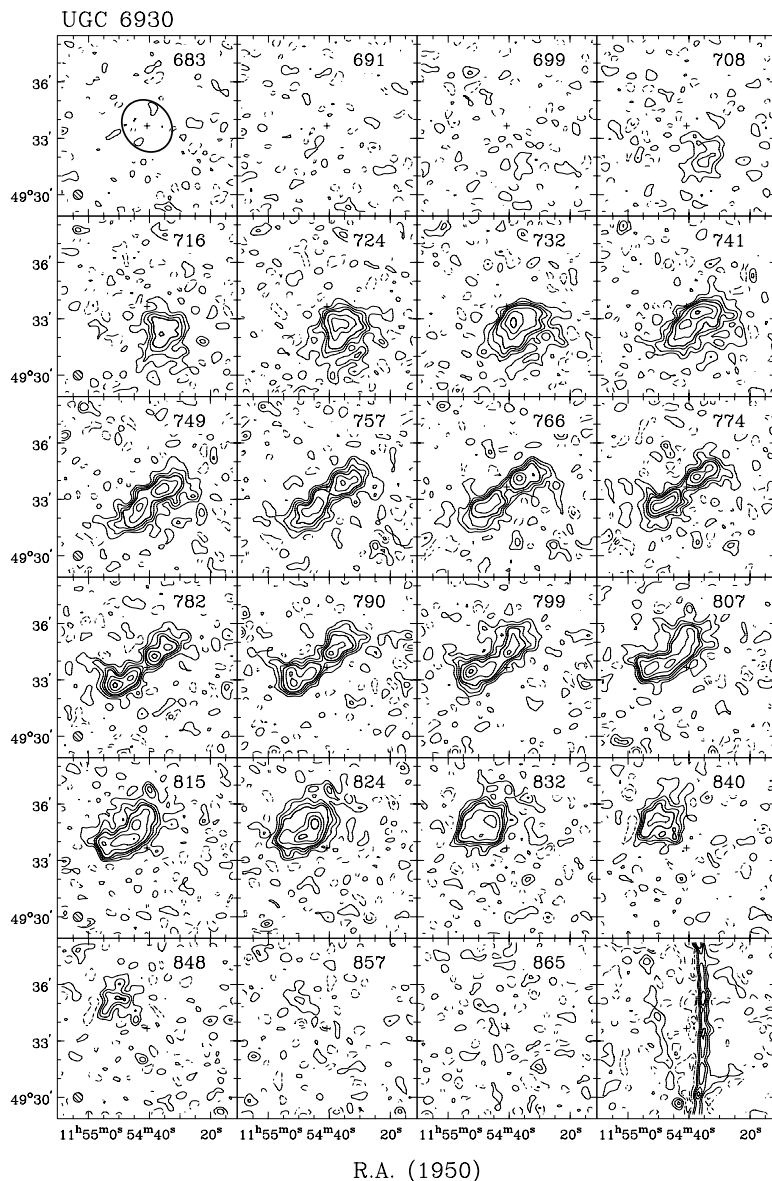
From velocity field:

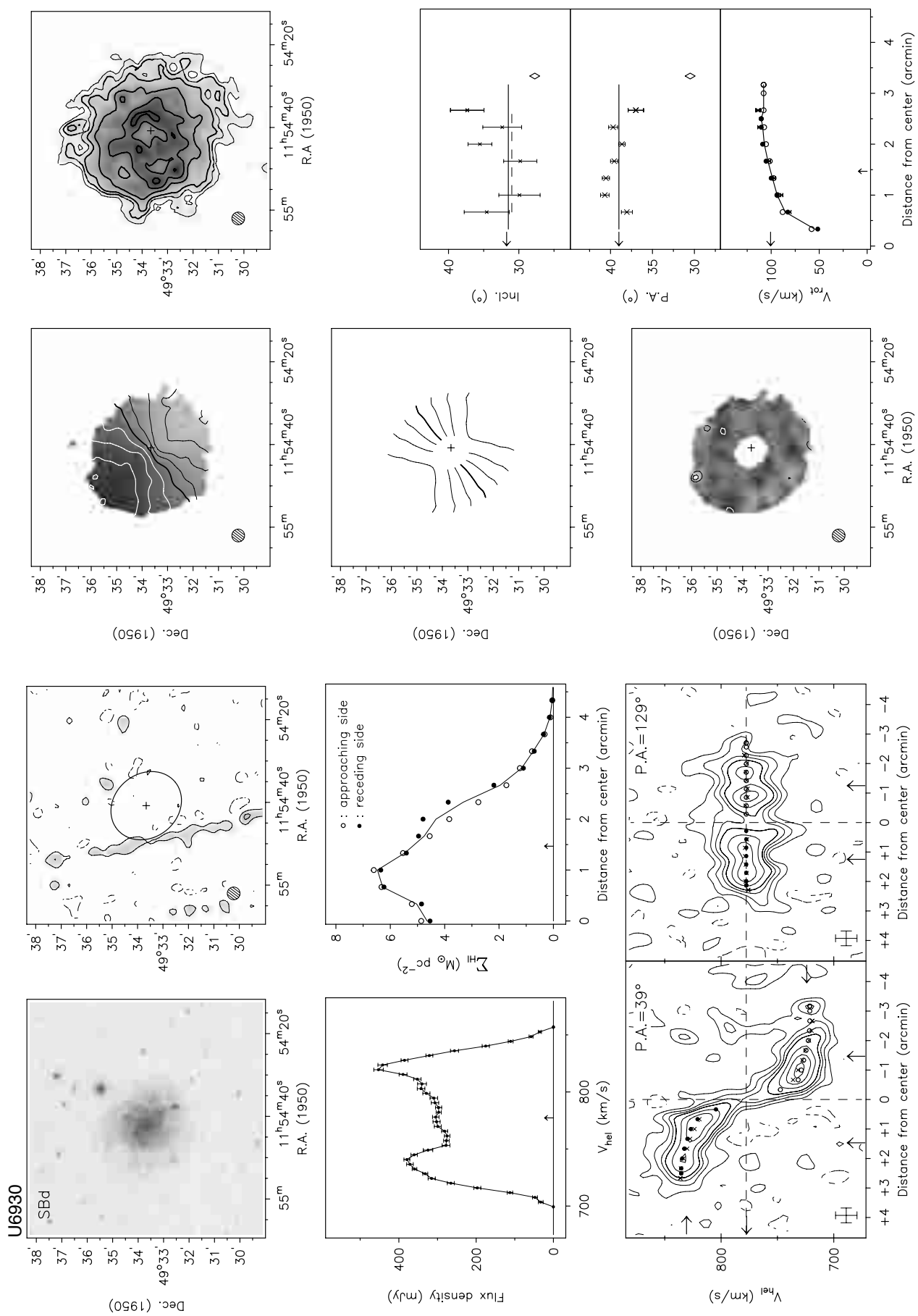
Hel. systemic velocity	(km s $^{-1}$)	777.7 ± 0.2
Dynamical center, α (1950)		11:54:41.9

 δ (1950) 49:33:40*From total HI map:*

Geometric center, α (1950)		11:54:43.1
δ (1950)		49:33:44
Position angle	(deg)	31
Inclination angle	(deg)	28
Diameter of HI disk	(arcmin)	6.4

Note: This low surface brightness galaxy is located nearest to the adopted cluster center. It is more face-on than 45 degrees and therefore not fit for a study of the TF-relation. The HI disk is not symmetrical and is slightly more extended toward the south-east at the higher column density levels.

Channel maps at a resolution of $30'' \times 30'' \times 19 \text{ km s}^{-1}$.Contour levels at $-3, -1.5, 1.5, 3, 4.5, \dots \times \sigma$.



Observing parameters for NGC 3992

Length of observation	(hours)	1×12
Date of observation		23Dec94
Field center, α (1950)		11:55:07
δ (1950)		53:31:54
Central frequency	(MHz)	1415.53
V_{hel} of central channel	(km s $^{-1}$)	1054
Primary beam FWHM	(arcmin)	37.4
Nr. of interferometers		40
Baselines (min-max-incr)	(m)	36-2700-72
Synthesized beam ($\alpha \times \delta$)	(arcsec)	12.1 \times 15.1
Bandwidth	(MHz)	5.0
Number of channels		127
Channel separation	(km s $^{-1}$)	8.31
Velocity resolution	(km s $^{-1}$)	9.97
rms noise in one channel	(K)	9.71
K-mJy conversion, equiv. of 1mJy/beam	(K)	3.29

Note: To achieve a sufficient velocity resolution over a 5 MHz bandwidth, only the XX dipoles could be correlated due to limitations of the backend.

Results from WSRT data

From continuum map:

21-cm flux density	(mJy)	30.2 ± 7.6
--------------------	-------	----------------

From global profile:

Integrated HI-flux	(Jy km s $^{-1}$)	74.6 ± 1.5
Hel. systemic velocity	(km s $^{-1}$)	1048.2 ± 1.2
HI profile width, 20% (km s $^{-1}$)		478.5 ± 1.4
50% (km s $^{-1}$)		461.4 ± 2.4

From velocity field:

Hel. systemic velocity	(km s $^{-1}$)	1049.5 ± 0.6
Dynamical center, α (1950)		11:55:00.7

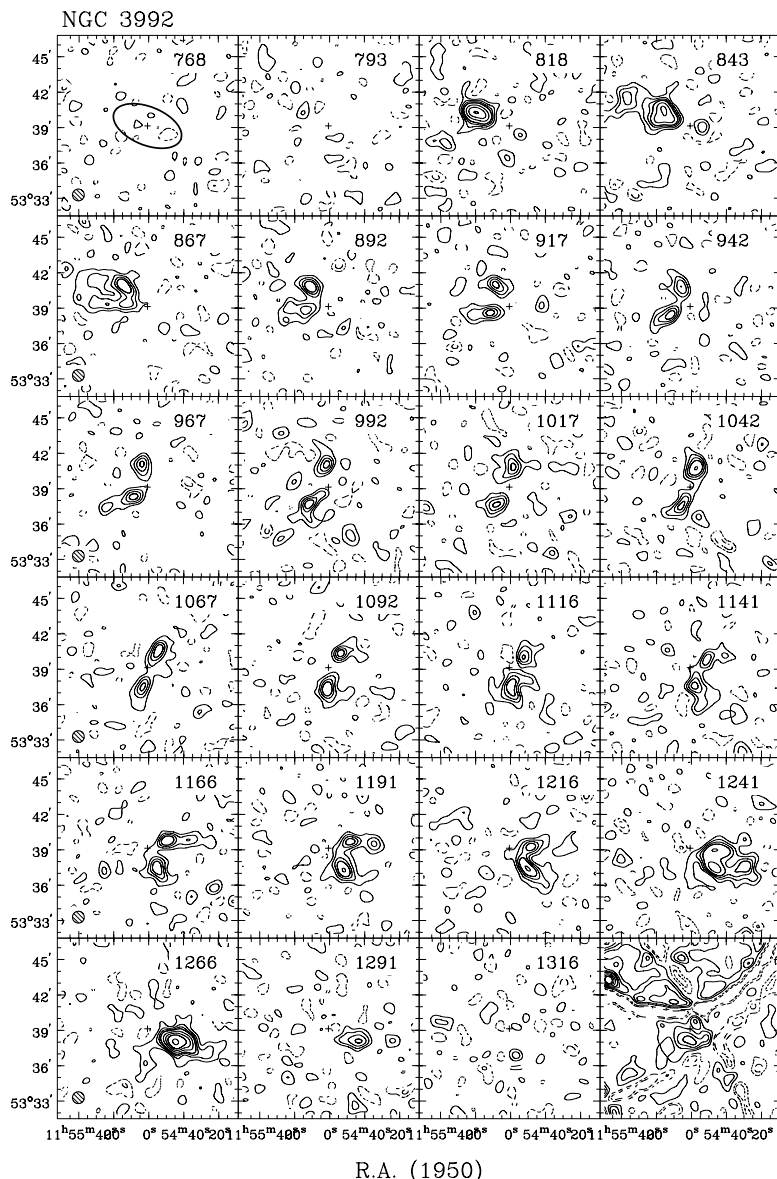
δ (1950) 53:39:09

From total HI map:

Geometric center, α (1950)		11:54:58.7
δ (1950)		53:39:03
Position angle	(deg)	251
Inclination angle	(deg)	52
Diameter of HI disk	(arcmin)	9.5

Contour levels for N3992

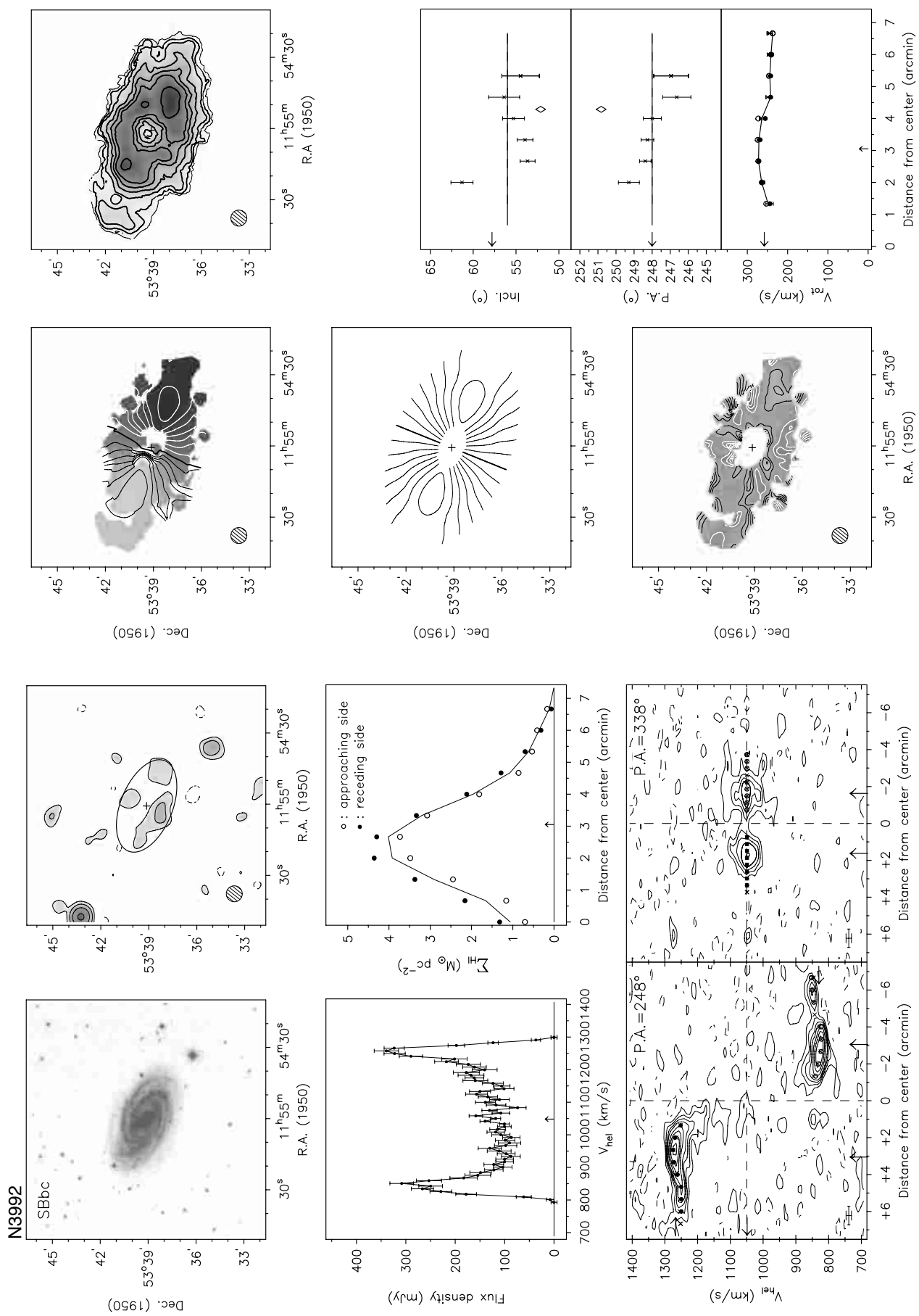
Channel maps:	$\sigma = 0.56$ (K)
Raw continuum map:	$\sigma = 0.16$ (K)
Cleaned continuum map:	$\sigma = 0.15$ (K)
Position-Velocity diagrams:	$\sigma = 0.55$ (K)
Velocity fields:	$1049.5 \pm n \times 30$ (km s $^{-1}$)
Residual velocity field:	$\pm n \times 5$ (km s $^{-1}$)
Integrated HI map:	0.45, 0.90, 1.36, 1.81, 2.26 $2.71, 3.16 (\times 10^{20} \text{ atoms cm}^{-2})$



Channel maps at a resolution of $60'' \times 60'' \times 17 \text{ km s}^{-1}$.

Contour levels at $-3, -1.5$ (dashed), $1.5, 3, 4.5, \dots \times \sigma$.

Note: NGC 3992 is the most massive spiral in the cluster. It has a prominent bar and well defined spiral arms. The rotation curve declines at 4 arcmin from the center by about 30 km s^{-1} and remains apparently flat in the outer parts. There are three dwarf companions detected in HI: U6923, U6940 and U6969.



Observing parameters for UGC 6940

Length of observation	(hours)	1×12
Date of observation		23Dec94
Field center, α (1950)		11:55:07
δ (1950)		53:31:54
Central frequency	(MHz)	1415.53
V_{hel} of central channel	(km s $^{-1}$)	1054
Primary beam FWHM	(arcmin)	37.4
Nr. of interferometers		40
Baselines (min-max-incr)	(m)	36-2700-72
Synthesized beam ($\alpha \times \delta$)	(arcsec)	12.1 \times 15.1
Bandwidth	(MHz)	5.0
Number of channels		127
Channel separation	(km s $^{-1}$)	8.31
Velocity resolution	(km s $^{-1}$)	9.97
rms noise in one channel	(K)	9.71
K-mJy conversion, equiv. of 1mJy/beam	(K)	3.29

Note: To achieve a sufficient velocity resolution over a 5 MHz bandwidth, only the XX dipoles could be correlated due to limitations of the backend.

Results from WSRT data

From continuum map:

21-cm flux density	
central point source (mJy)	<1.3 (3σ)
extended source (mJy)	<1.3 (3σ)

From global profile:

Integrated HI-flux	(Jy km s $^{-1}$)	2.1 ± 0.3
Hel. systemic velocity	(km s $^{-1}$)	1118.0 ± 1.7
HI profile width, 20% (km s $^{-1}$)		59.3 ± 3.8
50% (km s $^{-1}$)		40.6 ± 7.8

From velocity field:

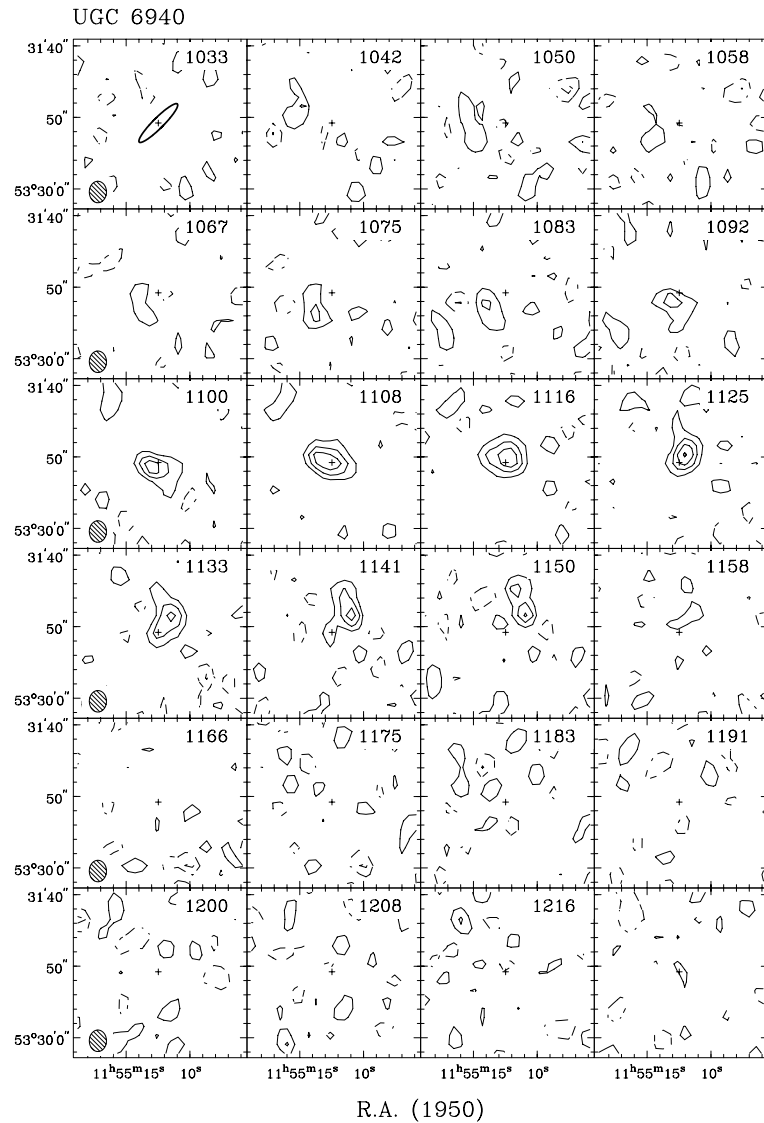
Hel. systemic velocity	(km s $^{-1}$)	1115.8 ± 2.5
------------------------	-----------------	------------------

From total HI map:

Geometric center, α (1950)		11:55:12.3
δ (1950)		53:30:56
Position angle	(deg)	311
Inclination angle	(deg)	57
Diameter of HI disk	(arcmin)	1.2

Contour levels for U6940

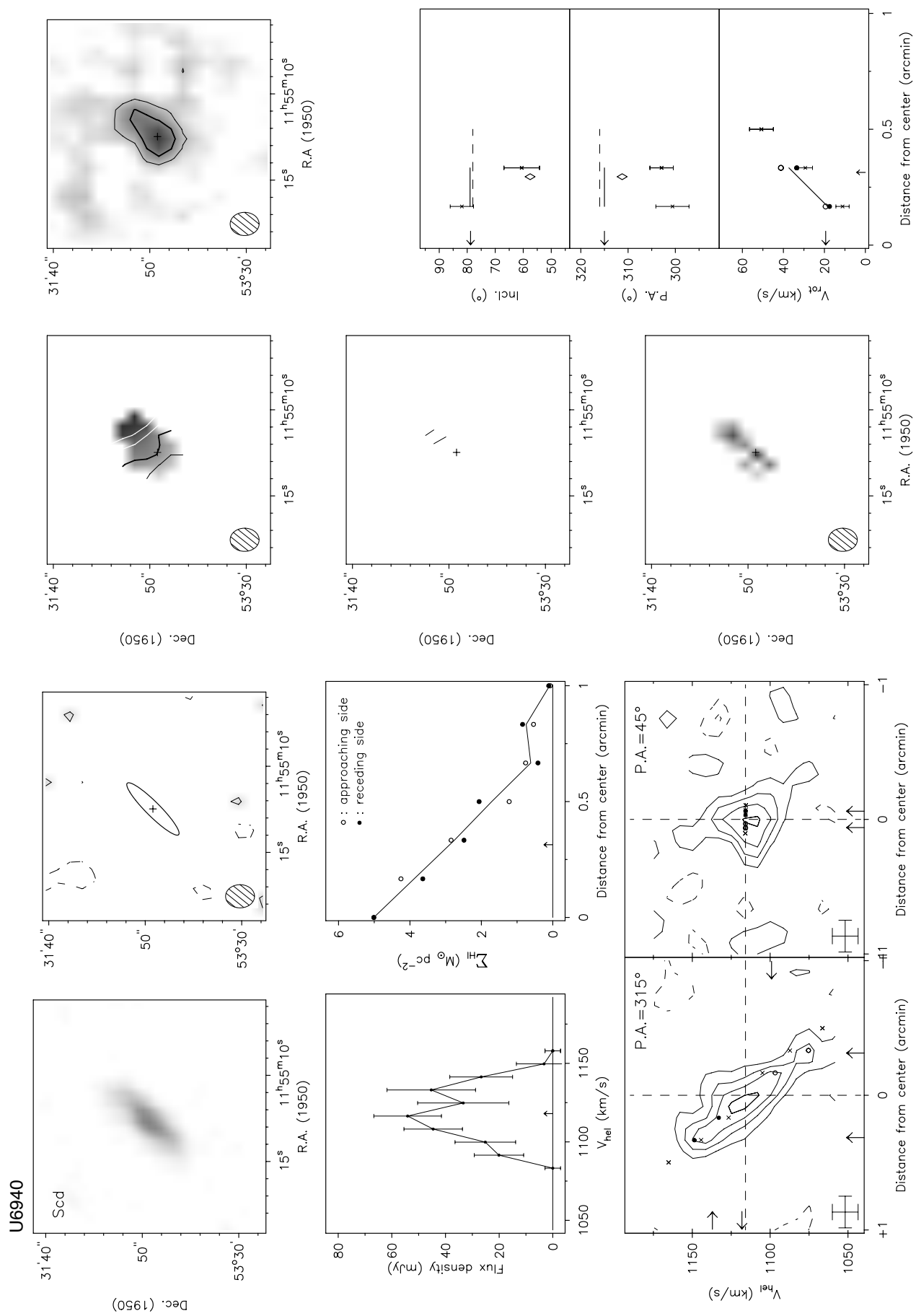
Channel maps:	$\sigma=5.93$ (K)
Raw continuum map:	$\sigma=1.45$ (K)
Cleaned continuum map:	$\sigma=1.42$ (K)
Position-Velocity diagrams:	$\sigma=5.10$ (K)
Velocity fields:	$1115.8 \pm n \times 10$ (km s $^{-1}$)
Residual velocity field:	$\pm n \times 5$ (km s $^{-1}$)
Integrated HI map:	0.82, 1.64, $2.46 (\times 10^{21} \text{ atoms cm}^{-2})$



Channel maps at a resolution of $12'' \times 15'' \times 17 \text{ km s}^{-1}$.

Contour levels at $-3, -1.5, 1.5, 3, 4.5, \dots \times \sigma$.

Note: This dwarf system is among the faintest in the cluster. It spans just a few synthesized beams across and the HI rotation curve only shows the solid body part. In this case, the orientation of the disk is adopted from the optical image.



Observing parameters for UGC 6962

Length of observation	(hours)	5×12
Dates of observation		17Aug90
		11Aug92, 24Jul93 and 2,8,13Mar94
Field center, $\alpha(1950)$		11:56:20
$\delta(1950)$		42:56:00
Central frequency	(MHz)	1416.79
V_{hel} of central channel	(km s^{-1})	760
Primary beam FWHM	(arcmin)	37.4
Nr. of interferometers		120
Baselines (min-max-incr)	(m)	36-2736-18
Synthesized beam ($\alpha \times \delta$)	(arcsec)	12.0 \times 18.8
Bandwidth	(MHz)	2.5
Number of channels		127
Channel separation	(km s^{-1})	4.14
Velocity resolution	(km s^{-1})	8.29
rms noise in one channel	(K)	2.84
K-mJy conversion, equiv. of 1mJy/beam	(K)	2.70

Contour levels for U6962

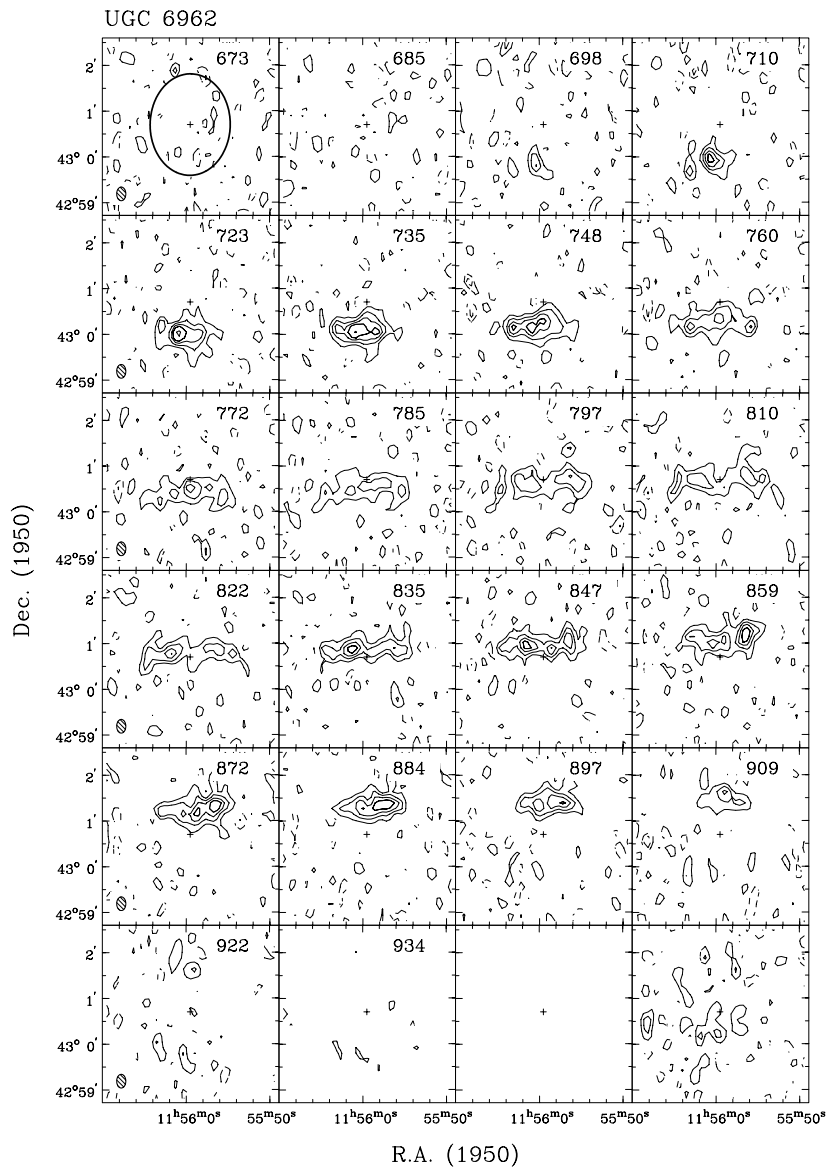
Channel maps:	$\sigma = 2.03$ (K)
Raw continuum map:	$\sigma = 1.31$ (K)
Cleaned continuum map:	$\sigma = 1.11$ (K)
Position-Velocity diagrams:	$\sigma = 1.69$ (K)
Velocity fields:	$810.1 \pm n \times 20$ (km s^{-1})
Residual velocity field:	$\pm n \times 5$ (km s^{-1})
Integrated HI map:	0.44, 0.88, $1.33 (\times 10^{21} \text{ atoms cm}^{-2})$

Results from WSRT data

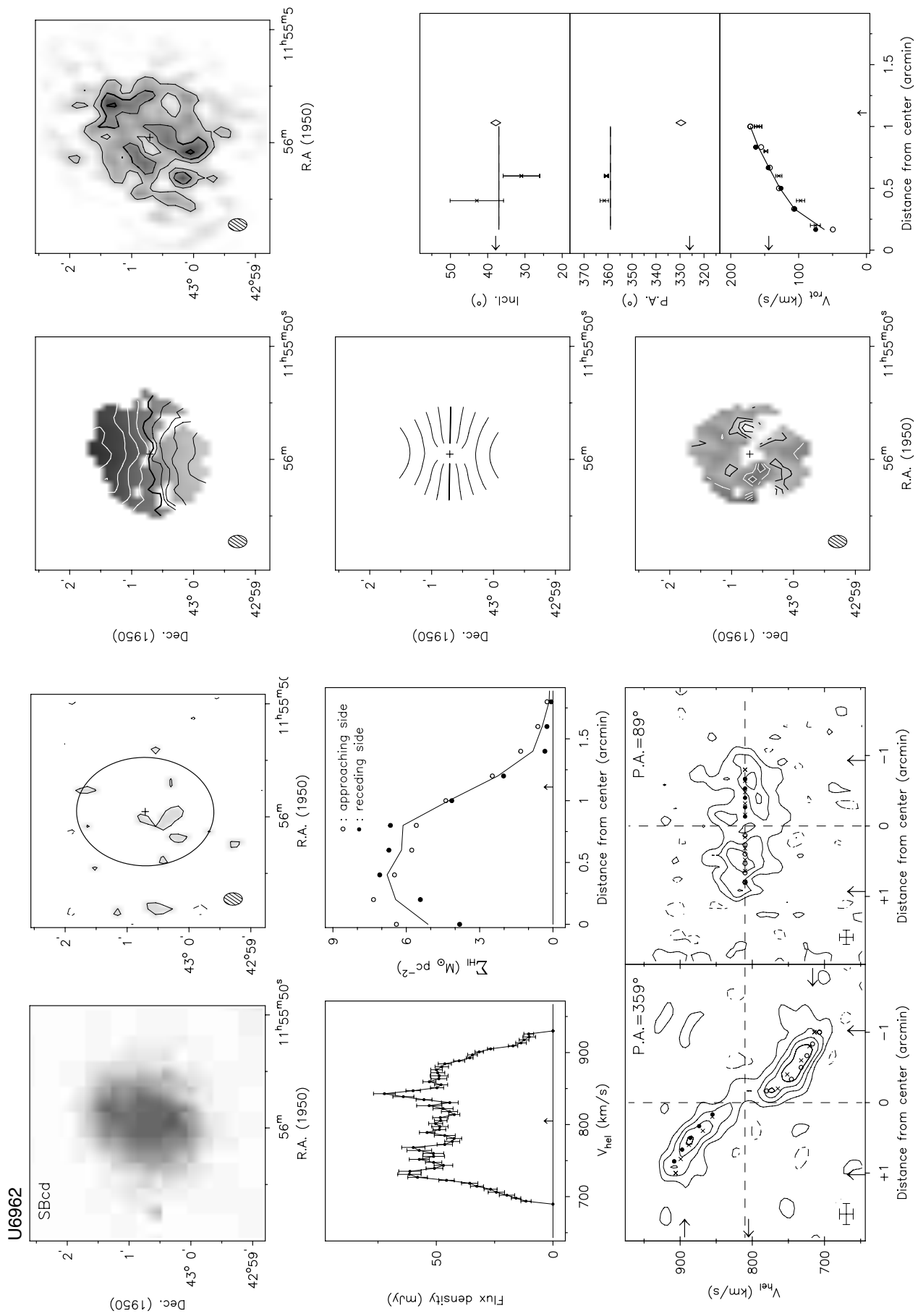
<i>From continuum map:</i>	
21-cm flux density	(mJy)
13.4 \pm 1.7	
<i>From global profile:</i>	
Integrated HI-flux	(Jy km s^{-1})
10.0 \pm 0.3	
Hel. systemic velocity	(km s^{-1})
807.4 \pm 3.2	
HI profile width, 20%	(km s^{-1})
220.3 \pm 6.6	
50%	(km s^{-1})
182.4 \pm 3.7	
<i>From velocity field:</i>	
Hel. systemic velocity	(km s^{-1})
810.1 \pm 2.6	
Dynamical center, $\alpha(1950)$	
11:55:59.5	
$\delta(1950)$	
43:00:42	
<i>From total HI map:</i>	
Geometric center, $\alpha(1950)$	
11:55:59.3	
$\delta(1950)$	
43:00:40	
Position angle	(deg)
329	
Inclination angle	(deg)
38	
Diameter of HI disk	(arcmin)
2.8	

Note: This galaxy is slightly interacting with U6973, only 3.5 arcmin to the ESE. The kinematic major axis is at an angle of roughly 35 degrees with respect to the major axis of the optical image (see chapter 1) and the HI map. This could be a sign of ongoing tidal interaction with U6973 which may result in a severe warp. The derived ‘rotation curve’ for U6962 is most likely affected by strong non-circular motion and should therefore not be taken at face value.

The detected continuum emission comes from a low level extended region.



Channel maps at a resolution of $12'' \times 18'' \times 19 \text{ km s}^{-1}$.
Contour levels at $-3, -1.5, 1.5, 3, 4.5, \dots \times \sigma$.



Observing parameters for NGC 4010

Length of observation	(hours)	1×12
Date of observation		21 Aug 93
Field center, α (1950)		11:56:03
δ (1950)		47:32:20
Central frequency	(MHz)	1416.11
V_{hel} of central channel	(km s $^{-1}$)	907
Primary beam FWHM	(arcmin)	37.4
Nr. of interferometers		40
Baselines (min-max-incr)	(m)	36-2700-72
Synthesized beam ($\alpha \times \delta$)	(arcsec)	12.5 \times 17.0
Bandwidth	(MHz)	2.5
Number of channels		127
Channel separation	(km s $^{-1}$)	4.15
Velocity resolution	(km s $^{-1}$)	8.29
rms noise in one channel	(K)	5.52
K-mJy conversion, equiv. of 1 mJy/beam	(K)	2.83

Results from WSRT data

From continuum map:

21-cm flux density	(mJy)	16.9 ± 1.6
Point source position, α (1950)		11:56:01.6

 δ (1950) 47:32:14*From global profile:*

Integrated HI-flux	(Jy km s $^{-1}$)	38.2 ± 0.3
Hel. systemic velocity	(km s $^{-1}$)	901.9 ± 0.8
HI profile width, 20% (km s $^{-1}$)		277.7 ± 1.0

50% (km s $^{-1}$) 264.1 ± 1.2 *From velocity field:*

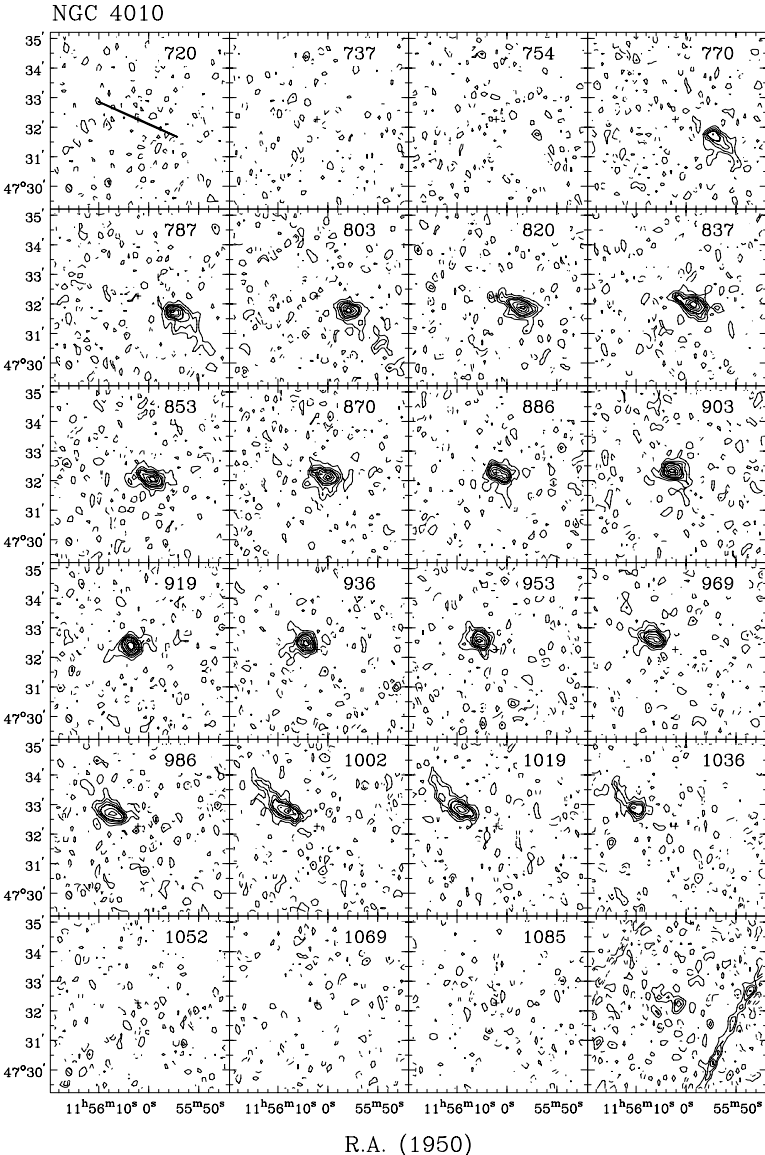
Hel. systemic velocity	(km s $^{-1}$)	899.4 ± 1.0
Dynamical center, α (1950)		11:56:02.1

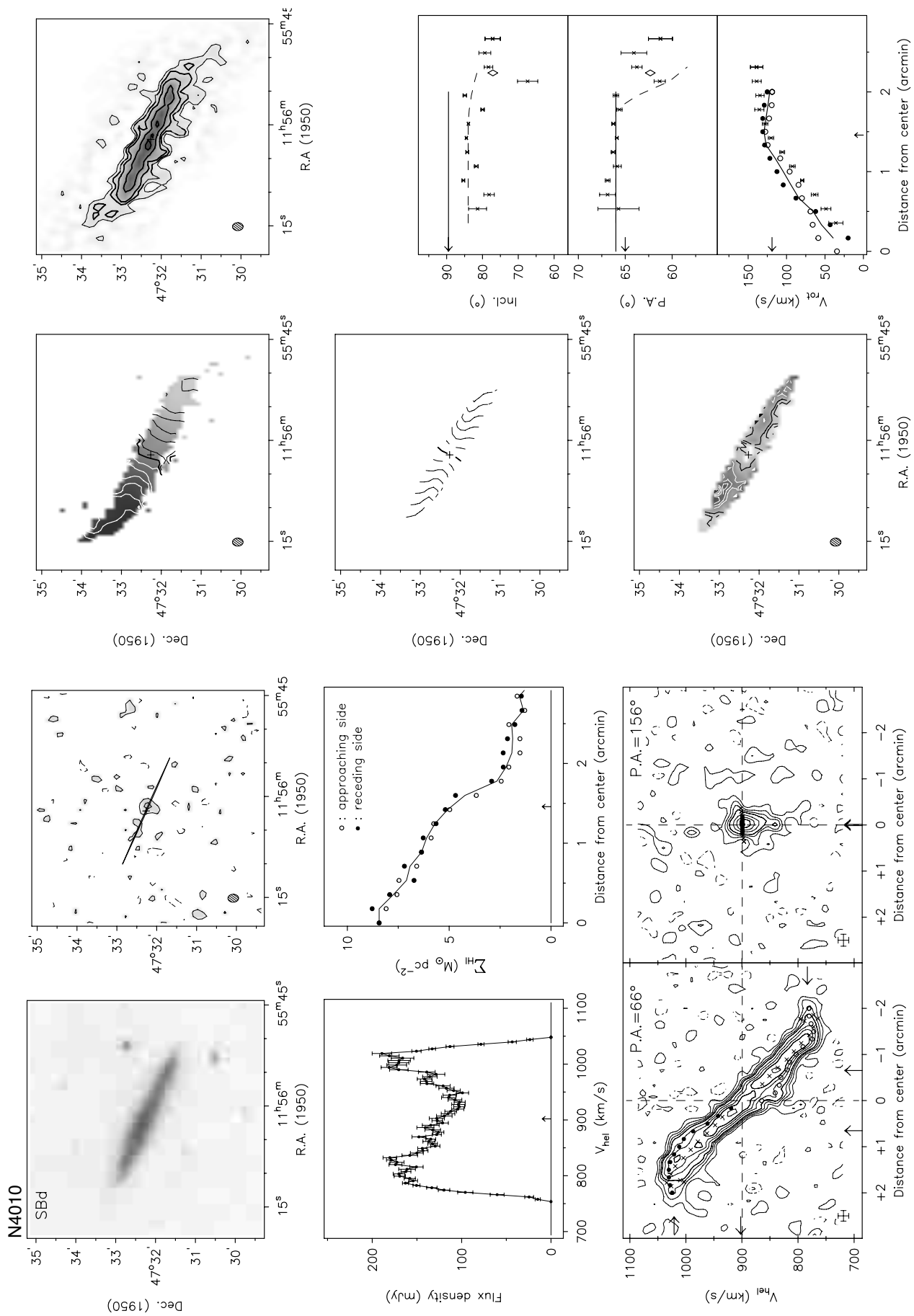
 δ (1950) 47:32:16*From total HI map:*

Geometric center, α (1950)		11:56:02.1
δ (1950)		47:32:16
Position angle	(deg)	62
Inclination angle	(deg)	77
Diameter of HI disk	(arcmin)	6.7

Contour levels for N4010

Channel maps:	$\sigma = 3.68$ (K)
Raw continuum map:	$\sigma = 1.52$ (K)
Cleaned continuum map:	$\sigma = 1.44$ (K)
Position-Velocity diagrams:	$\sigma = 3.19$ (K)
Velocity fields:	$899.4 \pm n \times 20$ (km s $^{-1}$)
Residual velocity field:	$\pm n \times 5$ (km s $^{-1}$)
Integrated HI map:	0.62, 1.24, 1.87, 2.49 3.11×10^{21} atoms cm $^{-2}$

Channel maps at a resolution of $12'' \times 17'' \times 19$ km s $^{-1}$.Contour levels at $-3, -1.5$ (dashed), $1.5, 3, 4.5, \dots \times \sigma$.



Observing parameters for UGC 6969

Length of observation	(hours)	1×12
Date of observation		23Dec94
Field center, α (1950)		11:55:07
δ (1950)		53:31:54
Central frequency	(MHz)	1415.53
V_{hel} of central channel	(km s $^{-1}$)	1054
Primary beam FWHM	(arcmin)	37.4
Nr. of interferometers		40
Baselines (min-max-incr)	(m)	36-2700-72
Synthesized beam ($\alpha \times \delta$)	(arcsec)	12.1×15.1
Bandwidth	(MHz)	5.0
Number of channels		127
Channel separation	(km s $^{-1}$)	8.31
Velocity resolution	(km s $^{-1}$)	9.97
rms noise in one channel	(K)	9.71
K-mJy conversion, equiv. of 1mJy/beam	(K)	3.29

Note: To achieve a sufficient velocity resolution over a 5 MHz bandwidth, only the XX dipoles could be correlated due to limitations of the backend.

Results from WSRT data

From continuum map:

21-cm flux density	
central point source (mJy)	<1.3 (3σ)
extended source (mJy)	<3.8 (3σ)

From global profile:

Integrated HI-flux (Jy km s $^{-1}$)	6.1 ± 0.5
Hel. systemic velocity (km s $^{-1}$)	1118.5 ± 2.4
HI profile width, 20% (km s $^{-1}$)	132.1 ± 6.4
50% (km s $^{-1}$)	123.5 ± 2.9

From velocity field:

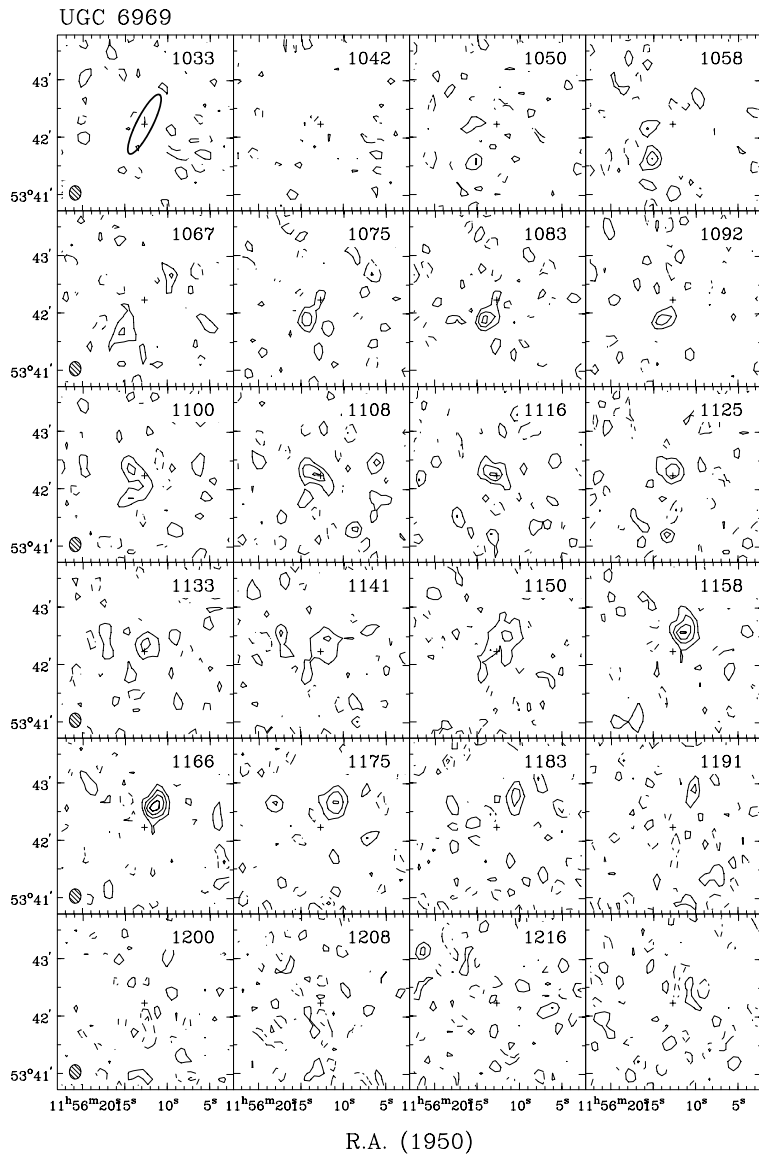
Hel. systemic velocity (km s $^{-1}$)	1117.6 ± 1.2
--	------------------

From total HI map:

Geometric center, α (1950)	11:56:12.7
δ (1950)	53:42:15
Position angle (deg)	327
Inclination angle (deg)	76
Diameter of HI disk (arcmin)	1.9

Contour levels for U6969

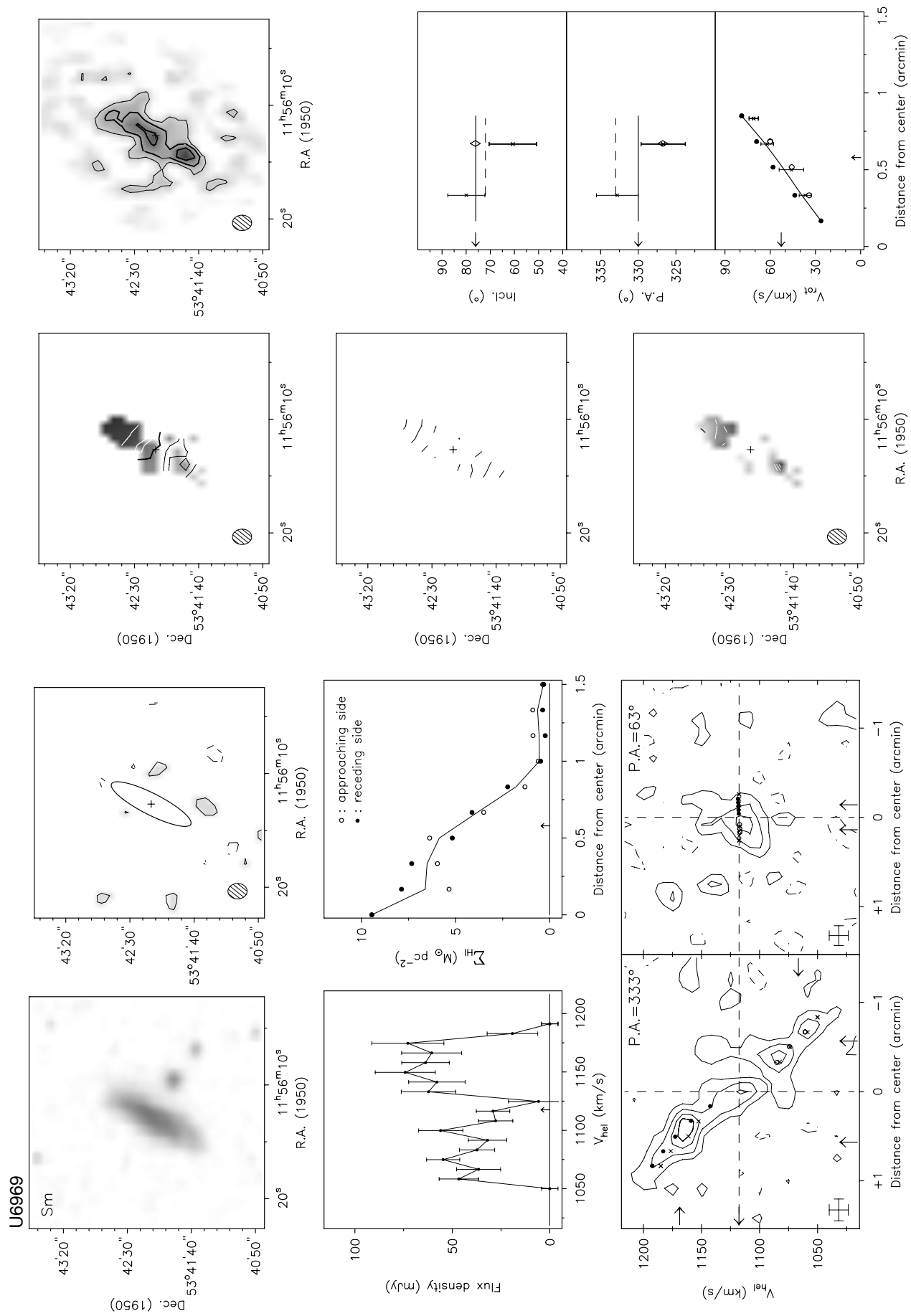
Channel maps:	$\sigma=5.93$ (K)
Raw continuum map:	$\sigma=1.45$ (K)
Cleaned continuum map:	$\sigma=1.42$ (K)
Position-Velocity diagrams:	$\sigma=5.26$ (K)
Velocity fields:	$1117.6 \pm n \times 15$ (km s $^{-1}$)
Residual velocity field:	$\pm n \times 5$ (km s $^{-1}$)
Integrated HI map:	0.98, 1.97, $2.95 (\times 10^{21} \text{ atoms cm}^{-2})$



Channel maps at a resolution of $12'' \times 15'' \times 17$ km s $^{-1}$.

Contour levels at $-3, -1.5$ (dashed), $1.5, 3, 4.5, \dots \times \sigma$.

Note: This dwarf galaxy is a companion of NGC 3992. The HI rotation curve shows only solid body rotation. Therefore, the dynamical center and inclination angle were adopted from the optical image.



Observing parameters for UGC 6973

Length of observation	(hours)	5×12
Dates of observation		17Aug90
		11Aug92, 24Jul93 and 2,8,13Mar94
Field center, α (1950)		11:56:20
δ (1950)		42:56:00
Central frequency	(MHz)	1416.79
V_{hel} of central channel	(km s $^{-1}$)	760
Primary beam FWHM	(arcmin)	37.4
Nr. of interferometers		120
Baselines (min-max-incr)	(m)	36-2736-18
Synthesized beam ($\alpha \times \delta$)	(arcsec)	12.0 \times 18.8
Bandwidth	(MHz)	2.5
Number of channels		127
Channel separation	(km s $^{-1}$)	4.14
Velocity resolution	(km s $^{-1}$)	8.29
rms noise in one channel	(K)	2.84
K-mJy conversion, equiv. of 1mJy/beam	(K)	2.70

Contour levels for U6973

Channel maps:	$\sigma = 2.03$ (K)
Raw continuum map:	$\sigma = 1.31$ (K)
Cleaned continuum map:	$\sigma = 1.11$ (K)
Position-Velocity diagrams:	$\sigma = 1.76$ (K)
Velocity fields:	$701.4 \pm n \times 25$ (km s $^{-1}$)
Residual velocity field:	$\pm n \times 5$ (km s $^{-1}$)
Integrated HI map:	0.83, 1.67, $2.78 (\times 10^{21} \text{ atoms cm}^{-2})$

Results from WSRT data

From continuum map:

21-cm flux density	(mJy)	127.5 ± 2.1
Central point source position		
α (1950)		11:56:17.7
δ (1950)		43:00:02

From global profile:

Integrated HI-flux	(Jy km s $^{-1}$)	22.9 ± 0.2
Hel. systemic velocity	(km s $^{-1}$)	700.5 ± 1.0
HI profile width, 20%	(km s $^{-1}$)	367.8 ± 1.8
50%	(km s $^{-1}$)	350.4 ± 1.2

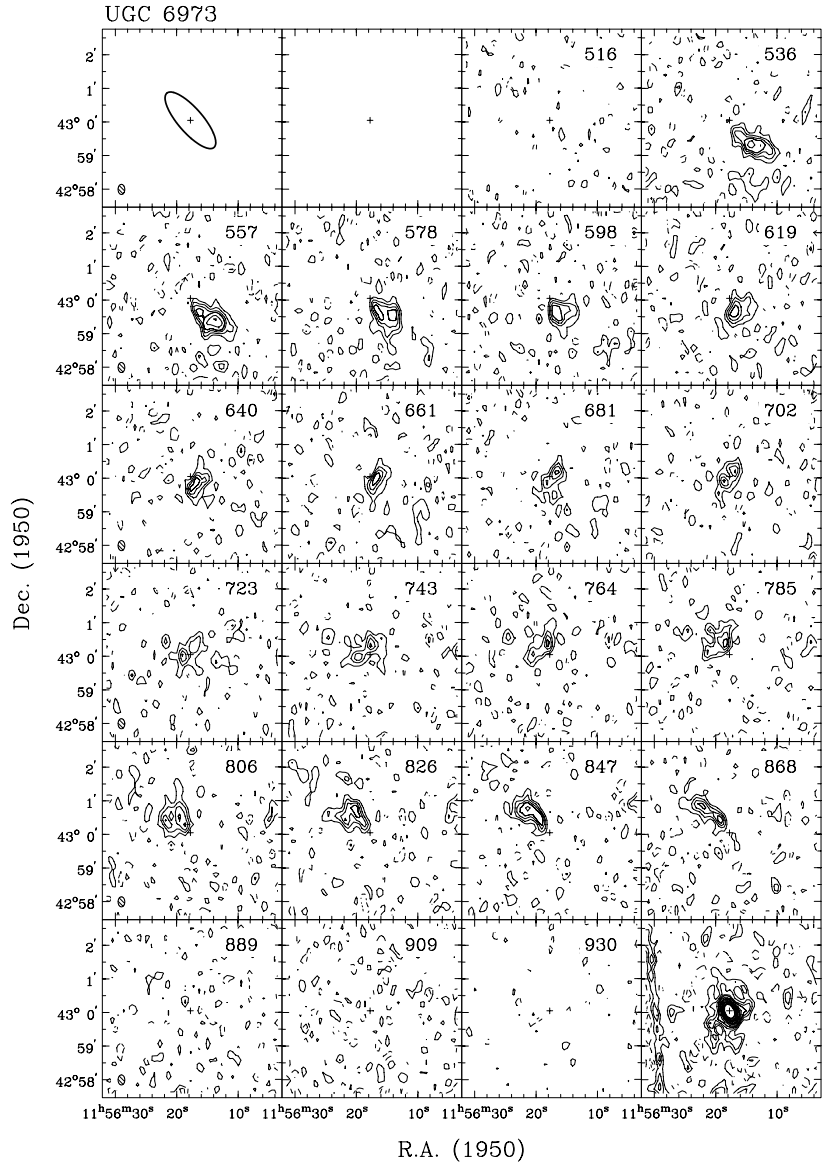
From velocity field:

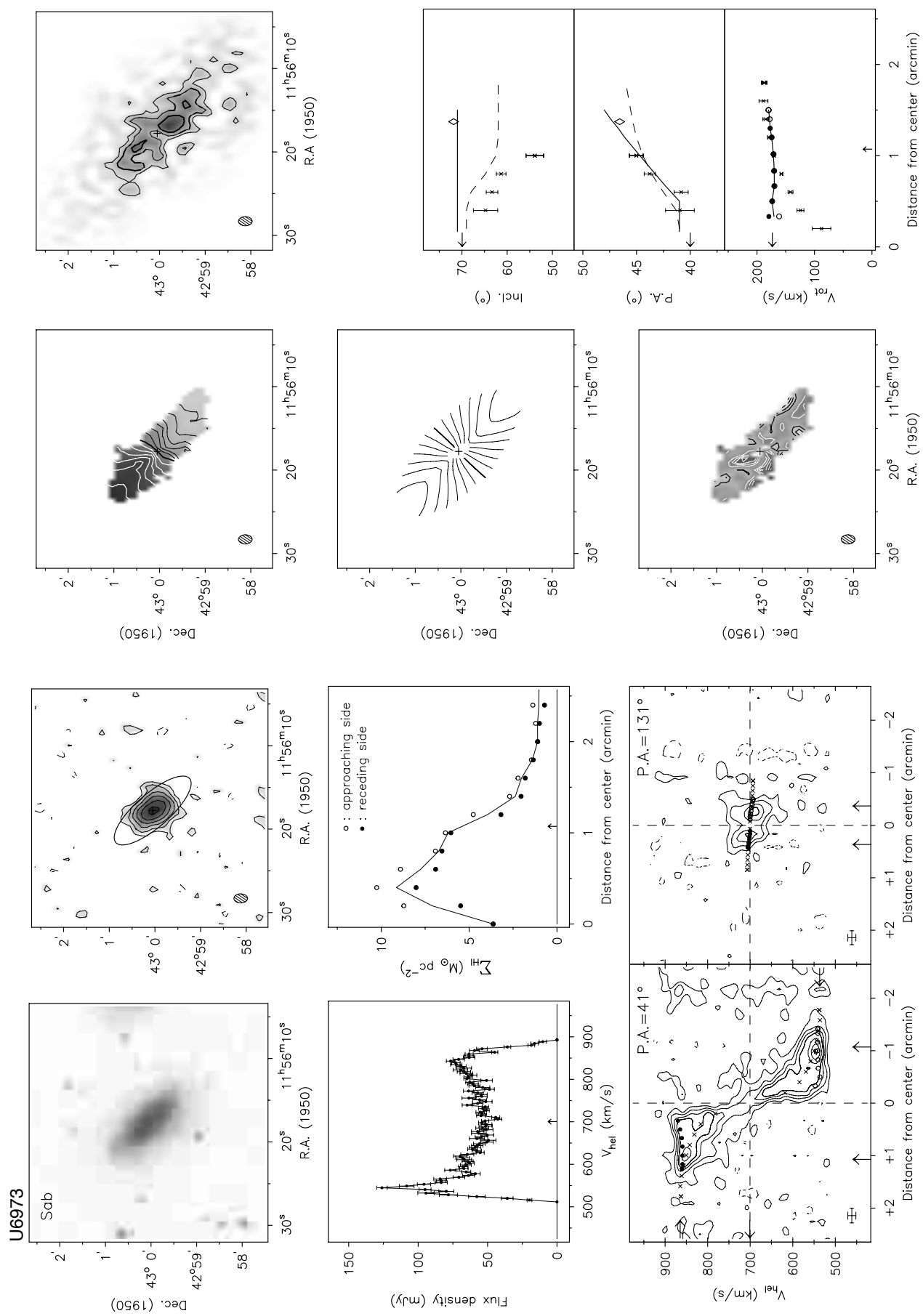
Hel. systemic velocity	(km s $^{-1}$)	701.4 ± 2.3
Dynamical center, α (1950)		11:56:17.8
δ (1950)		43:00:03

From total HI map:

Geometric center, α (1950)		11:56:17.2
δ (1950)		42:59:58
Position angle	(deg)	47
Inclination angle	(deg)	72
Diameter of HI disk	(arcmin)	4.4

Note: This galaxy is slightly interacting with U6962, only 3.5 arcmin to the WNW. The HI disk is somewhat warped and some very faint tidal debris can be seen in the channel maps. Due to severe beam smearing, the observed velocity field and the rotation curve derived from it are of limited use. The optical image, showing a bright red and dusty inner part, and the strong extended continuum emission suggest vigorous star formation in the central regions.

Channel maps at a resolution of $12'' \times 18'' \times 19 \text{ km s}^{-1}$.Contour levels at $-3, -1.5$ (dashed), $1.5, 3, 4.5, \dots \times \sigma$.



Observing parameters for UGC 6983

Length of observation	(hours)	2×12
Dates of observation		09Jan94
Field center, α (1950)		11:56:34
δ (1950)		52:59:08
Central frequency	(MHz)	1415.28
V_{hel} of central channel	(km s^{-1})	1100
Primary beam FWHM	(arcmin)	37.4
Nr. of interferometers		80
Baselines (min-max-incr) (m)		36-2718-18/54
Synthesized beam ($\alpha \times \delta$) (arcsec)		12.2×15.3
Bandwidth	(MHz)	2.5
Number of channels		127
Channel separation	(km s^{-1})	4.16
Velocity resolution	(km s^{-1})	4.99
rms noise in one channel	(K)	7.09
K-mJy conversion, equiv. of 1mJy/beam	(K)	3.22

Results from WSRT data

From continuum map:

21-cm flux density	
central point source (mJy)	<0.9 (3σ)
extended source (mJy)	<5.4 (3σ)

From global profile:

Integrated HI-flux	(Jy km s^{-1})	38.5 ± 0.6
Hel. systemic velocity	(km s^{-1})	1081.9 ± 0.8
HI profile width, 20% (km s^{-1})		188.4 ± 1.3
50% (km s^{-1})		173.0 ± 1.1

From velocity field:

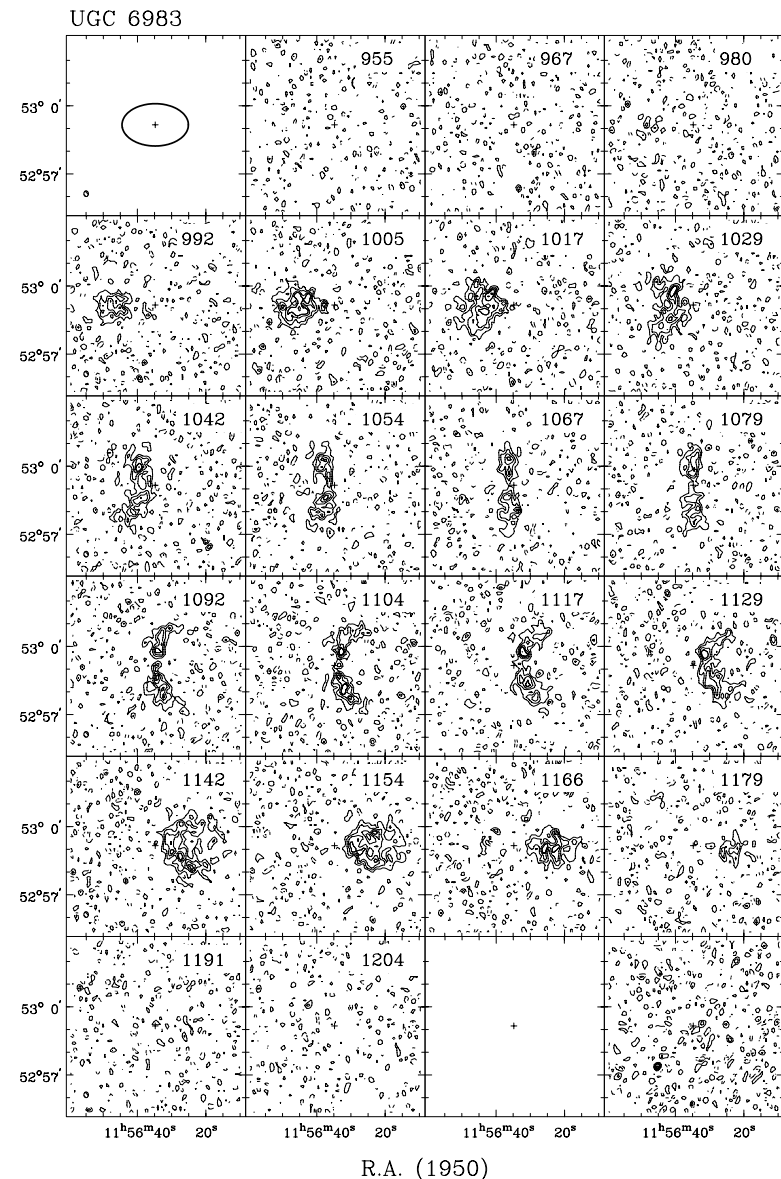
Hel. systemic velocity	(km s^{-1})	1082.1 ± 0.4
Dynamical center, α (1950)		11:56:34.7
δ (1950)		52:59:10

From total HI map:

Geometric center, α (1950)		11:56:35.4
δ (1950)		52:59:07
Position angle	(deg)	276
Inclination angle	(deg)	46
Diameter of HI disk	(arcmin)	6.1

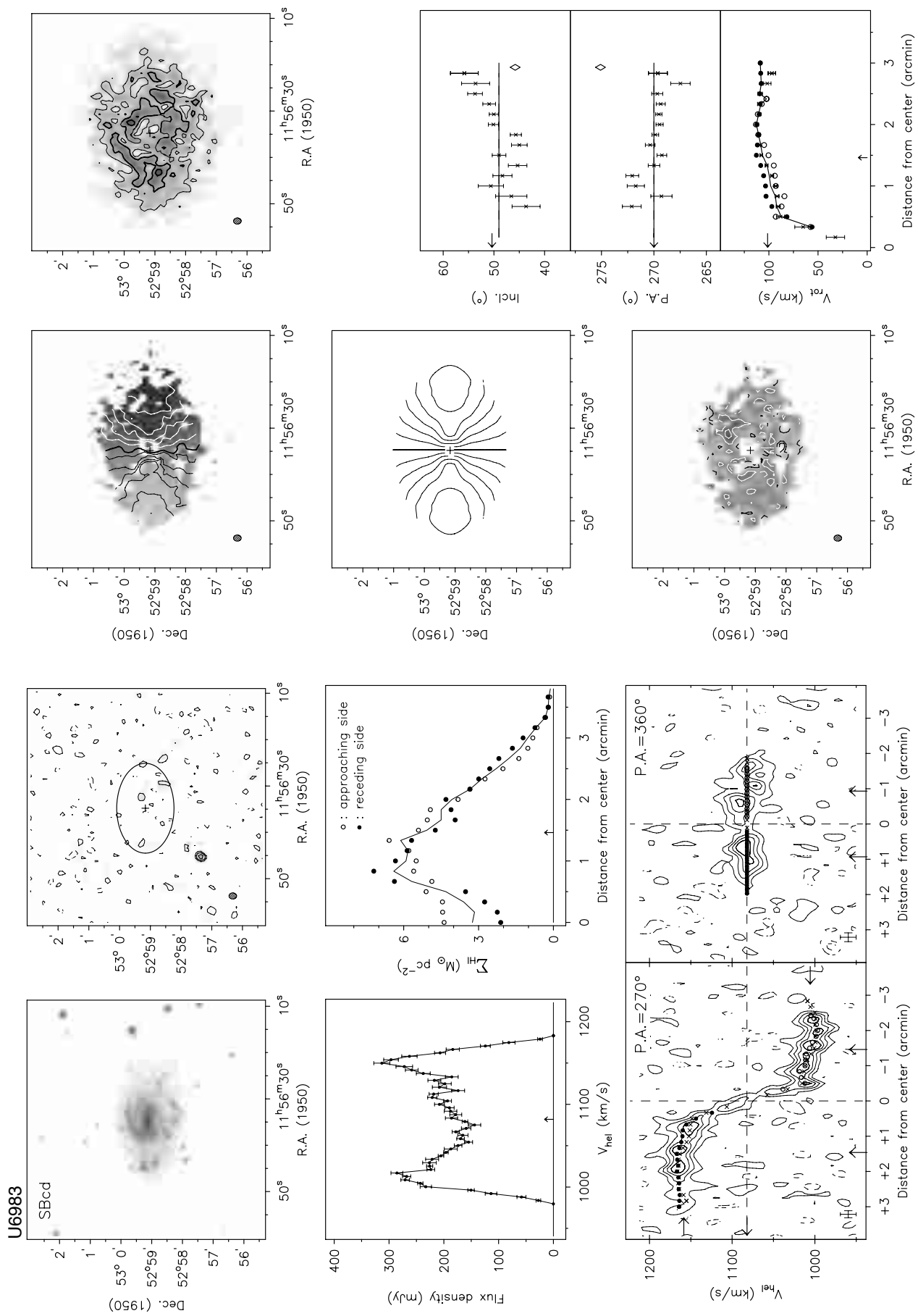
Contour levels for U6983

Channel maps:	$\sigma = 2.90$ (K)
Raw continuum map:	$\sigma = 1.05$ (K)
Cleaned continuum map:	$\sigma = 1.00$ (K)
Position-Velocity diagrams:	$\sigma = 2.50$ (K)
Velocity fields:	$1082.1 \pm n \times 15$ (km s^{-1})
Residual velocity field:	$\pm n \times 5$ (km s^{-1})
Integrated HI map:	0.52, 1.05, $1.57 (\times 10^{21} \text{ atoms cm}^{-2})$



Note: UGC 6983 is a beautiful, regular, low surface brightness galaxy with well defined spiral arms and a small bar.

Channel maps at a resolution of $12'' \times 15'' \times 19 \text{ km s}^{-1}$.
Contour levels at $-3, -1.5, 1.5, 3, 4.5, \dots \times \sigma$.



Observing parameters for NGC 4051

Length of observation	(hours)	1×12
Date of observation		01Feb94
Field center, α (1950)		12:00:36
δ (1950)		44:48:48
Central frequency	(MHz)	1417.09
V_{hel} of central channel	(km s $^{-1}$)	720
Primary beam FWHM	(arcmin)	37.4
Nr. of interferometers		40
Baselines (min-max-incr)	(m)	36-2700-72
Synthesized beam ($\alpha \times \delta$)	(arcsec)	10.5 \times 15.1
Bandwidth	(MHz)	2.5
Number of channels		127
Channel separation	(km s $^{-1}$)	4.14
Velocity resolution	(km s $^{-1}$)	4.96
rms noise in one channel	(K)	13.3
K-mJy conversion, equiv. of 1mJy/beam	(K)	3.80

Contour levels for N4051

Channel maps:	$\sigma = 1.37$ (K)
Raw continuum map:	$\sigma = 0.82$ (K)
Cleaned continuum map:	$\sigma = 0.63$ (K)
Position-Velocity diagrams:	$\sigma = 1.29$ (K)
Velocity fields:	$704.5 \pm n \times 20$ (km s $^{-1}$)
Residual velocity field:	$\pm n \times 5$ (km s $^{-1}$)
Integrated HI map:	0.56, 1.11, $1.67 (\times 10^{21} \text{ atoms cm}^{-2})$

Results from WSRT data

From continuum map:

21-cm flux density	(mJy)	26.5 ± 2.6
Central point source position		
α (1950)		12:00:36.3
δ (1950)		44:48:35

From global profile:

Integrated HI-flux	(Jy km s $^{-1}$)	35.6 ± 0.8
Hel. systemic velocity	(km s $^{-1}$)	700.3 ± 1.2
HI profile width, 20%	(km s $^{-1}$)	255.4 ± 1.8

50% (km s $^{-1}$)From velocity field:

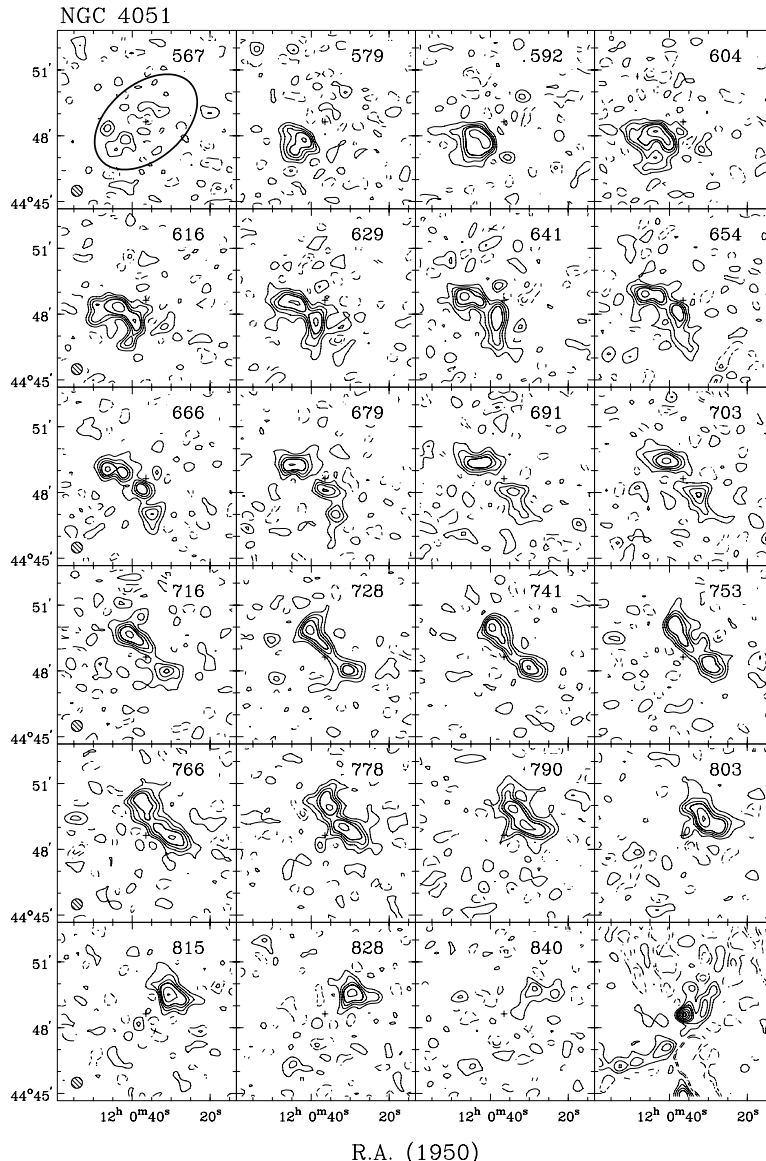
Hel. systemic velocity	(km s $^{-1}$)	704.5 ± 1.2
Dynamical center, α (1950)		12:00:36.6

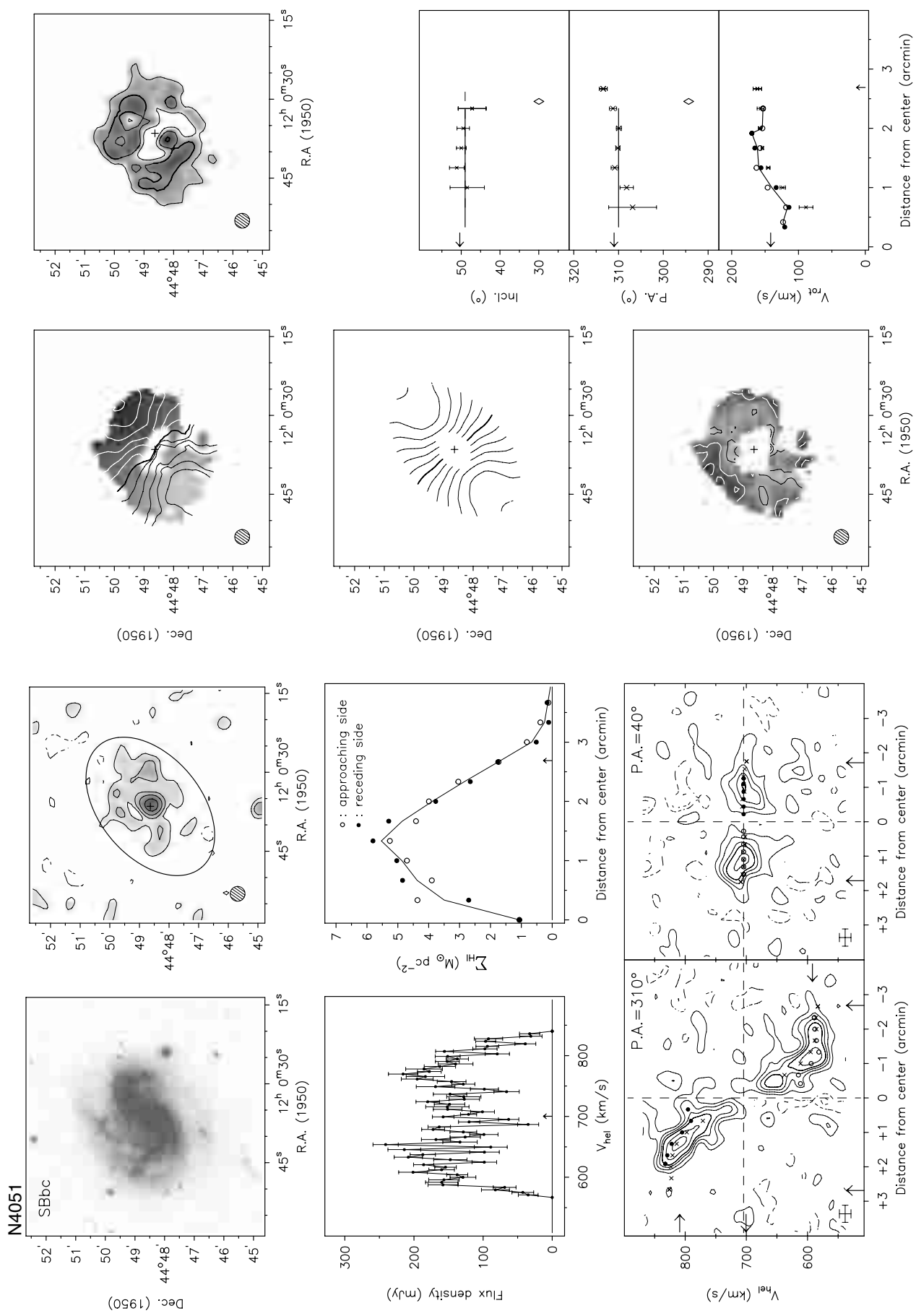
 δ (1950) 44:48:38From total HI map:

Geometric center, α (1950)		12:00:37.6
δ (1950)		44:48:42
Position angle	(deg)	294
Inclination angle	(deg)	30
Diameter of HI disk	(arcmin)	5.8

Note: This Seyfert galaxy is lopsided and has a central bar. The rotation curve is quite asymmetric as can be seen in the position-velocity diagrams. The position and inclinations angles derived from the velocity field are quite similar for the various rings and close to the values derived from the optical image. The upturn of the rotation curve in the inner part is uncertain but it is suggested by both the receding and approaching side.

The kinematic major axis seems to be somewhat bend and the iso-velocity contours in the observed velocity field are more separated in the north-eastern than in the south-western region. This suggests that non-circular motions are present in this system.

Channel maps at a resolution of $30'' \times 30'' \times 19 \text{ km s}^{-1}$.Contour levels at $-3, -1.5$ (dashed), $1.5, 3, 4.5, \dots \times \sigma$.



Observing parameters for NGC 4085

Length of observation	(hours)	1×12
Date of observation		13Jan94
Field center, α (1950)		12:02:57
δ (1950)		50:43:30
Central frequency	(MHz)	1416.69
V_{hel} of central channel	(km s $^{-1}$)	800
Primary beam FWHM	(arcmin)	37.4
Nr. of interferometers		40
Baselines (min-max-incr)	(m)	36-2700-72
Synthesized beam ($\alpha \times \delta$)	(arcsec)	12.0 \times 15.7
Bandwidth	(MHz)	5.0
Number of channels		63
Channel separation	(km s $^{-1}$)	16.5
Velocity resolution	(km s $^{-1}$)	19.8
rms noise in one channel	(K)	4.80
K-mJy conversion, equiv. of 1mJy/beam	(K)	3.20

Contour levels for N4085

Channel maps:	$\sigma = 4.64$ (K)
Raw continuum map:	$\sigma = 1.14$ (K)
Cleaned continuum map:	$\sigma = 1.06$ (K)
Position-Velocity diagrams:	$\sigma = 4.16$ (K)
Velocity fields:	$752.0 \pm n \times 20$ (km s $^{-1}$)
Residual velocity field:	$\pm n \times 5$ (km s $^{-1}$)
Integrated HI map:	1.77, 3.54 ($\times 10^{21}$ atoms cm $^{-2}$)

Results from WSRT data

From continuum map:

21-cm flux density	(mJy)	44.1 ± 1.3
Central point source position		
α (1950)		12:02:50.2
δ (1950)		50:37:54

From global profile:

Integrated HI-flux	(Jy km s $^{-1}$)	14.6 ± 0.9
Hel. systemic velocity	(km s $^{-1}$)	745.7 ± 5.0
HI profile width, 20%	(km s $^{-1}$)	277.4 ± 6.6
50%	(km s $^{-1}$)	255.4 ± 7.8

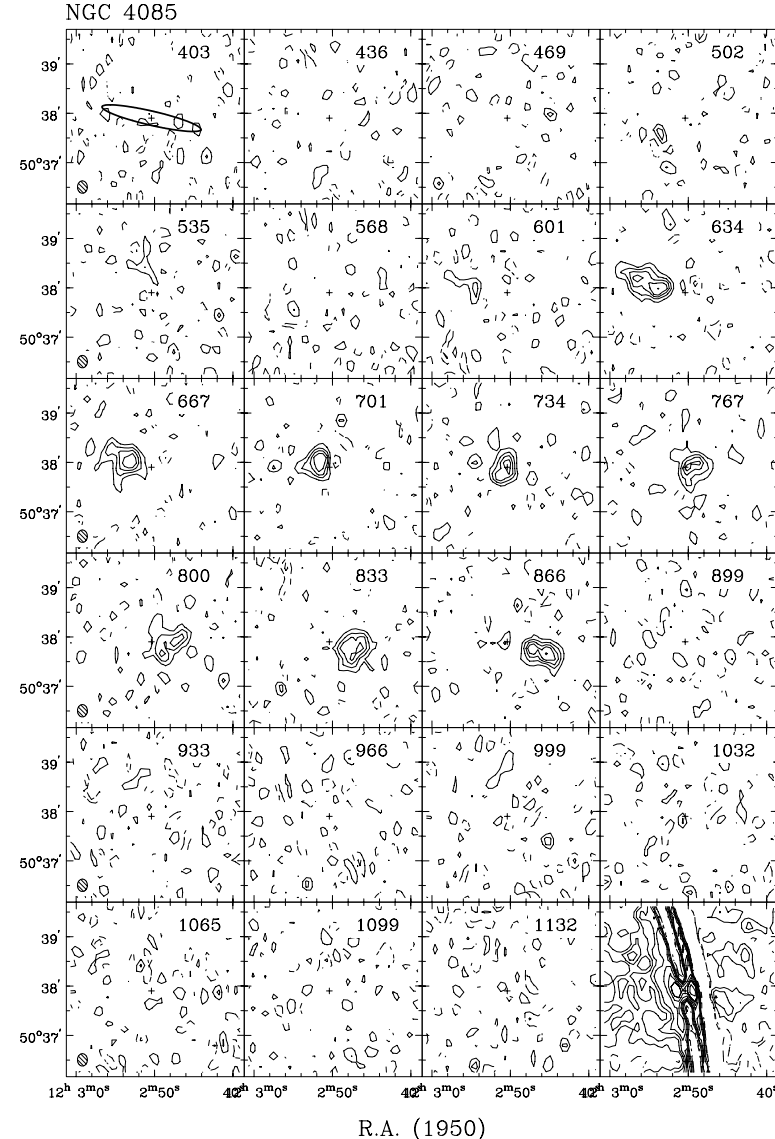
From velocity field:

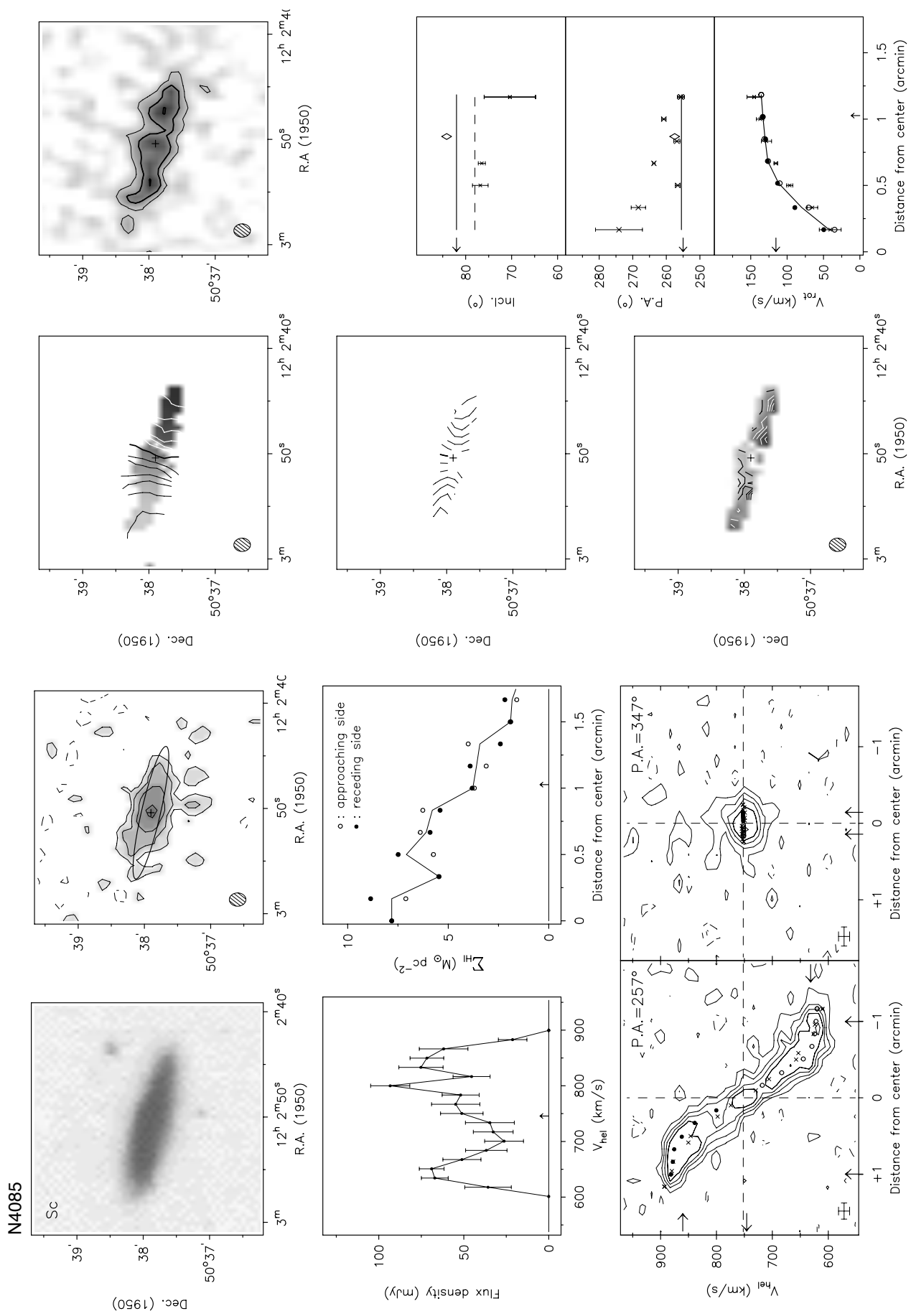
Hel. systemic velocity	(km s $^{-1}$)	752.0 ± 2.2
Dynamical center, α (1950)		12:02:50.3
δ (1950)		50:37:54

From total HI map:

Geometric center, α (1950)		12:02:50.8
δ (1950)		50:37:56
Position angle	(deg)	256
Inclination angle	(deg)	83
Diameter of HI disk	(arcmin)	3.9

Note: This galaxy is a companion of the strongly disturbed system NGC 4088 at 10 arcmin to the north. The HI disk does not extend much beyond D₂₅. The extent of the radial HI density profile is due to the high inclination of the ellipses along which the column density is measured and the effect of beam smearing along the minor axis.

Channel maps at a resolution of $12'' \times 15'' \times 20$ km s $^{-1}$.Contour levels at $-3, -1.5, 1.5, 3, 4.5, \dots \times \sigma$.



Observing parameters for NGC 4088

Length of observation	(hours)	1×12
Date of observation		13Jan94
Field center, α (1950)		12:02:57
δ (1950)		50:43:30
Central frequency	(MHz)	1416.69
V_{hel} of central channel	(km s $^{-1}$)	800
Primary beam FWHM	(arcmin)	37.4
Nr. of interferometers		40
Baselines (min-max-incr)	(m)	36-2700-72
Synthesized beam ($\alpha \times \delta$)	(arcsec)	12.0×15.7
Bandwidth	(MHz)	5.0
Number of channels		63
Channel separation	(km s $^{-1}$)	16.5
Velocity resolution	(km s $^{-1}$)	19.8
rms noise in one channel	(K)	4.80
K-mJy conversion, equiv. of 1mJy/beam	(K)	3.20

Contour levels for N4088

Channel maps:	$\sigma=1.21$ (K)
Raw continuum map:	$\sigma=0.33$ (K)
Cleaned continuum map:	$\sigma=0.29$ (K)
Position-Velocity diagrams:	$\sigma=1.19$ (K)
Velocity fields:	$761.5 \pm n \times 25$ (km s $^{-1}$)
Residual velocity field:	$\pm n \times 5$ (km s $^{-1}$)
Integrated HI map:	0.38, 0.75, 1.13, 1.51 $1.89 (\times 10^{21} \text{ atoms cm}^{-2})$

Results from WSRT data

From continuum map:

21-cm flux density	(mJy)	222.3 ± 1.9
Central point source position		
α (1950)		12:03:01.9
δ (1950)		50:49:04

From global profile:

Integrated HI-flux	(Jy km s $^{-1}$)	102.9 ± 1.1
Hel. systemic velocity	(km s $^{-1}$)	756.7 ± 1.2
HI profile width, 20%	(km s $^{-1}$)	371.4 ± 1.7
50%	(km s $^{-1}$)	342.1 ± 1.9

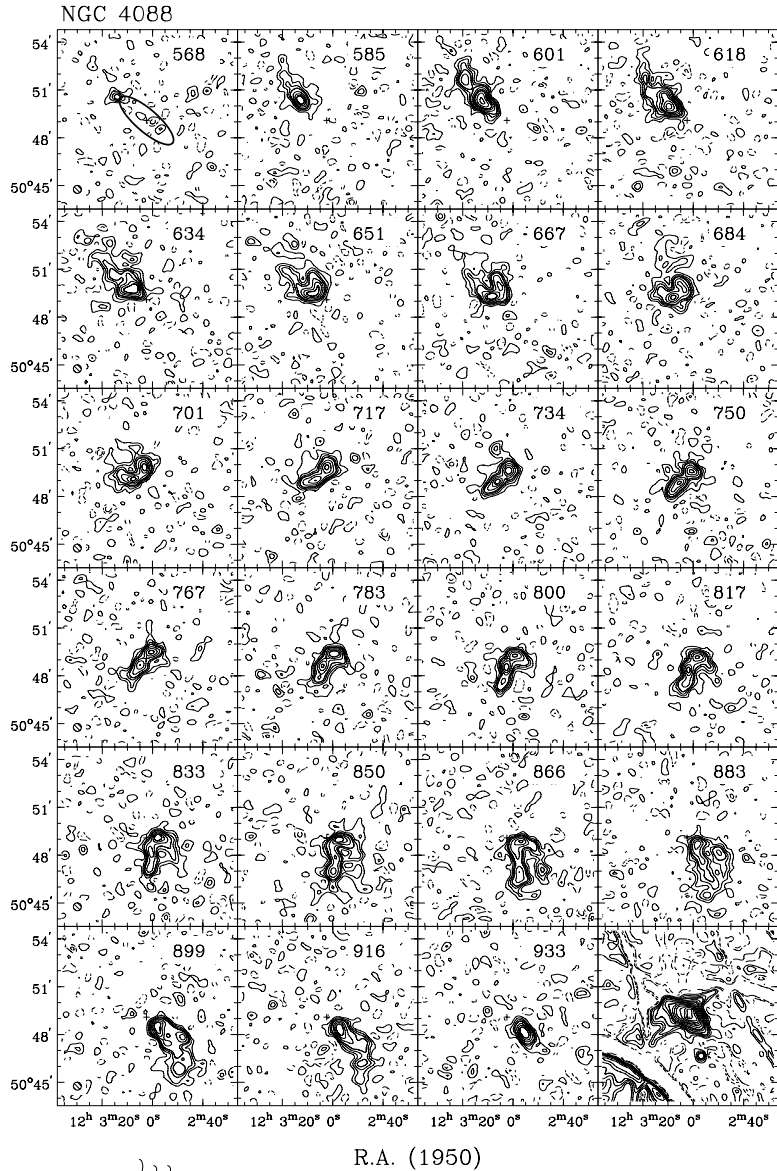
From velocity field:

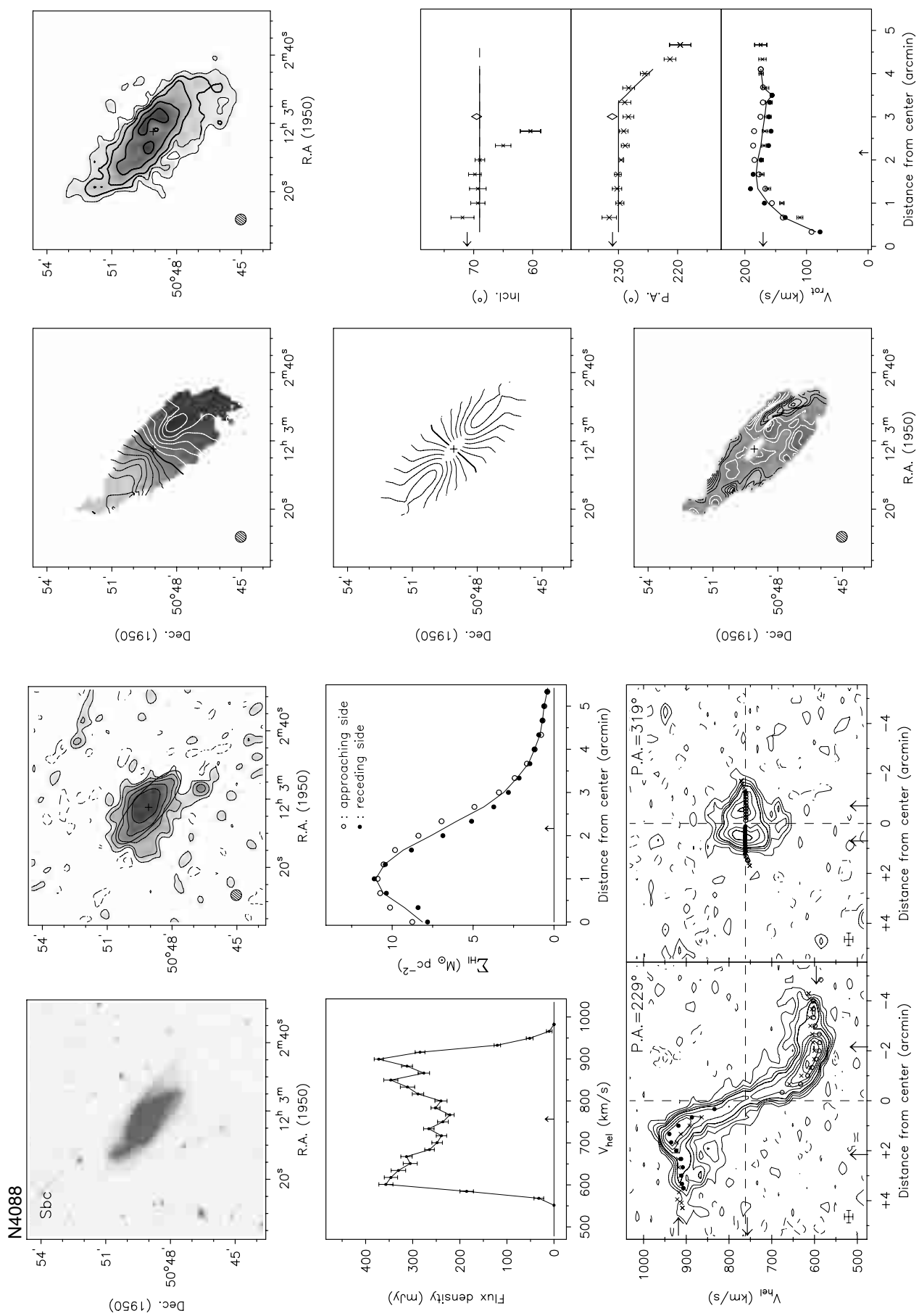
Hel. systemic velocity	(km s $^{-1}$)	761.5 ± 1.8
Dynamical center, α (1950)		12:03:02.4
δ (1950)		50:49:06

From total HI map:

Geometric center, α (1950)		12:03:03.6
δ (1950)		50:49:12
Position angle	(deg)	231
Inclination angle	(deg)	69
Diameter of HI disk	(arcmin)	8.5

Note: NGC 4088 is among the brightest systems in the cluster. It has a very high surface brightness and is very blue. The strong radio continuum emission and the 60 μ m flux suggest ongoing vigorous star formation. The disk is strongly distorted. The position-velocity diagram shows a strong asymmetry and comparison of the channel maps at 618 and 899 km s $^{-1}$ shows that the warp is asymmetric as well. The position angle changes more in the southern than in the northern part. The extended radio continuum emission seems to originate even outside the optical regions. NGC 4085 is located 10 arcmin to the south.

Channel maps at a resolution of 30'' × 30'' × 20 km s $^{-1}$.Contour levels at -3, -1.5 (dashed), 1.5, 3, 4.5, ... $\times \sigma$.



Observing parameters for NGC 4100

Length of observation	(hours)	1×12
Date of observation		06Jan94
Field center, α (1950)		12:03:36
δ (1950)		49:51:36
Central frequency	(MHz)	1415.20
V_{hel} of central channel	(km s $^{-1}$)	1120
Primary beam FWHM	(arcmin)	37.4
Nr. of interferometers		40
Baselines (min-max-incr)	(m)	36-2700-72
Synthesized beam ($\alpha \times \delta$)	(arcsec)	12.1×15.9
Bandwidth	(MHz)	5.0
Number of channels		63
Channel separation	(km s $^{-1}$)	16.61
Velocity resolution	(km s $^{-1}$)	19.93
rms noise in one channel	(K)	4.84
K-mJy conversion, equiv. of 1mJy/beam	(K)	3.13

Contour levels for N4100

Channel maps:	$\sigma = 1.24$ (K)
Raw continuum map:	$\sigma = 0.37$ (K)
Cleaned continuum map:	$\sigma = 0.30$ (K)
Position-Velocity diagrams:	$\sigma = 4.07$ (K)
Velocity fields:	$1071.2 \pm n \times 30$ (km s $^{-1}$)
Residual velocity field:	$\pm n \times 5$ (km s $^{-1}$)
Integrated HI map:	0.42, 0.84, $1.26 (\times 10^{21} \text{ atoms cm}^{-2})$

Results from WSRT data

From continuum map:

21-cm flux density	(mJy)	54.3 ± 1.7
Central point source position		
α (1950)		12:03:36.4
δ (1950)		49:51:40

From global profile:

Integrated HI-flux	(Jy km s $^{-1}$)	41.6 ± 0.7
Hel. systemic velocity	(km s $^{-1}$)	1074.4 ± 1.3
HI profile width, 20% (km s $^{-1}$)		401.8 ± 2.0
50% (km s $^{-1}$)		380.5 ± 1.8

From velocity field:

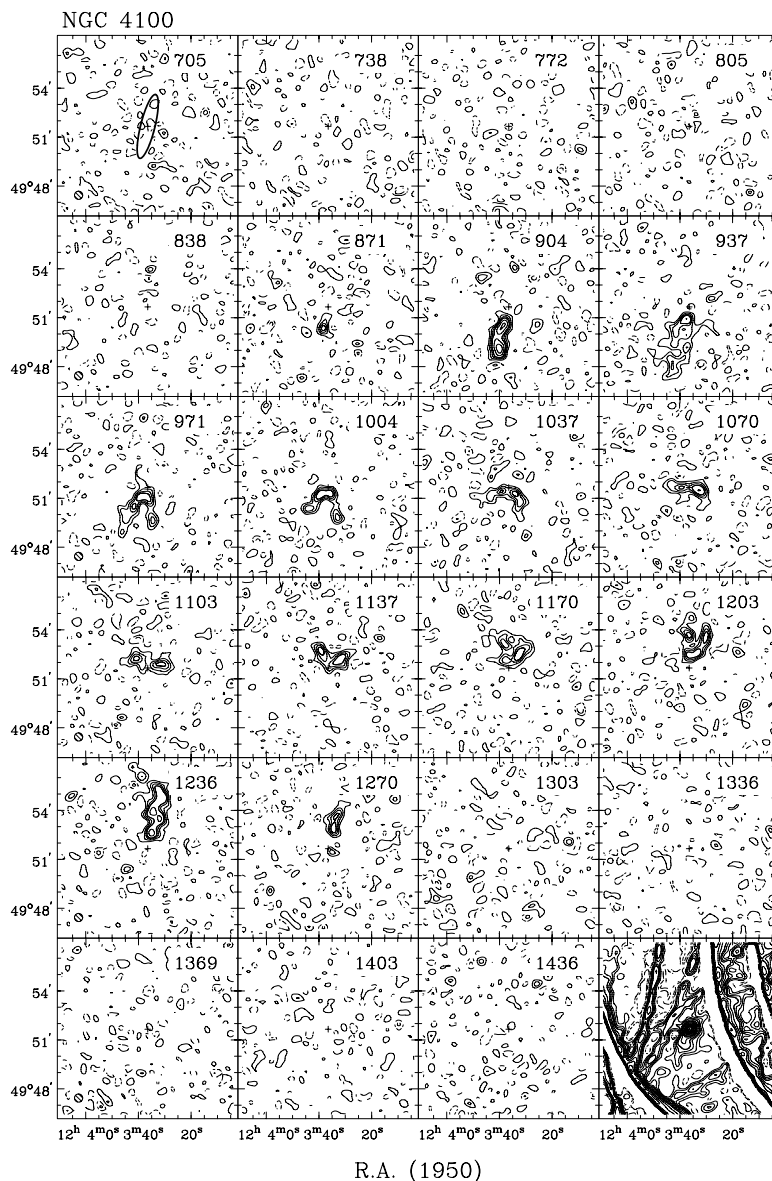
Hel. systemic velocity	(km s $^{-1}$)	1071.2 ± 0.9
Dynamical center, α (1950)		12:03:36.6
δ (1950)		49:51:40

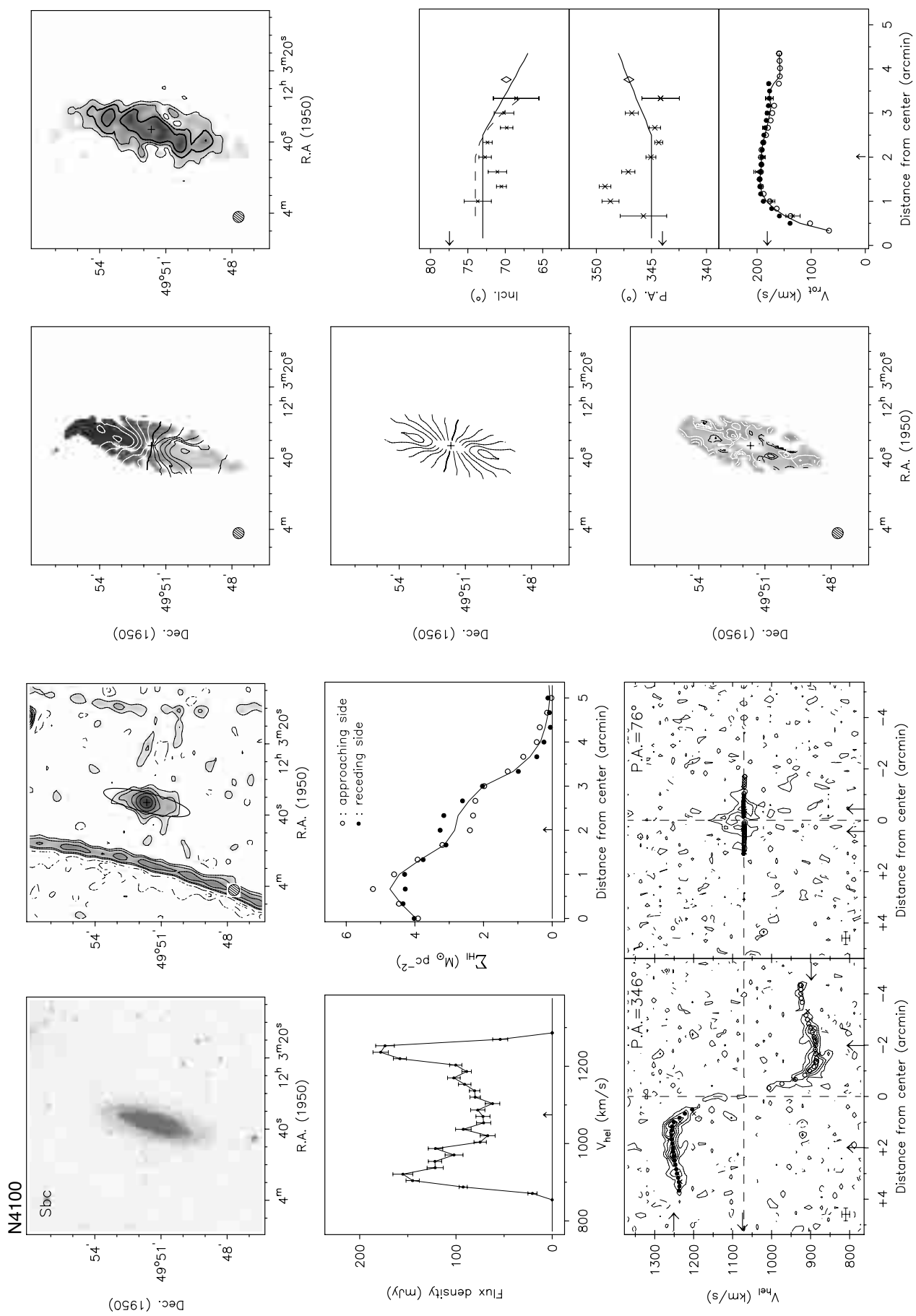
From total HI map:

Geometric center, α (1950)		12:03:36.5
δ (1950)		49:51:40
Position angle	(deg)	347
Inclination angle	(deg)	70
Diameter of HI disk	(arcmin)	6.9

Note: The optical appearance of this spiral suggests a mild warp toward face-on or a strong widening of the pitch-angle of the spiral arms in the outer regions. Also the HI distribution (see channel maps at 904 and 1236 km s $^{-1}$) indicates a warp. The decline of the rotation curve indicated by the position-velocity map is probably real. An unlikely inclination of 49 degrees would be required instead of the adopted 67 degrees to give a flat curve.

The position-velocity diagrams are presented at the highest spatial resolution. The other data are shown for a resolution of 30×30 arcsec.

Channel maps at a resolution of $30'' \times 30'' \times 20$ km s $^{-1}$.Contour levels at $-3, -1.5$ (dashed), $1.5, 3, 4.5, \dots \times \sigma$.



Observing parameters for NGC 4102

Length of observation	(hours)	4×12
Dates of observation		11Aug90
Field center, α (1950)		12:03:50
δ (1950)		53:02:00
Central frequency	(MHz)	1416.37
V_{hel} of central channel	(km s $^{-1}$)	850
Primary beam FWHM	(arcmin)	37.4
Nr. of interferometers		80
Baselines (min-max-incr)	(m)	36-2736-36
Synthesized beam ($\alpha \times \delta$)	(arcsec)	12.1 \times 15.1
Bandwidth	(MHz)	2.5
Number of channels		127
Channel separation	(km s $^{-1}$)	4.15
Velocity resolution	(km s $^{-1}$)	8.29
rms noise in one channel	(K)	3.30
K-mJy conversion, equiv. of 1mJy/beam	(K)	3.30

Contour levels for N4102

Channel maps:	$\sigma = 2.14$ (K)
Raw continuum map:	$\sigma = 1.25$ (K)
Cleaned continuum map:	$\sigma = 1.09$ (K)
Position-Velocity diagrams:	$\sigma = 1.99$ (K)
Velocity fields:	$845.4 \pm n \times 25$ (km s $^{-1}$)
Residual velocity field:	$\pm n \times 5$ (km s $^{-1}$)
Integrated HI map:	0.54, 1.09, $1.63 (\times 10^{21} \text{ atoms cm}^{-2})$

Results from WSRT data

From continuum map:

21-cm flux density	(mJy)	276.0 ± 1.5
Central point source position		
α (1950)		12:03:51.2
δ (1950)		52:59:21

From global profile:

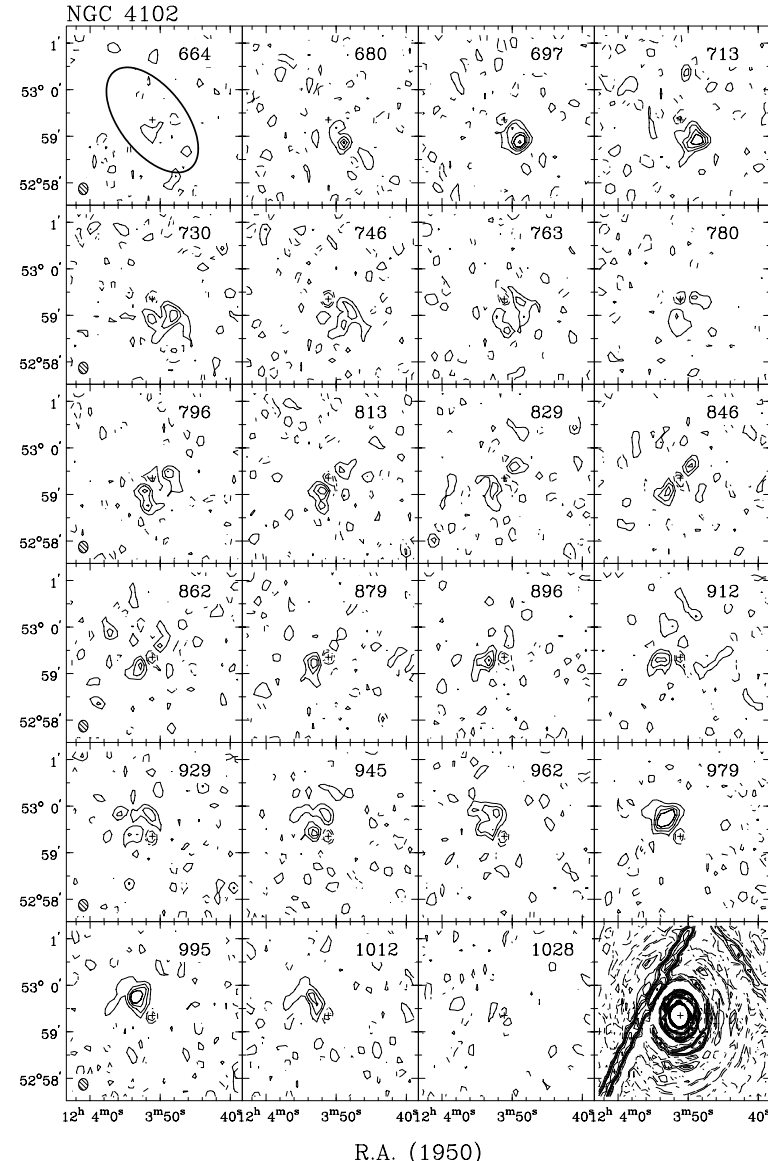
Integrated HI-flux	(Jy km s $^{-1}$)	8.0 ± 0.2
Hel. systemic velocity	(km s $^{-1}$)	846.3 ± 2.0
HI profile width, 20% (km s $^{-1}$)		349.8 ± 2.0
50% (km s $^{-1}$)		322.4 ± 8.5

From velocity field:

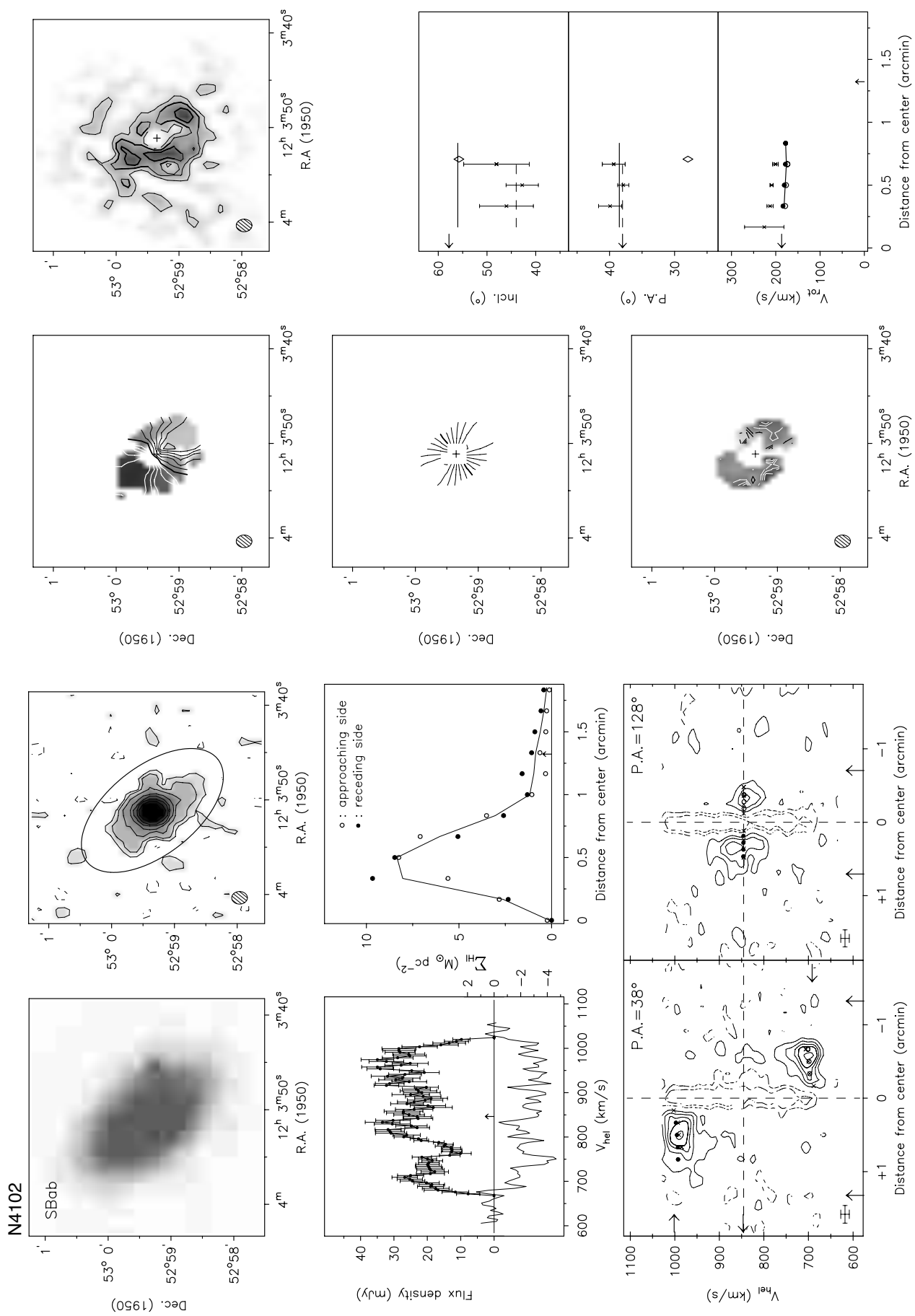
Hel. systemic velocity	(km s $^{-1}$)	845.4 ± 4.0
Dynamical center, α (1950)		12:03:51.2
δ (1950)		52:59:21

From total HI map:

Geometric center, α (1950)		12:03:51.2
δ (1950)		52:59:22
Position angle	(deg)	28
Inclination angle	(deg)	56
Diameter of HI disk	(arcmin)	2.3

Channel maps at a resolution of $12'' \times 15'' \times 19 \text{ km s}^{-1}$.Contour levels at $-3, -1.5$ (dashed), $1.5, 3, 4.5, \dots \times \sigma$.

Note: This LINER galaxy shows HI in absorption against the central radio continuum source. The absorption is seen over the full velocity width of the global profile. The rotation curve reaches its maximum very close to the center. The HI emission is concentrated in a ring-like structure that encompasses the bar. The position of the strong continuum source is taken as the dynamical center. The position angle derived from the total HI map is not meaningful due to the patchy-ness of the HI gas.



Observing parameters for NGC 4157

Length of observation	(hours)	1×12
Date of observation		29,31 Aug 93
Field center, α (1950)		12:08:35
δ (1950)		50:45:51
Central frequency	(MHz)	1416.75
V_{hel} of central channel	(km s^{-1})	774
Primary beam FWHM	(arcmin)	37.4
Nr. of interferometers		40
Baselines (min-max-incr)	(m)	36-2700-72
Synthesized beam ($\alpha \times \delta$)	(arcsec)	11.8×16.7
Bandwidth	(MHz)	5.0
Number of channels		63
Channel separation	(km s^{-1})	16.57
Velocity resolution	(km s^{-1})	19.88
rms noise in one channel	(K)	4.89
K-mJy conversion, equiv. of 1mJy/beam	(K)	3.06

Contour levels for N4157

Channel maps:	$\sigma = 1.34$ (K)
Raw continuum map:	$\sigma = 0.28$ (K)
Cleaned continuum map:	$\sigma = 0.33$ (K)
Position-Velocity diagrams:	$\sigma = 1.31$ (K)
Velocity fields:	$774.1 \pm n \times 30$ (km s^{-1})
Residual velocity field:	$\pm n \times 5$ (km s^{-1})
Integrated HI map:	0.39, 0.78, 1.16, 1.55 $1.94, 2.33 (\times 10^{21} \text{ atoms cm}^{-2})$

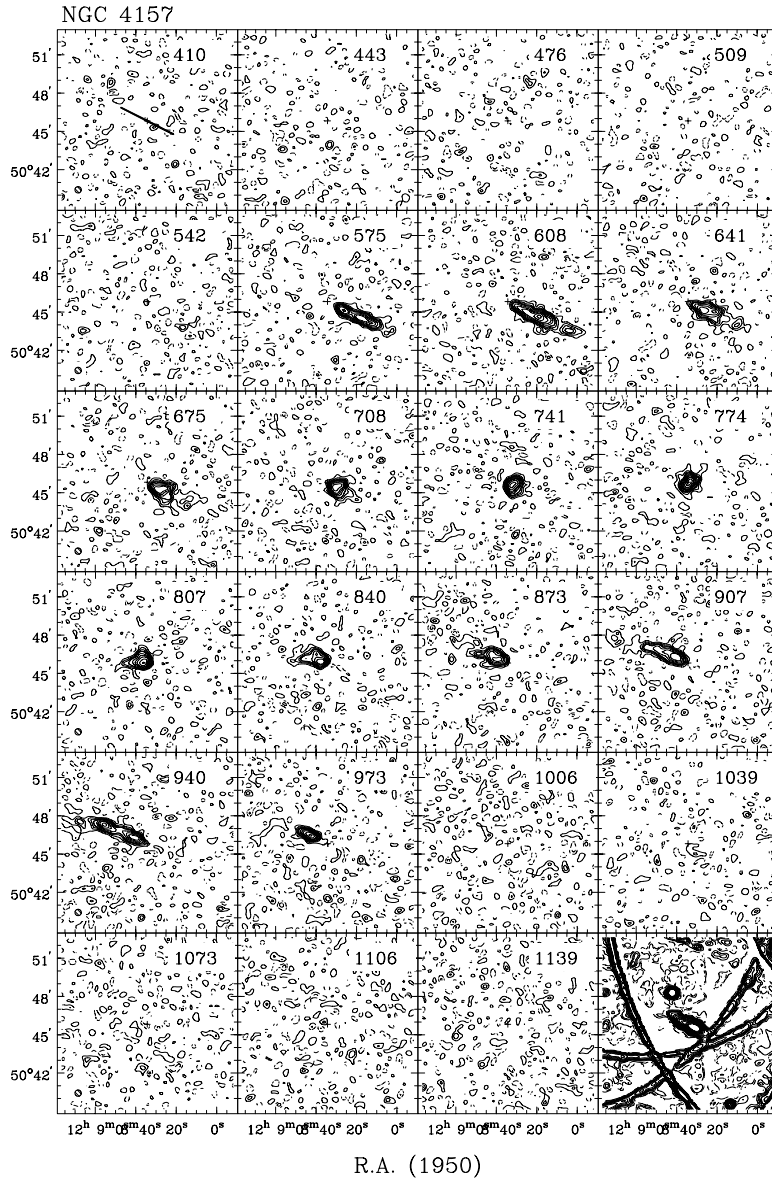
Results from WSRT data

<i>From continuum map:</i>	
21-cm flux density	(mJy) 179.6 ± 2.3
<i>From global profile:</i>	
Integrated HI-flux	(Jy km s^{-1}) 107.4 ± 1.6
Hel. systemic velocity	(km s^{-1}) 774.4 ± 1.8
HI profile width, 20%	(km s^{-1}) 427.6 ± 2.2
50%	(km s^{-1}) 400.7 ± 3.1
<i>From velocity field:</i>	
Hel. systemic velocity	(km s^{-1}) 774.1 ± 1.3
Dynamical center, α (1950)	12:08:34.4
δ (1950)	50:45:50
<i>From total HI map:</i>	
Geometric center, α (1950)	12:08:32.7
δ (1950)	50:45:41
Position angle	(deg) 66
Inclination angle	(deg) 80
Diameter of HI disk	(arcmin) 9.2

Note: Because of the high inclination of NGC 4157 the velocity field derived here with the standard methods is not adequate for a detailed dynamical study. The formal results from the tilted-ring fits are merely shown for completeness and to give the global picture. The inclination of almost 90 degrees as derived from the optical axis ratio assuming an intrinsic thickness of 0.2 is definitely too high given the dust features in the optical image.

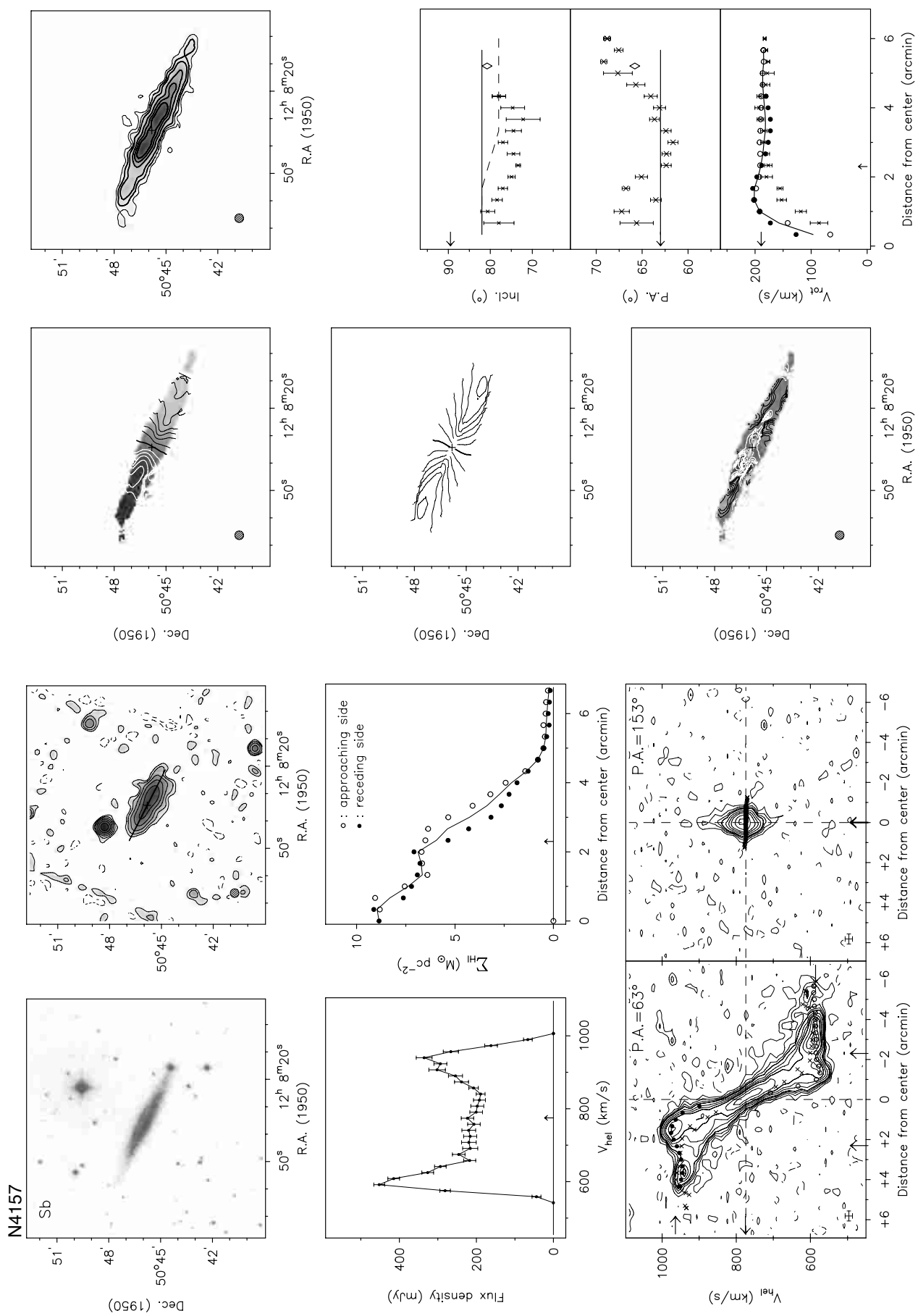
The rotation curve is declining by about 20 km s^{-3} at $\approx 2'$ from the center and remains flat in the outer parts. To explain such a decline as due to inclination effects, the inclination angle would have to become 65 degrees in the outer parts. Such a low inclination is excluded by the axis ratio of the total HI map. Therefore, the rotation curve must be really declining between 2 and 3 arcmin.

The extended radio continuum emission is asymmetric with respect to the center of the galaxy and originates partly in the halo.



Channel maps at a resolution of $30'' \times 30'' \times 20 \text{ km s}^{-1}$.

Contour levels at $-3, -1.5$ (dashed), $1.5, 3, 4.5, \dots \times \sigma$.



Observing parameters for NGC 4183

Length of observation	(hours)	1×12
Date of observation		02Aug93
Field center, α (1950)		12:10:47
δ (1950)		43:58:35
Central frequency	(MHz)	1415.95
V_{hel} of central channel	(km s $^{-1}$)	932
Primary beam FWHM	(arcmin)	37.4
Nr. of interferometers		40
Baselines (min-max-incr)	(m)	36-2700-72
Synthesized beam ($\alpha \times \delta$)	(arcsec)	11.8 \times 17.2
Bandwidth	(MHz)	2.5
Number of channels		127
Channel separation	(km s $^{-1}$)	4.15
Velocity resolution	(km s $^{-1}$)	8.30
rms noise in one channel	(K)	5.93
K-mJy conversion, equiv. of 1mJy/beam	(K)	2.97

Contour levels for N4183

Channel maps:	$\sigma = 3.86$ (K)
Raw continuum map:	$\sigma = 1.75$ (K)
Cleaned continuum map:	$\sigma = 1.51$ (K)
Position-Velocity diagrams:	$\sigma = 3.34$ (K)
Velocity fields:	$925.5 \pm n \times 20$ (km s $^{-1}$)
Residual velocity field:	$\pm n \times 5$ (km s $^{-1}$)
Integrated HI map:	1.06, 2.13, 3.19 $4.26 (\times 10^{21} \text{ atoms cm}^{-2})$

Results from WSRT data

From continuum map:

21-cm flux density	
central point source (mJy)	<1.5 (3 σ)
extended source (mJy)	<5.8 (3 σ)

From global profile:

Integrated HI-flux	(Jy km s $^{-1}$)	48.9 ± 0.7
Hel. systemic velocity	(km s $^{-1}$)	930.1 ± 1.0
HI profile width, 20%	(km s $^{-1}$)	249.6 ± 1.2
50%	(km s $^{-1}$)	232.5 ± 1.5

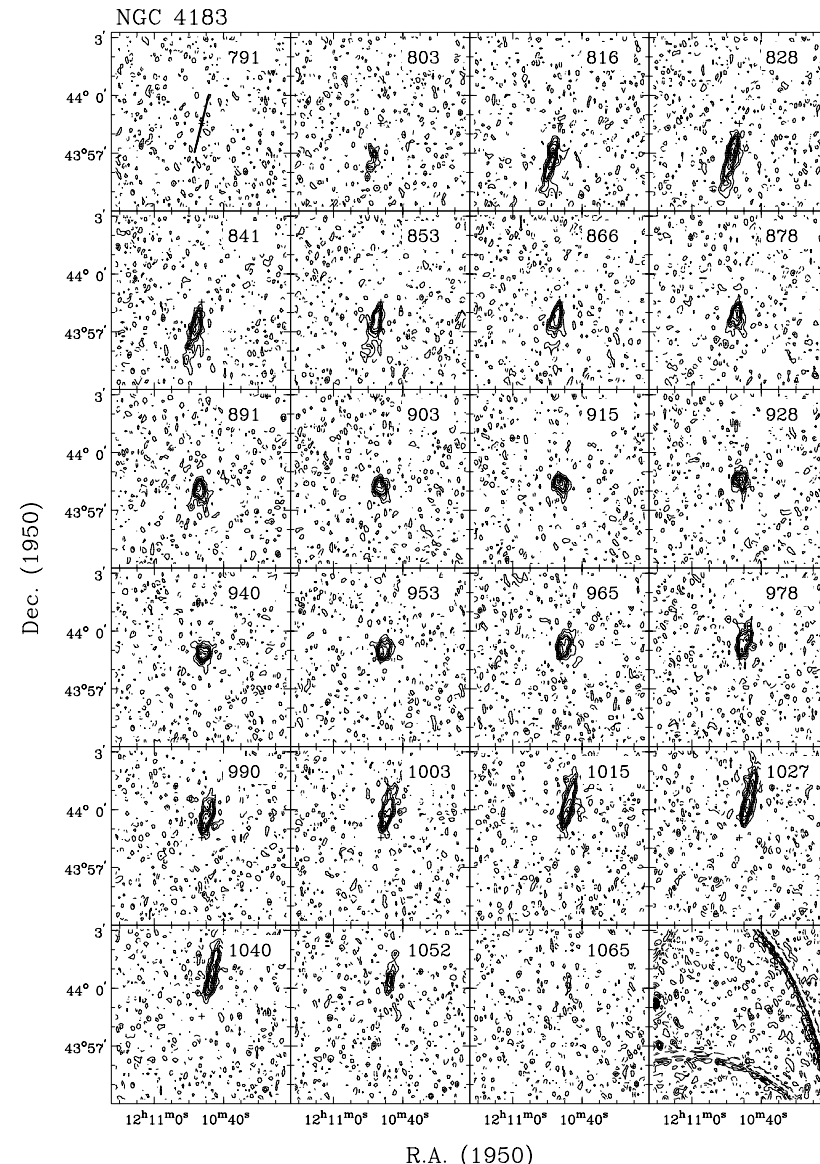
From velocity field:

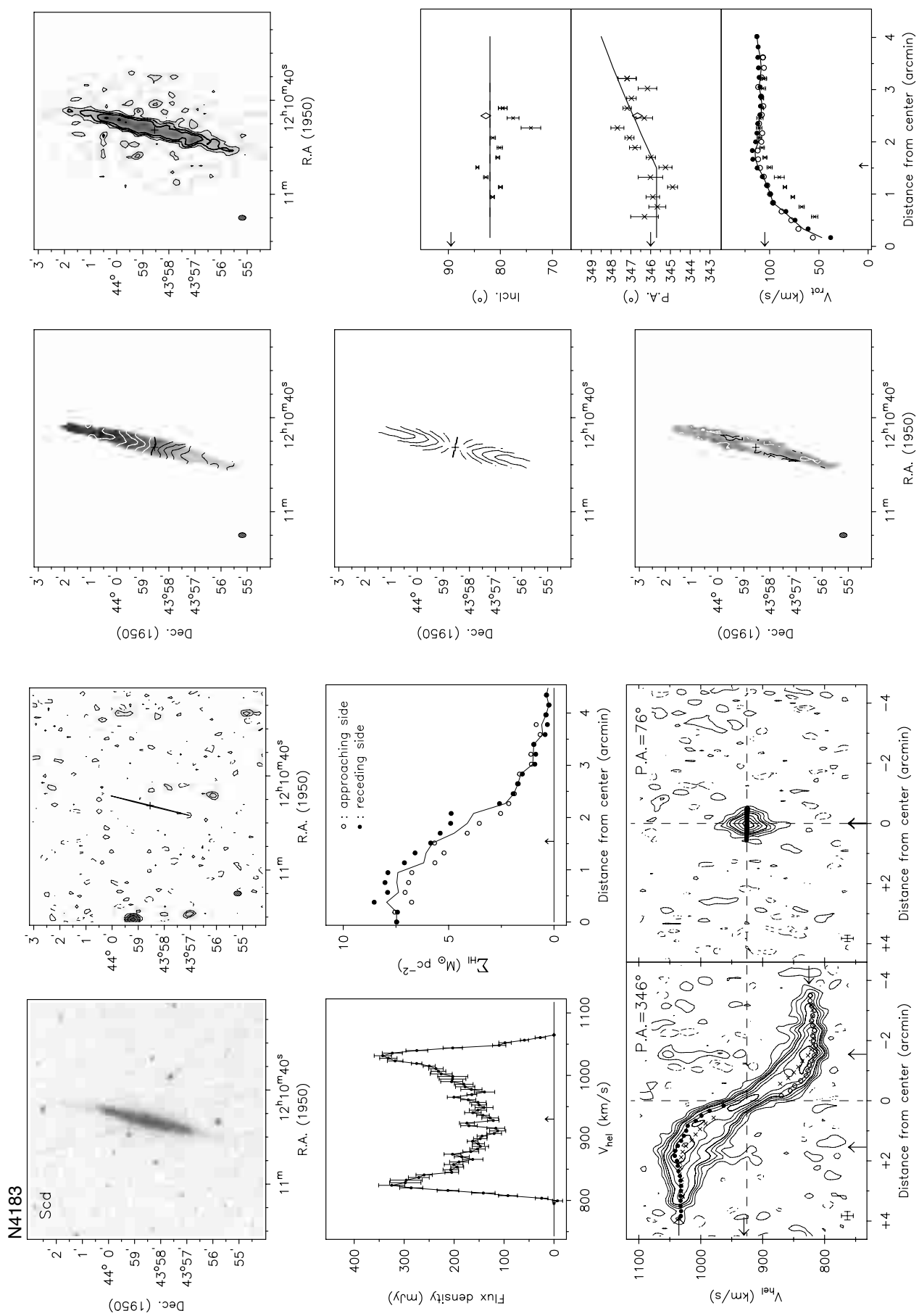
Hel. systemic velocity	(km s $^{-1}$)	925.5 ± 1.5
Dynamical center, α (1950)		12:10:46.2

 δ (1950) 43:58:33*From total HI map:*

Geometric center, α (1950)		12:10:45.8
δ (1950)		43:58:41
Position angle	(deg)	347
Inclination angle	(deg)	83
Diameter of HI disk	(arcmin)	6.1

Note: This galaxy is slightly warped in the outer regions. The inclination derived from the optical axis ratio is too high due to the assumed intrinsic thickness of 0.2 which is probably too large.

Channel maps at a resolution of $11'' \times 17'' \times 19$ km s $^{-1}$.Contour levels at $-3, -1.5$ (dashed), $1.5, 3, 4.5, \dots \times \sigma$.



Observing parameters for NGC 4217

Length of observation	(hours)	1×12
Date of observation		16Aug90
Field center, α (1950)		12:13:20
δ (1950)		47:20:00
Central frequency	(MHz)	1415.52
V_{hel} of central channel	(km s $^{-1}$)	1030
Primary beam FWHM	(arcmin)	37.4
Nr. of interferometers		40
Baselines (min-max-incr)	(m)	36-2700-72
Synthesized beam ($\alpha \times \delta$) (arcsec)		13.2×18.6
Bandwidth	(MHz)	5.0
Number of channels		63
Channel separation	(km s $^{-1}$)	16.60
Velocity resolution	(km s $^{-1}$)	33.20
rms noise in one channel	(K)	2.45
K-mJy conversion, equiv. of 1mJy/beam	(K)	2.45

Contour levels for N4217

Channel maps:	$\sigma=2.45$ (K)
Raw continuum map:	$\sigma=0.93$ (K)
Cleaned continuum map:	$\sigma=0.86$ (K)
Position-Velocity diagrams:	$\sigma=2.21$ (K)
Velocity fields:	$1028.8 \pm n \times 30$ (km s $^{-1}$)
Residual velocity field:	$\pm n \times 5$ (km s $^{-1}$)
Integrated HI map:	0.91, 1.82, 2.74 $3.65 (\times 10^{21} \text{ atoms cm}^{-2})$

Results from WSRT data

From continuum map:

21-cm flux density (mJy) 115.6 ± 2.2

From global profile:

Integrated HI-flux (Jy km s $^{-1}$) 33.8 ± 0.7
 Hel. systemic velocity (km s $^{-1}$) 1027.0 ± 3.0
 HI profile width, 20% (km s $^{-1}$) 428.1 ± 5.1
 50% (km s $^{-1}$) 395.6 ± 3.8

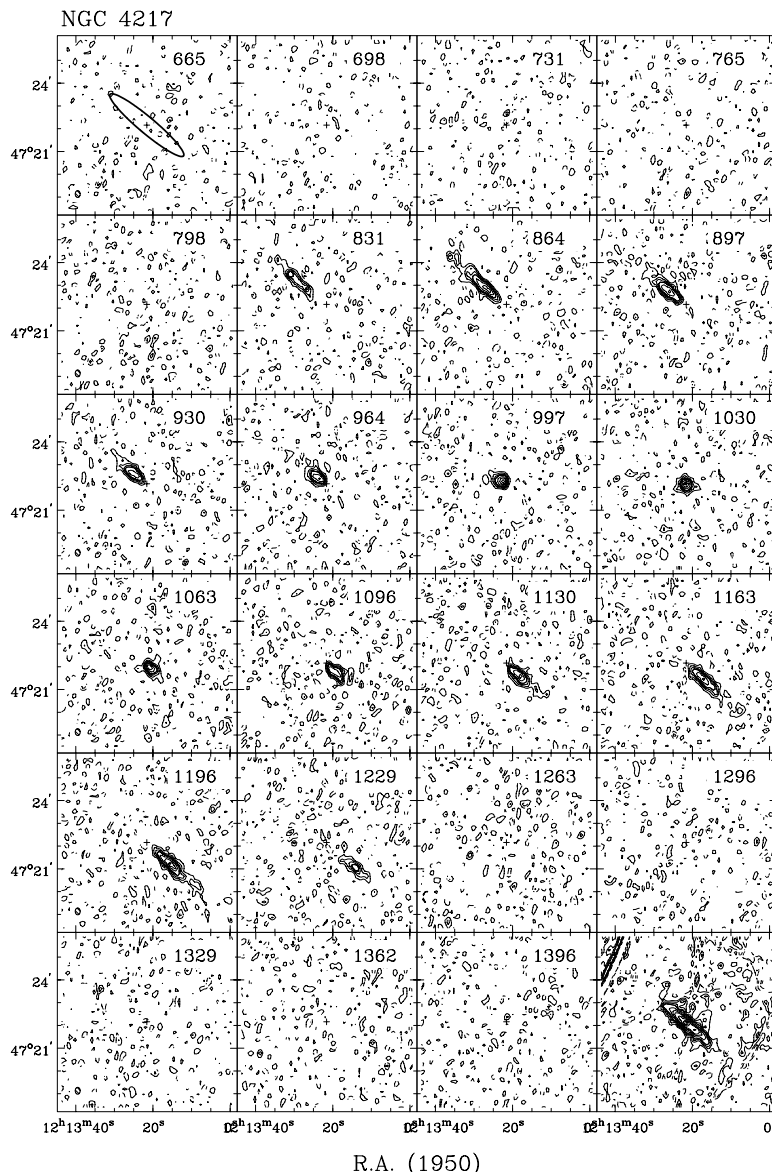
From velocity field:

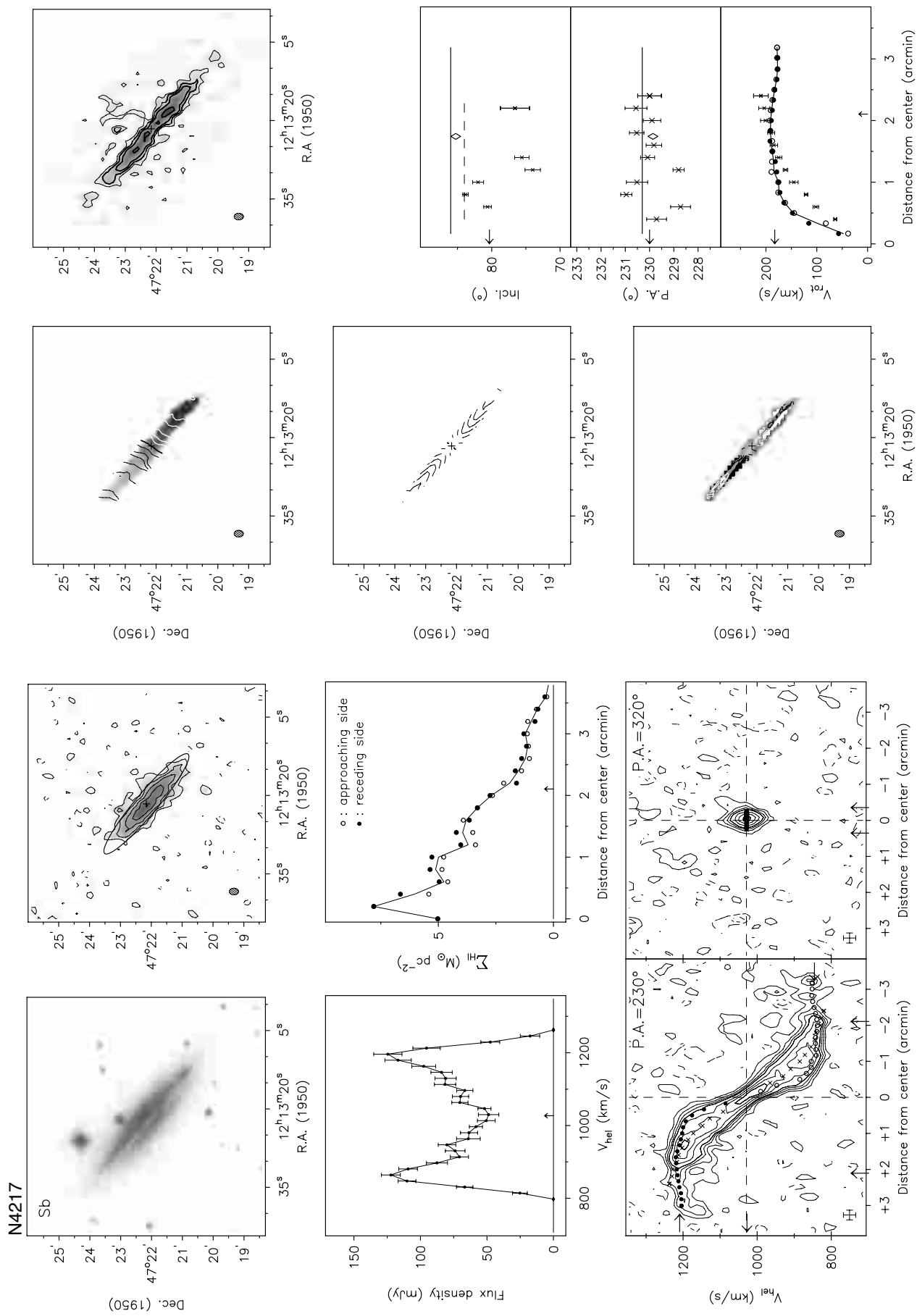
Hel. systemic velocity (km s $^{-1}$) 1028.8 ± 2.7
 Dynamical center, α (1950) 12:13:21.6
 δ (1950) 47:22:10

From total HI map:

Geometric center, α (1950) 12:13:21.8
 δ (1950) 47:22:11
 Position angle (deg) 230
 Inclination angle (deg) 85
 Diameter of HI disk (arcmin) 6.4

Note: This early type nearly edge-on spiral shows extended 21cm continuum emission. Some HI line emission may be absorbed by the strong continuum source. The inclination derived from the optical axis ratio is probably an underestimate of the true inclination because the prominent bulge makes the galaxy look rounder than the assumed intrinsic thickness of 0.2.

Channel maps at a resolution of $13'' \times 18'' \times 33 \text{ km s}^{-1}$.Contour levels at $-3, -1.5, 1.5, 3, 4.5, \dots \times \sigma$.



Observing parameters for NGC 4389

Length of observation	(hours)	2x12
Date of observation		28Aug92 04Dec93
Field center, α (1950)		12:23:05
δ (1950)		46:00:00
Central frequency	(MHz)	1416.90
V_{hel} of central channel	(km s $^{-1}$)	740
Primary beam FWHM	(arcmin)	37.4
Nr. of interferometers		80
Baselines (min-max-incr)	(m)	36-2736-36
Synthesized beam ($\alpha \times \delta$)	(arcsec)	12.0 \times 16.9
Bandwidth	(MHz)	2.5
Number of channels		127
Channel separation	(km s $^{-1}$)	4.14
Velocity resolution	(km s $^{-1}$)	8.29
rms noise in one channel	(K)	3.86
K-mJy conversion, equiv. of 1mJy/beam	(K)	2.97

Contour levels for N4389

Channel maps:	$\sigma = 2.53$ (K)
Raw continuum map:	$\sigma = 0.91$ (K)
Cleaned continuum map:	$\sigma = 0.83$ (K)
Position-Velocity diagrams:	$\sigma = 2.30$ (K)
Velocity fields:	$714.7 \pm n \times 15$ (km s $^{-1}$)
Residual velocity field:	$\pm n \times 5$ (km s $^{-1}$)
Integrated HI map:	0.41, 0.82, $1.23 (\times 10^{21} \text{ atoms cm}^{-2})$

Results from WSRT data

From continuum map:

21-cm flux density	(mJy)	23.3 ± 1.2
Central point source position		
α (1950)		12:23:08.6
δ (1950)		45:57:41

From global profile:

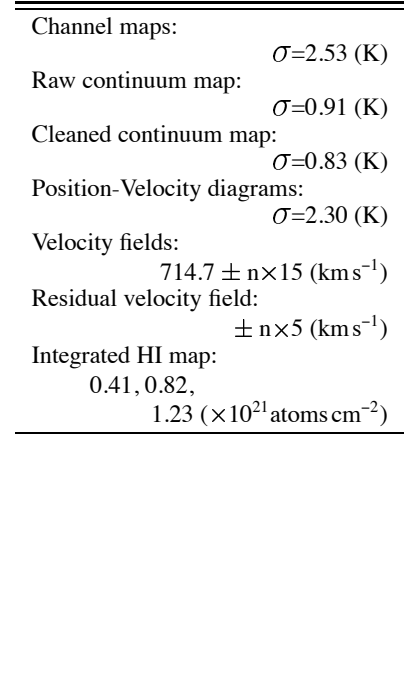
Integrated HI-flux	(Jy km s $^{-1}$)	7.6 ± 0.2
Hel. systemic velocity	(km s $^{-1}$)	718.4 ± 1.2
HI profile width, 20%	(km s $^{-1}$)	184.0 ± 1.5
50%	(km s $^{-1}$)	164.9 ± 1.6

From velocity field:

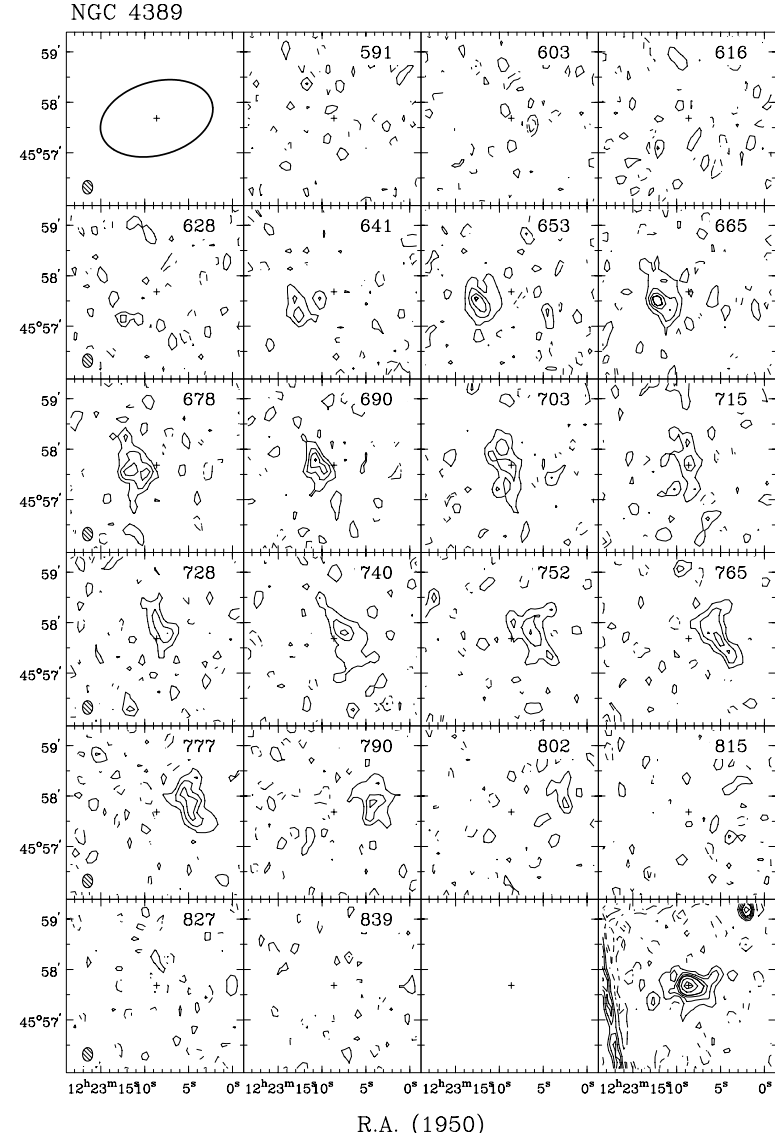
Hel. systemic velocity	(km s $^{-1}$)	714.7 ± 1.1
Dynamical center, α (1950)		12:23:08.6
δ (1950)		45:57:41

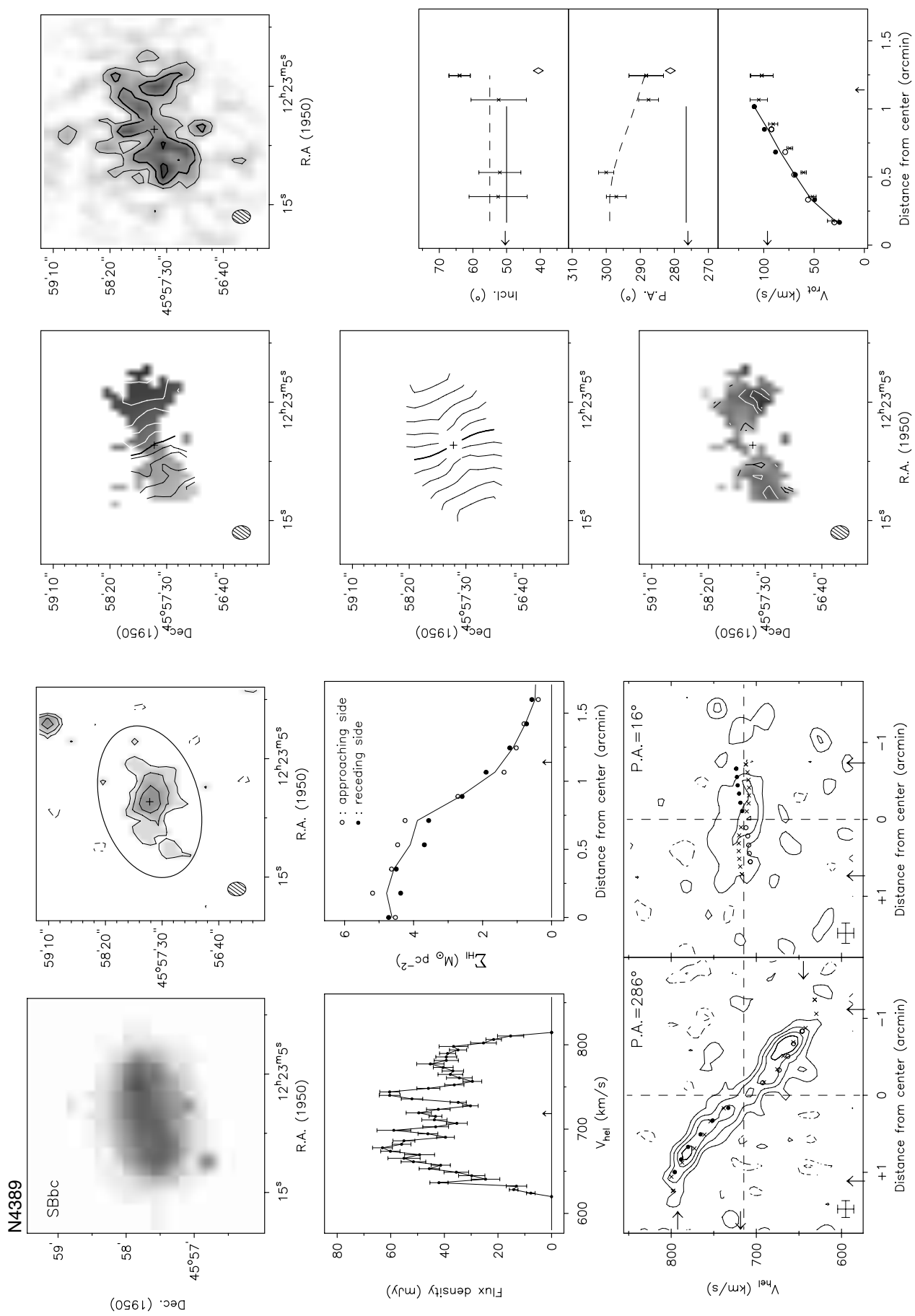
From total HI map:

Geometric center, α (1950)		12:23:08.2
δ (1950)		45:57:44
Position angle	(deg)	281
Inclination angle	(deg)	40
Diameter of HI disk	(arcmin)	2.6



Note: The morphology and kinematics of this galaxy are completely dominated by a prominent bar. The position angle of the bar almost coincides with the position angle of the outer isophotes. The position of the central 21cm continuum point source is the same as the center of the outer optical isophotes and is taken as the dynamical center. The HI gas is only found along the bar and the star forming regions at the end of the bar.

Channel maps at a resolution of $12'' \times 16'' \times 19$ km s $^{-1}$.Contour levels at $-3, -1.5, 1.5, 3, 4.5, \dots \times \sigma$.



Observing parameters for NGC 3718

Length of observation	(hours)	1×12
Date of observation		15Apr91
Field center, α (1950)		11:31:05
δ (1950)		53:23:00
Central frequency	(MHz)	1415.27
V_{hel} of central channel	(km s $^{-1}$)	1070
Primary beam FWHM	(arcmin)	37.4
Nr. of interferometers		40
Baselines (min-max-incr)	(m)	36-2700-72
Synthesized beam ($\alpha \times \delta$)	(arcsec)	12.9 \times 17.2
Bandwidth	(MHz)	5.0
Number of channels		53
Channel separation	(km s $^{-1}$)	16.61
Velocity resolution	(km s $^{-1}$)	33.22
rms noise in one channel	(K)	2.85
K-mJy conversion, equiv. of 1mJy/beam	(K)	2.71

Results from WSRT data

From continuum map:

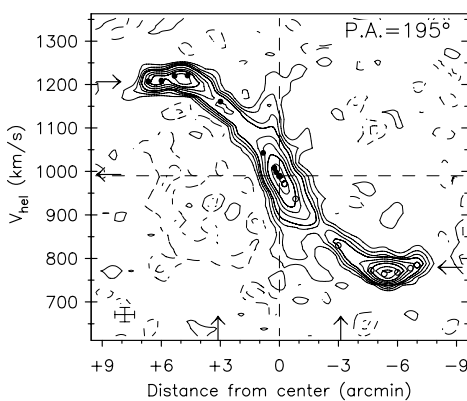
21-cm flux density	(mJy)	11.4 ± 0.4
Central point source position		
α (1950)		11:29:49.9
δ (1950)		53:20:39

From global profile:

Integrated HI-flux	(Jy km s $^{-1}$)	140.9 ± 0.9
Hel. systemic velocity	(km s $^{-1}$)	993.0 ± 0.8
HI profile width, 20%	(km s $^{-1}$)	492.8 ± 1.0
50%	(km s $^{-1}$)	465.7 ± 1.0

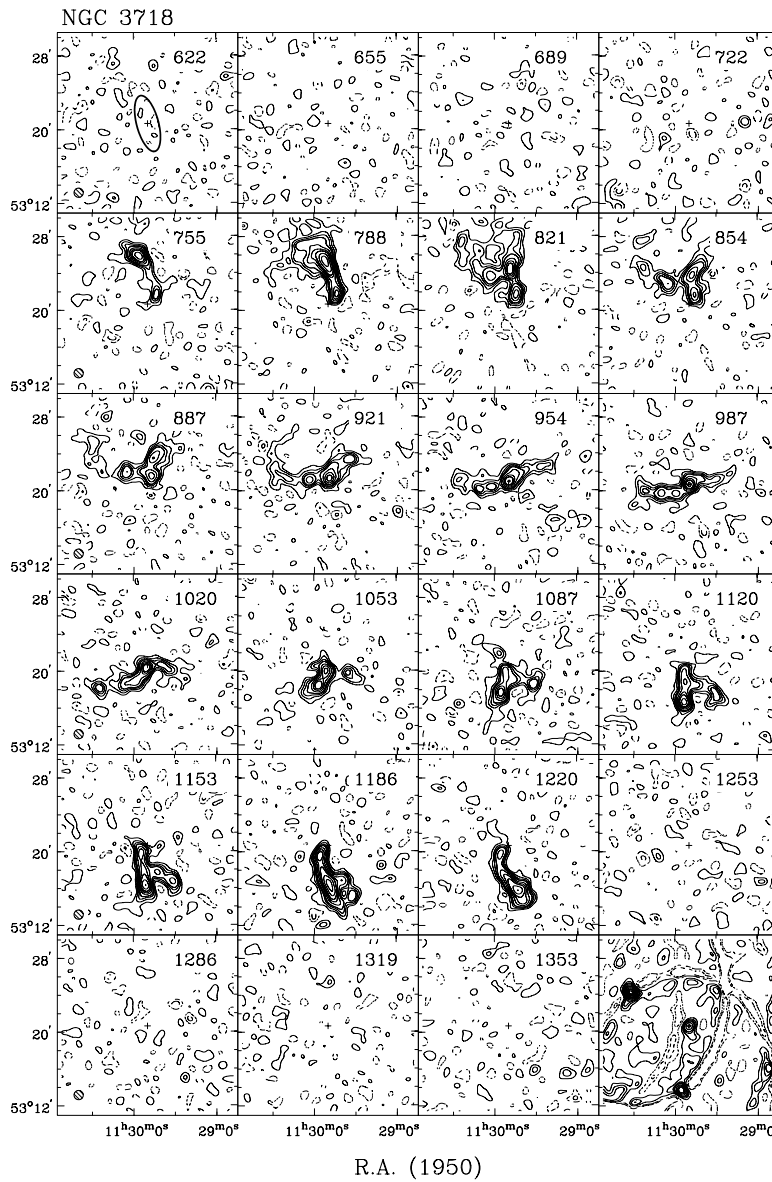
From XV-diagram:

Hel. systemic velocity	(km s $^{-1}$)	989.8
------------------------	-----------------	-------



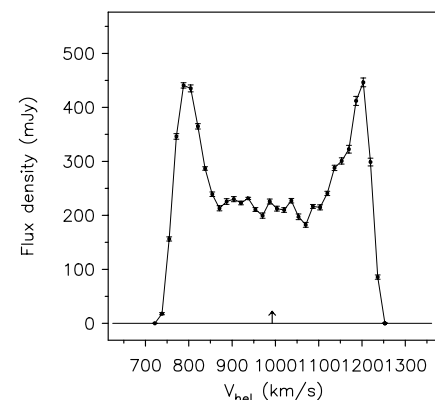
Contour levels for N3718

Channel maps:	$\sigma = 0.27$ (K)
Raw continuum maps:	$\sigma = 0.13$ (K)
Position-Velocity diagram:	$\sigma = 0.26$ (K)



Note: NGC 3718 is the largest galaxy in the cluster. It displays a symmetric but distorted morphology with extended spiral arms and a pronounced dust lane crossing its nucleus. The kinematics is very complex and shows an extremely warped HI disk. The inclination runs from roughly 75 degrees in the inner regions through edge-on to about 65 degrees in the outer regions. The change in position angle is more than 95 degrees. This system has been studied in detail by Schwarz (1985). The rotation curve as projected onto the position-velocity diagram is based on the results from his modelling.

NGC 3729 is located some 11 arcmin to the ENE.



Channel maps at a resolution of $60'' \times 60'' \times 33$ km s $^{-1}$.
Contour levels at -3, -1.5 (dashed), 1.5, 3, 4.5, ... $\times \sigma$.

Observing parameters for NGC 3729

Length of observation	(hours)	1×12
Date of observation		15 Apr 91
Field center, α (1950)		11:31:05
δ (1950)		53:23:00
Central frequency	(MHz)	1415.27
V_{hel} of central channel	(km s $^{-1}$)	1070
Primary beam FWHM	(arcmin)	37.4
Nr. of interferometers		40
Baselines (min-max-incr)	(m)	36-2700-72
Synthesized beam ($\alpha \times \delta$)	(arcsec)	12.9 \times 17.2
Bandwidth	(MHz)	5.0
Number of channels		53
Channel separation	(km s $^{-1}$)	16.61
Velocity resolution	(km s $^{-1}$)	33.22
rms noise in one channel	(K)	2.85
K-mJy conversion, equiv. of 1mJy/beam	(K)	2.71

Results from WSRT data

From continuum map:

21-cm flux density	(mJy)	18.0 ± 0.9
Central point source position		
α (1950)		11:31:04.8

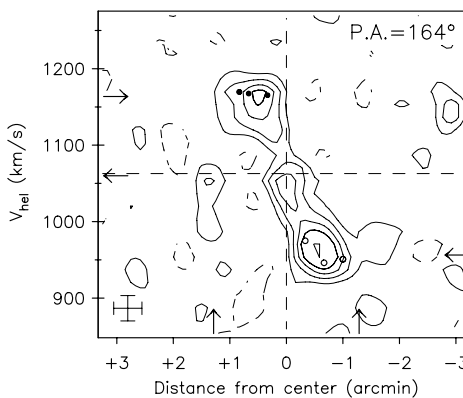
δ (1950) 53:24:08

From global profile:

Integrated HI-flux	(Jy km s $^{-1}$)	5.5 ± 0.3
Hel. systemic velocity	(km s $^{-1}$)	1059.8 ± 1.4
HI profile width, 20%	(km s $^{-1}$)	270.8 ± 1.5
50%	(km s $^{-1}$)	253.2 ± 3.9

From XV-diagram:

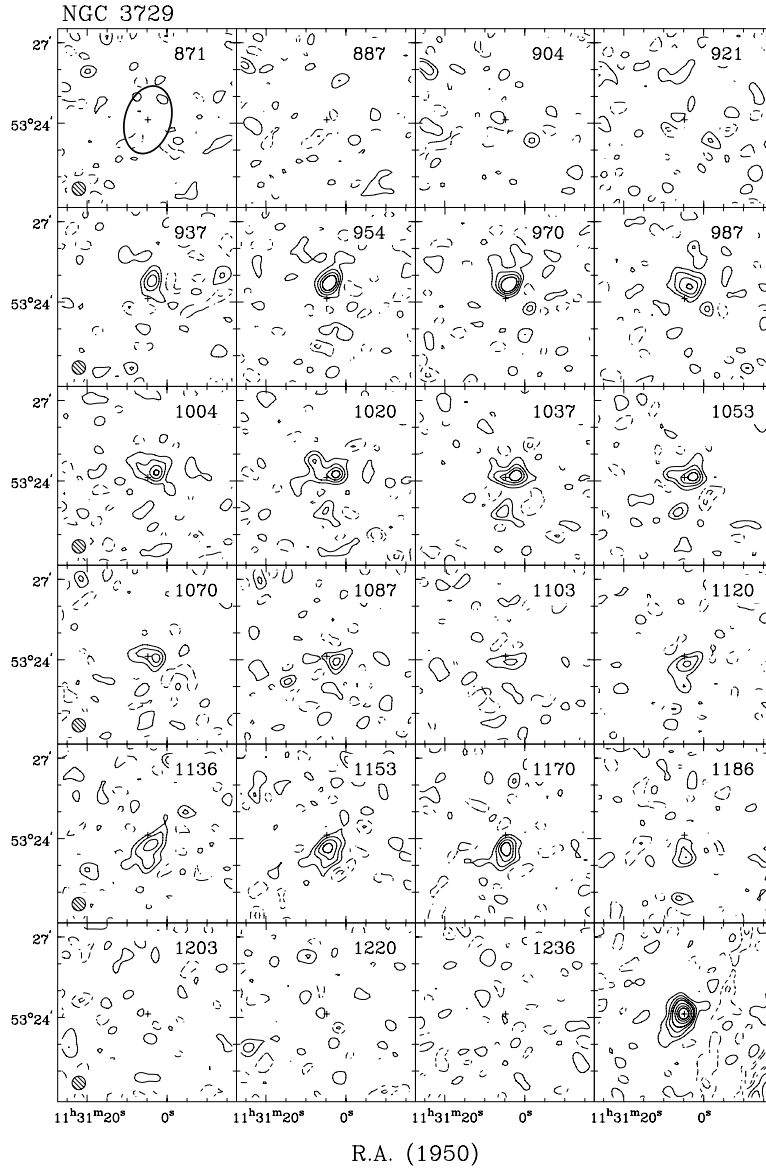
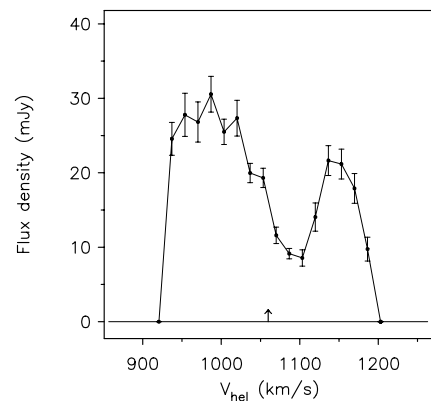
Hel. systemic velocity	(km s $^{-1}$)	1062.8
------------------------	-----------------	--------



Contour levels for N3729

Channel maps:	$\sigma = 0.77$ (K)
Raw continuum maps:	$\sigma = 0.32$ (K)
Position-Velocity diagram:	$\sigma = 0.75$ (K)

Note: NGC 3729 displays a bright ring-like structure which surrounds a diffuse bar and a double nucleus. On the north-eastern side, just outside the ring, a diffuse blue patch can be seen. The HI gas is only detected in the bright ring with a faint extension toward the blue patch. The large disturbed galaxy N3718 is located about 11 arcmin to the WSW.



Channel maps at a resolution of $30'' \times 30'' \times 33$ km s $^{-1}$.
Contour levels at -3, -1.5 (dashed), 1.5, 3, 4.5, ... σ .

Observing parameters for UGC 6773

Length of observation	(hours)	1×12
Date of observation		29Aug92
Field center, α (1950)		11:45:24
δ (1950)		50:05:00
Central frequency	(MHz)	1415.97
V_{hel} of central channel	(km s $^{-1}$)	940
Primary beam FWHM	(arcmin)	37.4
Nr. of interferometers		40
Baselines (min-max-incr)	(m)	36-2700-72
Synthesized beam ($\alpha \times \delta$) (arcsec)		12.6 \times 16.6
Bandwidth	(MHz)	2.5
Number of channels		127
Channel separation	(km s $^{-1}$)	4.15
Velocity resolution	(km s $^{-1}$)	8.29
rms noise in one channel	(K)	5.32
K-mJy conversion, equiv. of 1mJy/beam	(K)	2.88

Results from WSRT data

From continuum map:

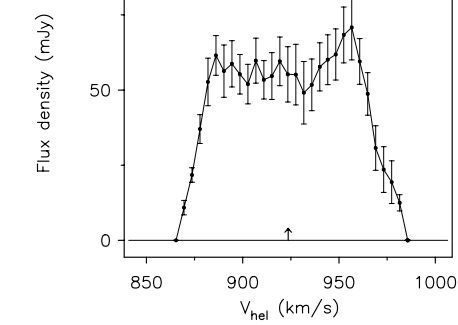
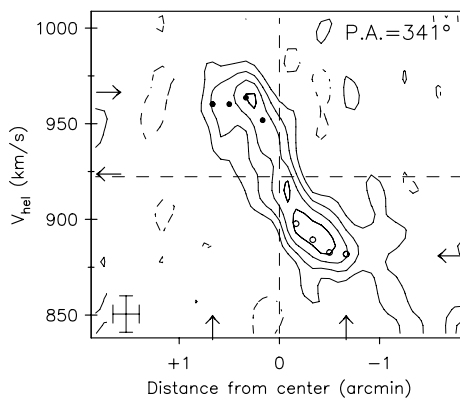
21-cm flux density	
central point source (mJy)	<1.2 (3 σ)
extended source (mJy)	<2.6 (3 σ)

From global profile:

Integrated HI-flux (Jy km s $^{-1}$)	5.6 ± 0.4
Hel. systemic velocity (km s $^{-1}$)	923.6 ± 1.6
HI profile width, 20% (km s $^{-1}$)	110.4 ± 2.3
50% (km s $^{-1}$)	91.1 ± 2.2

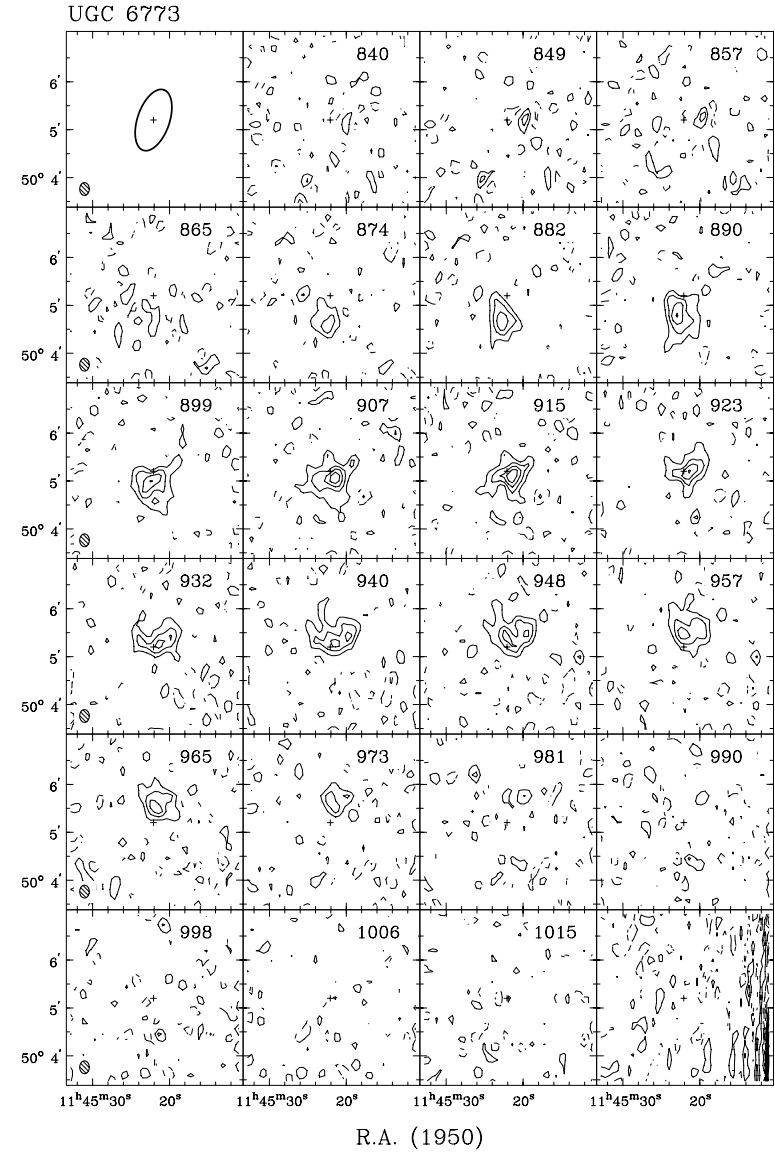
From XV-diagram:

Hel. systemic velocity (km s $^{-1}$)	922.3
--	-------



Contour levels for U6773

Channel maps:	$\sigma=3.45$ (K)
Raw continuum map:	$\sigma=1.47$ (K)
Position-Velocity diagram:	$\sigma=2.88$ (K)



Channel maps at a resolution of $12'' \times 16'' \times 19$ km s $^{-1}$.
Contour levels at $-3, -1.5, 1.5, 3, 4.5, \dots \times \sigma$.

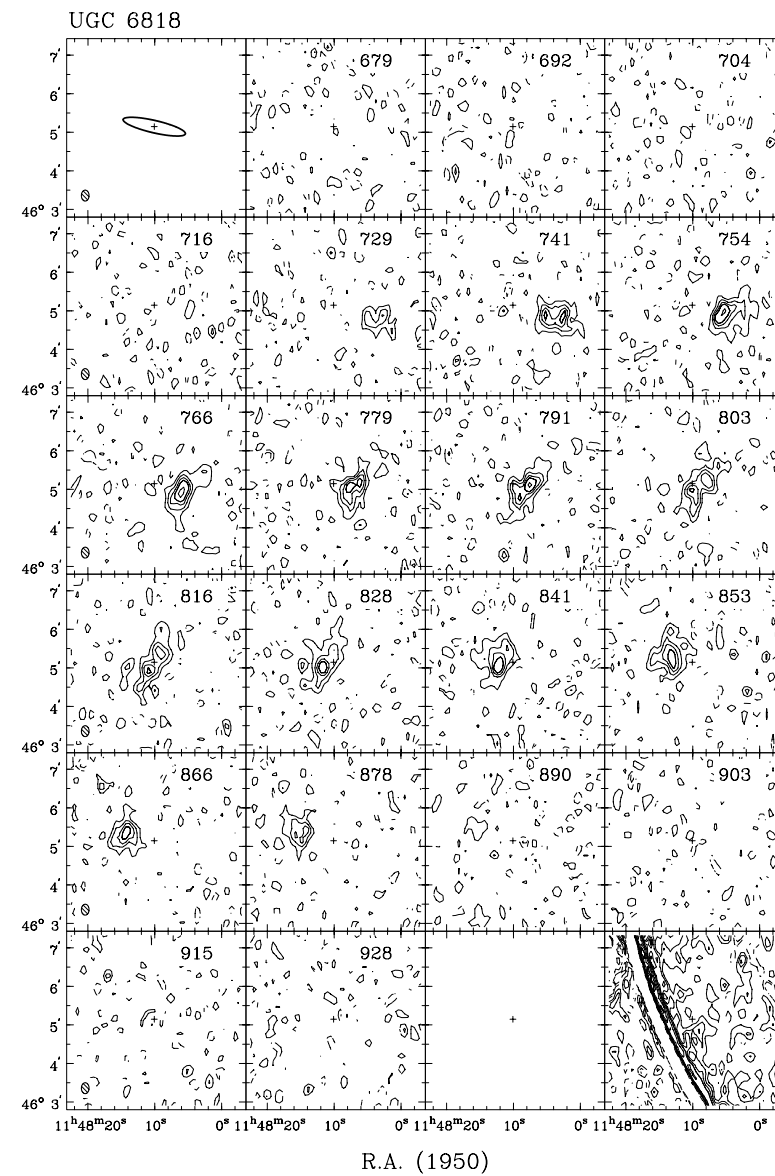
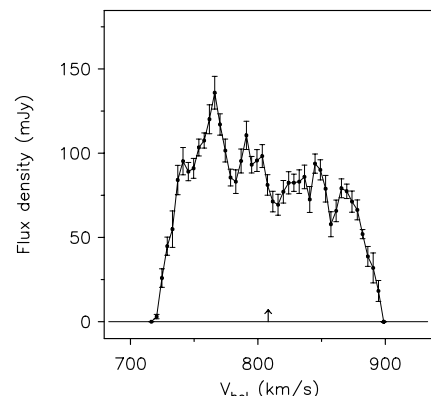
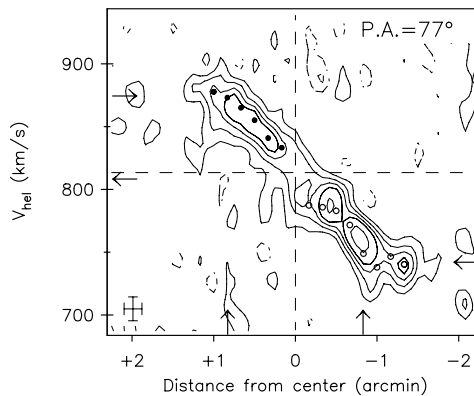
Observing parameters for UGC 6818

Length of observation	(hours)	1×12
Date of observation		19Aug90
Field center, α (1950)		11:48:10
δ (1950)		46:05:00
Central frequency	(MHz)	1416.51
V_{hel} of central channel	(km s $^{-1}$)	820
Primary beam FWHM	(arcmin)	37.4
Nr. of interferometers		40
Baselines (min-max-incr)	(m)	36-2700-72
Synthesized beam ($\alpha \times \delta$)	(arcsec)	12.6 \times 17.6
Bandwidth	(MHz)	2.5
Number of channels		127
Channel separation	(km s $^{-1}$)	4.15
Velocity resolution	(km s $^{-1}$)	8.29
rms noise in one channel	(K)	5.03
K-mJy conversion, equiv. of 1mJy/beam	(K)	2.72

Contour levels for U6818

Channel maps:	$\sigma = 4.04$ (K)
Raw continuum map:	$\sigma = 2.07$ (K)
Position-Velocity diagrams:	$\sigma = 3.36$ (K)

Results from WSRT data

From continuum map:21-cm flux density (mJy) 2.4 ± 1.0 From global profile:Integrated HI-flux (Jy km s $^{-1}$) 13.9 ± 0.2 Hel. systemic velocity (km s $^{-1}$) 808.1 ± 2.1 HI profile width, 20% (km s $^{-1}$) 166.9 ± 2.3 50% (km s $^{-1}$) 141.9 ± 5.7 From XV-diagram:Hel. systemic velocity (km s $^{-1}$) 813.4

Channel maps at a resolution of $12'' \times 17'' \times 19$ km s $^{-1}$.
Contour levels at $-3, -1.5$ (dashed), $1.5, 3, 4.5, \dots \times \sigma$.

Observing parameters for NGC 3985

Length of observation	(hours)	1×12
Date of observation		19Aug93
Field center, α (1950)		11:54:07
δ (1950)		48:36:48
Central frequency	(MHz)	1415.87
V_{hel} of central channel	(km s $^{-1}$)	957
Primary beam FWHM	(arcmin)	37.4
Nr. of interferometers		40
Baselines (min-max-incr)	(m)	36-2700-72
Synthesized beam ($\alpha \times \delta$) (arcsec)		12.3 \times 16.8
Bandwidth	(MHz)	2.5
Number of channels		127
Channel separation	(km s $^{-1}$)	4.15
Velocity resolution	(km s $^{-1}$)	8.30
rms noise in one channel	(K)	5.97
K-mJy conversion, equiv. of 1mJy/beam	(K)	2.91

Results from WSRT data

From continuum map:

21-cm flux density (mJy) 9.7 ± 1.4

From global profile:

Integrated HI-flux (Jy km s $^{-1}$) 15.7 ± 0.6

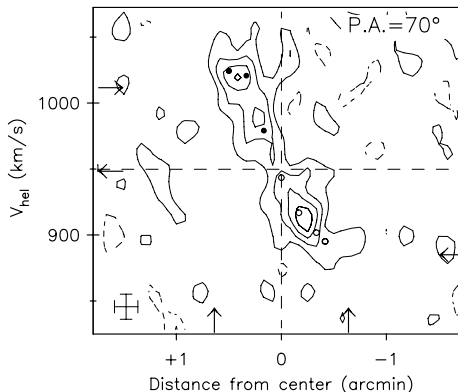
Hel. systemic velocity (km s $^{-1}$) 948.2 ± 2.0

HI profile width, 20% (km s $^{-1}$) 160.2 ± 3.7

50% (km s $^{-1}$) 88.0 ± 2.4

From XV-diagram:

Hel. systemic velocity (km s $^{-1}$) 949.8



Contour levels for N3985

Channel maps:

12 \times 16 arcsec: $\sigma = 3.79$ (K)

30 \times 30 arcsec: $\sigma = 1.14$ (K)

60 \times 60 arcsec: $\sigma = 0.39$ (K)

Raw continuum maps:

12 \times 16 arcsec: $\sigma = 1.69$ (K)

30 \times 30 arcsec: $\sigma = 0.63$ (K)

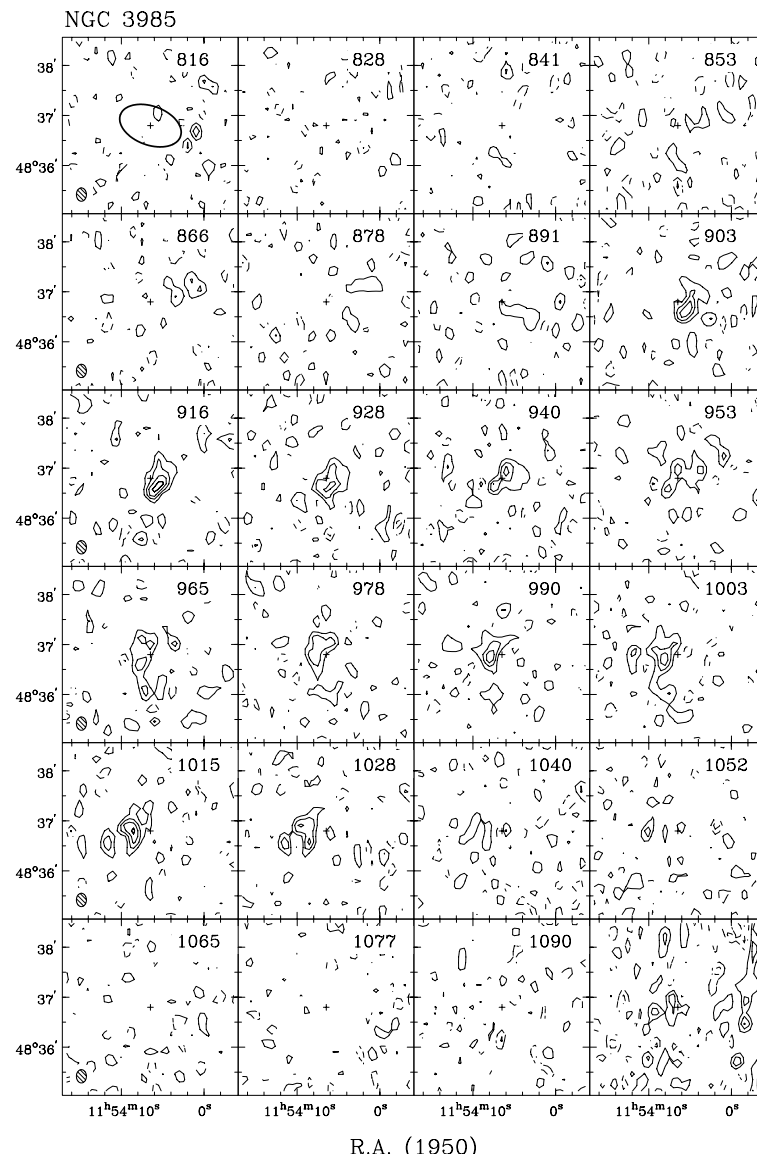
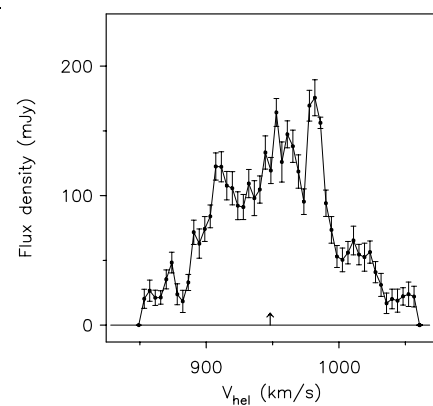
60 \times 60 arcsec: $\sigma = 0.36$ (K)

Position-Velocity diagram:

$\sigma = 3.35$ (K)

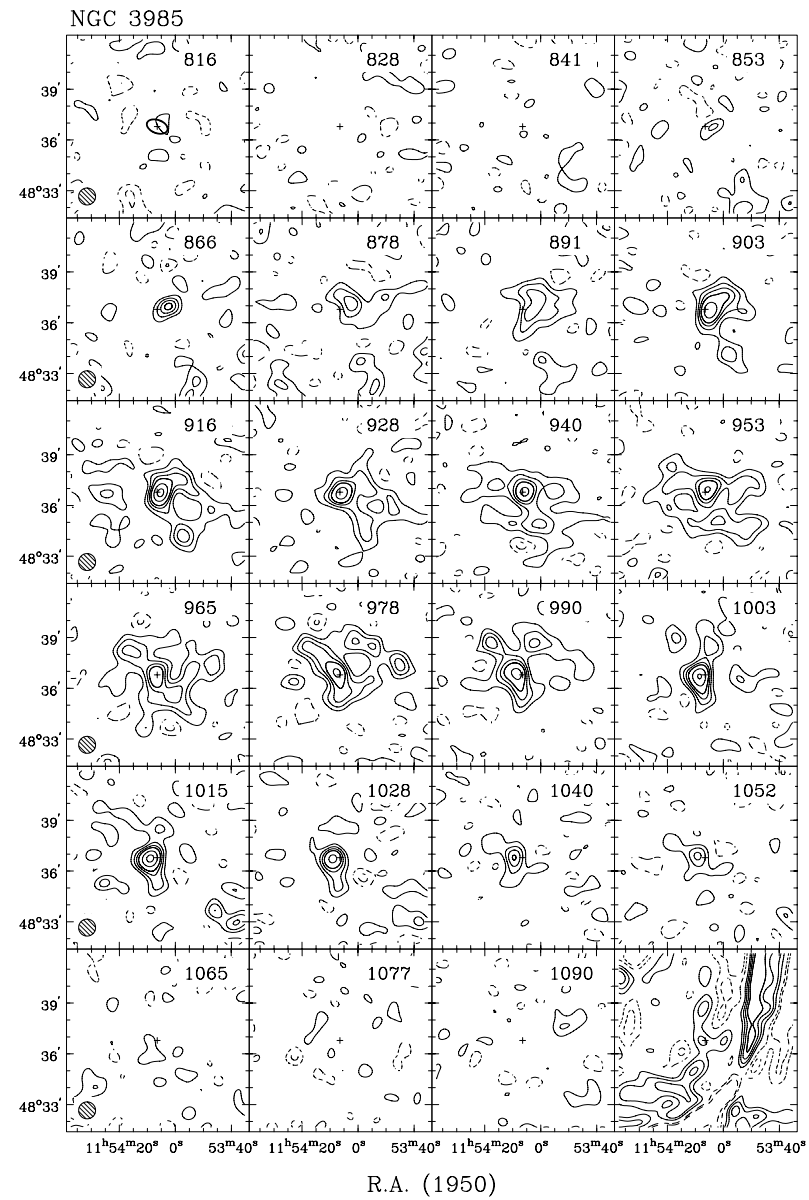
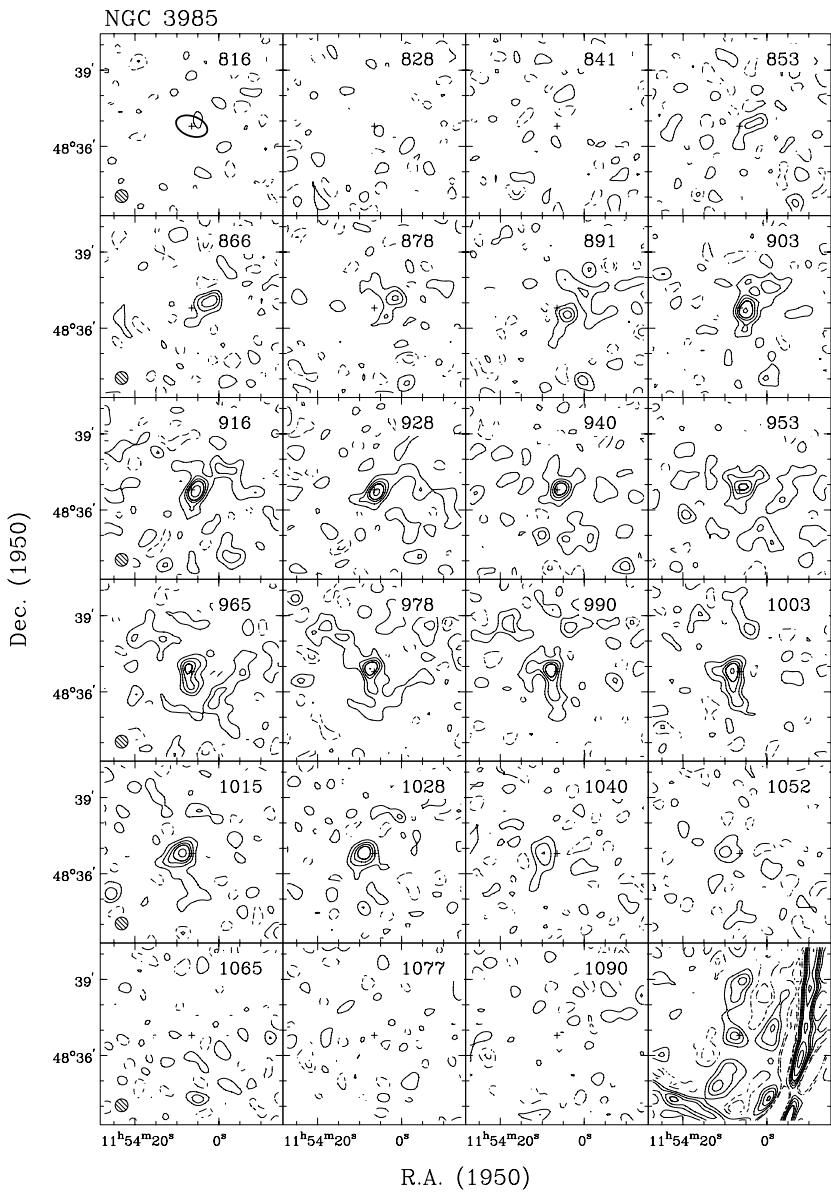
Note: This small high surface brightness galaxy displays smooth outer elliptical isophotes but the inner regions are irregular.

The HI kinematics is quite patchy and chaotic as is shown by the channel maps at various angular resolutions. Two components can be identified; 1) a high surface density disk in the inner region and 2) a very extended low surface density disk with a kinematic major axis nearly perpendicular to the optical major axis.



Channel maps at a resolution of $12'' \times 16'' \times 19$ km s $^{-1}$.

Contour levels at $-3, -1.5, 1.5, 3, 4.5, \dots \times \sigma$.



Observing parameters for UGC 6894

Length of observation	(hours)	1×12
Date of observation		18Apr91
Field center, α (1950)		11:52:50
δ (1950)		54:55:00
Central frequency	(MHz)	1416.69
V_{hel} of central channel	(km s $^{-1}$)	770
Primary beam FWHM	(arcmin)	37.4
Nr. of interferometers		40
Baselines (min-max-incr)	(m)	36-2700-72
Synthesized beam ($\alpha \times \delta$)	(arcsec)	12.5 \times 14.3
Bandwidth	(MHz)	2.5
Number of channels		127
Channel separation	(km s $^{-1}$)	4.14
Velocity resolution	(km s $^{-1}$)	8.29
rms noise in one channel	(K)	6.57
K-mJy conversion, equiv. of 1mJy/beam	(K)	3.37

Contour levels for U6894

Channel maps:	$\sigma = 3.12$ (K)
Raw continuum map:	$\sigma = 1.06$ (K)
Position-Velocity diagrams:	$\sigma = 2.72$ (K)

Results from WSRT data

From continuum map:

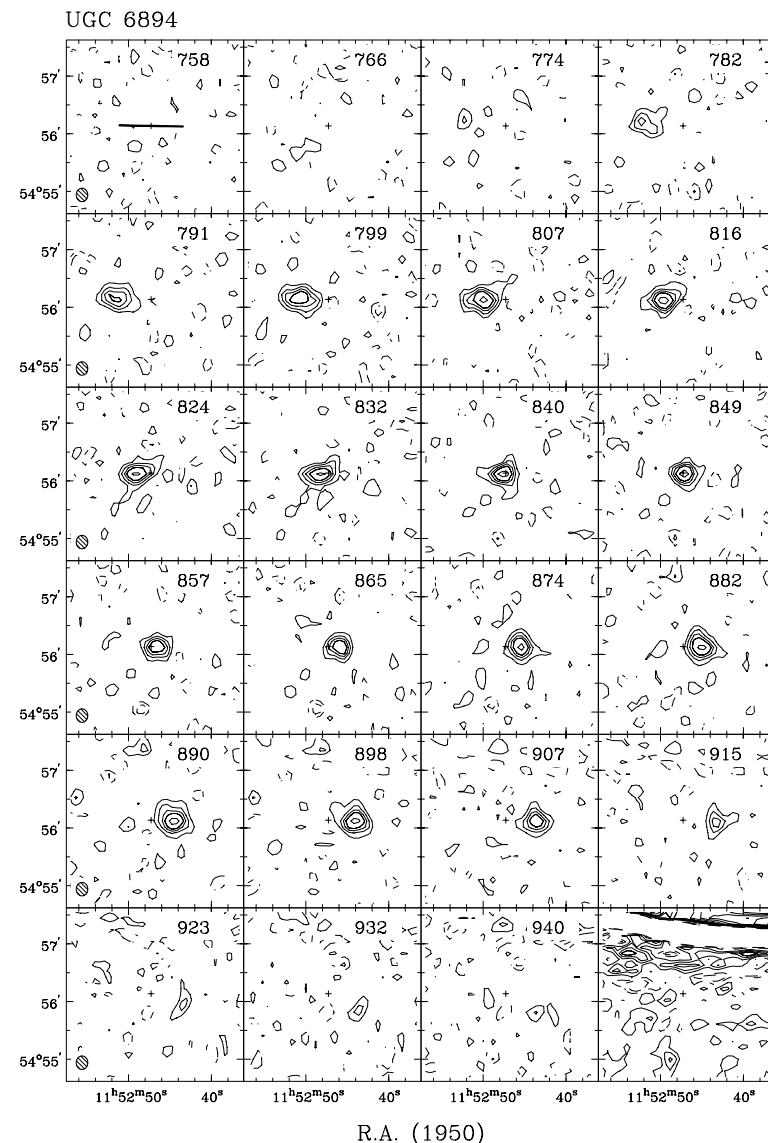
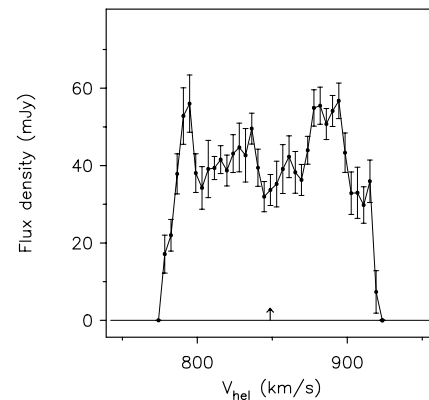
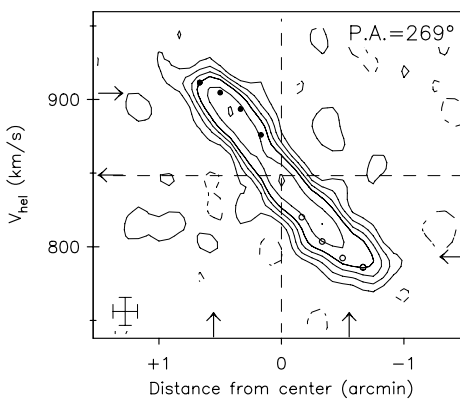
21-cm flux density	
central point source (mJy)	<1.2 (3 σ)
extended source (mJy)	<2.7 (3 σ)

From global profile:

Integrated HI-flux	(Jy km s $^{-1}$)	5.8 ± 0.2
Hel. systemic velocity	(km s $^{-1}$)	848.6 ± 1.8
HI profile width, 20%	(km s $^{-1}$)	141.8 ± 1.1
50%	(km s $^{-1}$)	132.2 ± 1.5

From XV-diagram:

Hel. systemic velocity	(km s $^{-1}$)	848.3
------------------------	-----------------	-------



Channel maps at a resolution of $12'' \times 14'' \times 19$ km s $^{-1}$.
Contour levels at $-3, -1.5, 1.5, 3, 4.5, \dots \times \sigma$.

Observing parameters for NGC 4013

Length of observation	(hours)	8.3×12
Dates of observation		Dec86-Mar87
Field center, α (1950)		11:55:40
δ (1950)		44:17:00
V_{hel} of central channel	(km s $^{-1}$)	820
Primary beam FWHM	(arcmin)	37.4
Nr. of interferometers		80
Baselines (min-max-incr)	(m)	36-2736-36
Synthesized beam ($\alpha \times \delta$)	(arcsec)	12.3 \times 17.6
Bandwidth	(MHz)	5.0
Number of channels		63
Channel separation	(km s $^{-1}$)	16.49
Velocity resolution	(km s $^{-1}$)	33.0
rms noise in one channel	(K)	0.96
K-mJy conversion, equiv. of 1mJy/beam	(K)	2.78

Contour levels for N4013

Channel maps:	$\sigma = 0.96$ (K)
Raw continuum maps:	$\sigma = 0.47$ (K)
Position-Velocity diagram:	$\sigma = 0.84$ (K)

Results from WSRT data

From continuum map:

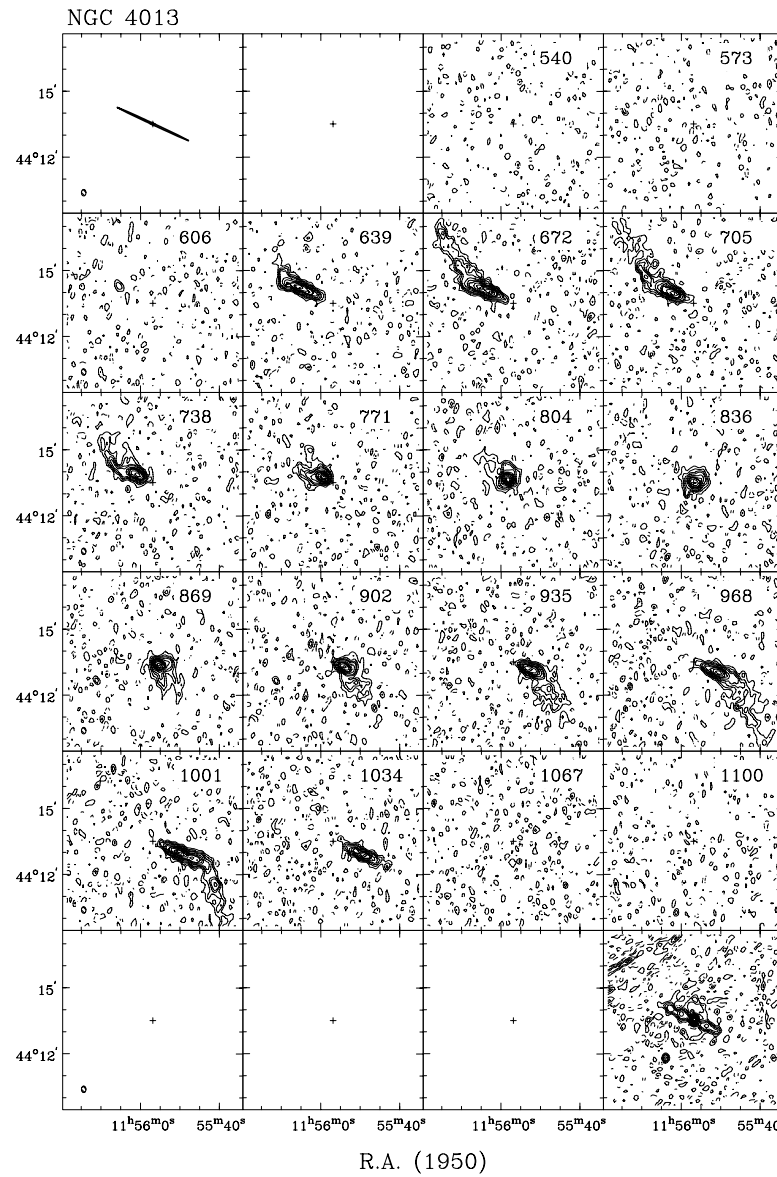
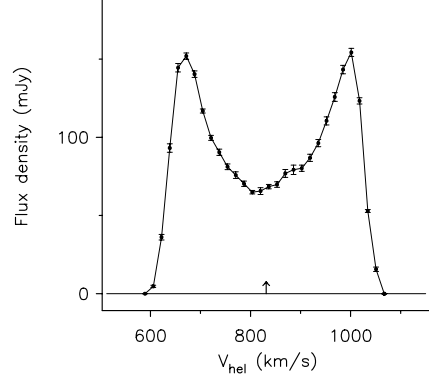
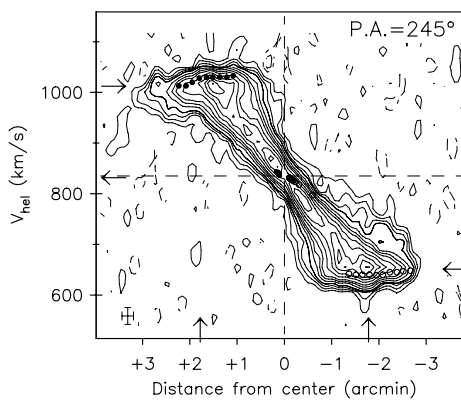
21-cm flux density	(mJy)	36.3 ± 0.8
Central point source position		
α (1950)		11:55:56.8
δ (1950)		44:13:33

From global profile:

Integrated HI-flux	(Jy km s $^{-1}$)	41.5 ± 0.2
Hel. systemic velocity	(km s $^{-1}$)	831.3 ± 0.6
HI profile width, 20%	(km s $^{-1}$)	425.0 ± 0.9
50%	(km s $^{-1}$)	395.0 ± 0.8

From XV-diagram:

Hel. systemic velocity	(km s $^{-1}$)	835 ± 3
------------------------	-----------------	-------------



Channel maps at a resolution of $12'' \times 17'' \times 33$ km s $^{-1}$.
Contour levels at -3, -1.5 (dashed), 1.5, 3, 4.5, ... σ .

Observing parameters for UGC 7089

Length of observation	(hours)	1×12
Date of observation		22 Dec 94
Field center, α (1950)		12:04:32
δ (1950)		43:17:41
Central frequency	(MHz)	1416.49
V_{hel} of central channel	(km s $^{-1}$)	850
Primary beam FWHM	(arcmin)	37.4
Nr. of interferometers		40
Baselines (min-max-incr)	(m)	36-2700-72
Synthesized beam ($\alpha \times \delta$)	(arcsec)	11.9 \times 17.9
Bandwidth	(MHz)	5.0
Number of channels		127
Channel separation	(km s $^{-1}$)	8.29
Velocity resolution	(km s $^{-1}$)	9.95
rms noise in one channel	(K)	8.34
K-mJy conversion, equiv. of 1 mJy/beam	(K)	2.83

Note: To achieve a sufficient velocity resolution over a 5 MHz bandwidth, only the XX dipoles could be correlated due to limitations of the backend.

Results from WSRT data

From continuum map:

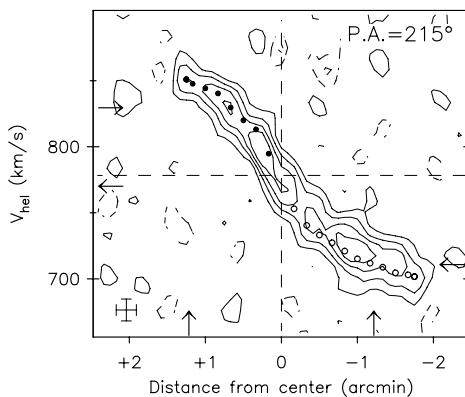
21-cm flux density	
central point source (mJy)	<1.2 (3 σ)
extended source (mJy)	<3.4 (3 σ)

From global profile:

Integrated HI-flux	(Jy km s $^{-1}$)	17.0 ± 0.6
Hel. systemic velocity	(km s $^{-1}$)	770.0 ± 1.5
HI profile width, 20%	(km s $^{-1}$)	156.7 ± 1.7
50%	(km s $^{-1}$)	97.7 ± 3.0

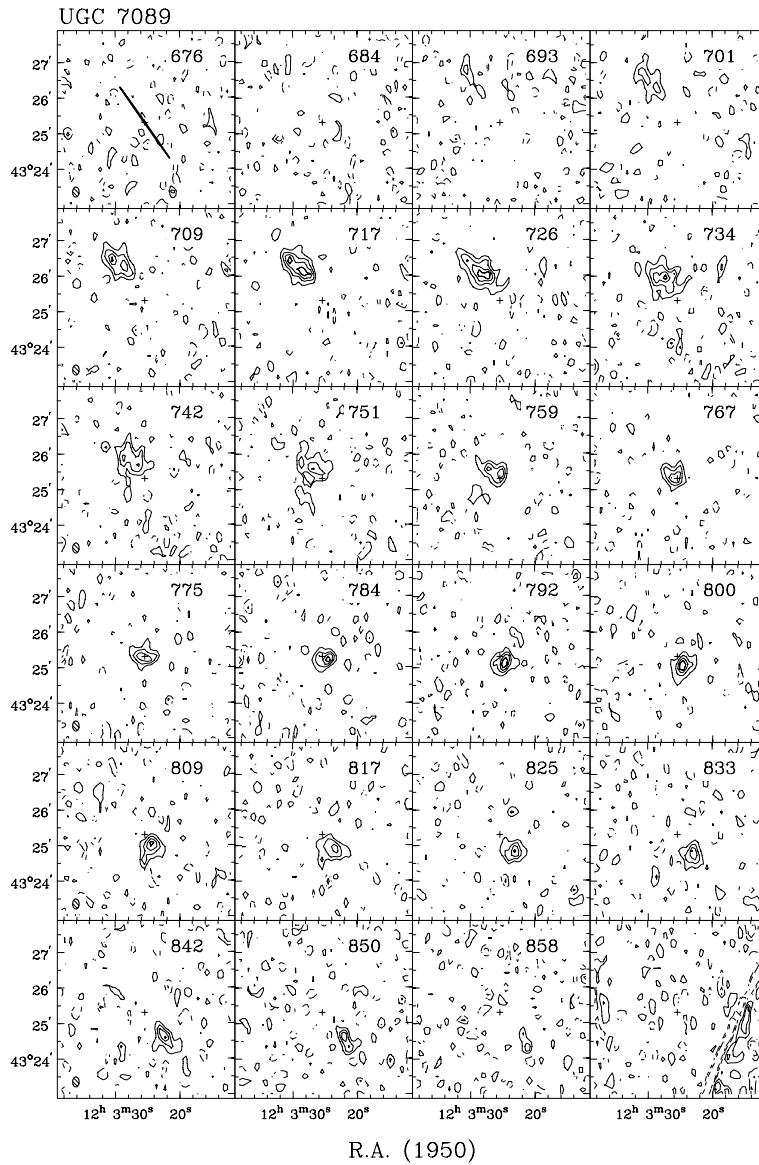
From XV-diagram:

Hel. systemic velocity	(km s $^{-1}$)	778.3
------------------------	-----------------	-------

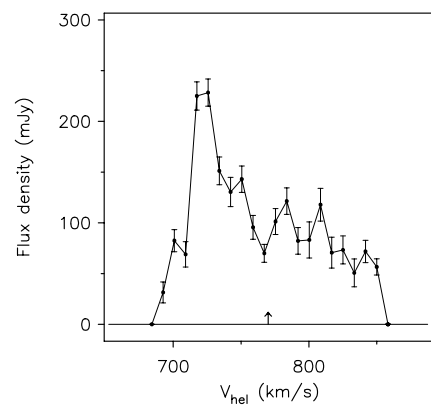


Contour levels for U7089

Channel maps:	$\sigma = 5.09$ (K)
Raw continuum map:	$\sigma = 1.13$ (K)
Position-Velocity diagram:	$\sigma = 4.52$ (K)



Note: This galaxy is a member of a rather tight group within the Ursa Major cluster. The group is dominated by the S0 system N4111 and several dwarf galaxies (U7094, N4117, N4118 and 1203+43). N4111 and N4118 were not detected in the HI line. UGC 7089 is strongly lopsided both optically and in the distribution of the HI gas which is more extended on the approaching side. The rotation curve, however, is quite symmetric and does not reach the flat part on either side of the galaxy.



Channel maps at a resolution of $11'' \times 17'' \times 17$ km s $^{-1}$.
Contour levels at -3, -1.5 (dashed), 1.5, 3, 4.5, ... σ .

Observing parameters for UGC 7094

Length of observation	(hours)	1×12
Date of observation		22Dec94
Field center, α (1950)		12:04:32
δ (1950)		43:17:41
Central frequency	(MHz)	1416.49
V_{hel} of central channel	(km s $^{-1}$)	850
Primary beam FWHM	(arcmin)	37.4
Nr. of interferometers		40
Baselines (min-max-incr)	(m)	36-2700-72
Synthesized beam ($\alpha \times \delta$)	(arcsec)	11.9 \times 17.9
Bandwidth	(MHz)	5.0
Number of channels		127
Channel separation	(km s $^{-1}$)	8.29
Velocity resolution	(km s $^{-1}$)	9.95
rms noise in one channel	(K)	8.34
K-mJy conversion, equiv. of 1mJy/beam	(K)	2.83

Note: To achieve a sufficient velocity resolution over a 5 MHz bandwidth, only the XX dipoles could be correlated due to limitations of the backend.

Results from WSRT data

From continuum map:

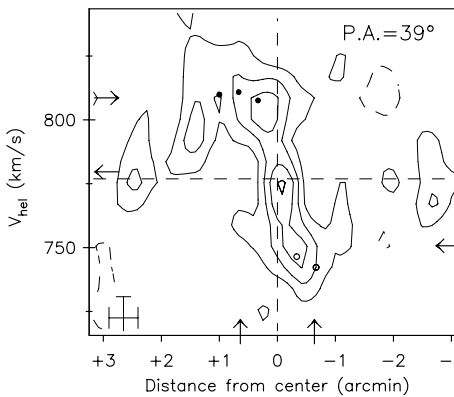
21-cm flux density	
central point source (mJy)	<1.2 (3 σ)
extended source (mJy)	<2.6 (3 σ)

From global profile:

Integrated HI-flux (Jy km s $^{-1}$)	2.9 ± 0.2
Hel. systemic velocity (km s $^{-1}$)	779.6 ± 1.6
HI profile width, 20% (km s $^{-1}$)	83.7 ± 1.7
50% (km s $^{-1}$)	71.9 ± 5.5

From XV-diagram:

Hel. systemic velocity (km s $^{-1}$)	776.9
--	-------

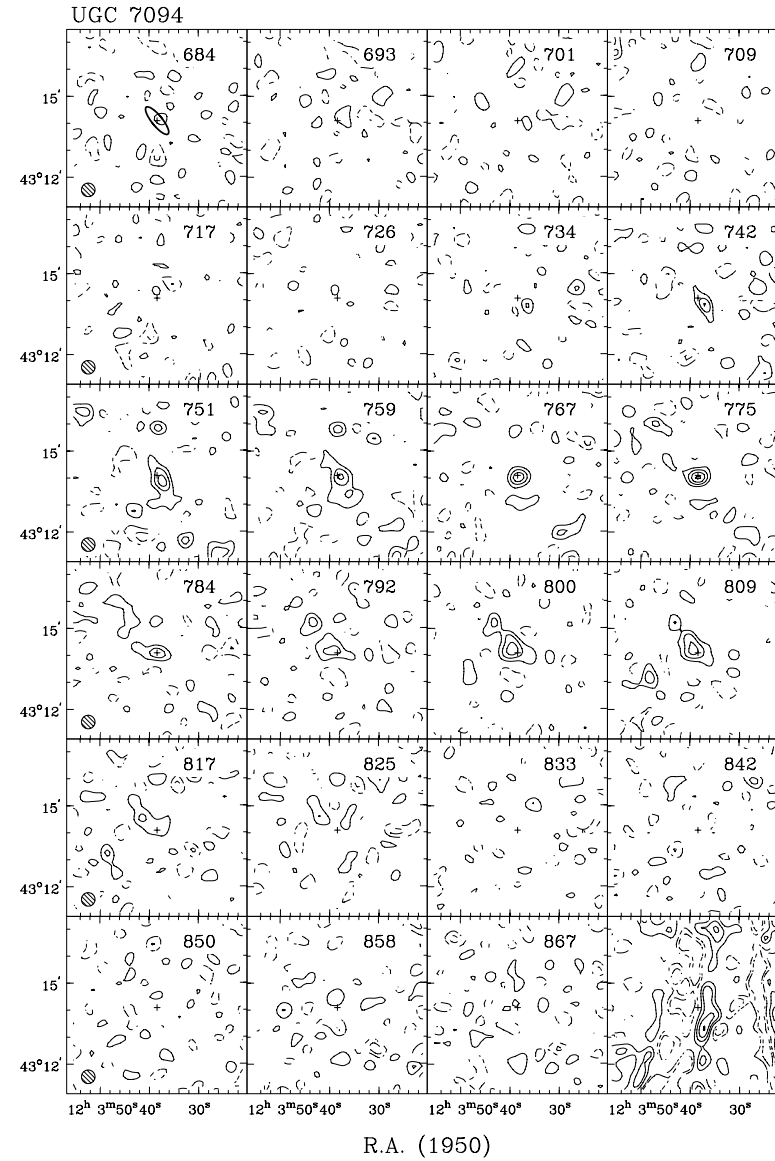
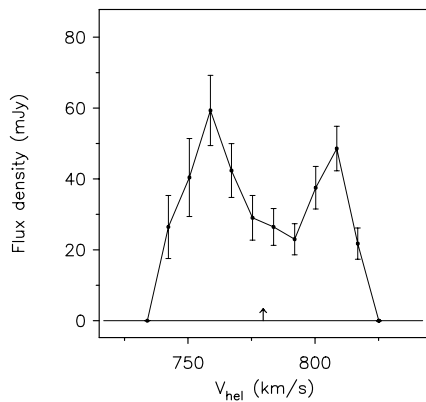


Contour levels for U7094

Channel maps:	$\sigma=1.57$ (K)
Raw continuum map:	$\sigma=0.36$ (K)
Position-Velocity diagram:	$\sigma=1.54$ (K)

Note: This edge-on galaxy is a member of a rather tight group within the Ursa Major cluster. The group is dominated by the S0 system N4111 and several dwarf galaxies (U7089, N4117, N4118 and 1203+43). N4111 and N4118 were not detected in the HI line.

The position-velocity diagram seems to suggest that the projected rotation curve of UGC 7094 reaches a maximum within 1 arcmin from the center and then declines to nearly zero at 2.5 arcmin from the center. This effect could be caused by a warp which reaches nearly face-on at the largest radii. However, the signal-to-noise level is too low to validate any model. 1203+43 is located only 5 arcmin to the south-west while N4111 and U7089 lie 11 arcmin to the north and nort-east respectively.



Channel maps at a resolution of $30'' \times 30'' \times 17$ km s $^{-1}$.

Contour levels at -3, -1.5 (dashed), 1.5, 3, 4.5, ... σ .

Observing parameters for NGC 4117

Length of observation	(hours)	1×12
Date of observation		22Dec94
Field center, α (1950)		12:04:32
δ (1950)		43:17:41
Central frequency	(MHz)	1416.49
V_{hel} of central channel	(km s $^{-1}$)	850
Primary beam FWHM	(arcmin)	37.4
Nr. of interferometers		40
Baselines (min-max-incr)	(m)	36-2700-72
Synthesized beam ($\alpha \times \delta$)	(arcsec)	11.9 \times 17.9
Bandwidth	(MHz)	5.0
Number of channels		127
Channel separation	(km s $^{-1}$)	8.29
Velocity resolution	(km s $^{-1}$)	9.95
rms noise in one channel	(K)	8.34
K-mJy conversion, equiv. of 1mJy/beam	(K)	2.83

Note: To achieve a sufficient velocity resolution over a 5 MHz bandwidth, only the XX dipoles could be correlated due to limitations of the backend.

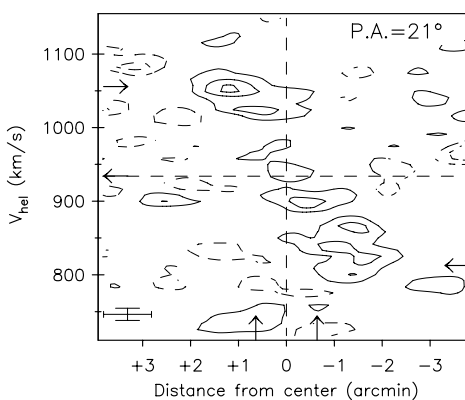
Results from WSRT data

From continuum map:

21-cm flux density	(mJy)	3.7 ± 1.2
Central point source position		
α (1950)	12:05:14.0	
δ (1950)	43:24:17	

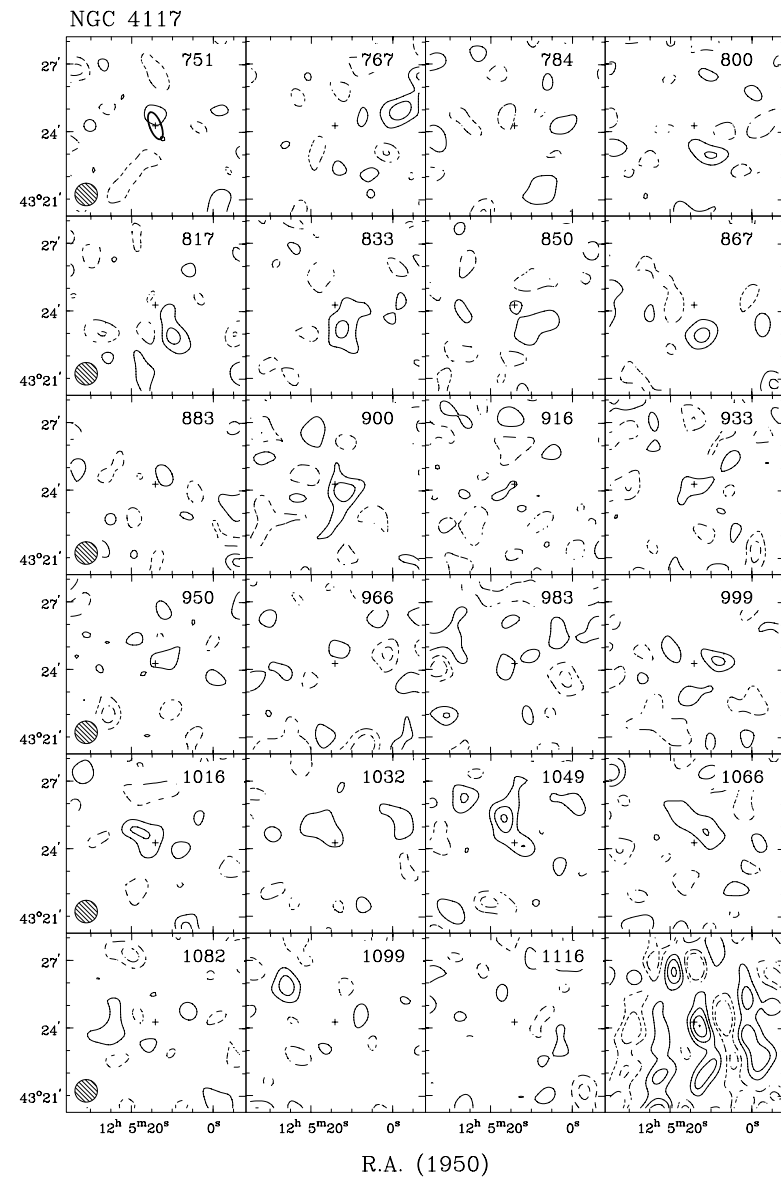
From global profile:

Integrated HI-flux	(Jy km s $^{-1}$)	6.9 ± 1.1
Hel. systemic velocity	(km s $^{-1}$)	934.0 ± 1.5
HI profile width, 20%	(km s $^{-1}$)	289.4 ± 7.5
50%	(km s $^{-1}$)	260.3 ± 5.2



Contour levels for N4117

Channel maps:	$\sigma = 0.56$ (K)
Raw continuum map:	$\sigma = 0.12$ (K)
Position-Velocity diagram:	$\sigma = 0.55$ (K)

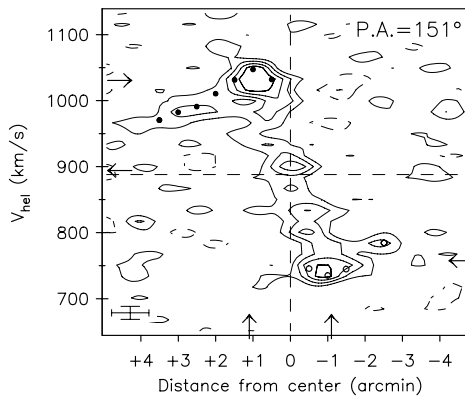


Channel maps at a resolution of $60'' \times 60'' \times 17$ km s $^{-1}$.
Contour levels at $-3, -1.5, 1.5, 3, 4.5, \dots \times \sigma$.

Observing parameters for NGC 4138

Length of observation	(hours)	1×12
Date of observation		19Dec94
Field center, α (1950)		12:06:59
δ (1950)		43:54:57
Central frequency	(MHz)	1416.26
V_{hel} of central channel	(km s $^{-1}$)	900
Primary beam FWHM	(arcmin)	37.4
Nr. of interferometers		40
Baselines (min-max-incr)	(m)	36-2700-72
Synthesized beam ($\alpha \times \delta$)	(arcsec)	12.1 \times 17.3
Bandwidth	(MHz)	5.0
Number of channels		63
Channel separation	(km s $^{-1}$)	16.59
Velocity resolution	(km s $^{-1}$)	19.91
rms noise in one channel	(K)	4.89
K-mJy conversion, equiv. of 1mJy/beam	(K)	2.88

Results from WSRT data

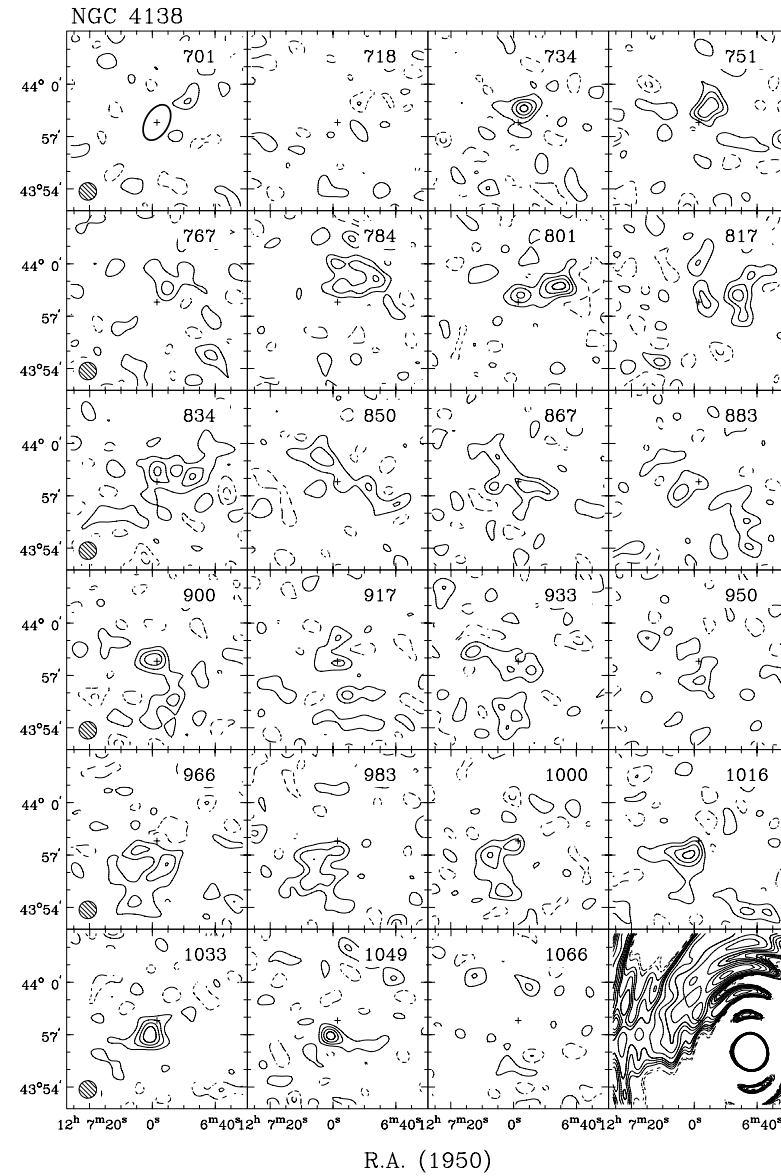
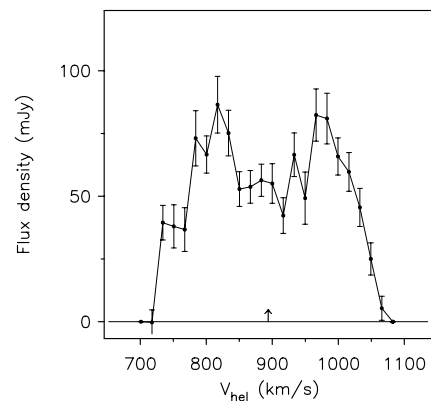
From continuum map:21-cm flux density (mJy) 16.7 ± 4.6 From global profile:Integrated HI-flux (Jy km s $^{-1}$) 19.2 ± 0.7 Hel. systemic velocity (km s $^{-1}$) 893.8 ± 3.9 HI profile width, 20% (km s $^{-1}$) 331.6 ± 4.5 50% (km s $^{-1}$) 266.0 ± 7.8 From XV-diagram:Hel. systemic velocity (km s $^{-1}$) 888.0

Contour levels for N4138

Channel maps:	$\sigma=0.58$ (K)
Raw continuum map:	$\sigma=0.29$ (K)
Position-Velocity diagrams:	$\sigma=0.57$ (K)

Note: A large fraction (20%) of the stars in this early type spiral is counter rotating. For that reason, N4138 has been studied extensively in the past. Jore *et al* (1996) have observed this galaxy at 21cm with the VLA and obtained HI data with high S/N. For deprojection of the rotation curve derived from the position-velocity diagram of our WSRT data, the optical position angle and inclination were used for the inner regions. In the outer regions, the position angle and inclination from the velocity field of Jore *et al* were used. The HI disk is strongly warped toward face-on but not strong enough to account for the observed decline.

The strong point source at 3 arcmin to the SW is 3C378.6.



Channel maps at a resolution of $60'' \times 60'' \times 20$ km s $^{-1}$.
Contour levels at $-3, -1.5, 1.5, 3, 4.5, \dots \times \sigma$.

Observing parameters for NGC 4218

Length of observation	(hours)	1×12
Date of observation		18Jul92
		14Aug92
Field center, α (1950)		12:13:18
δ (1950)		48:25:00
Central frequency	(MHz)	1416.84
V_{hel} of central channel	(km s $^{-1}$)	740
Primary beam FWHM	(arcmin)	37.4
Nr. of interferometers		40
Baselines (min-max-incr)	(m)	36-2700-72
Synthesized beam ($\alpha \times \delta$) (arcsec)		11.9 \times 16.4
Bandwidth	(MHz)	2.5
Number of channels		127
Channel separation	(km s $^{-1}$)	4.14
Velocity resolution	(km s $^{-1}$)	8.29
rms noise in one channel	(K)	5.71
K-mJy conversion, equiv. of 1mJy/beam	(K)	3.09

Contour levels for N4218

Channel maps:	$\sigma = 3.71$ (K)
Raw continuum maps:	$\sigma = 1.28$ (K)
Position-Velocity diagram:	$\sigma = 3.24$ (K)

Results from WSRT data

From continuum map:

21-cm flux density (mJy) 6.3 ± 0.8

From global profile:

Integrated HI-flux (Jy km s $^{-1}$) 7.8 ± 0.2

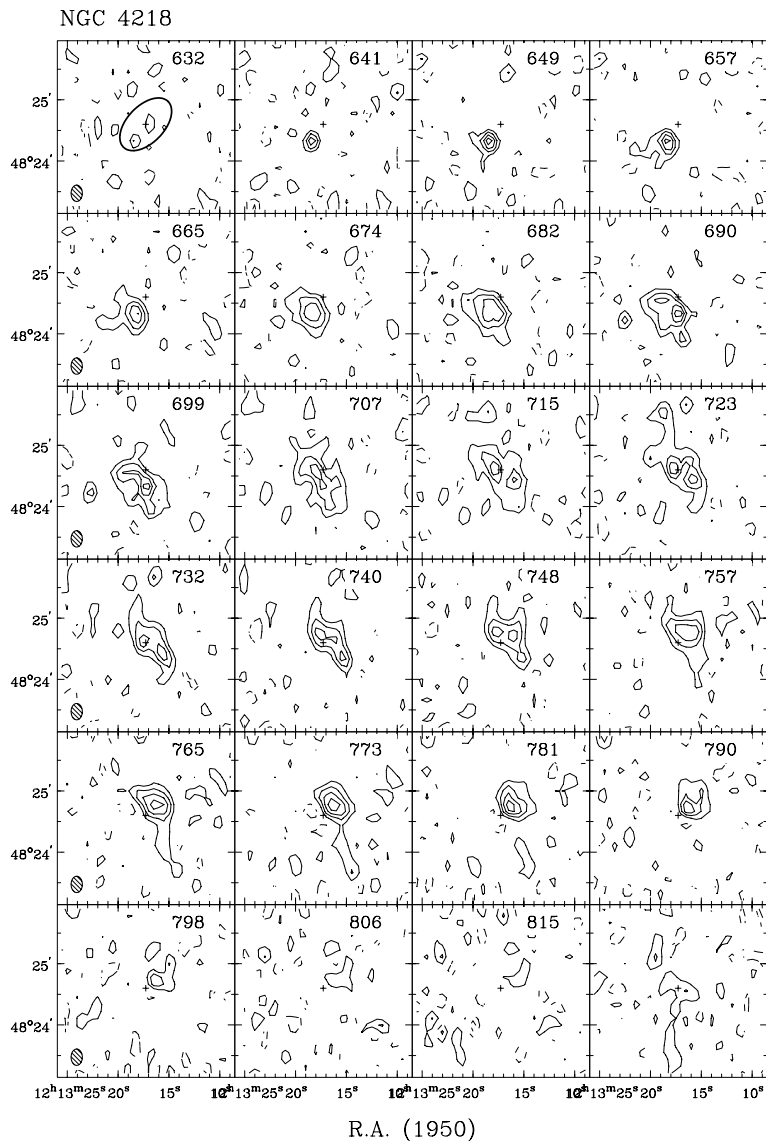
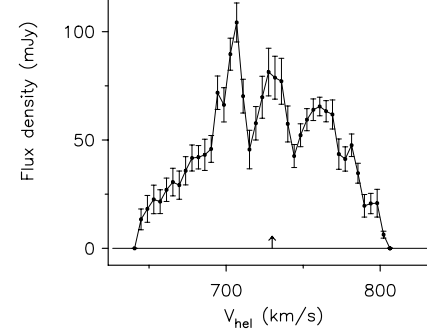
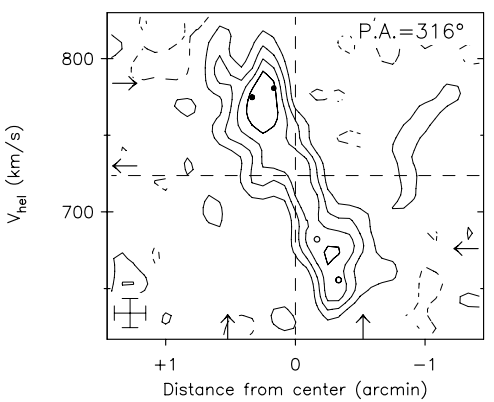
Hel. systemic velocity (km s $^{-1}$) 729.9 ± 1.7

HI profile width, 20% (km s $^{-1}$) 138.0 ± 5.0

 50% (km s $^{-1}$) 79.9 ± 1.9

From XV-diagram:

Hel. systemic velocity (km s $^{-1}$) 723.7



Channel maps at a resolution of $11'' \times 16'' \times 19$ km s $^{-1}$.

Contour levels at $-3, -1.5$ (dashed), $1.5, 3, 4.5, \dots \times \sigma$.

Observing parameters for NGC 4220

Length of observation	(hours)	1×12
Date of observation		01Jul92 14Aug92
Field center, α (1950)		12:13:18
δ (1950)		48:25:00
Central frequency	(MHz)	1416.82
V_{hel} of central channel	(km s $^{-1}$)	740
Primary beam FWHM	(arcmin)	37.4
Nr. of interferometers		40
Baselines (min-max-incr)	(m)	36-2700-72
Synthesized beam ($\alpha \times \delta$) (arcsec)		12.3×16.5
Bandwidth	(MHz)	5.0
Number of channels		63
Channel separation	(km s $^{-1}$)	16.57
Velocity resolution	(km s $^{-1}$)	33.14
rms noise in one channel	(K)	2.97
K-mJy conversion, equiv. of 1mJy/beam	(K)	2.97

Contour levels for N4220

Channel maps:	$\sigma=0.29$ (K)
Raw continuum maps:	$\sigma=0.18$ (K)
Position-Velocity diagram:	$\sigma=0.28$ (K)

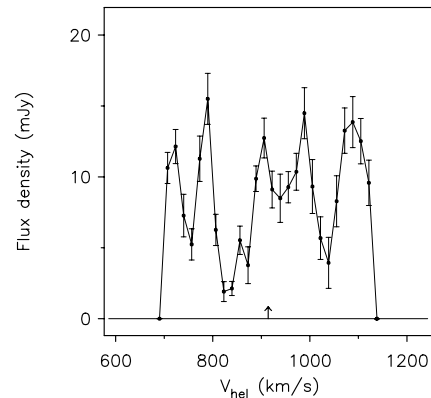
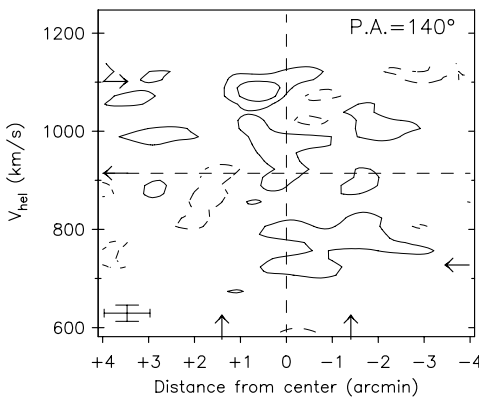
Results from WSRT data

From continuum map:

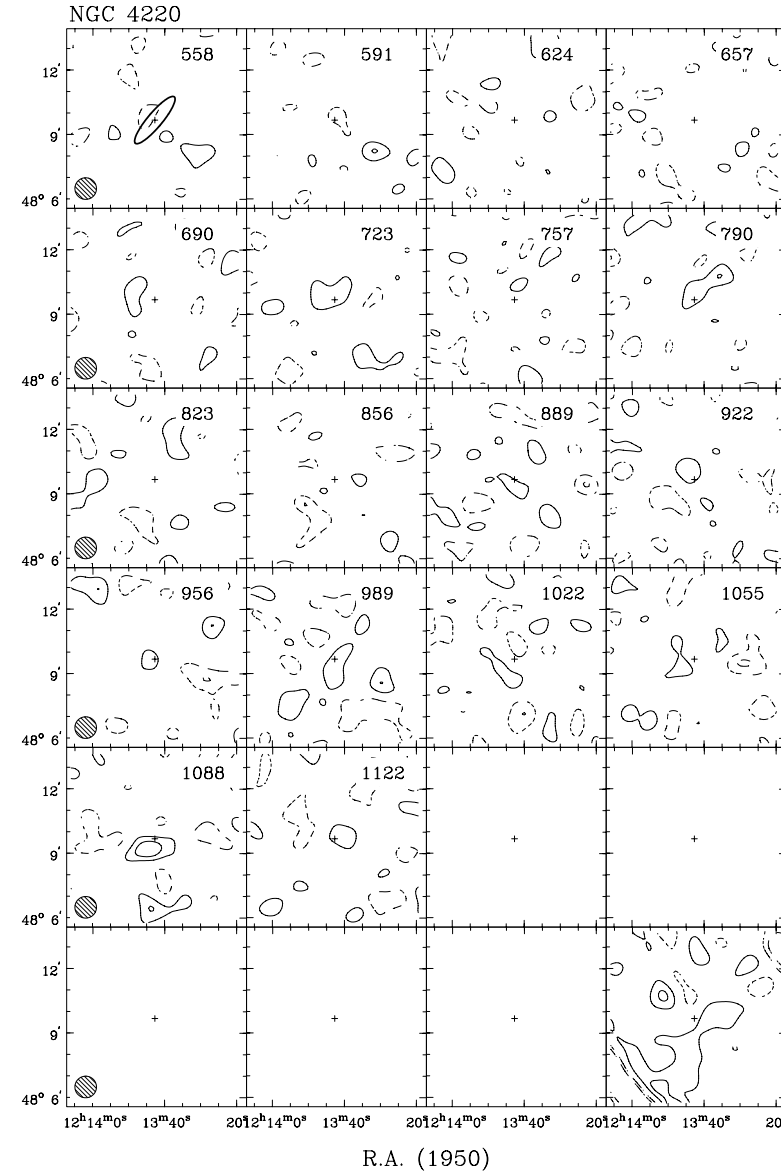
21-cm flux density	
central point source (mJy)	<0.9 (3 σ)
extended source (mJy)	<4.9 (3 σ)

From global profile:

Integrated HI-flux (Jy km s $^{-1}$)	4.4 ± 0.3
Hel. systemic velocity (km s $^{-1}$)	914.2 ± 1.2
HI profile width, 20% (km s $^{-1}$)	438.1 ± 1.3
50% (km s $^{-1}$)	423.3 ± 3.3



Note: This early type spiral has a very low HI content. The gas is barely detected and occurs only inside the optical region. No meaningful rotation curve could be derived from the position-velocity diagram.



Channel maps at a resolution of $60'' \times 60'' \times 33$ km s $^{-1}$.
Contour levels at $-3, -1.5, 1.5, 3, 4.5, \dots \times \sigma$.